Summer 9-1-2014

Multi- Modal Characterization Of Left Ventricular Diastolic Filling Physiology

Erina Ghosh
Washington University in St. Louis

Follow this and additional works at: https://openscholarship.wustl.edu/etd

WASHINGTON UNIVERSITY

School of Engineering and Applied Sciences
Department of Biomedical Engineering

Dissertation Examination Committee:
Sándor J. Kovács, Chair
Guy M. Genin
James G. Miller
Samuel A. Wickline
Frank C-P Yin

Multi- Modal Characterization Of Left Ventricular Diastolic Filling Physiology

By

Erina Ghosh

A dissertation presented to the
Graduate School of Arts and Sciences
Of Washington University in
partial fulfillment of the
requirements for the degree
of Doctor of Philosophy

August 2014

Saint Louis, Missouri

Table Of Contents

iii

List of Figures

List of Tables

Das, who was my mentor in high school. He made me believe in myself and ignited my passion for mathematics and sciences.

<div align="right">

Erina Ghosh

</div>

Washington University in St. Louis

August 2014

ABSTRACT OF THE DISSERTATION

Multi- Modal Characterization Of Left Ventricular Diastolic Filling Physiology

By

Erina Ghosh

Doctor of Philosophy in Biomedical Engineering

Washington University in St. Louis, 2014

Professor Sándor J. Kovács, Chair

Multiple modalities are clinically used to quantify cardiovascular function. Most clinical indexes derived from these modalities are empirically derived or correlation- based rather than causality based. Hence these indexes don't provide insight into cardiac physiology and the mechanism of dysfunction. Our group has previously developed and validated a mathematical model using a kinematic paradigm of suction- initiated ventricular filling to understand the mechanics of early transmitral flow and the associated physiology/ pathophysiology. The model characterizes the kinematics of early transmitral flow analogous to a damped simple harmonic oscillator with lumped parameters- ventricular stiffness, ventricular viscoelasticity/ relaxation and ventricular load.

The current research develops the theme of causal mechanism based quantification of physiology and uses the kinematic model to study intraventricular fluid mechanics in diastole. In the first project, the role of vortex rings in efficient diastolic filling was investigated. Vortex rings had been previously characterized by a dimensionless index called vortex formation time (VFT). We re- expressed VFT in terms of ventricular kinematic properties- stiffness, viscoelasticity and volumetric preload, using the kinematic model. This $VFT_{kinematic}$ could be

calculated using data from a clinical echocardiographic study. The VFT$_{kinematic}$ was a sensitive to physiologic changes as verified by its correlation with a clinically used echo- based index of filling pressure. Additionally, we demonstrated that VFT$_{kinematic}$, by factoring the ventricular expansion rate, could differentiate between normal filling pattern and pseudonormal filling pattern which is characteristic of moderate DD.

Continuing on our study of intraventricular fluid mechanics, we next studied the development of vortex ring in the ventricle. We discovered that as the vortex ring develops, the leading edge of the circulating flow passes through the main inflow tract. This causes an extra flow wave recorded in transmitral Doppler echocardiography (in addition to early and late filling waves) that had been observed previously. By using cardiac magnetic resonance (CMR) and echocardiography to independently measure intraventricular vortexes we were able to provide a causal explanation for the extra flow wave and its clinical consequences.

We developed another approach to quantify the effect of chamber kinematics on filling via directional flow impedances. In the ventricle, both pressure and flow rate are oscillatory and pressure oscillations cause flow rate changes. Hence a frequency based approach via impedance, to quantify the relationship between pressure and flow rate is intuitive. We developed expressions for longitudinal and transverse flow impedances which could be computed from cardiac catheterization and echocardiographic data. Longitudinal and transverse flow impedances allowed us to quantify the previously observed directionality of filling as a function of harmonics and use it as an index to measure pathophysiologic changes.

While fluid mechanics based indexes provide a method to evaluate LV chamber kinematics in diastole, an alternate approach for DF quantification is LV hemodynamic assessment. Since, LV filling is influenced by pressure changes before and during filling, we

investigated the spatial pressure gradient in the LV. We measured the pressure difference between the LV apex and mid-LV using catheterization and we found a larger gradient exists during isovolumic relaxation (2- 3 times) as compared to filling. Additionally, the rate of pressure decay as quantified by different models of relaxation was also significantly different at the two locations.

Additionally, we developed a new method for load independent hemodynamic analysis of the cardiac cycle. Load represents the pressure against which the ventricle has to fill and eject and most LV function indexes are load dependent, which can confound the diagnosis of dysfunction. We computed load independent cardiac cycle hemodynamics by normalizing LV pressure and the rate of change of pressure (dP/dt). Normalization revealed the presence of conserved kinematics during isovolumic relaxation particularly the normalized pressure at peak negative dP/dt while a similar feature was not observed during the contraction. These studies demonstrate the advantage of mechanism based approaches to quantify diastolic physiology.

Chapter 1: Introduction

1.1 Introduction

Assessing cardiac function, specifically diastolic function (DF) is an essential step in diagnosing the state of diastolic dysfunction (DD). DD is a precursor to both diastolic heart failure (DHF) which is also known as heart failure with normal/ preserved ejection fraction (HFnEF/ HFpEF) and systolic heart failure (SHF) which is alternately known as heart failure with reduced ejection fraction (HFrEF) [1, 2]. The gold standard for DF quantification are data obtained by invasive measurement of diastolic pressures by cardiac catheterization [3]. However, Doppler echocardiography remains the clinically preferred method for noninvasive DF quantification [4, 5]. A multitude of clinical diagnostic indexes have been described in literature. Most of these indexes are derived using correlative methods. The drawback of using purely correlative methods is that it doesn't take into account the interdependency between various parameters thus reducing the power of the method. Moreover, correlative-method based indexes provide no insight into DF mechanism.

Causal mechanisms on the other hand incorporate physiology and reveal mechanistic insight and hence they are more robust. Our laboratory has been using causal mechanism based modeling to model cardiac function for several years. Numerous indexes have been developed and validated [6-11] which provide mechanistic insight into physiology of diastole. Continuing on the theme of modeling physiology using mathematical and physical principles, this thesis aims to quantify the relationship between intraventricular flow and DF. In addition we also examine isovolumic relaxation (IVR) phase of diastole using pressure phase plane analysis. We use the current knowledge of cardiovascular physiology along with principles of fluid mechanics, physics and mathematics to develop mechanism-based hypotheses. We validate our hypotheses using clinical data obtained using echocardiography, cardiac catheterization and cardiac

magnetic resonance imaging. Since this work combines various aspects of the cardiac physiology such as electrical, mechanical and different levels of complexity from the ventricle to the intracellular processes, it is useful to review the basics of cardiac physiology. Hence we present a concise review of the aspects of cardiac physiology which are discussed in the subsequent chapters.

1.2 Cardiac structure

The heart is divided into 4 chambers- the right atrium (RA) and the right ventricle (RV) on the
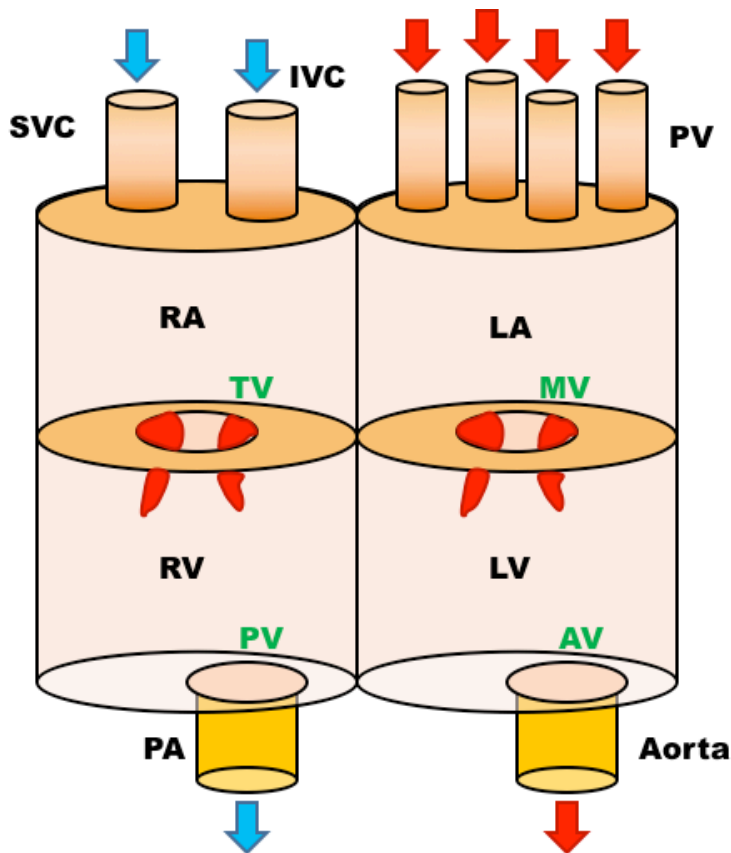
Fig 1.1: Schematic representation of the four- chambered heart. Each cylinder represents the left and right side of the heart. Deoxygenated blood flow is denoted by blue arrows. Oxygenated blood is denoted by red arrows. Valves are marked in green font. SVC = superior vena cava, IVC = inferior vena cava, TV = tricuspid valve, PV = pulmonic valve, PA = pulmonary artery, PV (black font) = pulmonary vein, MV = mitral valve, AV = aortic valve. See text for details.

right side and the left atrium (LA) and the left ventricle (LV) on the left side. The right side of the heart receives deoxygenated blood from the systemic circulation and sends it to the lungs via pulmonary arteries. Specifically, the RA receives blood through the superior and inferior vena cava which enters the RV through the tricuspid valve. The RV then acts as a volume pump and

ejects this blood into the pulmonary artery via the pulmonic valve. The blood gets oxygenated in the lungs and it is then carried into the LA by the pulmonary veins. From the LA the blood is aspirated into the LV via the mitral valve which pumps it back to the systemic circulation through the aortic valve. A schematic diagram of this process is shown below in Fig 1.1.

The right and left circulations are separate. The right and left side of the heart can be thought of as 2 different chambers connected through the lung. While there is no direct connection between the right heart and the left heart, the 2 sides communicate indirectly through the septum via pressure and volume changes. The four chambers are enclosed in the pericardium which has a fixed volume. Hence any changes in pressure and volume to one side are reflected on the other side.

1.2.1 Cellular organization

The bulk of the myocardium is made up of contractile cardiomyocytes. These cells are the basic force- generating unit in the heart. Cardiomyocyte share the properties of both skeletal and smooth muscle cells. Cardiomyocytes are striated with dark and light bands due to the parallel arrangement of actin and myosin filaments. Force is generated in the cardiomyocyte in the myofibrils. A schematic diagram is shown in Fig 1.2. Myofibrils are comprised of sarcomeres. Each sarcomere is bound by the Z-discs (not shown) which are a part of the I-band which transmits the generated force. The thin actin filaments and the thick myosin filaments are arranged in a repeating pattern along the length of the sarcomere. The thin filaments are anchored in the Z-discs. The thick filaments are linked together at the M- band. The thick and the think filaments interact together through the proteins troponin and tropomyosin and connect the M- and the Z- bands [12]. These sarcomeres form the core force- generating portion of the heart.

4

Another important organelle in the cardiomyocytes is the sarcoplasmic reticulum. The
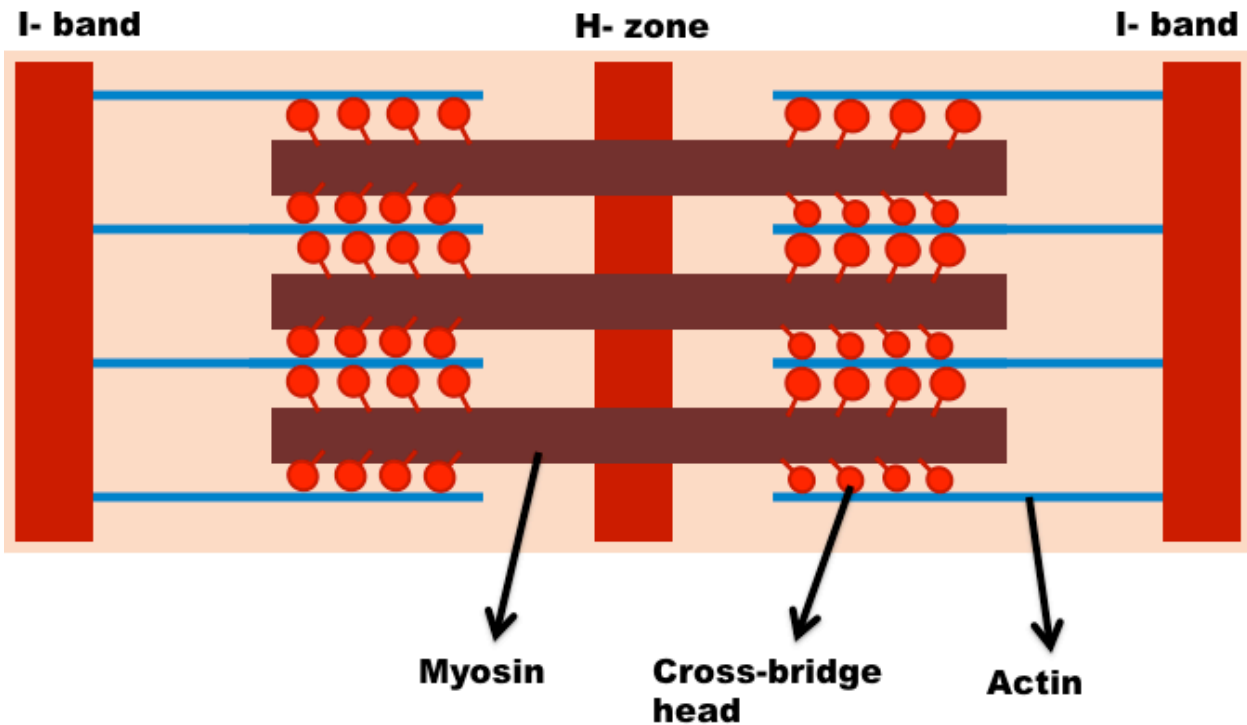
Fig 1.2: Schematic representation of a sarcomere which actin, myosin and cross- bridges. See text for details

sarcoplasmic reticulum is a membrane- bound organelle which stores intracellular calcium and regulates the concentration of calcium in the cytoplasm. It plays a vital role in excitation-contraction coupling and in the regulating the contractile properties of the cardiomyocytes. The sarcoplasmic reticulum release stored calcium in response to changes in the membrane potential. These membrane potential changes are transmitted to the sarcoplasmic reticulum via t-tubules which are invaginations of the cellular membrane.

1.2.2 Ventricular myoarchitecture

The end of each cardiomyocyte branches and is attached to adjacent cardiomyocytes creating a 3 dimensional network of fibers. Myofibrils are formed by myocytes joined end to end. Groups of myocytes are surrounded by fibrous connective tissue made up of collagen [13]. The collagen

forms a structural matrix of the myocardium [14]. The collagen matrix has 3 components- the epimysium, perimysium and endomysium. The epimysium forms a sheath which surrounds the entire muscle, the perimysium forms extensions from the epimysium which surround groups of myofibrils and the endomysium forms the weave.

Apart from these cell types, the ventricular tissue also contains pacemaker cells and a collection of cells which specialize in electrical conduction. These comprise of the bundle of His and the Purkinje fibers. The bundle of His transmits impulses from the atrioventricular node to ventricles. The bundle of His branches off into the right and left bundle and which then give rise to thin filaments called the Purkinje fibers. The Purkinje fibers are located in the subendocardium and they conduct electrical potentials quickly throughout the myocardium.

1.3 Cardiac function

1.3.1 Cardiac cycle

The cardiac cycle can be divided into 2 phases- systole and diastole. Systole begins when the ventricles contract and increase pressure. The initial part of systole occurs when all the valves are closed and hence this phase is known as isovolumic contraction (IVC). As ventricular pressure rises it reaches the aortic (left side) and pulmonary artery (right side) pressure and the aortic and pulmonary valves open. This is the beginning of the ejection phase in which blood is ejected out of the ventricles into the pulmonary circulation (right side) and through the aorta to systemic circulation (left side). The maximum ventricular pressures occur during ejection and then the ventricular pressure begins to drop. When the ventricular pressure drops below the aortic and pulmonary artery pressure, the valves close. This marks the end of systole. The next part of the cardiac cycle is diastole.

At the beginning of diastole, the ventricular pressure drops and all the valves are closed. This phase is known as isovolumic relaxation (IVR). As the ventricular pressure drops below the left and right atrial pressures, the mitral and tricuspid valves respectively open and this marks the beginning of filling. Ventricular filling occurs in 2 phases. The first phase is early rapid filling which is initiated by suction. As blood is aspirated into the ventricle the pressure continues to drop while the volume of the ventricle is increasing. This creates negative chamber compliance (dP/dV <0). The early filling wave contour is determined by atrioventricular pressure gradient which is governed by left ventricular mechanics. The second phase of filling is caused by the atrial contraction (in atrial systole) which pushes in the second wave of blood into the ventricles. Filling ends when the ventricle starts contracting. This causes the mitral and tricuspid valves to close and systole begins.

1.3.2 Electrical conduction

The contraction of the heart is initiated by electrical impulses. The source of these electrical impulses in a normal heart is the sino-atrial node located in the right atrium near the superior vena cava. These primary pacemaker cells generate electrical impulses in a periodic fashion modulated by the effect of the parasympathetic and sympathetic nerves. From the primary pacemaker cells, the action potentials are transmitted to the atrioventricular (AV) node. The AV node then transmits the electrical potential to the ventricles via the bundles of His. The left and right bundles travel through the ventricular septum and at the ventricular apex, the form the Purkinje fibers. These fibers are present in the subendocardium throughout the ventricular wall and efficiently transmit the impulse to the myocardium. This activation pathway helps in synchronized contraction and relaxation of the myocardium which enables efficient filling and ejection.

The electrical activity of the heart is measured using an electrocardiogram (ECG). ECG records the electrical potentials of the heart during the cardiac cycle. Starting with the activation of the sino- atrial node, as the impulse propagates through the atria towards the AV node, it gives rise to the P-wave on the ECG. It is quickly followed by the QRS complex as the electrical action potential travels through the ventricular myocardium. The AV node also functions as a critical delay allowing the atria to contract before the ventricles contract. This delay is measured as the PR interval on the ECG. Ventricular repolarization is recorded on the ECG as the T- wave. Fig 1.3 shows a typical ECG.
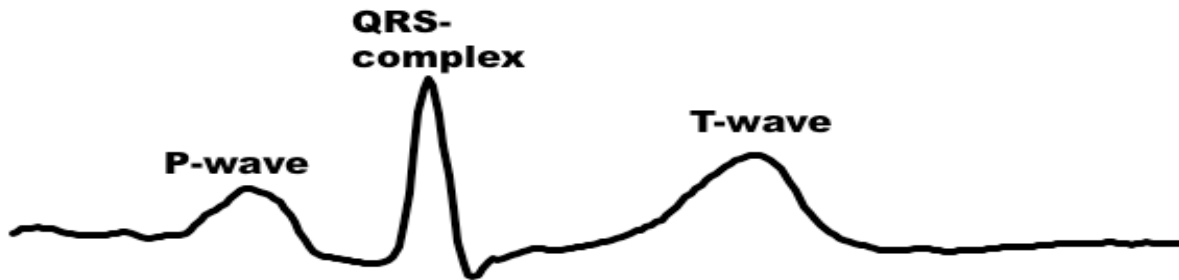
Fig 1.3: A typical electrocardiogram for one cardiac cycle. See text for details.

A common way to visualize the cardiac cycle is using a Wiggers diagram (Fig 1.4). Wiggers diagram shows the left ventricular, aortic and left atrial pressures aligned with left ventricular volumes and the electrocardiogram (ECG). The ECG QRS complex causes the ventricles depolarization at end diastole and causes the ventricles to contract. Ventricular repolarization occurs after the T-wave. Atrial depolarization is seen as the P- wave on the ECG.

1.3.3 Left ventricular function

This thesis focuses on left ventricular diastolic function. The LV is a thick walled chamber which functions as a pressure pump during systole and a volume pump during diastole. In systole the
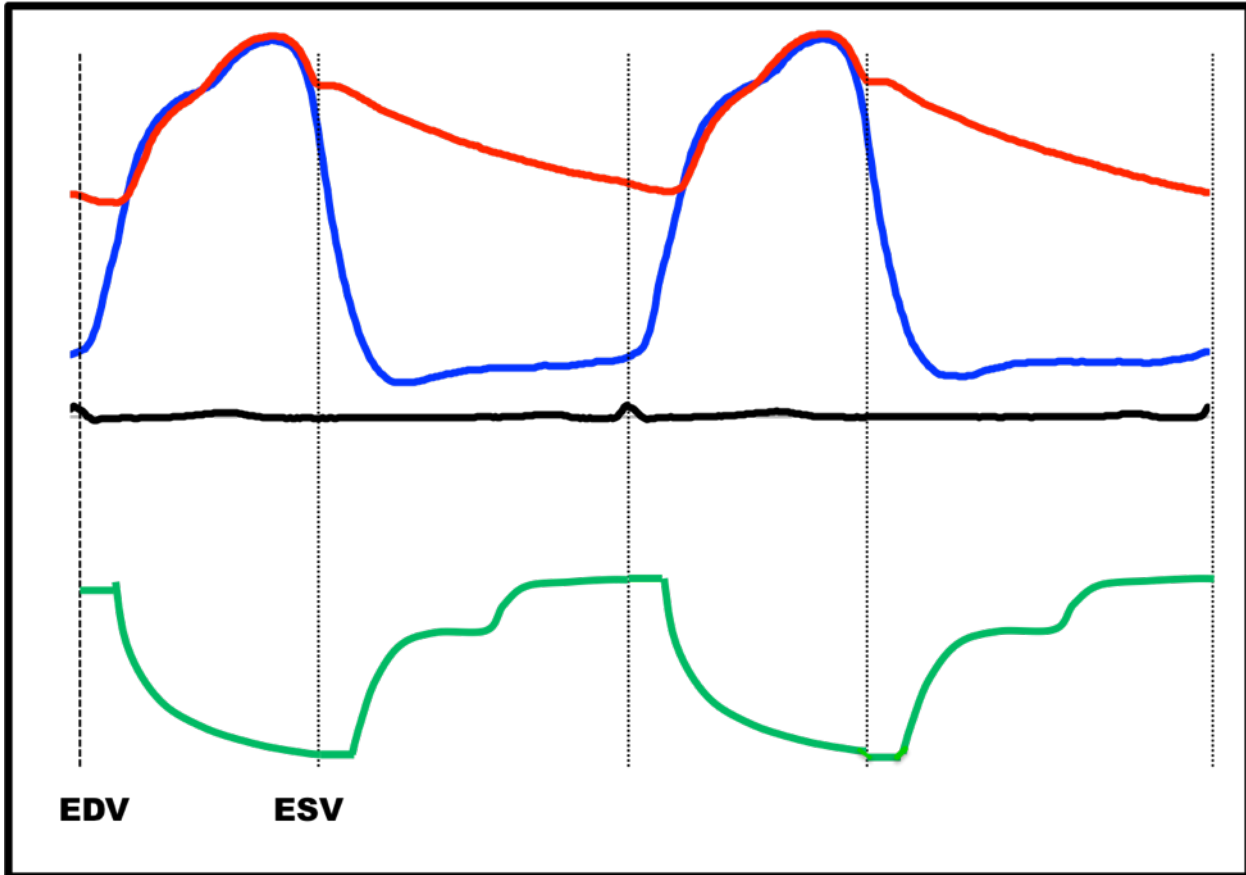
Fig 1.4: Wiggers diagram showing aortic pressure (red), LV pressure (blue), ECG (black) and LV volume (green) for 2 complete cardiac cycles. The pressures and ECG are recordings from a subject, the volume is a schematic representation of LV volume variation. EDV = End diastolic volume, ESV = End systolic volume

LV increases pressure to eject blood into the aorta. In diastole it fills by increasing its volume by expanding longitudinally into the left atrium. This is done by the mitral annular plane moving towards the left atrium and filling the LV with the blood which was previously in the left atrium. The RV is a volume pump both during diastole and systole. The RV fills and ejects primarily by changing its shape.

The LV actively contracts and relaxes and LV chamber mechanics play a crucial role in generating pressure which powers filling and ejection. The electrical activation of the

9

myocardium signals the ventricle to contract and relax. The myocardial structure and organization of the tissue play an important role in amplifying the force generated by the individual myocyte contraction. The pressure gradient generated as a result of this causes flow. The pattern of intraventricular flow is intimately connected to LV chamber mechanics. In the following sections, the cellular mechanism of contraction and relaxation, the role of myocardial tissue organization and the resultant ventricular flow patterns are described.

1.3.4 Myocyte mechanics

Cardiomyocyte contraction and relaxation occurs as a result of actin -myosin cross-bridge formation. An action potential is generated by the pacemaker cells and is transmitted to the ventricle via the electrical conduction system. The action potential travels through the cardiomyocyte via the gap junctions. The action potential depolarizes the surface membrane of the cardiomyocyte which causes calcium to enter the cells. This increase in calcium concentration is detected by the ryanodine receptors in the membrane of the sarcoplasmic reticulum. The sarcoplasmic reticulum stores calcium ions, which are released into the cytoplasm when the ryanodine receptors get activated. This increases the cytoplasmic concentration of calcium. This calcium binds to troponin calcium binding site and moves the tropomyosin off the cross-bridge binding site. This allows the cross-bridge heads of the myosin filaments to bind to actin. The cross-bridge cycle is an active process. Hydrolysis of ATP causes the cross-bridge head binds to actin. The cross-bridge head pulls the thin filament towards the M-band (center of the sarcomere). The concerted action of multiple cross-brides in the same sarcomere generates sufficient force to shorten the sarcomere. The force generated in each sarcomere combines to create ventricular contraction.

The next part of the cross-bridge cycle consists of cross-bridge detachment. ATP binds to the myosin causing the myosin head to detach. The intracellular calcium is taken up by the sarcoplasmic reticulum via the sarcoplasmic/ endoplasmic ATPase pump. Calcium is also ejected from the cell via the sodium/ calcium exchanger as the cell membrane repolarizes.

1.3.5 Ventricular wall mechanics

Our understanding of the myocardial architecture is continuously evolving. The ventricular myocardium has been described using different kinds of arrangement [15]. Discrete muscle bundles, which follow a complex helical pathway through the ventricular wall form the Torrent-Guasp band. The muscle layers are arranged in distinct sheets or laminae. Additionally the orientation of the muscle layers varies in a continuum from subepicardium to subendocardium. As the ventricle contracts and relaxes this myocardial architecture helps to amplify the force generated by individual myocyte. The transmural differential shear stress created by this arrangement causes the ventricle to twist during systole and untwist during diastole. The myocardial fiber arrangement allows the ventricle to change its longitudinal dimension predominantly, giving rise to directional anisotropy in left ventricular volume accommodation. In the normal heart, the longitudinal direction is the primary direction of increase and decrease for the endocardial chamber.

In diastole, as the ventricle relaxes and untwists, the mitral annular plane moves into the atrium and the ventricle elongates. However, the position of ventricular apex remains fixed relative to the sternum. As a result of the chamber elongation in the long- axis, the myocardial wall thins and the endocardium expands radially. In a normal heart, the change in longitudinal direction is much greater than the radial direction and this allows the ventricle to fill at lower

pressures as a volume pump. With diastolic dysfunction, the longitudinal expansion of the ventricle is impaired and the radial expansion increases to compensate for the change which is accompanied by increased filling pressures. In systole, as the ventricle contracts and twists, the mitral annular plane moves towards the ventricular apex and the ventricular walls thicken as the endocardial radius decreases. This increases the pressure in the LV and allows for ejection. As the mitral valve plane moves towards the apex, it increases atrial volume and along with a drop in atrial pressure (due to repolarization in atrial diastole), the atria can aspirate blood from the pulmonary veins. Hence ventricular contraction during systole helps fill the atria.

1.3.6 Constant- volume attribute of the heart

A very important feature of the four-chambered heart which was elucidated by Bowman and Kovács [10] is the constant- volume attribute. The four- chambered heart is enclosed in a pericardium which is a stiff, double-walled membrane. The volume of the pericardium remains nearly constant during the cardiac cycle ($< 5\%$ change). This implies that the total volume of the 2 atrium and 2 ventricles remains nearly constant. This intriguing result is a cause of the atrioventricular volume reciprocation. As the ventricles fill in diastole, the valve planes move into the atrium and the ventricles expand radially by a small amount. In systole, the atria fill and the ventricles eject and hence the mitral/ tricuspid valve plane moves towards the apex. Interestingly, this property is valid for both sides of the heart individually.

This constant- volume attribute also contributes in synchronizing the ventricular and atrial filling and ejection. Moreover, this synchronization enables lower pressures during filling and ejection and an energetically efficient cardiac cycle. The constant- volume attribute also enables us to mathematically connect ventricular filling to tissue motion. Since the volume

change in the LV is primarily accommodated in the longitudinal direction, the longitudinal tissue velocity and the transmitral filling velocity are related by the mitral valve area [16].

1.4 Cardiac flow

The electrical conduction pathway generates contraction and relaxation in the myocardium. These mechanical changes in the myocardium create pressure differences between the atrium, the ventricle, the pulmonary circulation and the systemic circulation. Flow in the heart is regulated by the four valves. These valves are passive and they respond to pressure differences. As the pressure in upstream chamber (with respect to the valve) becomes greater than the pressure in the downstream chamber, the valve connecting the two chambers open. Similarly, when the pressure in upstream chamber falls below the downstream chamber, the valve closes shut. Once the valve opens, the pressure difference powers the flow.

1.4.1 Left heart flow

Chapters 3-6 of this thesis focus on characterizing the flow features of the LV, particularly the formation of early diastolic intraventricular vortex. Hence in this section, flow in the left heart with focus on the LV is described. The left heart receives oxygenated blood from the pulmonary circulation via the pulmonary veins (PV). There are four PVs which carry oxygenated blood, two from each lung. Since there is no valve between the veins and the LA, there is flow in all phases of the cardiac cycle. In ventricular systole (which starts at the ECG QRS complex), the LV contracts and the LA relaxes which generates negative stiffness (dP/dV<0) which allows the LA to suck in blood. This flow to the left heart from the PV is denoted as the S (for systolic) wave in echocardiographic terms. In ventricular diastole, when the LV aspirates blood from the LA, it

13

again leads to a drop in LA pressures (with respect to the pulmonary pressure) and this leads to another wave of blood flowing into the LA from the PV which is denoted as the D-wave (for diastolic) in echocardiographic terms. In atrial systole, the atria contracts, increases pressure and ejects blood out to the LV and to the PVs. This is flow from the LA to the PV and in echocardiographic terms it is known as the Ar- wave.

1.4.2 Left ventricular flow

In ventricular systole, flow begins when the aortic valve opens and blood is ejected from the LV into the aorta for systemic circulation. As the LV ejects, the pressure initially increases till it reaches maximum pressure before decreasing. LV ejection occurs in a single continuous wave. Ejection ends when the aortic valve closes and then the LV relaxes and pressure falls. The next stage is filling which happens when LV pressure falls below LA pressure and the mitral valve opens. On mitral valve opening blood from the LA is aspirated into the LV. This column of blood forms a laminar jet with a flat profile. This has been measured by Doppler echocardiography and named the E-wave (for early filling). The E-wave velocity is solely determined by LV kinematic parameters. This relationship has been quantified by a causal kinematic model described in Chapter 2, Section 2.7. Depending on the duration of the R-R interval (which determines the heart rate), the next step following the E-wave is diastasis. Diastasis is a period of equilibrium when there is no atrioventricular pressure gradient and no flow through the mitral valve as a result. The LV has been shown to achieve its equilibrium volume at diastasis [17]. Diastasis also marks the end of ventricular relaxation. The next phase of filling is the atrial contraction (after the ECG P-wave) which pushes another wave of blood through the mitral valve. This wave is measured using Doppler echocardiography and named the

A-wave (for atrial filling). The A-wave velocity is governed by both the LA and the LV kinematics. The A-wave ends when the mitral valve closes in response to an increase in LV pressure over LA pressure.

1.4.3 Vortex formation in the LV

During the E-wave, as the column of blood enters the LV the shear forces acting on the boundary of this column create turbulence. Hence the flow starts to get a parabolic profile with shear and viscous forces acting on the boundary of the flow column and little to no resistive forces acting on the center. The shear forces also create vorticity in the boundary layer which can give rise to multiple small vortices. At the mitral leaflet tips, the fluid in the boundary layer forms a vortex ring. The incoming fluid gets entrained in the vortex ring. The vortex ring grows till it reaches an optimum size at which point it pinches off. This vortex ring slowly moves towards the apex and the circulating flow in the vortex ring helps in preventing coagulation and thrombus formation. The vortex rings expands as filling progresses and helps in coapting the mitral leaflets. The vortex formed during filling is toroidal and asymmetric. When the A-wave adds more blood into the ventricle, it adds to the preexisting early filling vortex ring or creates a new vortex ring. The formation of vortex ring helps during ejection when the flow is directed towards the outflow tract. It also makes the filling- ejection process energetically more efficient as it conserves the momentum of the filling wave and utilizes it to power ejection.

A similar process also occurs in the right ventricle which also fills by vortex formation. Both in the LV and the RV, the shape of vortexes and vortex ring dynamics are influenced by the anatomy of the ventricle and the mechanics of ventricular expansion. Changes in ventricular

hemodynamics, myocardial structure or cardiomyocyte mechanics adversely affect the vortex formation process and reduce the efficiency of filling.

1.5 Thesis overview

The main focus of this research is on understanding the effect of changing left ventricular chamber kinematics on intraventricular flow especially diastolic vortexes. The next chapter of this thesis describes the method used to collect data which is analyzed in Chapters 3- 9 and the Appendices. It also contains information on methods used to process and analyze the different types of acquired data.

Chapter 3 describes the derivation of vortex formation time (VFT)- a dimensionless index used to quantify early diastolic filling vortex. In this work, we use a kinematic model to derive VFT and connect vortex formation to chamber kinematics. In Chapter 4, we validate the kinematic derivation of VFT using clinical data. We calculate VFT using our method from clinically measured echocardiographic data and compare it to VFT calculated by the standard method in the same dataset. We also demonstrate the advantage of using a kinematic definition of VFT by comparing the standard and kinematic definition of VFT to clinically used index of diastolic function quantification. In Chapter 5, we show the benefit of using a kinematic model based VFT in classifying subjects with normal and pseudonormal filling. Typically, these subjects are difficult to distinguish based on transmitral flow and the standard definition of VFT also can't differentiate between them. However, the kinematic model based VFT can.

In Chapter 6, we propose a vortex based causal hypothesis for L-waves. L-waves have been observed in mid- diastole but the mechanism of formation is poorly understood. Our work using echocardiography and cardiac MRI shows that L-waves are a consequence of recirculating

flow in the vortex rings. Additionally, we predict that L-waves should form in the RV by the same mechanism. Using echocardiography in the RV and cardiac MRI we show RV L-waves which have not been previously reported.

Chapter 7 describes a method to compute directional flow impedances from clinically measured data. LV filling is anisotropic, in a normal LV, volume accommodation is primarily in a longitudinal direction rather than radial direction. However, previously there was no good way to quantify this attribute. Flow impedances allow for the interaction of pressure and flow rate and thus effectively quantify the resistance faced by filling in the longitudinal and transverse/ radial direction. Our method uses LV pressures measured from cardiac cath and flow rate measured by Doppler echocardiography to calculate longitudinal and transverse impedance. We found that consistent with previous reports, longitudinal volume accommodation is preferred over transverse and our method allowed us to quantify this property.

Chapter 8 uses LV pressure data obtained from cardiac catheterization to compute the spatiotemporal heterogeneities in isovolumic pressure decay. Previous work has focused on quantifying pressure gradients during filling. Our work shows that the pressure gradient of greater magnitude exists during isovolumic relaxation. Moreover, the rate of relaxation (as quantified by dP/dt) is also spatially heterogeneous. Our results indicate that apical relaxation is slower than mid- LV relaxation.

In Chapter 9 a new method for load independent analysis of pressures and pressure derivatives during the cardiac cycle is proposed. The values of LV pressure and pressure derivative are normalized to 0 and 1 (for pressures) and -1 and +1 (for pressure derivatives). This method of normalization revealed conserved features of the cardiac cycle. During isovolumic relaxation, the normalized pressure at which peak negative dP/dt is reached is conserved across a

large number of beats recorded from different subjects under various loading conditions. Hence this result hints to the presence of conserved mechanisms in the relaxation process.

Reference:

1. Zile MR, Brutsaert DL. New Concepts in Diastolic Dysfunction and Diastolic Heart Failure: Part I- Diagnosis, Prognosis, and Measurements of Diastolic Function. *Circulation*. 2002, 105: 1387-1393.

2. Kass DA, Bronzwaer JGF, Paulus WJ. What mechanisms underlie diastolic dysfunction in heart failure? *Circ. Res*. 2004; 94: 1533- 1542.

3. Kass DA. Assessment of diastolic function. Non- invasive modalities. *Cardiol. Clin*. 2000; 18 (3): 571- 586.

4. Appleton CA, Firstenburg MS, Garcia MJ, Thomas JD. The echo- Doppler evaluation of left ventricular diastolic function. *Cardiol. Clin*. 2000; 18 (3): 513- 546.

5. Nagueh SF, Appleton CP, Gillebert TC, Marino PN, Oh JK, Smiseth OA, Waggoner AD, Flachskampf FA, Pellikka PA, Evangelista A. Recommendations for the Evaluation of Left Ventricular Diastolic Function by Echocardiography. *J. Am. Soc. Echocardiogr*. 2009; 22(2):107-133.

6. Kovács SJ, Barzilai B, Pérez JE. Evaluation of diastolic function with Doppler echocardiography: the PDF formalism. *Am. J. Physiol*. 1987; 87: H178-H187.

7. Dent CL, Bowman AW, Scott MJ, Allen JS, Lisauskas JB, Janif M, Wickline SA, Kovács SJ. Echocardiographic characterization of fundamental mechanisms of abnormal diastolic filling in diabetic rats with a parameterized diastolic filling formalism. *J Am Soc Echocardiogr*. 2001; 14(12):1166-72.

8. Riordian MM, Kovács SJ. Quantitation of mitral annular oscillations and longitudinal "ringing" of the left ventricle: a new window into longitudinal diastolic function. *J. Appl. Physiol*. 2006; 100:112-119.

9. Shmuylovich L, Kovács SJ. A load-independent index of diastolic filling: model-based derivation with in-vivo validation in control and diastolic dysfunction subjects. *J. Appl. Physiol*. 2006; 101: 92-101.

10. Bowman AW, Kovács SJ. Assessment and consequences of the constant-volume attribute of the four-chambered heart. *Am. J. Physiol*. 2003; 285:H2027-H2033.

11. Ghosh E, Shmuylovich L, Kovács SJ. Derivation of the fluid mechanics to left ventricular early, rapid filling relation, with in-vivo validation. *J. Appl. Physiol*. 2010; 109 (6): 1812-1819.

12. Braunwald E. Structure and function of the normal myocardium. *Br. Heart J*. 1971; 33 supplement, 3- 8.

13. Ho SY. Anatomy and myoarchitecture of the left ventricular wall in normal and in disease. *Eur. J. Echocardiogr*. 2009; 10: iii3- iii7

14. Gaasch WH, LeWinter MM. Left ventricular diastolic dysfunction and heart failure. Lea and Febiger, Malvern PA, 1994.

15. Pope AJ, Sands GB, Smaill BH, LeGrice IJ. Three- dimensional transmural organization of perimysial collagen in the heart. *Am. J Physiol. Heart Circ. Physiol*. 2008; 295: H1243-H1252.

16. Lisauskas JB, Singh J, Courtois MR, Kovács SJ, Jr. The relation of the peak Doppler E-wave to peak mitral annulus velocity ratio to diastolic function. *Ultrasound Med. Biol*. 2001; 27: 499-507.

17. Shmuylovich L, Chung CS, Kovács SJ. Point: Left ventricular volume during diastasis is the physiological in vivo equilibrium volume and is related to diastolic suction. *J Appl Physiol.* 2010; 109(2): 606-608.

Chapter 2: Methods

2.1 Methods to evaluate diastolic function

Accurate quantification of diastolic function (DF) is crucial to detecting diastolic dysfunction. Clinically, many different invasive and non-invasive modalities are used to measure different aspects of DF. These different modalities together provide a comprehensive measurement of diastolic function. Each modality has its advantages and disadvantages and clinically a combination of different techniques is used. A variety of indexes have been derived from these modalities and these indexes are quantified to clinically evaluate dysfunction.

The gold standard for hemodynamic assessment of DF is data obtained by cardiac catheterization [1, 2]. It is an invasive procedure which measures cardiac pressure and volumes. A typical pressure volume loop measured during cardiac catheterization is shown in Fig 2.1. These pressure and volume data are used to compute

Fig 2.1: Schematic pressure- volume loop with the different phases of cardiac cycle marked. See text for details.

different indexes such as: time constant of isovolumic relaxation (τ), the chamber stiffness computed at different time points such as diastasis and end-diastole, the end-systolic pressure volume relationship (ESPVR), the end-diastolic pressure volume relationship (EDPVR), the

maximum elastance and the arterial elastance. The procedure for collecting, processing and analyzing hemodynamic data from cardiac catheterization is discussed in detail later.

Apart from invasive cardiac catheterization, a number of non-invasive imaging techniques have been developed for diagnostic purposes. The most common clinically used method to evaluate DF is echocardiography. Echocardiography uses ultrasonic frequencies to probe cardiac structure. In addition Doppler echocardiography uses the Doppler effect to quantify motion of blood and tissue. Echocardiography allows real-time measurement of cardiac function with high temporal resolution. Thus echocardiography has been used to measure left ventricular chamber size, mitral leaflet motion, aortic leaflet motion as a function of time. Doppler echocardiography has been used to measure transmitral flow, aortic flow, pulmonary vein flow. Tissue Doppler has been typically used to measure the velocity of the mitral annular plane in the long axis direction. Similar evaluation techniques have also been used to quantify right ventricular function.

One drawback of these echocardiographic methods is that they measure velocities at a single region of interest. This drawback has been overcome by color M-mode imaging. In this technique, flow velocities are measured along the entire echo scan line (rather than a selected point on the line). This allows simultaneous multi-point interrogation of flow velocities. Furthermore, speckle tracking methods have been developed to quantify chamber strain at different sections/ locations in the tissue. Another advance in echocardiographic imaging is the development of 3 dimensional echocardiography which has been utilized in detecting valve function abnormalities.

2.2 Overview of research methodology

All the data presented in the following chapters (except Chapter 6) of this thesis were obtained from the Cardiovascular Biophysics Laboratory database. This is a unique database containing simultaneous cardiac catheterization and echocardiography data. This is the largest database of its kind in the world and it has been enrolling subjects for several decades. It has simultaneous echo- cath data from over 500 subjects. Over the years, the quality and amount of data had increased due to advances in catheter technology, ultrasound imaging advances, improved data acquisition systems and advanced methods for automated data processing. However, the basic structure of data acquired has remained the same. Fig 2.2 summarizes in a flowchart our method of data acquisition and analysis. The next sections in this chapter describe the method used to collect echo- cath data and the semi- automated method of processing this data. The last section of this chapter describes mathematical models used to analyze echocardiographic transmitral images and hemodynamic phase planes obtained from cardiac catheterization data.
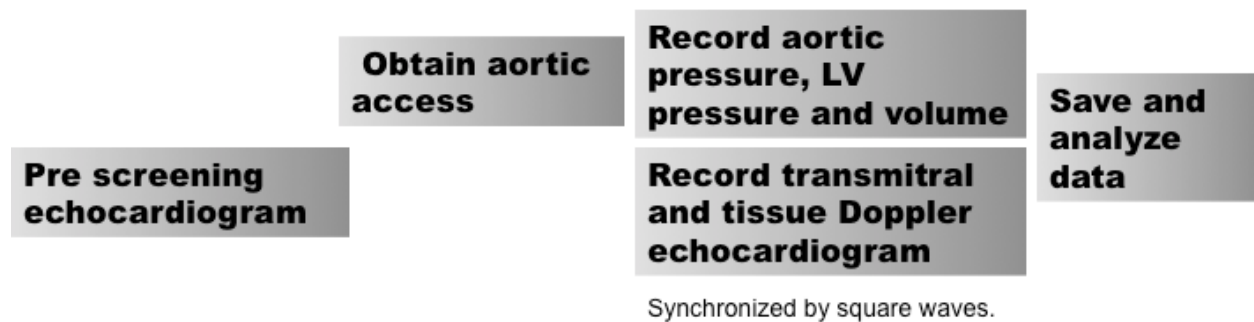
Fig 2.2: Sequence of data acquisition in cardiac catheterization lab.

The data presented in Chapter 6 were collected from cardiac MRI and echocardiography in healthy volunteers. This chapter describes the MRI and echocardiographic imaging protocol and the data processing methods.

2.3 Simultaneous echocardiography and cardiac catheterization: Experiment protocol

2.3.1 Subject Selection

Subjects are referred by their physicians for elective diagnostic cardiac catheterization to evaluate the possibility of coronary artery disease and recruited to participate in the study by the sponsor. All the enrolled subjects will have met the following criteria: (i) scheduled for elective diagnostic left-heart catheterization, in a fasting, non-sedated state, (ii) judged to be clinically stable and (iii) willing to participate by giving informed consent in accordance with a study protocol approved by the Washington University Medical Center Human Research Protection Office (HRPO). Subject's inclusion in the study requires the subject to have no pacemaker, be in normal sinus rhythm, have no evidence of valvular disease, have no active ischemia and have no evidence of akinetic/ hypokinetic wall motion. Subjects in sinus rhythm and having no pacemakers or AICDs are screened after meeting study inclusionary requirements. The enrolled subject population is typical inpatients or same-day catheterization patients encountered in clinical practice. This assures a realistic age, gender and racial mix characteristic of clinical practice.

2.3.2 Echocardiographic prescreening

Prior to catheterization, subjects have a complete 2D/echo-Doppler screening study using an echocardiographic imaging system (Acuson, HP, or Philips ie33) with 2.5 MHz transducer. With the patient supine, both parasternal and transapical views are obtained. Parasternal views are obtained at the level of the mitral and aortic valves in order to visualize both valves. Additional parasternal views are obtained at the mitral leaflet tip and mid-LV in order to estimate LV size.

Continuous wave Doppler is used to record aortic outflow and mitral inflow from the apical view for determination of isovolumic relaxation time using a sweep speed of 10 cm/sec. Pulmonary S- and D- waves and transmitral E- and A- waves are recorded in pulsed Doppler mode with sample volumes gated at the pulmonary veins and mitral leaflet tips respectively. For pulsed Doppler imaging the wall filter is set at 125 Hz or 250 Hz, the baseline is adjusted to take advantage of the full width of the display, and the velocity scale is adjusted to exploit the dynamic range of the output without aliasing. Septal and lateral E'- and A'-waves are recorded in tissue Doppler mode with sample volumes at the septal and lateral sides of the mitral annulus, respectively. In addition, color M-Mode imaging is used to obtain diastolic early and late filling intraventricular velocity maps.

If a poor echo window, bicuspid aortic valve or significant calcification or stenosis of the aortic valve is observed by echocardiography, then the routine cardiac catheterization study proceeds, but the subject is not enrolled in the simultaneous high-fidelity catheterization and echocardiography portion of the study. If the subject has an appropriate echocardiographic window and no aortic valve abnormalities then the simultaneous high-fidelity catheterization and echocardiography study proceeds.

2.3.3 Cardiac catheterization protocol

After appropriate sterile skin prep and drape of the patient, local anesthesia (1% xylocaine) is given and percutaneous right or left femoral arterial access is obtained in preparation for the performance of the catheterization by the sponsor, using a valved sheath (6-F, Arrow Inc, Reading, PA). After arterial access and placement of a 64 cm sheath (Arrow Inc, Reading, PA), a 6F micromanometer-tipped pigtail (triple pressure transducer) pressure-volume, conductance

catheter (Model 560-1, 560-5, Millar Instruments, Houston, TX) is directed into the mid-LV in a retrograde fashion across the aortic valve under fluoroscopic control. Prior to insertion, the manometer-tipped catheter is calibrated against "zero" by submersion just below the surface of NS bath at 37° C, and again after insertion relative to hydrostatic "zero" using the lumen with respect to the mid-thoracic fluid filled transducer (HP). It is balanced using a transducer control unit (Model TC-510, Millar Instruments, Houston, TX) and pressures are fed to the catheterization laboratory amplifier (Quiton Q-Cath Physiological Recording System) and simultaneously into the input ports of the physiological amplifier of the Doppler imaging system for synchronization (Philips iE33). The LV and AO pressures, LV volume from the conductance catheter and one ECG channel are also simultaneously recorded on disk in digital format using our multichannel Physiologic Data acquisition system, consisting of a Pentium class computer with 100Mb hard disk, 64Mb RAM and NB-M10-16H digitized board. The sampling rates for up to 8 channels of data are controlled using Leycom Software (Leycom Sigma-5, CardioDynamics, Rjinsburg, The Netherlands).

Ventriculography is subsequently performed using a 6F bent, pigtail catheter (Cordis) using 35cc of contrast injected at 11cc/s. The image is calibrated for volume using a cm grid placed at the mid-axillary level. The remainder of the catheterization and coronary angiography proceeds in the usual manner.

2.3.4 Simultaneous echocardiography protocol

Fig 2.3 shows a schematic representation of the data acquisition setup for simultaneous cardiac catheterization and echocardiography in cath lab. After the catheter gains access to the LV and while pressures and volumes are being recorded, another echocardiographic examination is

performed. The subjects are imaged using the apical 4 chamber view. Pulsed wave Doppler is used to image transmitral flow at the mitral valve level and at the level of mitral leaflet tips. To synchronize the echocardiographic images with pressure waveforms, a fiducial marker in the
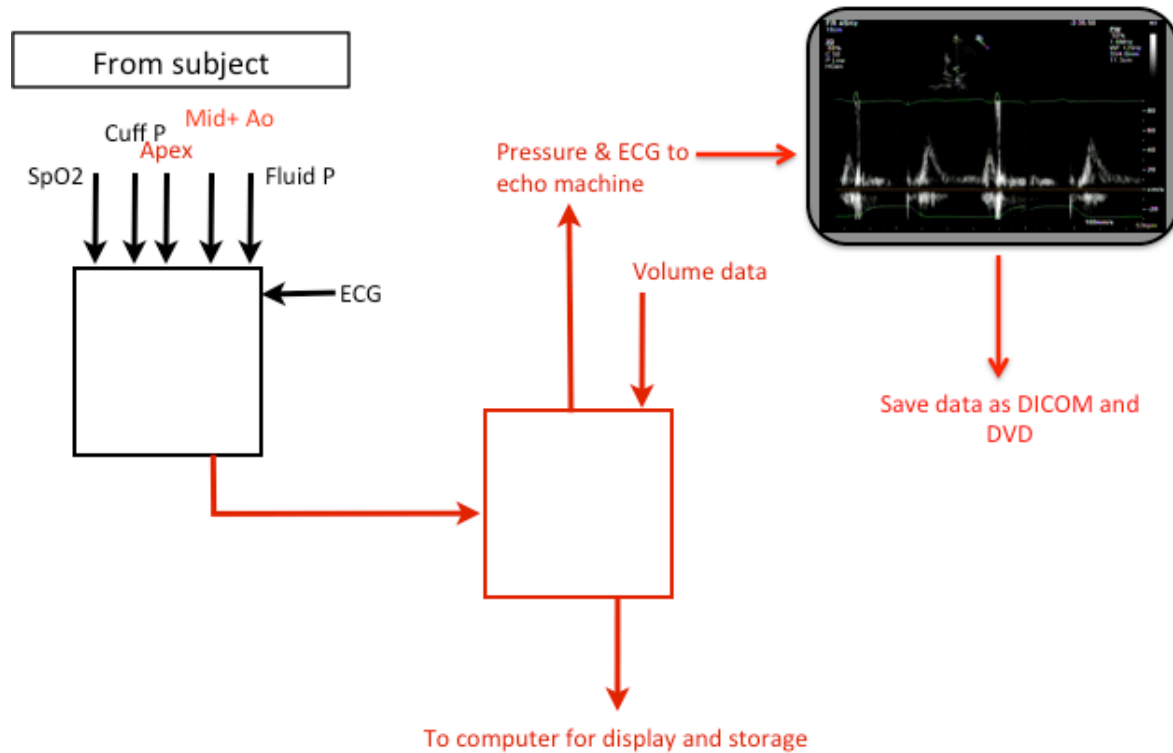
Fig 2.3: Schematic representation of data acquisition setup in catheterization lab. Red font is used to denote additional data channels for our system. Black font represents data channels used in a regular cath procedure.

form of a square wave is sent from the catheter transducer unit to both the pressure signal in the PC and the echocardiographic imager. Approximately 40 to 50 beats are recorded during quiet respiration.

In addition 10-15 cardiac cycles via DTI are recorded with the sample volume being located at lateral and septal portion of the mitral annulus along with the simultaneous LV pressure signal. Images of individual beats are captured in DICOM format from the disk for offline analysis using custom image processing software. The entire case is also recorded onto

VHS tape (Accuson and HP) or burned to DVD (ie33), with the resulting continuous data stream is processed offline.

2.4 Semi- automated processing of acquired data

The hemodynamic data obtained from cardiac catheterization is saved as a compressed .arj file. Echocardiographic data is for the prescreening portion (acquired as described in 2.3.2) is saved on a DVD as DICOM files. Echocardiographic data obtained simultaneously with cardiac catheterization is burned to a DVD and extracted as an .avi file. This section describes the method used to process these data types.

2.4.1 Extracting pressure- volume and ECG data

The data are extracted from the compressed format and stored in a tab delimited text file. The next step is identifying square waves in the hemodynamic data. The square waves are sent via the catheter transducer unit to the distal, middle and proximal pressure channels in the sequence. The square waves are atleast 1s long and have amplitude of 100 mm Hg. An automated script finds square waves by looking for extended minima in the pressure derivative signal that are flanked by extreme maxima and minima, and manual analysis is employed to confirm the start and stop of the automatically discovered square waves. If the square wave amplitudes or absolute values deviate from 0 mmHg and 100 mmHg then the entire pressure signal is shifted and scaled appropriately.

2.4.2 Processing ECG signal and identifying features

To identify cardiac cycles in the hemodynamic data, the ECG signal was analyzed. This analysis was done in multiple steps, of which the first step was automated identification of R- peaks. A custom MATLAB code was written which identified local maxima in the baseline filtered ECG signal over successive windows determined from the dominant frequency of the Fourier transform of the ECG signal.

The other features of the ECG signal- QRS complex, P- wave and the T-wave were analyzed. The QRST complex was analyzed by applying linear approximations to the upslope and downslope of the R-wave and determining crossover points with the baseline zero voltage level of the DC filtered signal. The first minima preceding and following those crossover points define the Q and S waves respectively. The maximum in the absolute value of the ECG signal between the S wave and the time at which minimum pressure occurs defines the T-wave peak. Linear approximation of the T-wave upslope and downslope define the start and end of the T-wave respectively, and the maximum in the absolute value of the ECG signal between the end of the T-wave and the start of the following R-wave defines the P-wave peak. Linear approximation to the upslope and downslope of the P-wave defined the approximate start and end of the P-wave. Following automated analysis, manual analysis was performed to adjust any errors due to lack of P-wave or spurious ECG data.

2.4.3 Processing hemodynamic data and analyzing pressure

The next step was to analyze pressure data for each cardiac cycle. The cardiac cycles were based on the R-peaks derived as described above. For each beat the later R-peak defined the beat, for example the 2nd R- peak defined the 1st beat. To remove errors due to respiratory modulation of

the pressure signal, the data were filtered to remove low frequencies (0.15 Hz and below). The maximum and minimum pressures in each R- R interval were defined as the maximum and minimum pressures of the cardiac cycle. The pressure derivative was calculated using the difference method and its maximum and minimum values were the peak positive dP/dt and peak negative dP/dt. This analysis was done on both the LV pressure channels and the aortic pressure channel. The end- diastolic pressure (EDP) was defined as the maximum pressure between R-wave peak and the minimum pressure of the beat. Typically this was the pressure at R-wave peak but in the case of 1st degree AV block, the ventricular pressure reaches a maximum and then falls back to the diastatic pressure.

A full analysis of pressure data was also performed. The mitral valve opening pressure was estimated to be the pressure between maximum and minimum pressures which was closest in magnitude to EDP. The diastasis pressure was defined as the pressure at P-wave peak, when the P-wave is present otherwise the LV EDP was used. Diastasis start was determined using an iterative process. Starting with an initial guess which was the mid- point of minimum pressure and pressure at P- wave peak, a linear regression was done of the pressure between the assumed start of diastasis and time of minimum pressure, as well as a linear regression of the pressures between the assumed start of diastasis and the time of P-wave peak. The intersection of these linear regressions defines the next guess of the start of diastasis, and this process was repeated until it converged on a single value or a set of repeated values. If the process converged on a loop of values then the average of those values defined the time at which diastasis starts.

2.4.4 Extracting echocardiographic data

The prescreening echocardiographic data were saved in the form of DICOM images. A custom MATLAB script was written to read the DICOM images and display them. The program also allowed saving of user- selected images as bitmap files which could be used for further analysis. For each subject, images from different echo views were saved. These were then manually categorized based on the type of view.

The continuous transmitral Doppler and tissue Doppler data obtained simultaneously with the cardiac catheterization was in video format. The echo video was synchronized with the hemodynamic data by matching the time point of the square wave start on the video, with the time point of square wave on the pressure channel. A time offset is introduced into the video to align the transmitral contours to the pressure signal.

With this offset in place, the R-wave peak times are used to determine the corresponding frame number in the video file (29.97 frames per second on DVD or 14.99 frames per second on VHS) where the R-wave for that beat occurs. Typically the frame that comes several frames beyond the R-wave is extracted to ensure no loss of A-wave signal. These frames are extracted programmatically from the video file based on the previously determined R-wave peaks.

2.4.5 Transmitral and tissue Doppler image analysis

A custom MATLAB script is used to determine the conventional features of transmitral flow and tissue Doppler. The program reads in echo images of a particular view (Doppler E- and A-waves or tissue Doppler E'- and A'- waves) as folders containing bitmap images. The interface allows the user to mark the time sampling rate (TSR) and the velocity sampling rate (VSR) for each image. TSR and VSR specify the number of pixels in the image which quantify 1s and 1 m/s

respectively. The next step is to mark and crop a single E- and A- wave. For this, first the R- R interval enclosing the E- and A-wave is marked manually. Then the E-wave peak is marked and a straight line connecting the peak to the start and end of the E-wave is used to calculate the acceleration time, deceleration time and the duration of the E-wave. The A- wave is marked using a similar procedure. A similar MATLAB- based user interface is used to read in tissue Doppler images and mark the E'- and A'- waves. This program also allows marking of the oscillations of the mitral annulus as denoted by E"- and E"'- waves.

The cropped images are saved as bitmap files along with the extracted parameters such as peak velocities and durations. These cropped images are used for quantification of kinematic model parameters based on the parametrized diastolic filling (PDF) formalism which is described in the subsequent sections.

2.5 Cardiac MRI and echocardiography: Experimental protocol

This protocol was used to collect data which was used to quantify intraventricular flow and detect transmitral diastatic L-waves. This work is presented in Chapter 6.

2.5.1 Subject selection

Healthy volunteers with no history of cardiac disease and willing to participate by giving informed consent in accordance to the study protocol approved by the Washington University Medical Center Human Research Protection Office (HRPO) were recruited for the study. These volunteers also had no implants, metallic fragments or any other standard contraindication to MR imaging. These volunteers underwent an echocardiographic exam followed by cardiac MR scan which is described in the following sections.

2.5.2 Doppler echocardiographic imaging
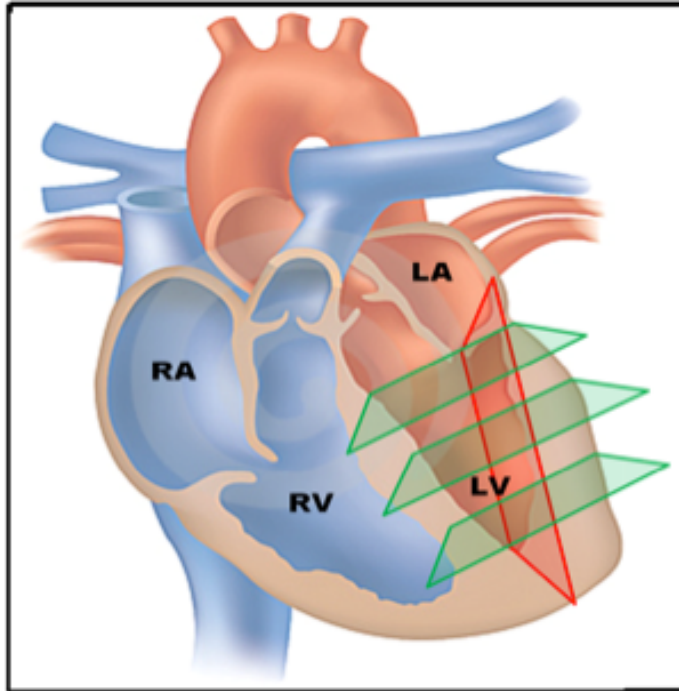
Fig 2.4: Variation in sample volume location using 2D Doppler. The red plane shows the variation in long axis direction and the green planes show short-axis variation in sample volume location.

All subjects enrolled in the study had a complete 2D/ echo-Doppler study in accordance with ASE criteria [3]. This included apical four-chamber 2D-echo Doppler views of the mitral valve recorded using a 2.5/3.5 MHz transducer in a dedicated echo imaging machine (Philips iE33). Intraventricular flow was mapped by 2D Doppler by placing the sample volume at different locations in the LV. First the sample volume was moved along the long axis and Doppler E- and A-waves were recorded. Then the sample volume was moved along the short- axis (septal to lateral direction). This allowed us to measure the variation in flow profiles as a function of location. This is shown in Fig 2.4. Color M-mode imaging was done to measure intraventricular flow along the long axis of the LV. Additionally we measured, the pulmonary vein flow velocity, the aortic outflow velocity and mitral valve plane velocity by tissue Doppler. Parasternal M-mode imaging was used to image mitral leaflet tips with special care taken to image mitral leaflet tips.

2.5.3 Cardiac MR imaging protocol

Volunteers also underwent cardiac MR scan. Anatomical information was obtained from standard functional CMR imaging consisting of balanced turbo field echo (b-TFE) cine images in 2-chamber, 3-chamber, 4-chamber and short axis views. Typical parameters were: slice thickness 2 mm and in-plane resolution 1.25 X 1.25 mm^2. In addition, in the same imaging session, 3 dimensional, time-resolved and 3 directional velocity mapping (PC-MRI) was performed to measure intraventricular flow patterns. A respiratory-gated phase contrast (gradient echo) sequence was used. The parameters employed for parallel acquisition techniques (SENSE), were: spatial resolution: 2.5 x 2.6 x 4 mm^3 (acquired) and 2.0 x 2.0 x 2.0 mm^3 (reconstructed), short echo and repetition times (TE= 2.6 ms and TR= 4.6 ms), flip angle = 10° (for short TE), velocity encoding (VENC) = 120 cm/s and SENSE factor of 2. Retrospective ECG triggering was used to ensure complete coverage of the R-R interval, including late diastole.

2.6 Processing and analysis of echocardiography and MRI data

All the echo and MRI data were extracted in the form of DICOM files. The following sections describe how the different data types were processed. More information about their processing and analysis is given in Chapter 6.

2.6.1 Transmitral Doppler processing

The DICOM images containing the transmitral Doppler and 2D Doppler mapping of intraventricular flow was converted into bitmap files using a custom MATLAB program as described in Section 2.4.4. These images were then cropped using another custom MATLAB program as described in Section 2.4.5. Additionally, the images were mapped by identifying the

position of the sample volume in the ventricle (by quantifying in terms of distance from the mitral valve plane). A custom MATLAB program was written which used the cropped Doppler images and marked L-waves. L-waves occur between the E- and the A-waves. The program allowed the user to mark the L-wave peak. Since some L-wave acceleration slopes can be merged with the E-wave deceleration slope, the program allowed the user to select only marking the deceleration slope. In other cases the user marked both the acceleration and deceleration slopes. The results of this analysis were saved along with the position of the sample volume where the flow was recorded.

2.6.2 Color M-mode image processing

Color M-mode images measure flow along the entire echo scan line. Typically, the scan line is placed along the long- axis of the ventricle (from LV apex to base). Hence color M-mode images contain flow information at different locations in the LV. A typical color M-mode image has
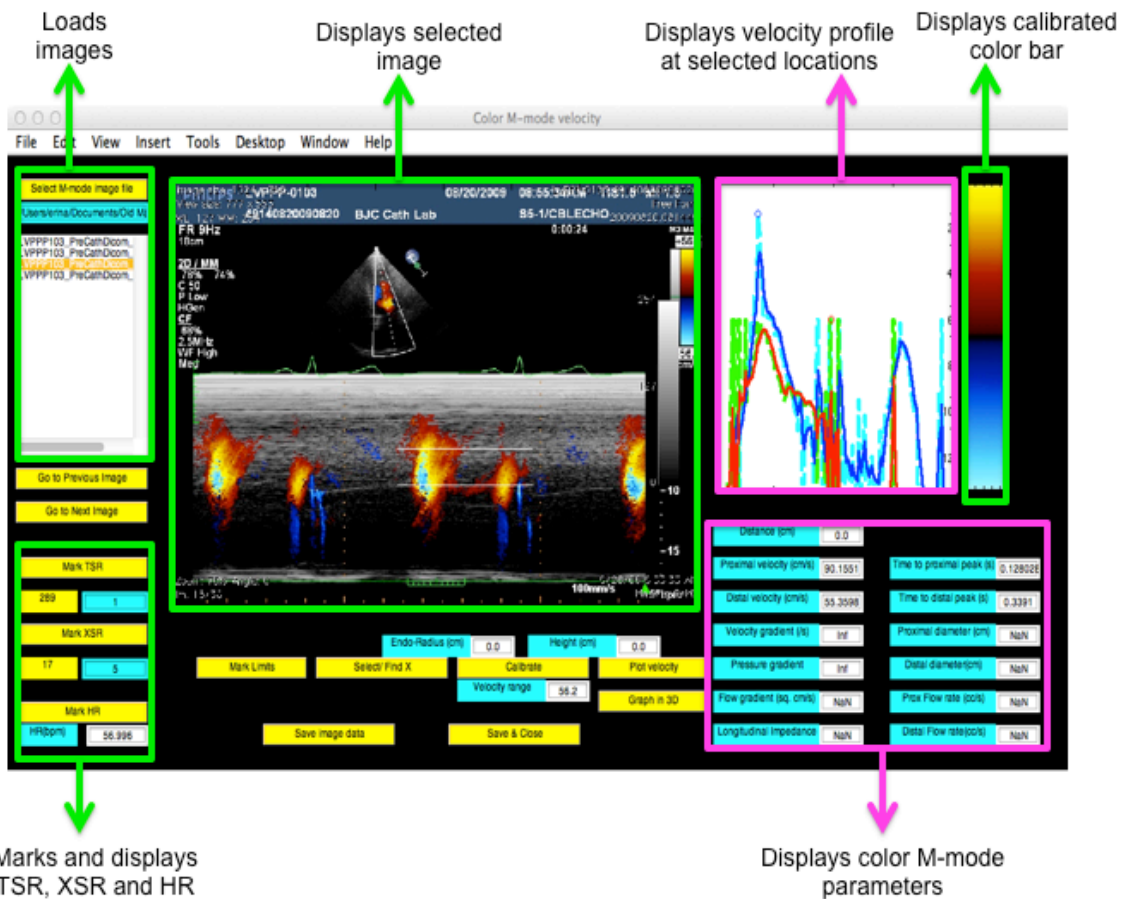
Fig 2.5: Graphic user interface for reading and analyzing color M- mode images.

time and distance on the X- and Y- axis. Color is used to represent velocity. Each color M-mode image also has a color bar which shows the velocity range measured in that particular image and the correspondence between the colors and velocity. To analyze the color M-mode images the first step is to convert the image into a 3 dimensional contour map where velocity was represented by the height of the map. This was done by a custom MATLAB program which is summarized in Fig 2.5.

The program reads in color M-mode image files and displays them. The time sampling rate and the distance sampling rate are marked by the user. The next step is calibrating the color bar to correlate the color values with velocity values. For this the user first enters the maximum velocity value encoded in the image. Then the user selects the top row of pixels in color bar, the middle (or zero) level of the color bar and then the bottom level in that order. The user also selects a particular column at which the pixels are sampled. The color values of the pixel are correlated with velocity by creating an array which contains the red, green and blue pixel values (normalized to 1) along with the velocity corresponding to the set of values (linearly interpolated). The next step is marking the enclosing R-R interval for the E- and A- flame. Then the E- and A- flame is marked by selecting the upper left point to specify the left boundary and the top boundary and selecting the bottom right point to specify the right boundary and bottom boundary of the rectangle enclosing the beat to be analyzed. In this step the user also marks the zone of aliasing. Aliasing occurs when the velocity in the LV exceeds the maximum encoded velocity of the color bar. Aliasing can be determined visually in an image by the sharp change from positive to negative velocity in surrounding pixels (or vice versa). The program allows the user to specify the left and the right boundary of the aliased region (i.e. the time points of start and end of aliasing). Once the selected beat has been marked the program automatically

interpolates the color data to create a contour map. Moving along in time, for each column of pixels (which represents different points on the LV), the program distinguishes between color and grayscale pixels. For the color pixels it searches for the shortest distance between the normalized set of red, green, blue pixel values and the red, green, blue pixel values of the colorbar and assigns the velocity value of the match. For the pixels in the aliased range it determines whether the pixel is aliased or not. In case the pixel is aliased, the velocity is computed, then the difference between the computed velocity and the maximum velocity is added on to the maximum velocity to get the actual velocity. Thus the program loops for all pixels, computes the velocity map, saves the data as a 2 dimensional array and displays the resulting contour map.

The next step in analyzing color M-mode images is to select different locations in the LV (by selecting different Y- axis levels on the color M-mode). A custom MATLAB program was used to read in the saved array containing the velocity values for a single beat. The user then selects 2 different levels on the image at which the velocity is sampled as a function of time. The program outputs a 2 dimensional graph of velocity as a function of time at the specified locations and 3 dimensional graph showing the position of the 2 lines along the LV with the variation in velocity profile. This is shown in Chapter 6, Fig 6.5.

2.6.3 Cardiac MR image processing

The cardiac MR data was collected in the form of multi- frame DICOM files for each of the functional scans. The phase- contrast velocity encoded MRI was extracted in the form of single frame DICOM images. Since the goal of the MRI analysis was to quantify and extract intraventricular velocity data, this section describes the method used to process the phase-contrast MR data.

The 3 directional velocity data was measured by 3 consecutive scans encoding velocity in
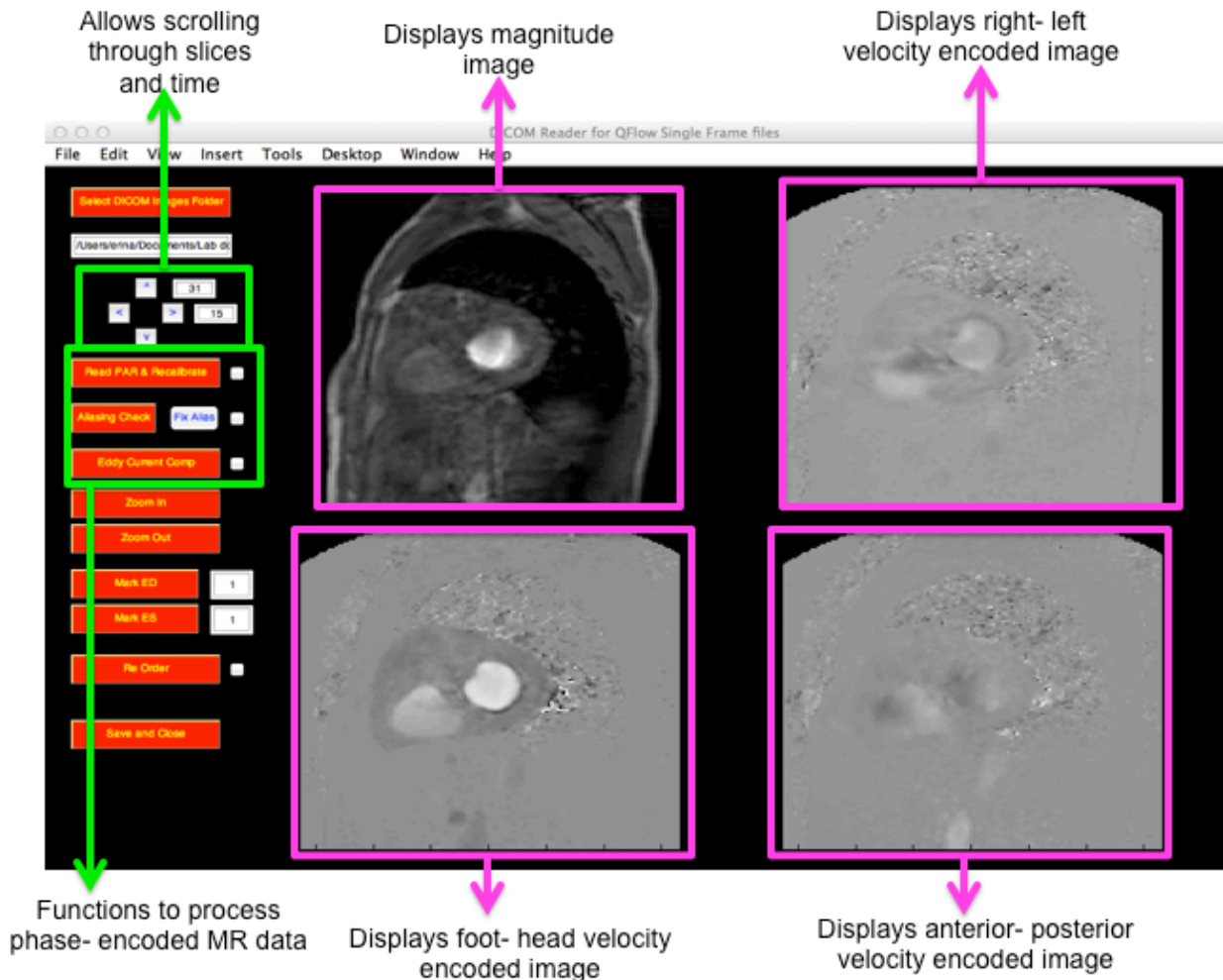
Fig 2.6: Graphic user interface to read in phase- encoded MR data from 3 velocity scans and display them. The program also allows for recalibration and error correction. See text for details.

each orthogonal direction. Each velocity encoded scan had 3 sets of image stacks- a magnitude image stack, a phase- contrast angiography image stack and a phase- encoded image stack. The phase- encoded image stack had the required velocity information. Thus for each subject the 3 phase encoded images (corresponding to each direction) and 1 magnitude image stack was read in by a custom MATLAB program. This is shown in Fig 2.6. The graphic user interface (GUI) displayed the magnitude image and the three grayscale velocity encoded images for a particular short- axis slice and time point (in the cardiac cycle). Scroll buttons on the GUI enable the user

to scan through all the slices and time points recorded. The next step in the data processing is recalibrating the images. Recalibrating assigns the correct velocity values to the phase-encoded images. This is done by reading the PAR file for each scan which has the rescale coefficients. After the image stacks are rescaled, eddy current compensation is done by selecting a static portion of the tissue. The average velocity recorded in this portion for the entire stack is used to perform a first order correction of velocities. The next step is to detect aliasing and correct for aliasing. Similar to color M-mode images, aliasing is an abrupt change in velocities due to actual velocities being greater than the encoding velocity. In the MR scans it is detected automatically by looking for discontinuities in velocity profile in space and time. Once the aliased pixel is identified, the program can automatically correct the aliased pixel velocity. The next step in processing is identifying the end- diastolic and end- systolic phase. This is done manually by looking at the slices containing the mitral and aortic valves respectively. Once the end- diastole and end- systole are marked, the image stacks are reordered such that end- diastole is the last phase of the cardiac cycle. These processed and reordered stacks are then saved as 3, 4 dimensional arrays. Each array has velocity information in one direction, for a 3 dimensional space and time. Flow visualization is done using a separate MATLAB program which uses these 4 dimensional arrays as output.

2.7 Kinematic modeling of diastolic filling

2.7.1 Theory: Parametrized diastolic filling (PDF) formalism

At mitral valve opening LVP continues to decrease while LV volume increases, thereby initiating filling via mechanical suction of atrial blood. Suction-initiated filling has been modeled kinematically using the parametrized diastolic filling (PDF) formalism [4] which characterizes the

kinematics in analogy to the recoil from rest of a previously displaced, damped simple harmonic oscillator (SHO). The motion of this system is characterized in terms of 3 parameters- k, the spring constant, c, the damping constant and x_o, the initial SHO displacement. Eq. 2.1 is second order linear differential equation which describes the damped SHO kinematics.

$$\frac{d^2x}{dt^2} + c\frac{dx}{dt} + kx = 0 \qquad\qquad \text{Eq. 2.1}$$

The PDF formalism models the ventricle relaxing to the motion of the damped SHO and hence ventricular filling (as quantified by transmitral flow) contour is inscribed by the velocity of the damped simple harmonic oscillator system. Hence the parameters of the model have physiologic analogs- k represents LV chamber stiffness, c represents the chamber relaxation/ viscoelasticity and x_o represents the volumetric load at the beginning of filling.

Solving Eq 2.1 with the initial conditions that the initial displacement is x_o and initial velocity is 0 gives two solution regimes- the overdamped and the underdamped. Eq. 2.2 represents the underdamped solution and Eq. 2.3 represents the overdamped solution.

$$E(t) = -\frac{kx_o}{\omega}\exp(-c\frac{t}{2}).\sin(\omega t) \qquad \text{where } \omega = \frac{\sqrt{4k-c^2}}{2} \qquad \text{Eq. 2.2}$$

$$E(t) = -\frac{kx_o}{\beta}\exp(-c\frac{t}{2}).\sinh(\beta t) \qquad \text{where } \beta = \frac{\sqrt{c^2-4k}}{2} \qquad \text{Eq. 2.3}$$

These expressions provide an excellent fit to all clinically encountered E- waves.

The PDF formalism has also been applied to tissue Doppler mitral annular longitudinal velocity [5]. During filling the annulus moves towards the atrium allowing longitudinal elongation of the ventricle according to the rules of harmonic oscillatory motion. Thus E'-wave velocity is characterized by three SHO parameters- k', c' and x_o'. By analogy, the differential equation is:

$$\frac{d^2x}{dt^2} + c'\frac{dx}{dt} + k'x = 0 \qquad\qquad \text{Eq. 2.4}$$

Using analogous initial conditions, initial displacement is x_o' and initial velocity is 0 gives 2 solution regimes- the underdamped and overdamped which are given below:

$$E'(t) = -\frac{k'x_o'}{\omega'}\exp(-c'\frac{t}{2}).\sin(\omega't) \qquad \text{where} \quad \omega' = \frac{\sqrt{4k'-c'^2}}{2} \qquad \text{Eq. 2.5}$$

$$E'(t) = -\frac{k'x_o'}{\beta'}\exp(-c'\frac{t}{2}).\sinh(\beta't) \qquad \text{where} \quad \beta' = \frac{\sqrt{c'^2-4k'}}{2} \qquad \text{Eq. 2.6}$$

2.7.2 Automated method for PDF analysis

The automated fitting of the Doppler E- and A-waves and tissue Doppler E'- and A'-waves is
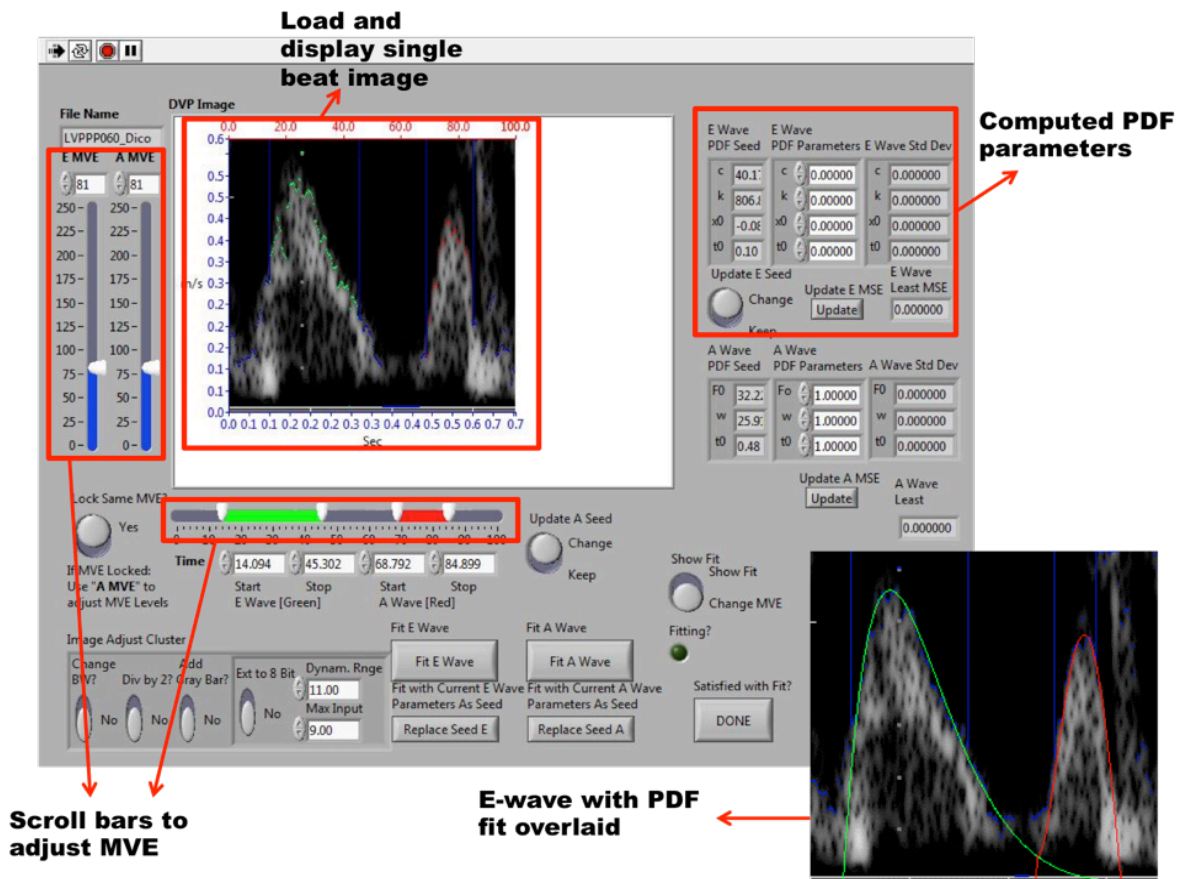
Fig 2.7: Graphic user interface used for PDF- model based fit for transmitral flow. The inset on the lower right shows the final PDF fit overlaid on the E-wave. MVE = maximum velocity

done using a custom LabView program [6-8]. The cropped images from Section 2.4.5 are loaded onto the program as shown in Fig. 2.8. The next step is to select time points in the beginning and end of the E-wave and the A- wave. These time points are selected such that only clean (noise-free) portion of the flow profile is selected. The user also sets the threshold value such that the selected pixels approximate the transmitral flow profile. The user-selected MVE points are the input to the computer program that automatically fits the PDF model solution for velocity as a function of time using a Levenberg- Marquardt (iterative) algorithm. The fitting is accomplished with the requirement that the mean square error between the clinical (input) data (MVE) and the PDF model predicted contour be minimized. Since the model is linear, a unique set of parameters is obtained for each Doppler E-wave derived MVE used as input. Thus numerically unique k, c and x_o values are generated for each E-wave and k', c' and x_o' for each E'-wave.

In the event the fit is obviously suboptimal when superimposed on the E-wave (or E'-wave) image (i.e. the algorithm attempted to fit noise included in the MVE for example) the MVE is modified using more/less points, thereby modifying the model predicted contour with consequent modification of PDF parameters to achieve a better fit.

2.8 Kinematic model of isovolumic relaxation

2.8.1 Theory: Chung model of relaxation

The pressure decay during LV isovolumic relaxation has been quantified by different models. The most commonly used method is an exponential decay model developed by Weiss et al [9] which fits the isovolumic pressure contour from peak negative dP/dt to mitral valve opening. Another method developed to quantify pressure decay during isovolumic relaxation was the logistic model [10]. These models are described in greater detail in Chapter 8.

A kinematic model was developed in our lab by Chung and Kovács [11] which models the pressure decay during isovolumic relaxation analogous to the motion of a damped simple harmonic oscillator. The equation for this model is given by:

$$\frac{d^2P}{dt^2} + \frac{1}{\mu}\frac{dP}{dt} + E_k\left(P - P_\infty\right) = 0$$

Eq. 2.7

In this expression E_k is the stiffness constant which represents the restoring forces and μ is the damping constant which represents the decaying contractile forces. A third parameter of this model is the pressure asymptote, P_∞. Similar to the PDF model (Eq. 2.1), the Chung model equation (Eq. 2.7) can be solved to yield solutions in 2 regimes- underdamped and overdamped.

The Chung model fits the isovolumic pressure decay contour from before peak negative dP/dt till mitral valve opening. Since this model is based on a causal kinematic mechanism it provides mechanistic information on the interplay of the decaying contractile forces and the opposing recoil forces in the myocardium. It also provides a better fit for a variety of clinically obtained pressure contours [12] as compared to the exponential or logistic model.

2.8.2 Automated method for fitting and parameter extraction

A custom MATLAB program was written to automatically fit isovolumic pressure decay contour with the kinematic model. Kinematic model parameters- μ, Ek, P_∞ were extracted for each individual beat by applying a Levenberg-Marquardt (LM) Algorithm to the pressure and pressure derivative data defined by the extracted isovolumic pressure decays contour. The algorithm is described in detail elsewhere [13], but the salient features are described briefly below. The algorithm requires initial guesses for the kinematic parameters and the dP(t)/dt data over the isovolumic pressure decay contour.

The initial parameters are derived from Eq. 2.7. The start of the fit (t_o) is at the inflection point of dP/dt (i.e. $d^2P/dt^2 = 0$). The Eq. 2.7 is evaluated at this time point. It is also evaluated at peak negative dP/dt (where again $d^2P/dt^2 = 0$). Using the 2 derived expressions P_∞ can be expressed in terms of pressures and pressure derivatives. By solving Eq. 2.7 at t= t_o, the expressions for E_k and μ can be evaluated [12].

Beginning with these initial guesses, the Levenberg- Marquardt algorithm minimizes χ^2 by iterating through parameter space, where χ^2 is defined by $\sum(\Delta P)/\sigma$, with ΔP defined by the error between model predicted and measured dP(t)/dt along the isovolumic pressure decay contour, and σ defined as the error in measured dP(t)/dt. Iteration ends when subsequent χ^2 values change by less than a predetermined threshold value. Upon completion, the root mean square error (RMSE) between model-predicted dP(t)/dt and measured dP(t)/dt is calculated using the LM-determined best fit kinematic parameters.

Reference:

1. Feltes TF, Bacha E, Beekman RH, Cheatham JP, Feinstein JA et al. Indications for cardiac catheterization and intervention in pediatric cardiac disease. *Circulation*. 2011; 123: 2607- 2652.

2. Anwaruddin S, Martin JM, Stephens JC, Askari AT. Cardiovascular Hemodynamics: An Introductory Guide. Chapter 8; Springer Science and Business Media, 2012.

3. Nagueh SF, Appleton CP, Gillebert TC, Marino PN, Oh JK, Smiseth OA, Waggoner AD, Flachskampf FA, Pellikka PA, Evangelista A. Recommendations for the Evaluation of Left Ventricular Diastolic Function by Echocardiography. *J. Am. Soc. Echocardiogr*. 2009; 22(2):107-133.

4. Kovács SJ, Barzilai B, Pérez JE. Evaluation of diastolic function with Doppler echocardiography: the PDF formalism. *Am. J. Physiol*. 1987; 87: H178-H187.

5. Riordian MM, Kovács SJ. Quantitation of mitral annular oscillations and longitudinal "ringing" of the left ventricle: a new window into longitudinal diastolic function. *J. Appl. Physiol*. 2006; 100:112-119.

6. Hall AF, Kovács SJ. Automated method for characterization of diastolic transmitral Doppler velocity contours: Early rapid filling. *Ultrasound Med. Biol*. 1994; 20: 107-116.

7. Hall AF, Nudelman SP, Kovács SJ, Jr. Evaluation of Model-Based Processing Algorithms for Averaged Transmitral Spectral Doppler Images. *Ultrasound Med Biol*. 1998 24:1, 55-66.

8. Hall AF, Kovács SJ Jr. Processing parameter effects on the robustness of the solution to the "Inverse Problem" of diastole from Doppler echocardiographic data. *Conf Proc IEEE Eng Med Biol Soc*.1993; I385-387.

9. Weiss JL, Frederiksen JW, Weisfeldt ML. Hemodynamics determinants of the time course of fall in canine left ventricular pressure. J. Clin. Invest. 1976; 58: 751- 760.

10. Matsubara H, Takaki M, Yasuhara S, Araki J, Suga H. Logistic time constant isovolumic relaxation pressure- time curve in the canine left ventricle. Circulation. 1995; 92: 2318-2326.

11. Chung CS, Kovács SJ. The physical determinants of left ventricular isovolumic pressure decline: Model-based prediction with in-vivo validation. Am J Physiol Heart Circ Physiol. 2008;294:H1589-H1596.

12. Shmuylovich L, Kovács SJ. Stiffness and relaxation components of the exponential and logistic time constants may be used to derive a load-independent index of isovolumic pressure decay. Am J Physiol Heart Circ Physiol. 2008; 295(6): H2551-2559.

13. Press WH, Flannery BP, Teukolsky SA, Vetterling WT. Numerical recipes: The art of scientific computing. Cambridge University Press. 1st Edition. 1987.

Chapter 3: Quantification of early diastolic LV vortex formation time via the PDF formalism: A kinematic model of filling.

Published as: Ghosh E, Shmuylovich L, Kovács SJ. Determination of early diastolic LV vortex formation time (T*) via the PDF formalism: a kinematic model of filling. *Conf Proc IEEE Eng Med Biol Soc*. 2009:2883-6.

Abstract

The filling (diastolic) function of the human left ventricle is most commonly assessed by echocardiography, a non-invasive imaging modality. To quantify diastolic function (DF) empiric indices are obtained from the features (height, duration, area) of transmitral flow velocity contour, obtained by echocardiography. The parameterized diastolic filling (PDF) formalism is a kinematic model developed by Kovács et al which incorporates the suction pump attribute of the left ventricle and facilitates DF quantitation by analysis of echocardiographic transmitral flow velocity contours in terms of stiffness (k), relaxation (c) and load (x_o). A complementary approach developed by Gharib et al, uses fluid mechanics and characterizes DF in terms of vortex formation time (VFT) derived from streamline features formed by the jet of blood aspirated into the ventricle. Both of these methods characterize DF using a causality-based approach. In this paper, we derive VFT's kinematic analogue $VFT_{kinematic}$ in terms of k, c and x_o. A comparison between $VFT_{kinematic}$ and $VFT_{standard}$ obtained from averaged transmitral velocity and mitral annulus diameter, is presented. We found that VFT calculated by the two methods were comparable and $VFT_{kinematic}$ correlated with the peak LV recoil driving force kx_o.

3.1 Introduction

3.1.1 Vortex formation in the LV

At the beginning of filling as the mitral valve opens, a jet of blood is aspirated into the left ventricle (LV). As this jet of blood moves towards the apex, due to shear forces acting on the boundary of this jet, it begins to curl and form a toroidal asymmetric three-dimensional vortex ring. The growth of this vortex ring has been quantified by a dimensionless index – vortex formation time (VFT). Vortex formation is optimized to make the momentum transfer between filling and ejection maximally efficient [1]. VFT represents the efficiency of the vortex formation process. Studies have shown [2] that VFT between 3.5- 5 represents the formation of a single vortex ring while higher VFT values are indicative of a pinched off vortex ring and a series of trailing jets. These studies found that circulation of the vortex ring increased till VFT reached the value of 4 and then plateaued. Hence the value of VFT between 3.5- 5 was deemed to be efficient. Vortex formation confers many biological and mechanical advantages. Mechanically, vortexes prevent loss of momentum as the incoming jet of blood hits the stagnant volume in the LV. By optimizing swirling of blood in the LV, redirects the jet of blood towards the outflow tract prior to ejection. Hence the LV has to do less work in ejecting blood. From a biological perspective, swirling of the blood prevents coagulation and thrombus formation. Hence efficient vortex formation is vital to diastolic function (DF).

3.1.2 Quantifying vortexes

Vortex structures comprise of fluid particles which have both a rotational and an irrotational component of velocity. Vortex structures are quantified by calculating the vorticity of each fluid

particle. Vorticity is defined as the curl of the velocity and hence it exists only in rotational flow. The rotating fluid particles combine together to form vortex structures [3]. The shape of these vortex structures depends on the velocity of the surrounding layers. A vortex layer is formed as a boundary between fluid flow and chamber walls. When rotating flow encounters an edge (such as a leaflet tips), the flow closest to the edge starts to decelerate and it gives rise to a rotating fluid structure. The outer layers in the rotating fluid structure have higher velocity and this creates a rotating vortex ring. Apart from vorticity, vortex rings can also be quantified by circulation which is the sum of the vorticity in a specified region.

3.1.3 Relation between LV kinematics and vortex formation

As the ventricle relaxes in diastole, the chamber walls become less stiff and the pressure falls. The pressure change in the ventricle is caused by chamber kinematics, which have been quantified as a function of stiffness, viscoelasticity and preload using the PDF formalism (see Chapter 2). As the LV pressure drops, it falls below atrial pressure creating a pressure gradient which results in mitral valve opening. This pressure difference also powers transmitral filling. Since transmitral flow, which subsequently forms vortex rings in the LV, is a result of the pressure difference between the atrium and the ventricle we hypothesized that vortex ring attributes such as VFT are related to the PDF derived chamber kinematic parameters. Moreover the effective orifice diameter through which transmitral flow enters is also a function of LV chamber kinematics. The left heart is a constant volume pump. During the cardiac cycle, the mitral annulus moves basally i.e. towards the atrium and apically alternately such that the total volume contained in the left atrium + LV remains constant (~95%) [5]. Hence the increase in LV endocardial chamber volume during filling is largely due to the motion of mitral annulus towards

the atrium (Fig 3.1A). Fig. 3.1A is a schematic diagram of the left heart and it shows how the internal dimensions of the LV change with filling. It shows that the ratio of transmitral filling velocity (Doppler E-wave) to the longitudinal mitral annular tissue velocity (Doppler E'-wave) is proportional to the ratio of the cross-sectional area of the LV chamber to the mitral orifice [6].

3.2 Methods

3.2.1 Formulating VFT$_{standard}$

VFT has been defined by Gharib et al [7] as the ratio of the length of the fluid column to the diameter of the nozzle through which the fluid is ejected (in a piston- cylinder setup).

$$VFT = \int_0^t \frac{U(t)}{D(t)} \cdot dt$$
Eq. 3.1

In context of the LV this definition has been reexpressed as:

$$VFT_{standard} = \frac{\overline{U}}{\overline{D}} \cdot t$$
Eq. 3.2

Where Ū is mean early transmitral flow velocity, T is the direction of flow and D is orifice diameter. The numerator in this expression represents the E-wave area. Since the Doppler E-wave has been approximated as a triangle (See Chapter 2) this numerator can be alternately expressed as the area of a triangle with height equal to peak E-wave velocity and base equal to flow duration. Thus Eq. 3.2 can be written as:

$$VFT_{standard} = (E_{peak} \text{ X } E_{dur})/(2 \text{ X } D)$$
Eq. 3.3

The orifice diameter, D is measured by M-mode imaging in the parasternal long axis view as the peak mitral leaflet separation. Thus VFT$_{standard}$ can be calculated using echocardiography only. However, Eq. 3.3 is based on certain approximations. The area under the E-wave which

represents the length of the fluid column has been approximated as the area under the triangle. This doesn't take into account the curvilinear nature of E-wave. The expression also approximates the time varying mitral leaflet separation by the peak leaflet separation. Moreover due to the constant- volume attribute of the left heart [5] the change in LV effective orifice diameter is linked to the change in LV volume via the longitudinal motion of the LV. By selecting one point in the cardiac cycle to measure peak mitral leaflet separation, Eq. 4.2 ignores this physiological aspect of DF.

An alternate way of simplifying the expression for VFT is by replacing the numerator and denominator with the expressions in terms of PDF parameters. The numerator is the velocity time integral of the area under the E-wave. For the denominator, the effective mitral orifice diameter is computed.
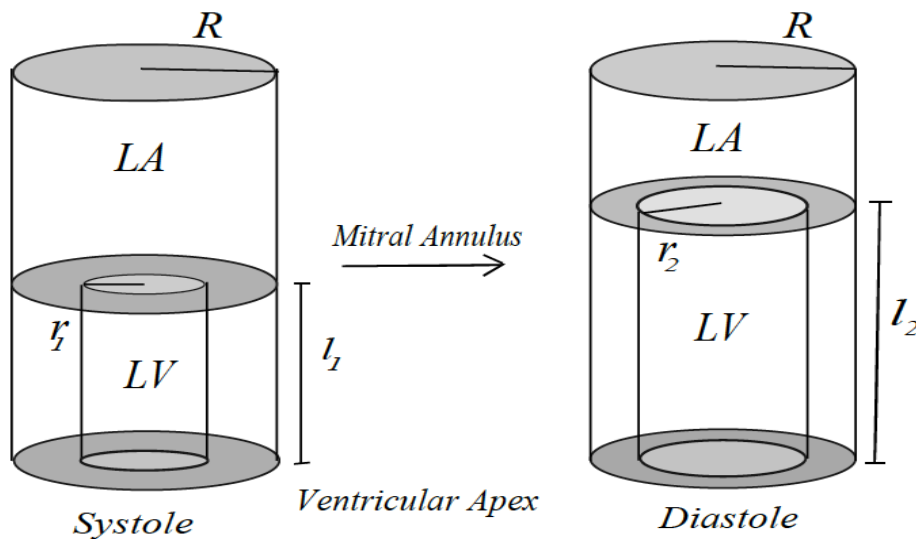
Fig 3.1: Schematic diagram of the left heart from (3) illustrating the constant volume property of the left heart. *LA* = Left Atrium, *LV* = Left Ventricle, *R* = Epicardial radius, *r1* = Effective orifice diameter at systole, *r2* = Effect orifice diameter in diastole, *l1* = Ventricular long axis diameter in systole, *l2* = Ventricular long axis diameter in diastole. The cylinder on the left represents a ventricle in systole and the cylinder on the right illustrates a ventricle in diastole. See text for details.

3.2.2 Deriving effective orifice diameter

VFT can also be expressed in terms of the transmitral blood flow velocity (E-wave) and mitral annulus

velocity (E'-wave). The equations that provide the contour of each of these waves utilize the PDF parameters – k, c and x_o for the E-wave and k', c' and x_o' for the E'-wave. The transmitral flow and the mitral annular motion are connected via the constant volume physiology (Chapter 1, [5]). Using this aspect of physiology we can model the left heart as a cylinder with fixed outer dimensions (Fig 3.1). The radius of this cylinder is R (epicardial radius). The mitral valve plane divides the cylinder into the left atrium (at the top) and the LV (at the bottom). In the ventricular portion the inner chamber dimensions at the beginning of filling are r_1 (endocardial radius) and l_1 (endocardial chamber length). As the mitral valve opens and blood is aspirated into the LV, the mitral annular plane moves upwards towards the atrium. The endocardial radius also changes as the wall thins radially. The final dimensions of the endocardial chamber are r_2 and l_2. This allows us to write a couple of equations. First the volume of the blood entering the LV is equal to the increase in the endocardial chamber volume.

$$\frac{\pi}{4}(D(t))^2 \cdot E(t) \cdot t = \pi r_2^2 l_2 - \pi r_1^2 l_1 \qquad \text{Eq. 3.4}$$

In this equation D(t) is the effective chamber diameter as a function of time. E(t) represents the E-wave velocity as a function of time (same as U(t) in Eq. 3.1). Since ventricular tissue is incompressible, the chamber tissue volume did not change from the start to the end of filling. Hence we can write:

$$\pi(R^2 - r_1^2)l_1 = \pi(R^2 - r_2^2)l_2$$

$$\Rightarrow \pi(r_2^2 l_2 - r_1^2 l_1) = \pi R^2 (l_2 - l_1) \qquad \text{Eq. 3.5}$$

We can rearrange Eq. 3.5 and substitute it into the right hand side of Eq. 3.4 to express D(t) as a function of E(t) and R.

$$R^2(l_2 - l_1) = (D(t))^2 \cdot E(t) \cdot t \cdot \frac{1}{4}$$

$$\Rightarrow 4 \cdot R^2 \cdot E'(t) = (D(t))^2 \cdot E(t)$$

$$\Rightarrow \frac{1}{D(t)} = \frac{1}{2R} \cdot \sqrt{\frac{E(t)}{E'(t)}} \qquad \text{Eq. 3.6}$$

In this equation, E'(t) represents the velocity of the mitral annular plane as measured by tissue Doppler imaging.

3.2.3 Deriving VFT$_{kinematic}$

Starting with Eq. 3.1, we replaced U(t) by the PDF derived E(t) and the orifice diameter (D(t)) were calculated using Eq. 3.6. Hence:

$$VFT = \frac{1}{2R} \int_0^t E(t) \cdot \sqrt{\frac{E(t)}{E'(t)}} \cdot dt$$

$$\Rightarrow VFT = \frac{1}{2R} \int_0^t \sqrt{\frac{(E(t))^3}{(E'(t))}} \cdot dt \qquad \text{Eq. 3.7}$$

The PDF formalism provides, closed form algebraic expressions for E-wave and E'-wave contours which are solutions to the SHO equation of motion. For underdamped kinematics ($c^2 - 4mk < 0$) the E-wave and E'-wave are:

$$E(t) = -\frac{kx_o}{m\omega} e^{\frac{-ct}{2}} (\sin(\omega t))$$

$$E'(t) = -\frac{k'x_o'}{m\omega'} e^{\frac{-c't}{2}} (\sin(\omega' t))$$

For over-damped kinematics the expressions are:

$$E(t) = -\frac{kx_o}{m\omega}e^{\frac{-ct}{2}}(\sinh \omega t)$$

$$E'(t) = -\frac{k'x_o'}{m\omega'}e^{\frac{-c't}{2}}(\sinh \omega't)$$

Where $\omega = \sqrt{(4mk - c^2)}/2m$ and $\omega' = \sqrt{(4mk' - c'^2)}/2m$ for under-damped

kinematics and $\omega = \sqrt{(c^2 - 4mk)}/2m$ and $\omega' = \sqrt{(c'^2 - 4mk')}/2m$ for over-damped kinematics.

Substituting into Eq. 3.7 yields the vortex formation time in terms of PDF parameters. For the

underdamped regime:

$$VFT_{kinematic} = K \int_0^t \sqrt{\frac{\sin^3(\omega t)}{\sin(\omega't)}}e^{\frac{-t(3c-c')}{4}}dt \qquad \text{Eq. 3.8}$$

For the overdamped regime:

$$VFT_{kinematic} = K \int_0^t \sqrt{\frac{\sinh^3(\omega t)}{\sinh^3(\omega't)}}e^{\frac{-t(3c-c')}{4}}dt \qquad \text{Eq. 3.9}$$

Where $K = \frac{1}{2R} \cdot \sqrt{\frac{k^3 x_o^3 \omega'}{k'x_o'\omega^3}}$

3.2.4 Calculating VFT$_{kinematic}$ from PDF parameters: Numerical simulation

A numerical simulation using Matlab (Matlab 6.0, MathWorks, Natick, MA) was done to

calculate $VFT_{kinematic}$ from the PDF parameters. The E-wave parameters x_o, c and k, the E'-wave

parameters – x_o', c and k' were generated using a random number generator assuming a uniform

56

distribution. The limits of the distribution for each parameter were determined using values obtained by fitting actual E- and E'-waves with the PDF model. The six parameters were used to calculate the $VFT_{kinematic}$ using Eq. 3.8 and Eq. 3.9 and integrating over the duration of the E'-wave. The $VFT_{kinematic}$ value was taken as the value of vortex formation time at the time the E'-wave velocity maximum (E'$_{peak}$).

3.2.5 Calculating VFT$_{standard}$ and comparison with VFT$_{kinematic}$

$VFT_{standard}$ was calculated using the mean E-wave velocity and the mitral annulus diameter at peak diastole. The vortex formation time was calculated for the whole duration of the E-wave. To compare the $VFT_{kinematic}$ obtained from the PDF model to the $VFT_{standard}$ derived in [7], we calculated $VFT_{standard}$ using Eq. 3.3. The mitral annulus area was taken to be 4 cm^2 [6]. Since $VFT_{kinematic}$ was calculated at instant of peak E'- wave velocity we extrapolated it to the end of E-wave.

Fig 3.2: (Top) E-wave (positive velocity curve) and E'-wave (negative velocity curve) plotted against time. (Bottom) $T^*_{kinematic}$ plotted against time for the duration of E'-wave. The PDF parameters for this set of waves were: k= 300 3g/s^2, c= 23g/s, x_o = 3.9cm, k' = 434 g/s^2, c' = 21 1g/s, x_o'= 0.7cm

3.3 Results

The simulation program generated E- and E'-waves and calculated the vortex formation time as function of time. The vortex formation time was plotted against time and $VFT_{kinematic}$ was determined. The extrapolated value of $VFT_{kinematic}$ was determined. The vortex formation time ($VFT_{standard}$) was determined using the method in [7]. The two vortex formation times were compared. The results are shown below.

A sample E- and E'-wave generated by the simulation and the $VFT_{kinematic}$ plotted against time is shown in Fig. 3.2A. The selected E- and E'-waves are underdamped. The peak velocity of E-wave is 32 cm/s and peak velocity of E'- wave is 8 cm/s. The $VFT_{kinematic}$ has been plotted for the duration of E'-wave (0.174s). The time point of peak E'-wave velocity has been marked in the Fig. 3.2B. The vortex formation time at this point is 3.4. The extrapolated value (extrapolated to the end of E-wave) of $VFT_{kinematic}$ is 14.6. The $VFT_{standard}$ calculated using the same E-and E'-wave is 2.4. In agreement with prior observation, the dimensionless vortex formation time increases linearly with time till near the end of E'-wave [8].

3.4 Discussion

Historically, alternative approaches have been used to model LV filling and characterize the operative physiologic mechanisms. These include electrical circuit analog models, finite element fluid-tissue interaction models, lumped parameter fluid-chamber models and kinematic models. Most of these approaches involve coupled, nonlinear partial differential equations with up to dozens of parameters, all of which need to be specified at the initiation of model computation. These types of models are not 'invertible', i.e. model parameters cannot be uniquely determined from physiologic data used as input. Two of the approaches can use physiologic data as input to

determine model predicted parameters. These include a kinematic approach, the PDF formalism, and the fluid mechanics approach advanced by Gharib et al [7].

3.4.1 Role of vortexes in ventricular filling

In Gharib et al's fluid mechanics approach, diastolic function of the chamber is quantitated in terms of vortex formation time. Because the chamber is part of a constant volume 4-chamber pump, tissue motion is necessarily accompanied by fluid motion. Given the approximate shape of the LV as a truncated ellipsoid of revolution that recoils by long axis extension during diastole with concomitant radial expansion of the interior of the chamber wall, the geometry of the arrangement assures that the blood aspirated by the left ventricle in early diastole forms an asymmetric vortex ring [9].

This arrangement has important biological and fluid mechanics advantages. The biological advantage is that vortex formation 'rinses' the endocardial surface with each heart beat, thereby avoiding areas of stagnation that can form thrombi and generate arterial obstruction outside the heart. The fluid mechanics advantage is that fluid transport into a closed container with an expanding inner boundary is made more efficient by development of a vortex ring. This is characterized by the vortex formation time, determined by time-averaged speed of transmitral flow (E-wave), the duration of the flow relative to the diameter of the orifice (mitral annulus diameter). Previous work [7, 10] has focused on finding an optimal value of *VFT* which can be used as an index of diastolic function. Also *VFT* has been shown to independently correlate with the transmitral thrust, minimum LV pressure and the pressure drop time constant of isovolumic relaxation [8].

3.4.2 Relating chamber kinematics to vortex formation

The left ventricle during early diastole acts as a suction pump and the elastance and recoil of the ventricular wall provides the energy for the pressure gradient which aspirates blood from the atrium into the ventricle. Hence we hypothesized that the vortex formation time could be calculated from modeling filling kinematically in terms of the analog stiffness, damping and initial spring displacement of an equivalent SHO. Consistent with known physiology, we assumed that the external radial dimension of the left ventricle remains constant during the filling so that the ventricle lengthens as its wall thins while it fills. Using the constant volume attribute of this simplified, and idealized geometric atrioventricular arrangement [5], time varying mitral valve diameter was calculated in terms of the epicardial dimension and the ratio of transmitral blood flow velocity (E-wave) and the mitral annulus velocity (E'-wave). This approach allowed for the determination of *VFT* without a direct measurement of time varying mitral diameter. Using the PDF formalism, we expressed the E- and the E'-wave contours in terms of SHO kinematics.

We derived the expression for *VFT* as a function of time in terms of PDF parameters. This expression provides *VFT* at every instant during the E-wave. By calculating the instantaneous values of transmitral blood velocity and the mitral annulus diameter this method also provides a value of the vortex formation time. For consistency with the constant volume atrioventricular chamber approximation we calculated the vortex formation time up to the duration of the E'-wave. We denoted the vortex formation time at the peak of E'-wave as *VFT_{kinematic}*. Previous work [8] has shown that *VFT* increases linearly with time. Hence we linearly extrapolated *VFT_{kinematic}* to the end of the E-wave. We calculated the *VFT_{standard}* by taking the E-

wave velocity averaged over the duration of E-wave, the maximum mitral annulus diameter and the duration of the E-wave.

3.4.3 Limitations

The calculation of $VFT_{standard}$ and $VFT_{kinematic}$ in the LV require several approximations. The first approximation is in the calculation of the orifice diameter in Eq. 3.3. For the purpose of this simulation it was assumed to be a constant value. However, Gharib et al [7] have calculated this value as the peak mitral leaflet separation during the E-wave. Both these values ignore the changing orifice diameter during the E-wave. To calculate the effective diameter for $VFT_{kinematic}$, Eq. 3.6 is used. While this expression uses physiology to compute the diameter and it is a better approximation, it is only applicable till the end of the E'-wave. After the E'-wave the derivation used in Eq. 3.6 is no longer true. Typically the E'-wave is shorter than E-wave hence $VFT_{kinematic}$ can't be calculated for the entire duration of the E-wave. Moreover, unlike the numerical simulation during echocardiographic examination, Doppler E- and E'- waves are not recorded simultaneously. Hence it is difficult to calculate the exact chamber motion for a given E-wave.

3.5 Conclusion

We found that the $VFT_{kinematic}$ and $VFT_{standard}$ were comparable, consistent within the approximations of our geometric model indicating the applicability of our approach to calculate vortex formation time. In addition, we also found that $VFT_{kinematic}$ was strongly correlated (R^2 = 0.517) with peak driving force of transmitral flow (kx_o) and the rate of change of the transmitral flow velocity (R^2 = 0.377, E_{peak}/ E_{dur}).

Reference:

1. Hong GR, Pedrizzetti G, Tonti G, Li P, Wei Z, Kim JK, Baweja A, Liu S, Chung N, Houle H, Narula J, Vannan MA. Characterization and Quantification of Vortex Flow in the Human Left Ventricle by Contrast Echocardiography Using Vector Particle Image Velocimetry. *J Am Coll Cardiol Img* 2008; 1(6): 705-717.

2. Gharib M, Rambod E, Shariff K. A Universal Time-Scale of Vortex Formation Time. *J. Fluid. Mech*. 1998; 360:121-140.

3. Kheradvar A, Pedrizzetti G. Vortex formation in the cardiovascular system. Springer-Verlag, London Limited. 2012.

4. Bauman L, Chung CS, Karamanoglu M, Kovács SJ. The peak atrioventricular pressure gradient to transmitral flow relation: kinematic model prediction with in vivo validation. *J. Am. Soc. Echocardiogr*. 2004; 17(8): 839- 844.

5. Bowman AW, Kovács SJ. Assessment and consequences of the constant-volume attribute of the four-chambered heart. *Am. J. Physiol*. 2003; 285:H2027-H2033.

6. Lisauskas JB, Singh J, Courtois MR, Kovács SJ, Jr. The relation of the peak Doppler E-wave to peak mitral annulus velocity ratio to diastolic function. *Ultrasound Med. Biol*. 2001; 27: 499-507.

7. Gharib M, Rambod E, Kheradvar A, Sahn DJ, Dabiri JO. Optimal vortex formation as an index of cardiac health. *Proc Nat Acad Sciences* 2006; 103(16): 6305 -6308.

8. Kheradvar A, Gharib M. On Mitral Valve Dynamics and its Connection to Early Diastolic Flow. *Annal Biomed Engg* 2008; 37: 1-13.

9. Kovács SJ, McQueen DM, Peskin CS. Modeling cardiac fluid dynamics and diastolic function. *Phil. Trans. R. Soc. Lond. A*. 2001; 359: 1299- 1314.

10. Kheradvar A, Milano M, Gharib M. Correlation Between Vortex Ring Formation and Mitral Annulus Dynamics During Ventricular Rapid Filling. *J. Am. Soc. Artificial Organs*. 2007; 53:8-16.

Chapter 4: The vortex formation time to left ventricular early, rapid filling relation: model-based prediction with echocardiographic validation

Abstract

During early rapid filling, blood aspirated by the left ventricle (LV) generates an asymmetric toroidal vortex whose development has been quantified using vortex formation time (VFT), a dimensionless index defined by the length to diameter ratio of the aspirated (equivalent cylindrical) fluid column. Since LV wall-motion generates the atrioventricular pressure gradient resulting in the early transmitral flow (Doppler E-wave) and associated vortex formation, we hypothesized that the causal relation between VFT and diastolic function (DF), parametrized by stiffness, relaxation and load, can be elucidated via kinematic modeling. Gharib et al approximated E-wave shape as a triangle and calculated VFT_{Gharib} as triangle (E-wave) area (cm) divided by peak (Doppler M-mode derived) mitral orifice diameter (cm). We used a validated, kinematic model of filling for the E-wave as a function of time, parametrized by stiffness, viscoelasticity and load. To calculate $VFT_{kinematic}$ we computed the curvilinear E-wave area (using the kinematic model) and divided it by peak effective orifice diameter. The derived VFT to LV early, rapid filling relation predicts VFT to be a function of peak E-wave to peak mitral annular tissue velocity (Doppler E'-wave) ratio as $(E/E')^{3/2}$. Validation utilized 262 cardiac cycles of simultaneous echocardiographic high-fidelity hemodynamic data from 12 subjects. VFT_{Gharib} and $VFT_{kinematic}$ were calculated for each subject and were well-correlated ($R^2=0.66$). In accordance with prediction, $VFT_{kinematic}$ to $(E/E')^{3/2}$ relationship was validated ($R^2 = 0.63$). We conclude that $VFT_{kinematic}$ is a DF index computable in terms of global, kinematic filling parameters of stiffness, viscoelasticity and load. Validation of fluid mechanics to chamber kinematics relation unites previously unassociated DF assessment methods and elucidates the mechanistic basis of the strong correlation between VFT and $(E/E')^{3/2}$.

4.1 Introduction

4.1.1 Fluid mechanics based approach to quantify diastolic function

The ability to quantify diastolic function (DF) is important in diagnosing heart failure with normal ejection fraction or diastolic heart failure [1, 2]. Various approaches to model DF have been proposed, including ones involving fluid mechanics. An index based on this approach to quantify filling efficiency is vortex formation time (*VFT*) [3]. *VFT* is a dimensionless measure of the time needed for optimal vortex ring formation [4]. Gharib et al defined [5] *VFT* as the ratio of the velocity of transmitral flow to the orifice diameter integrated over the duration of flow (Chapter 3, Eq 3.3). *In-vitro* values of *VFT* have been calculated using a left heart flow simulator [6]. However, calculating *VFT* as defined above using clinical data is challenging and hence approximations are applied. Gharib et al [7], for example, approximated both early transmitral flow velocity (Doppler E-wave) and the effective orifice diameter as having constant values. While these approximations allow for clinical estimation of *VFT*, valuable physiologic information may be lost in the process.

4.1.2 Kinematic approach to model diastolic function

An alternate approach for DF quantification involves kinematic modeling of the filling process. This is available via the parametrized diastolic filling (PDF) formalism[8], which has elucidated and characterized new relationships in the physiology of diastole[9]. It has been validated in a broad range of clinical applications [10- 14]. The PDF formalism accounts for suction initiated filling and generates accurate Doppler E-wave contours mathematically parametrized by lumped chamber attributes corresponding to load, stiffness and viscosity/relaxation.

In diastole chamber wall relaxation unmasks stored elastic strain allowing the left ventricle (LV) to recoil and act as a suction pump [15] by aspirating blood into the ventricle. Therefore filling and LV relaxation and recoil are closely coupled. Hence we hypothesized that *VFT* calculated by fluid mechanics and kinematic approaches should be equivalent. The specific mathematical expression relating *VFT* to chamber stiffness, relaxation and load parameters encountered clinically has not been previously determined. Thus we derive the closed form mathematical expression for *VFT* using the PDF model. Validation of the derivation consists of determining the linear correlation between *VFT$_{kinematic}$* and *VFT$_{Gharib}$* using human, in-vivo data. We show that the derived expression provides new mechanistic insight into the physiologic determinants of *VFT* and reveal that *VFT* and the ratio of peak E-wave velocity to peak mitral annular E'-wave peak (*E/E'*) ratio are directly related [16].

4.2 Methods

4.2.1 Inclusion criteria

We selected twelve datasets from the existing Cardiovascular Biophysics Laboratory database of simultaneous Doppler echocardiographic transmitral flow and micromanometric catheter recorded LV pressure recordings obtained during elective, diagnostic cardiac catheterization. Prior to data acquisition, subjects provided signed, informed consent for participation in accordance with Washington University Human Research Protection Office (HRPO) criteria. All the subjects had normal ejection fraction (EF; 74±6 %). Among these 12, 6 datasets had end-diastolic pressure (LVEDP) less than 15 mm Hg, 3 datasets had 15 mm Hg < LVEDP< 20 mm Hg and 3 datasets had LVEDP > 20 mm Hg. The data selection criteria included presence of normal sinus rhythm, normal valvular function and clearly identifiable Doppler E- and A-waves

(early and late transmitral flow velocity) and Doppler E'- and A'-waves (early and late mitral annular tissue velocity). A total of 262 cardiac cycles of simultaneous echocardiographic-high fidelity hemodynamic data were analyzed.

4.2.2 Doppler data acquisition

The method of simultaneous echocardiographic transmitral flow and pressure-volume data recording has been previously detailed [17] and is reviewed in Chapter 2. Our echocardiographic data acquisition methodology is performed in accordance with published American Society of Echocardiography [18] criteria. Briefly, immediately before catheterization, patients are imaged in a supine position using a Philips iE33 system. Two dimensional images in apical 2- and 4-chamber views were obtained. In accordance with convention, the apical 4-chamber view was used for Doppler E-wave recording with the sample volume located at the leaflet tips. For E'-wave recording, the lateral aspect of the mitral annulus was chosen. This site was selected because recent studies have shown [18] that in patients with normal EFs, E' data recorded from the lateral aspect of the annulus have the best correlations with LV filling pressures and invasive indices of LV stiffness. We also recorded Doppler M-mode images using the parasternal short axis view for determination of annular diameter.

4.2.3 Doppler data analysis

In accordance with convention, Doppler E-waves were first approximated as triangles. Duration of the E-wave (E_{dur}) and peak E-wave velocity (E_{peak}) was determined manually using standard criteria [19]. The same analysis was applied to tissue Doppler E'-waves. The peak mitral leaflet separation was measured in accordance with Gharib et al [7] as the maximum separation between

the leaflets in M-mode images. The epicardial dimension was also measured from the M-mode images using the method described by Foppa et al [20].

In addition, we computed the PDF formalism determined kinematic parameters for each Doppler E- and E'-wave. A model-based image processing algorithm (see Chapter 2) was applied to E-and E'- waves to generate PDF parameters for E- (c, k, x_o) and the E'-wave (c', k', x_o') [8,17, 21, 22,23].

Since echocardiographic imagers do not simultaneously record E- and E'-waves, we matched E- and E'-waves having the same R-R interval (±15 ms) to calculate E/E' values for each subject. We analyzed an average of 22 beats from each dataset. Although all the beats were acquired with the patients in a resting state (i.e. similar loading conditions), physiologic, beat-to-beat variation in wave amplitude and duration was observed, as expected. This resulted in beat to beat variation of the parameters (for example the standard deviation of peak E'-wave velocity; E'_{peak} was 124.8% of the mean). We therefore averaged the parameters over multiple (~ 22) beats in each subject so that the effect of physiologic, beat-to-beat respiratory variation was accounted for yielding a robust value for E/E', VFT etc.

4.2.4 Calculation of VFT$_{standard}$

VFT$_{standard}$ was calculated according to Eq. 3.3 (See Chapter 3 for details). The parameters were measured from Doppler transmitral flow images by approximating the E-waves as triangle. This is detailed in Chapter 2. Peak mitral valve leaflet tip separation (D_{M-mode}) was determined from M-mode images. The diameter was averaged over multiple images in each subject to remove measurement errors. For each E-wave, the conventional E-wave indexes- E_{peak} and E_{dur} were used with the average D_{M-mode} to calculate VFT$_{standard}$.

4.2.5 Derivation and calculation of the effective mitral orifice diameter

The total 4-chambered heart volume remains constant (~95%) during the cardiac cycle. Accordingly the left heart (atrium + ventricle) can also be approximated as a constant-volume pump [24]. We used this physiologic attribute to predict the effective mitral orifice diameter for filling. The derivation is detailed in Chapter 3 (Section 3.2.2). Fig. 3.1 shows the left heart as a cylinder of fixed height and external (epicardial) dimension. In diastole long axis LV dimension increases (lengthening of the ventricle) with concurrent increase in the endocardial diameter. The apex remains fixed near the sternum. The endocardial to the epicardial diameter ratio is related to the rate of lengthening of the ventricle (mitral annulus velocity; tissue Doppler E'-wave) to rate of ventricular filling (transmitral flow velocity; Doppler E-wave) ratio. The effective mitral orifice diameter is related to E- and E'-waves according to Eq. 3.6. The estimated effective orifice diameter (D_{est}) was computed using peak E'-wave velocity and E-wave velocity at the time of E'$_{peak}$.

4.2.6 Derivation and calculation of VFT$_{kinematic}$

We derived the kinematic equivalent of *VFT* via the PDF formalism. The E-wave velocity-time integral (VTI) was expressed using PDF parameters. Effective flow orifice diameter was computed by incorporating constant volume physiology as described above, by relating transmitral flow to annulus velocity. For the underdamped wave, this E-wave area can be evaluated as:

$$E - VTI = x_o \left(1 + \exp\left(-c\pi / 2\omega\right)\right) \qquad \text{Eq. 4.1}$$

Combining Eq. 4.1 and Eq 3.6 gives the expression for VFT$_{kinematic}$ as:

$$VFT_{kinematic} = \frac{x_o\left(1 + \exp\left(-c\pi / 2\omega\right)\right)}{D_{est}}$$

Eq. 4.2

where $D_{est} = D_{epi}\sqrt{\dfrac{E'_{peak}}{E_{peak}}}$. D_{epi} is the epicardial diameter computed from the parasternal M-mode

images using a method similar to calculating $D_{M\text{-mode}}$.

4.2.7 Derivation of relation between VFT and E/E'
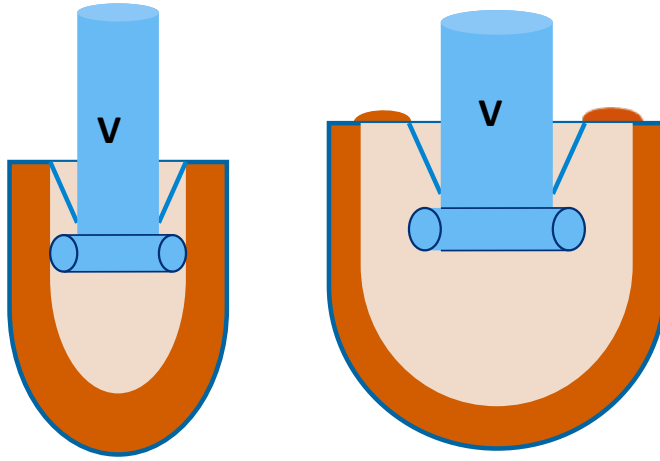
Fig 4.1: Schematic representation of 2 LVs. The image on the left is a normal size LV and the image on the right is a dilated LV. Both LVs fill with the same volume V.

The E-wave volume can be approximated as a fluid cylinder whose diameter equals the effective mitral orifice diameter. To appreciate how *VFT* depends on dimensions of the filling column consider two ventricles having different effective orifice diameters filling with the same volume (*V*) (Fig 4.1). The volume for a cylinder of height L and diameter D is $V = \pi L(D^2/4)$. *VFT* for the fluid cylinder is defined as:

$$VFT = \frac{L}{D} = \frac{4V}{\pi D^3}$$

Eq. 4.3

As the effective mitral orifice diameter decreases for the same E-wave volume, *VFT* increases as the cube of the diameter. Invoking the constant-volume attribute, (Eq. 3.6) *VFT* becomes:

$$VFT \cong \frac{1}{D^3} = \left(\frac{E}{E'}\right)^{3/2}$$

Eq. 4.4

This analysis is applicable in the setting of essentially similar values for E-wave volume. In the datasets analyzed we found very small variation (the standard deviation in the values was ±7.7 ml) in E-wave volumes among the subjects, thus justifying the derivation in Eq. 4.4. This derivation uses the basic definition of VFT and hence is equally applicable to $VFT_{standard}$ and $VFT_{kinematic}$. We tested this prediction by determining the correlation of $VFT_{kinematic}$ and $VFT_{standard}$ to $(E/E')^{3/2}$.

4.2.8 Numerical and statistical analysis

A MATLAB program (MATLAB 6.0 MathWorks, Natick, MA) was used to determine a triangle fit to Doppler E- and E'- waves. As in previous work [16, 22] we used a model-based image processing program to compute PDF parameters (see Chapter 2). $VFT_{kinematic}$ and $VFT_{standard}$ values were computed for each subject using a custom MATLAB program. Data from multiple beats for each subject was averaged to determine VFT and E/E' values. Regression analysis was performed to validate the relationship between $VFT_{kinematic}$ and $VFT_{standard}$ and both the $VFTs$ and $(E/E')^{3/2}$. The average values were correlated and Pearson's product moment correlation coefficient (R^2) for each linear regression was determined.

4.3 Results

The subject demographics are described in Table 4.1. We measured the peak mitral leaflet separation and epicardial diameter from M-mode images and calculated $VFT_{standard}$, $VFT_{kinematic}$ and E/E' for all datasets as described above. The values are listed in Table 4.2. The $VFT_{standard}$ values calculated ranged from 2.5 to 4.7 (3.9 ± 0.7).

Parameter	Mean ± SD
Number of Subjects	12 (6 females, 6 males)
Age (yrs)	56 ± 12
Weight (pounds)	178 ± 40
Systolic Pressure (P_{max} mmHg)	137 ± 28
EF (%)	74 ± 6
LVEDP (mmHg)	16 ±3

Table 4.1: Subject Demographics. Values are given in the form of mean ± SD.

Subject Number	Mitral Leaflet separation (cm)	Epicardial diameter (cm)	$VFT_{kinematic}$	$VFT_{standard}$	E/E'	Average E-wave velocity (cm/s)	Average E'-wave velocity (cm/s)
1	3.1	6.6	1.79	2.49	2.33	59	24
2	3.1	6.1	2.17	3.23	2.33	67	28
3	2.5	6.0	3.94	3.84	5.50	71	13
4	2.8	6.1	4.05	4.56	4.42	71	16
5	3.0	7.2	3.33	3.93	4.89	77	27
6	2.8	7.6	2.51	2.60	7.25	50	7.3
7	2.7	6.5	3.32	3.76	5.27	70	13
8	2.7	6.5	5.32	4.26	10.0	80	8.8
9	2.3	6.2	3.35	3.86	6.36	55	9.0
10	3.4	6.2	3.33	3.08	4.59	68	14
11	2.7	6.6	4.86	3.87	11.8	68	6.2
12	3.0	9.2	4.61	4.74	9.32	89	9.2

Table 4.2: Values of peak mitral leaflet separation (cm), epicardial diameter (cm), $VFT_{kinematic}$, $VFT_{standard}$ and E/E' measured and calculated for each of the 12 subjects. For each subject $VFT_{kinematic}$, $VFT_{standard}$ and E/E' were calculated over multiple beats and the averaged value is shown here.

4.3.1 Validating the derivation of VFT$_{kinematic}$

We validated $VFT_{kinematic}$ by computing the regression relation between VFT$_{standard}$ and $VFT_{kinematic}$. The regression relationship obtained was: $VFT_{kinematic} = 1.22 * VFT_{Gharib} - 0.96$, $R^2 = 0.66$. Fig. 4.2 shows $VFT_{kinematic}$ vs. VFT$_{standard}$ for data obtained from 12 datasets with the regression line. The values of $VFT_{kinematic}$ ranged from 1.8 to 5.3 (4.3 ± 0.8) (Table 4.2).

4.3.2 Analysis of the differences between the two components of VFT$_{kinematic}$ vs. VFT$_{standard}$
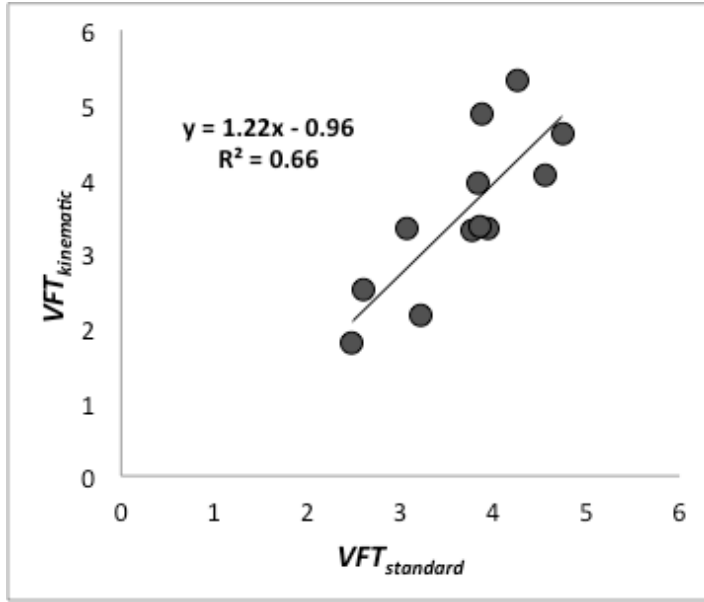
Fig 4.2: Validation of $VFT_{kinematic}$ as an analog of $VFT_{standard}$. The regression relation between $VFT_{standard}$ vs. $VFT_{kinematic}$ for 12 subjects is shown. The slope of the regression line (1.22) indicates that $VFT_{kinematic}$ is of the same order of magnitude as $VFT_{standard}$ See text for details.

In order to understand the differences in the two VFTs, we compared the two methods for calculating the E-wave area and the two methods for calculating the effective flow orifice diameter. The regression relation between the estimated orifice diameter (from the constant volume attribute) and the measured the peak leaflet separation (from M-mode images) was

$D_{est} = 1.32 *$ (Peak leaflet separation) - .01, $R^2 = 0.35$. Fig. 4.3a shows the plot
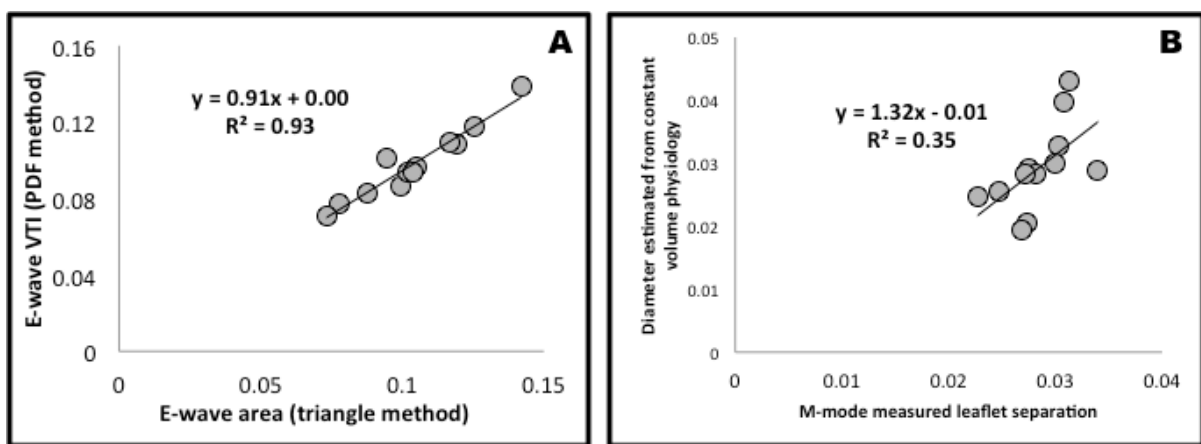
Fig 4.3: a) Comparison of the estimated effective orifice diameter (D_{est}) to the peak mitral leaflet separation (D_{M-mode}). D_{est} is calculated using the constant volume attribute and D_{M-mode} is calculated from M-mode images of LV wall motion. The regression relation shows that the two diameters have the same order of magnitude. b) Comparison of the E-wave area measured by the triangle method vs the area calculated by integrating the area under the contour. The regression relation indicates that the calculated area by the two methods is similar. See text for details.

of measured leaflet separation vs. estimated diameters for 12 subjects. We also calculated the

correlation between triangle approximated E-wave area and the PDF model derived E-wave area

and found the regression relation to be E-wave area (from integral) = 0.91*E-wave area (from triangle), $R^2 = 0.93$. Fig. 4.3b shows this relation.

4.3.3 Relationship between VFT and E/E'

In accordance with our mathematical derivation of the relation between *VFT* and *E/E'*, we

determined the correlation $VFT_{standard}$ and $VFT_{kinematic}$ vs. $(E/E')^{3/2}$ (Fig 4.4a). $VFT_{kinematic}$ correlated with *E/E'* according to $VFT_{kinematic} = 0.07 * (E/E')^{3/2} + 2.33$, $R^2 = 0.63$ The regression relation between $VFT_{standard}$ and $(E/E')^{3/2}$ is given by: $VFT_{standard} = 0.03 * (E/E')^{3/2} + 3.24$, $R^2 = 0.19$ (Fig 4.4b).
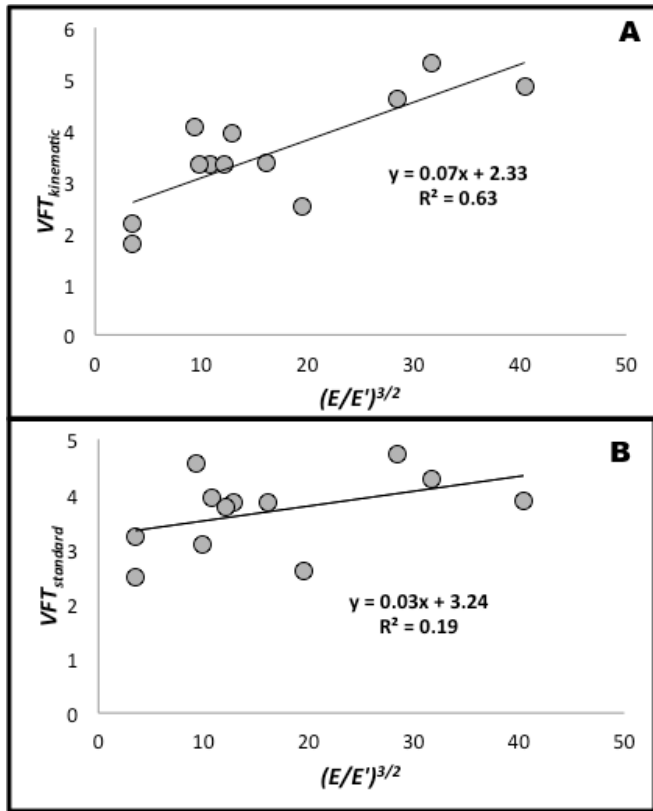
Fig 4.4: a) Correlation of $VFT_{kinematic}$ to $(E/E')^{3/2}$ for all 12 subjects. The correlation coefficient obtained for this relation was $R^2 = 0.63$. b) Correlation of $VFT_{standard}$ to $(E/E')^{3/2}$ for all 12 subjects. The correlation coefficient obtained for this relation was $R^2 = 0.19$. See text for details.

4.4 Discussion

VFT has been previously derived using a fluid mechanics based approach and shown to be an index of diastolic function and cardiac health [7]. To further elucidate and characterize the relationship between chamber physiology and VFT we derived an alternate expression for *VFT* using a kinematic modeling based approach. Since ventricular tissue relaxation and recoil generates the AV pressure gradient which drives transmitral flow, we hypothesized that a causal connection exists

between chamber kinematics and *VFT*. Accordingly, we derived a kinematic expression for *VFT* and validated it by correlating *VFT_{kinematic}* to VFT_{standard}, as computed by Gharib's methodology, in the same subjects. Furthermore, the derived mathematical expression for *VFT_{kinematic}* provided novel mechanistic insight by elucidating the relationship between *VFT* and *E/E'*- an established DF index.

4.4.1 Insight and background on vortex rings

Insight into the mathematical connection between chamber kinematics and *VFT* requires consideration of the physics of vortex rings. When a stream of fluid is injected into a large static fluid volume whose boundary is far removed, at a certain distance from the nozzle a vortex ring develops and grows [3, 5, 25, 26]. Its features and temporal evolution depend on fluid properties (usually assumed to be ideal), the geometry (flow orifice size), and the dynamics (injection velocity). For certain parameters, the stream forms a single, growing vortex; for other parameter values a series of vortices that peel off the injected fluid column can form [5]. The opportunity for optimization between the dynamic boundary of the receiving, suitably shaped, fluid chamber (LV chamber), and the entering fluid column (Doppler E-wave) with fluid mechanics determined vortex ring formation can therefore be immediately appreciated [7, 27].

Indeed vortex ring formation in the mammalian LV during the early rapid filling phase of diastole (Doppler E-wave) has been studied both theoretically [3, 5, 25, 26, 27, 28] and experimentally [4, 6, 29]. Vortex ring formation has both biologic/physiologic and mechanical consequences. The physiologic advantage is that the vortex ring 'rinses' the highly trabeculated endocardial surface preventing thrombus formation associated with stasis of blood, and facilitates mitral leaflet coaptation prior to systole. The mechanical advantages of vortex formation include redirection of flow to optimize ejection and minimizing fluid stream collision [29], thereby avoiding excessive

dissipation of fluid energy, enhancing simultaneous reciprocation of atrial and ventricular volumes during the cardiac cycle in keeping with the near constant-volume property of the four-chambered heart and facilitating efficient contraction [24].

Prior in-vitro studies have used LV simulators and prosthetic valves to quantitate vortex formation. Gharib et al [7] have calculated *VFT* using traditional approaches (*Eq. B3*) to clinical echo data and found an optimum range of *VFT* values for normal human hearts. Other groups have used Gharib's method to calculate *VFT* and found reduced *VFT* in the setting of reduced systolic function [30, 31], and reduced *VFT* in patients with Alzheimer's disease [32].

4.4.2 Connecting kinematics and vortex ring formation

In order to appreciate the causal relation between *VFT* and the physiologic DF determinants we derived *VFT* using a kinematic model of filling. The motivation behind deriving *VFT* using kinematics is to elucidate and characterize the coupling between chamber properties (stiffness, relaxation) and fluid flow. The kinematic approach characterizes filling in terms of load, stiffness and relaxation/viscosity, familiar to physiologists and cardiologists. Therefore $VFT_{kinematic}$ complements and advances our understanding of the proper way to interpret $VFT_{standard}$. Eq. 4.2 expresses $VFT_{kinematic}$ in terms of PDF parameters- k, c, x_o which have established physiologic analogs [8, 17, 33, 34].

The regression value of $VFT_{standard}$ vs. $VFT_{kinematic}$ relation ($R^2 = 0.66$) supports our prediction that $VFT_{kinematic}$ is analogous to $VFT_{standard}$. The slope of the regression relation (1.22) indicates that the two *VFTs* are of similar magnitude, further validating the functional equivalence of the two expressions.

4.4.3 Understanding the differences in computing VFT$_{kinematic}$ vs. VFT$_{standard}$

The correlation between *VFT$_{kinematic}$* and VFT$_{standard}$ indicates that although these two parameters are similar, they are not equivalent. The key to understanding the differences between them is in the approximations used in their determination. VFT$_{standard}$ applies two major approximations - 1) a constant effective mitral valve orifice area, and 2) a constant inflow velocity. *VFT$_{kinematic}$* also employs approximations, but these are mitigated by key physiological principles. *VFT$_{kinematic}$* treats the time-varying E-wave as a time-varying inflow velocity in accordance with the PDF model. In addition, *VFT$_{kinematic}$* incorporates the near 'constant-volume property' of the left heart for effective orifice area estimation, thereby providing a more physiologically realistic estimate than M-mode obtained at a single instant of filling.

Since computing *VFT* from Eq. 3.1 is not feasible, our approximations enable us to calculate *VFT* from routine clinical data. The different approximations used in *VFT$_{kinematic}$* vs. VFT$_{standard}$ are the reason why the two *VFTs* are not equivalent. In addition, there are practical limitations in acquiring data in a clinical setting. (See Limitations) Hence the very good correlation observed between the two *VFTs* is reassuring.

The differences in the definition of *VFT$_{kinematic}$* from VFT$_{standard}$ arise from the method used to calculate the E-wave area and the effective mitral orifice diameter. To understand how much each of these terms differed we compared the values of D_{est} (from the constant-volume attribute) to $D_{M\text{-}mode}$ in Fig 4.3a and the E- wave area, calculated by the two different methods in Fig. 4.3b. Fig. 4.3b indicates that E-wave area calculated by approximating it as a triangle is nearly equivalent to the area obtained by integration. Hence observed differences in VFT arise from the differences in how effective mitral orifice diameter is approximated.

The correlation between D_{est} and $D_{M\text{-}mode}$ is modest as expected ($R^2 = 0.35$; Fig 4.3a) because of the inherent limitation in measurement of leaflet separation due to transducer position and angulation relative to LV long axis direction. $VFT_{standard}$ incorporates $D_{M\text{-}mode}$ measured using M-mode echo and hence it is subject to the same limitations. The measurement of epicardial dimension (for calculating D_{est}) is subject to the same challenges as well. To mitigate the effect of this limitation we incorporate constant-volume physiology in effective flow orifice diameter determination. This effectively reduces the sensitivity of the D_{est} to measurement errors while incorporating physiology. Our method of effective flow orifice diameter calculation is further validated by the slope (1.32) in Fig 4.3a indicating that D_{est} and $D_{M\text{-}mode}$ are of similar order of magnitude.

4.4.4 New insight into physiology of filling- Relation to E/E'

The derivation of $VFT_{kinematic}$ also sheds light on the relationship between VFT and E/E'. Since the near constant-volume physiology relates effective flow orifice diameter to this ratio, $VFT_{kinematic}$ is a function of E/E'. A more detailed analysis shows that VFT is proportional to $(E/E')^{3/2}$. This dependence is explained in detail in Section 4.2.7.

The VFT to $(E/E')^{3/2}$ relation has clinical implications. E/E' is a widely used non-invasive DF index [16] since E/E' alone or in conjunction with other indexes are correlates of diastolic dysfunction [35]. E/E' has also been shown to be a marker for elevated LVEDP [18]. From the physiologic perspective, E/E' reflects the ratio of global (3-dimensional, long-axis + short-axis) relaxation\volume accommodation via the E-wave and longitudinal (1-dimensional) relaxation\volume accommodation via the E'-wave, thereby accounting for the (2 dimensional, i.e. short-axis) radial motion as a result of volume conservation. VFT, incorporating the near constant-volume attribute encompasses this feature of E/E' and hence it is sensitive to changes in

magnitude of radial accommodation of the E-wave volume. The relationship between *VFT* and *E/E'* has been observed previously [36] but the causal physiology has not been elucidated.

In accordance with prediction, $VFT_{kinematic}$ achieved a correlation of $R^2 = 0.63$ with $(E/E')^{3/2}$ (Fig. 4.4a). $VFT_{standard}$ has a lower correlation with $(E/E')^{3/2}$ ($R^2 = 0.19$) (Fig. 4.4b). This result agrees with previous observation [36] and our theoretical prediction. The poor correlation between $VFT_{standard}$ and $(E/E')^{3/2}$ is due to the approximations used by $VFT_{standard}$. Our derivation (Eq. 4.4) shows that VFT is a correlate of $(E/E')^{3/2}$. The correlation of $VFT_{kinematic}$ to $(E/E')^{3/2}$ validates this in the setting of the approximations made and shows that $VFT_{kinematic}$ is physiologically a more faithful estimate of *VFT* than $VFT_{standard}$.

We used Fig. 4.3 to identify the terms which introduce major differences between $VFT_{standard}$ and $VFT_{kinematic}$. We concluded that using mitral leaflet separation measured by M-mode echo introduces errors in estimation of effective flow orifice diameter. Hence using D_{M-mode} to approximate the effective flow orifice diameter makes $VFT_{standard}$ less sensitive to E/E'. When *VFT* is calculated more physiologically, using a kinematic approach incorporating near constant-volume physiology, the causal E/E' to $VFT_{kinematic}$ connection is restored.

4.4.5 Limitations

Due to the format in which E-waves and M-mode data are recorded clinically, computing *VFT* as defined by Eq. 3.1 requires modifications. To derive $VFT_{standard}$ Gharib et al approximated the Doppler E-wave velocity as a constant during early filling. They also assumed that the effective orifice diameter is constant during early filling.

To calculate the effective mitral orifice diameter (D_{est}) we approximated the left heart by a constant-volume cylinder. This model incorporates longitudinal motion and concomitant wall-

thinning as the only degree of freedom for incoming volume accommodation. In the in vivo setting for a normal ventricle, blood is accommodated primarily by longitudinal elongation and also by slight (epicardial) radial expansion, the "crescent effect" [37] Hence the near constant-volume approximation has slight limitations. However use of the constant-volume approximation for the left heart is legitimized by its ability to provide effective mitral orifice diameter at E'_{peak} when volume accommodation is primarily due to longitudinal elongation.

In deriving $VFT_{kinematic}$, we assumed simultaneous E- and E'-wave onset. It is possible that some E-waves are slightly delayed (by a few ms) beyond E'-wave onset. To determine whether the assumption of E- and E'-wave non-simultaneity influences the value of VFT; we defined a time-delay constant and performed numerical experiments. We then plotted the relationship between VFT and the time-delay constant and found insignificant variation in VFT. Thus the assumption that E'-wave and E-waves have simultaneous onset is warranted.

The machine imposed limitation of non-simultaneous E- and E'-wave recording was handled by selecting matched E- and E'-waves with R-R intervals within ±15ms of each other. Since all the cardiac cycles analyzed had diastasis, the minor difference in R-R intervals only affects diastasis duration rather than the E- or the E'-wave duration [38]. Hence our method is limited to E- and E'- waves with a clear diastatic interval.

In accordance with convention [5] we used Doppler M-mode in the parasternal short axis view for D_{M-mode} and epicardial dimension determination. Although M-mode echo may underestimate [39] mitral leaflet separation and epicardial dimension, using the same recording method in all subjects is a systematic effect and should apply to all VFT values equally. We also assume that the maximum mitral effective flow orifice diameter occurred at the peak of the E'-wave during the cardiac cycle.

This study aimed to understand *VFT* in the context of a range diastolic function with normal systolic function. Hence we restricted our analysis to subjects with normal EFs but a range of LVEDPs encountered clinically. However for *VFT* to achieve broader clinical use, further application in a more diverse population with a larger variation in EF and systolic function is justified.

4.5 Conclusion

Vortex formation time *(*VFT$_{standard}$) is a fluid mechanics derived index reflecting optimum vortex formation and diastolic filling efficiency. Incorporating near constant-volume (left heart) physiology and chamber kinematics we derived *VFT*$_{kinematic}$, the analogue of VFT$_{standard}$. Validation utilized simultaneous echocardiography-catheterization data from 12 patients with normal EFs and varying EDP. Excellent correlation between *VFT*$_{kinematic}$ vs. VFT$_{standard}$ (R^2 = 0.66) was observed. The derivation of *VFT*$_{kinematic}$ revealed it to be a function of *(E/E')$^{3/2}$*, whose observed correlation (R^2 = 0.63) using in-vivo human data further validated the new relationship. *VFT*$_{kinematic}$ provides physiologic and mechanistic insight into the coupling between transmitral flow and chamber properties. Further application and validation in additional, well-defined clinical subsets is warranted.

Reference:

1. Gheorghidae M, Pang PS. Acute Heart Failure Syndromes. *J. Am. Coll. Cardiol*. 53: 557-573, 2009.

2. Zile MR, Brutsaert DL. New Concepts in Diastolic Dysfunction and Diastolic Heart Failure: Part I *Circulation*. 105:1387-1393, 2002.

3. Mohseni K, Gharib M. A Model for Universal Time Scale of Vortex Ring Formation. *Phys. Fluids*. 10(10):2436-2438, 1998.

4. Kheradvar A, Milano M, Gharib M. Correlation Between Vortex Ring Formation and Mitral Annulus Dynamics During Ventricular Rapid Filling. *J. Am. Soc. Artificial Organs*. 53:8-16, 2007.

5. Gharib M, Rambod E, Shariff K. A Universal Time-Scale of Vortex Formation Time. *J. Fluid. Mech*. 360:121-140, 1998.

6. Kheradvar A, Gharib M. On Mitral Valve and its Connection to Early Diastolic Flow. *Ann Biomed Eng*. 37:1-13, 2009.

7. Gharib M, Rambod E, Kheradvar A, Sahn DJ, Dabiri JO. Optimal Vortex Formation as an Index of Cardiac Health. *Proc. Natl. Acad. Sci*. 103:6305-6308, 2006.

8. Kovács SJ, Barzilai B, Pérez JE. Evaluation of Diastolic Function with Doppler Echocardiography: the PDF formalism. *Am. J. Physiol*. 87:H178-H187, 1987.

9. Kovács SJ, Meisner JS, Yellin EL. "Modeling of diastole." In: *Cardiology Clinics*, edited by MH Crawford and S. J. Kovács. Philadelphia, PA: Saunders, 2000, p. 459-487.

10. Rich MW, Stitziel NO, Kovács SJ. Prognostic value of diastolic filling parameters derived using novel image processing techniques in patients >= 70 years of age with congestive heart failure. *Am. J. Cardiol*. 84:82-86, 1999.

11. Riordian MM, Kovács SJ. Elucidation of Spatially Distinct Compensatory Mechanisms in Diastole: Radial Compensation for Impaired Longitudinal Filling in Left Ventricular Hypertrophy. *J. Appl. Physiol.* 104:513-520, 2008.

12. Meyer TE, Kovács SJ, Ehsani AA, Klein A, Holloszy JO, Fontana L. Long-term caloric restriction ameliorates the decline in diastolic function in humans. *J. Am. Coll. Cardiol.* 47: 398-402, 2006.

13. Kovács SJ, Rosado J, McGuire ALM, Hall AF. Can transmitral Doppler E-waves differentiate hypertensive hearts from normal? *Hypertension.* 30: 788-795, 1997.

14. Shmuylovich L, Kovács SJ. Load independent index of diastolic filling: model-based derivation with in vivo validation in control and diastolic dysfunction subjects. *J. Appl. Physiol.* 101:92-101, 2006.

15. Shmuylovich L, Chung CS, Kovács SJ, Yellin EL, Nikolic SD. Point-Counterpoint. Left ventricular volume during diastasis IS/IS NOT the physiologic in-vivo equilibrium volume and IS/IS NOT related to diastolic suction. *J. Appl. Physiol.* 2009; 109 (2): 606-608.

16. Lisauskas JB, Singh J, Courtois MR, Kovács SJ. The relation of the peak Doppler E-wave velocity to peak mitral annulus velocity ratio in diastolic function. *Ultrasound Med. Biol.* 27:499-507, 2001.

17. Kovács SJ, Sester R, Hall AF. Left Ventricular Chamber Stiffness from Model-based Image Processing of Transmitral Doppler E-waves. *Coron. Artery Dis.* 8:179-187, 1997.

18. Nagueh SF, Appleton CP, Gillebert TC, Marino PN, Oh JK, Smiseth OA, Waggoner AD, Flachskampf FA, Pellikka PA, Evangelista A. Recommendations for the Evaluation of

Left Ventricular Diastolic Function by Echocardiography. *J. Am. Soc. Echocardiogr*. 22(2):107-133, 2009.

19. Feigenbaum H. *Echocardiography* (5th Ed). Baltimore, MD: Lea and Febiger, 1994 p. 677.

20. Foppa M, Duncan BB, Rohde LEP. Echocardiography-based left ventricular mass estimation. How should we define hypertrophy? *Cardiovasc. Ultrasound*. 3:17, 2005.

21. Hall AF, Aronovitz JA, Nudelman SP, Kovács SJ. Automated Method of Characterization of Diastolic Transmitral Doppler Velocity Contours: Late Atrial Filling. *Ultrasound Med Biol*. 20:859-869, 1994.

22. Hall AF, Kovács SJ. Automated Method for characterization of Diastolic Transmitral Doppler Velocity Contours: Early rapid filling. *Ultrasound Med Biol*. 20: 107-116, 1994.

23. Riordian MM, Kovács SJ. Quantitation of Mitral Annular Oscillations and Longitudinal 'Ringing' of the Left Ventricle: A New Window into Longitudinal Diastolic Function. *J. Appl. Physiol.* 100:112-119, 2006.

24. Bowman AW, Kovács SJ. Assessment and Consequences of the Constant-Volume Attribute of the Four-Chambered Heart. *Am.J.Physiol*. 285;H2027-H2033, 2003.

25. Krueger P, Gharib M. The significance of Vortex Ring Formation to the Impulse and Thrust of a Starting Jet. *Phys. Fluids*. 15(5):1271-1281, 2003.

26. Shusser M, Gharib M. Energy and Velocity of a Forming Vortex Ring. *Phys Fluids*. 12(3):618-621, 1999.

27. Pedrizzetti G, Domenichini F. Nature Optimizes the Swirling Flow in the Human Left Ventricle. *Phys Rev Lett*. 95:108101-1-108101-4, 2005.

28. Dabiri JO. Optimal Vortex Formation as a Unifying Principle in Biological Propulsion. *Annu. Rev. Fluid Mech.* 41:17-33, 2009.

29. Hong G, Pedrizzetti G, Tonti G, Li P, Wei Z, Kim JK, Baweja A, Liu S. Chung N, Houle H, Narula J, Vannan MA. Characterization and Quantification of Vortex Flow in the Human Left Ventricle by Contrast Echocardiography Using Vector Particle Image Velocimetry. *J. Am. Coll. Cardiol.: Cardiovascular Imaging.* 1(6):705-717, 2008.

30. Jiamsripong P, Calleja AM, Alharthi MS, Cho EJ, McMahon EM, Heys JJ, Milano M, Sengupta PP, Khaderia BK, Belohlavek M. Increase in late diastolic filling force is associated with impaired transmitral flow efficiency in acute moderate elevation left ventricular afterload. *J. Ultrasound Med. 28*(2), 175-182, 2009.

31. Jiamsripong P, Calleja AM, Alharthi MS, Dzsinich M, McMahon EM, Heys JJ, Milano M, Sengupta PP, Khaderia BK, Belohlavek M. Impact of acute moderate elevation in left ventricular afterload on diastolic transmitral flow efficiency: Analysis by vortex formation time. *J. Am. Soc. Echocardiogr. 22*(4), 427-431, 2009.

32. Roher AE, Belohlavek M, Maarouf CL, Kokjohn TA, Garami Z, Beach TG, Sabbagh MN. Echocardiography vortex formation time reveal cardiac diastolic transmitral flow dysfunction in alzheimer's disease patients. *Alzheimers Dement.* 5(4, Supplement 1), P293-P293, 2009.

33. Bauman L, Chung CS, Karamanoglu M, Kovács SJ. The Peak Atrioventricular Pressure Gradient to Transmitral Flow Relation: Kinematic Model Prediction with in-vivo Validation. *J.Am.Soc.Echocardiogr* 17(8):839-844, 2004.

34. Lisauskas JB, Singh J, Bowman AW, Kovács SJ. Chamber Properties from Transmitral Flow: Prediction and Validation of Average and Passive Left Ventricular Stiffness. *J. Appl. Physiol*. 91:154-162, 2001.

35. Liang HY, Cauduro SA, Pellikka PA, Bailey KR, Grossardt BR, Yang EH, Rihal C, Seward JB, Miller FA, Abraham TP. Comparison of Usefulness of Echocardiographic Doppler Variables to Left Ventricular End-Diastolic Pressure in Predicting Future Heart Failure Events. *Am. J. Cardiol*. 97(6):866-871, 2006.

36. Lee LC, Tan YL, Tan HC, Omar AR, Chai P, Yeo TC, Low AFH, Yip JWL, Chia BL, Poh KK. Abstract 3289: Vortex Formation Index in Heart Failure: Novel Non-invasive Assessment of Fluid Dynamics using Transthoracic Echocardiography. *Circulation*. 116:II_741, 2007.

37. Waters EA, Bowman AW, Kovács SJ. MRI-determined left ventricular "crescent effect": a consequence of the slight deviation of contents of the pericardial sack from the constant-volume state. *Am J Physiol Heart Circ Physiol*. 288(2):H848-53, 2005.

38. Chung CS, Kovács SJ. Consequences of Increasing Heart Rate on Deceleration Time, Velocity Time Integral and E/A. *Am. J. Cardiol*. 47:398-402, 2006.

39. Anwar AM, Soliman OII, Cate FJT, Nemes A, McGhie JS, Krenning BJ, van Geuns RJ, Galema TW, Geleijnse ML. True mitral annulus diameter is underestimated by two-dimensional echocardiography as evidenced by real-time three-dimensional echocardiography and magnetic resonance imaging. *Int. J Cardiovasc. Imaging* 23: 541-547, 2007.

40. Boskovski MT, Shmuylovich L, Kovács SJ. Transmitral Flow Velocity- Contour Variation After Premature Ventricular Contractions: A Novel Test of the Load-

Independent Index of Diastolic Filling. *Ultrasound Med. and Biol*. 34(12):1901-1908, 2008.

41. Riordian MM, Chung CS, Kovács SJ. Diabetes and Diastolic function: Stiffness and Relaxation from Transmitral Flow. *Ultrasound Med Biol*. 31: 1589-1596, 2005.

Chapter 5: The Vortex Formation Time to Diastolic Function Relation:

Assessment of pseudonormalized vs. normal filling

Abstract

In early diastole, the suction pump feature of the left ventricle opens the mitral valve and aspirates atrial blood. The ventricle fills via a blunt profiled cylindrical jet of blood that forms an asymmetric toroidal vortex ring inside the ventricle whose growth has been quantified by the (dimensionless) vortex formation time, $VFT_{standard}$ = {transmitral velocity time integral}/{mitral orifice diameter}. It can differentiate between hearts having distinguishable early transmitral (Doppler E-wave) filling patterns. An alternative validated expression, $VFT_{kinematic}$ re-expresses $VFT_{standard}$ by incorporating left heart, near 'constant-volume pump' physiology thereby revealing $VFT_{kinematic}$'s explicit dependence on maximum rate of longitudinal chamber expansion (E'). In this work, we show that $VFT_{kinematic}$ can differentiate between hearts having indistinguishable E-wave patterns, such as pseudonormal (PN; 0.75< E/A< 1.5 and E/E'>8) vs. normal. Thirteen age-matched normal and 12 PN datasets (738 total cardiac cycles), all having normal LVEF, were selected from our Cardiovascular Biophysics Laboratory database. Doppler E-, lateral annular E'-waves and M-mode data (mitral leaflet separation, chamber dimension) was used to compute $VFT_{standard}$ and $VFT_{kinematic}$. $VFT_{standard}$ did not differentiate between groups [normal (3.58±1.06) vs. PN (4.18±0.79), p = 0.13]. In comparison $VFT_{kinematic}$ for normal (3.15±1.28) vs. PN (4.75±1.35) yielded p=0.006. Hence, the applicability of $VFT_{kinematic}$ for diastolic function quantitation has been broadened to include analysis of pseudonormal filling patterns in age matched groups.

5.1 Introduction

5.1.1 Importance of quantifying diastolic function

The ability to quantify diastolic function (DF) quantitatively is crucial in order to properly diagnose heart failure with preserved ejection fraction (HFpEF) or diastolic heart failure (DHF) [1, 2] and to assess the success of therapy. The preferred noninvasive method for DF assessment is Doppler echocardiography and various Doppler indexes are used to quantify DF [3, 4]. Most of these indexes are empiric (based on Doppler echocardiographic waveform features rather than on mechanisms) or correlation-based, irrespective of causal relations. Hence these indexes cannot provide mechanistic insight into the physiology of DF.

One important step in diagnosing DHF is classifying the stages of diastolic dysfunction. This is typically done by measuring echocardiographic transmitral flow (Doppler E- and A-waves). The different features of the E- and A- waves such as E_{peak}, E_{dur}, deceleration time (DT), E/A ratio are used to classify DF into four stages- normal, delayed relaxation, pseudonormal and constrictive restrictive pattern [4]. While distinguishing between normal, delayed relaxation and constrictive restrictive filling patterns using Doppler E- and A-waves is relatively straightforward, categorizing pseudonormal filling presents a challenge [5]. As the name implies, pseudonormal filling is similar to normal filling and hence indistinguishable. Thus other imaging techniques and indexes are needed to identify pseudonormal filling.

5.1.2 Kinematic model-based approach for DF quantification

A mechanism based approach for DF quantitation is available and is provided by the parametrized diastolic filling (PDF) formalism [6] as discussed previously in Chapter 2. Because the heart is a mechanical oscillator, the formalism treats mechanical suction initiated early rapid

(Doppler E-wave) filling in analogy to the recoil from rest, of a previously displaced, damped simple harmonic oscillator. Model predicted fit to the clinical E-wave is excellent and the fitting process specifies 3 parameters: k, the stiffness constant, c, the viscoelastic damping/relaxation constant and x_o, the volumetric preload. The PDF formalism has been validated in a broad range of normal and pathophysiologic settings (in humans and animals). The PDF parameters and indexes derived from them have been rigorously shown to have direct clinical relevance [7-11]. The PDF formalism has been automated [12, 13] and solves the 'inverse problem of diastole' [14] by providing a unique set of PDF parameters for each analyzed E-wave.

5.1.3 Fluid mechanics based approach to DF quantification

An alternate approach for DF characterization utilizes fluid mechanics. The left ventricle (LV) fills by aspirating atrial blood which forms an asymmetric toroidal (doughnut-shaped) vortex as it curls around the mitral leaflet tips [15]. The vortex ring expands as the ventricle fills and the outer boundary of the vortex rinses the highly trabeculated endocardium preventing thrombus formation while concomitantly facilitating mitral leaflet coaptation during diastasis [16]. The pattern of flow and vortex formation is affected by cardiac dysfunction and has been previously characterized via echocardiography using vortex formation time (*VFT*) (Chapter 3 and 4).

Gharib et al [17] used Doppler E-wave data to calculate $VFT_{standard}$ in subjects with normal LVEF and normal E-wave patterns and subjects with dilated cardiomyopathy and abnormal E-wave patterns. They found that subjects with normal E-wave patterns had a normal range of values (3.5-5.5) whereas subjects with dilated cardiomyopathy had lower $VFT_{standard}$.

5.1.4 Applying a kinematic model-based fluid mechanics approach

We have previously derived and validated a complementary method of calculating VFT ($VFT_{kinematic}$) [18, 19] involving the PDF formalism [6] (See Chapter 3 for details). Our derivation

made use of the near 'constant-volume' physiologic attribute of the left heart [20] that provides the algebraic relationship between effective mitral orifice area (diameter) and longitudinal annular tissue motion (E'). Our results demonstrated very good correlation between $VFT_{kinematic}$ and $(E/E')^{3/2}$, an established echocardiographic index of DF [19, 21].

In this work we test the hypothesis that $VFT_{kinematic}$ can distinguish between normal and diastolic dysfunction (pseudonormal filling) states where both groups are age-matched and have indistinguishable, normal E-wave patterns. To test our hypothesis we analyzed 738 beats and computed $VFT_{kinematic}$ and $VFT_{standard}$ in 25 subjects and performed an intergroup comparison.

5.2 Methods

5.2.1 Subject selection criteria

Echocardiographic data from 25 subjects were selected from the Cardiovascular Biophysics Laboratory database. Prior to data acquisition, subjects provided signed, informed consent for participation in accordance with the Institutional Review Board (Human Research Protection Office) at Washington University School of Medicine. The inclusion criteria were: normal sinus rhythm, absence of valvular abnormalities and the absence of wall motion abnormalities or bundle branch block on the ECG, normal LVEF, normal valvular function and clearly identifiable E- and A-waves and E'-waves. In addition all subjects also had Doppler M-mode images of the mitral leaflet motion recorded in the parasternal view.

We dichotomized subjects into normal and pseudonormal (PN) groups, according to American Society of Echocardiography [4] criteria. In both groups 0.75< E/A< 1.5, in the normal group, lateral E'$_{peak}$ velocity was >10 cm/s and E/E'< 8 and in the PN group, lateral E'$_{peak}$ velocity was reduced (<10 cm/s) resulting in E/E'> 8. All subjects (both groups) had normal LV

ejection fraction (>50%) and either normal coronary anatomy or insignificant (<50%) coronary artery narrowing. Because diastolic filling patterns [21] and $VFT_{standard}$ depend on age [17] we specifically age-matched the groups so that age could not be a distinguishing metric.

5.2.2 Doppler echocardiography
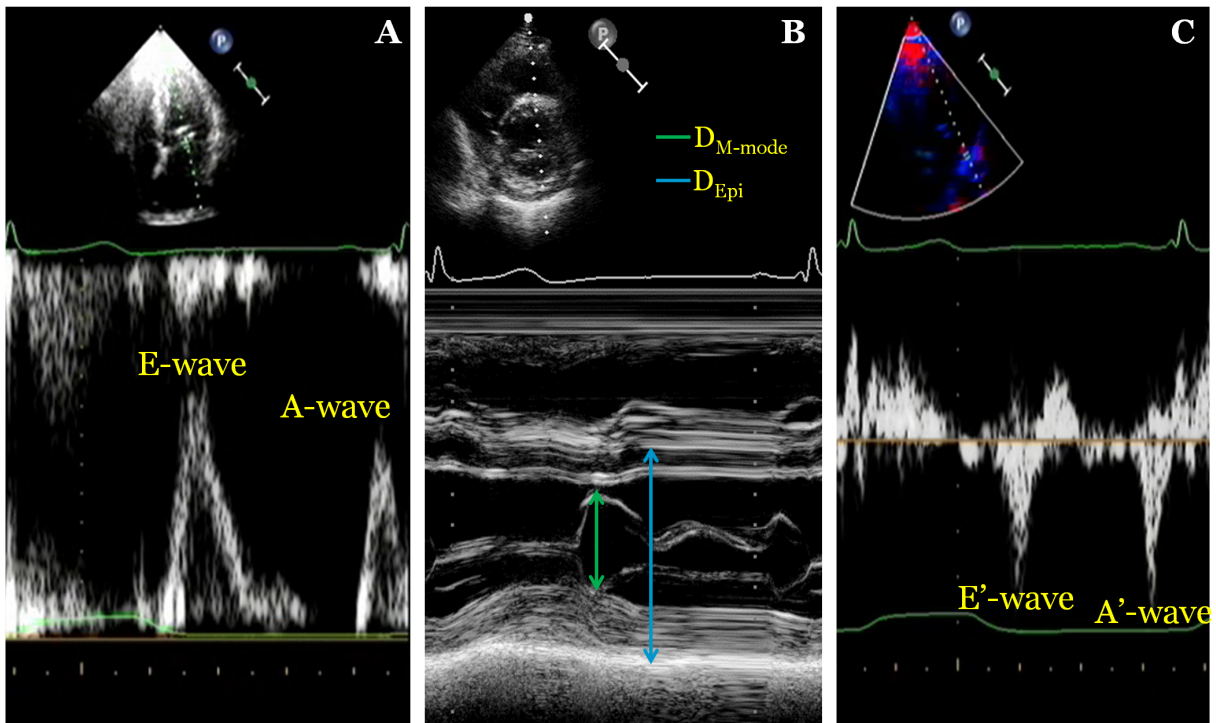
Fig 5.1: (A) Typical Doppler transmitral flow image showing one cardiac cycle with Doppler E- and A-wave marked. (B) Typical parasternal M-mode image with peak mitral leaflet separation (D_{M-mode}) in green and epicardial diameter (D_{epi}) in blue. (C) Typical tissue Doppler, lateral mitral annulus motion image with Doppler E'- and A'-wave marked. See text for details.

Our data acquisition method has been previously detailed (Chapter 2) and [11, 19]. Briefly, echocardiography was performed in accordance with published American Society of Echocardiography (ASE) criteria [4]. Immediately before catheterization, patients were imaged in a supine position using a Philips iE33 system (Best, Netherlands). Two-dimensional images in apical two and four chamber views were obtained with the sample volume gated at 1.5 to 2.5mm

directed between the tips of the mitral valve leaflets and orthogonal to the mitral valve plane (to minimize misalignment effects). The wall filter was set at 125 Hz or 250 Hz, the baseline adjusted to take advantage of the full height of the display and the velocity scale adjusted to exploit the dynamic range of the output without aliasing. The four-chamber view was used to record Doppler E-waves and tissue Doppler E'-waves (Fig 5.1A and 5.1C). For E'-wave recording the lateral aspect of mitral annulus was selected because recent studies have shown that in patients with normal ejection fraction, lateral E' has the best correlation with LV filling pressures and invasive indices of LV stiffness [23]. Doppler M-mode images recorded in the parasternal short axis view (as shown in Fig. 5.1B) were used to determine mitral leaflet separation for effective orifice diameter computation following the ESE/ASE guidelines [24].

5.2.3 Doppler echocardiographic data analysis

Using methods described previously (Chapter 2 and 4), transmitral Doppler waveforms and the tissue Doppler E'-waves were analyzed using two methods: 1) the conventional method and 2) the PDF formalism, using best E-wave contour fit criteria in computing the PDF (x_o, c, k) parameters. In the conventional method, the E-wave is approximated as a triangle such that its height is peak velocity (E_{peak}) and its base is the duration (E_{dur}). The same method is used to analyze Doppler E'-wave and determine E'_{peak} and E'_{dur}.

The second method of E-wave analysis employs the PDF formalism [6] which solves the 'inverse-problem of diastole' [14] (See Chapter 2). The method of PDF parameter determination has been automated and detailed previously [10, 13] and has an inter-observer variability of 8% [25].

The peak mitral leaflet separation was calculated from M-mode images in accordance with [17]. The epicardial dimension D_{epi} was also measured from the same M-mode image using

the method described by Foppa et al [26]. Fig 5.1B shows a typical M-mode image with the diameters marked.

5.2.4 Calculation of VFT

The method of calculating $VFT_{kinematic}$ and $VFT_{standard}$ has been previously detailed [19] (See Chapter 4). Briefly, $VFT_{standard}$ is defined as the E-wave area (triangle method) divided by the maximum mitral leaflet separation.

$$VFT_{s\tan dard} = \frac{E_{peak} \times E_{dur}}{2 \times D_{M-\bmod e}}$$

Eq. 5.1

Using Eq. 5.1, $VFT_{standard}$ is calculated for each E-wave using the needed parameters determined from the conventional method described in the previous section. The diameter is measured from parasternal M-mode image as shown in Fig. 5.1B. We have previously shown [19] that the E-wave area calculated via the triangle method is equivalent to E-wave area calculated by integrating the PDF fit curvilinear contour of the E-wave.

$VFT_{kinematic}$ also uses the same E-wave area divided by the orifice diameter expression. However E-wave area is calculated using the PDF formalism derived curvilinear fit and the flow orifice diameter is derived by incorporating the near constant-volume attribute of the left heart [19, 20]. The previously derived and validated expression for $VFT_{kinematic}$ is:

$$VFT_{kinematic} = \frac{x_o(1 + \exp(-c\pi/2\omega))}{D_{epi}\sqrt{E'/E}}$$

Eq. 5.2

where D_{epi} is a constant, the epicardial diameter measured from M-mode images (blue line in Fig. 5.1B), c, x_o are PDF parameters and ω is the angular frequency of a full oscillation, the initial half of which corresponds to the E-wave. These are obtained by analyzing the Doppler E-

wave (Fig. 5.1A) using the PDF formalism. In the denominator, E'_{peak} and E_{peak} are obtained as in the conventional analysis.

5.2.5 Numerical and statistical analysis

Images were recorded in DICOM format and converted into bitmap images using a custom MATLAB program (MATLAB 6.0 MathWorks, Natick, MA). Another MATLAB script was written to compute the conventional triangle fit to Doppler E- and E'-waves. The PDF parameters were computed using an error-minimizing algorithm (Levenberg-Marquardt algorithm) as detailed in previous work [19]. *VFT$_{kinematic}$* and *VFT$_{standard}$* values were computed for each beat using a custom MATLAB program. *VFT$_{standard}$* was calculated for each E-wave using Eq. 1 and *VFT$_{kinematic}$* was calculated by matching E- and E'-waves with close R-R intervals (<10 ms difference). For each subject the values of *VFT* were averaged for all the beats. Student's t-test (two-tailed) was used to determine the significance of difference between the two groups. $p < 0.05$ was considered statistically significant. Regression analysis was performed to validate the relationship between both the VFTs and $(E/E')^{3/2}$. The average values were correlated and Pearson's product moment correlation coefficient (R^2) for each linear regression was determined.

5.3 Results

5.3.1 Subject demographics

A total of 738 beats from 25 subjects were analyzed (average 30 beats/ subject). Table 5.1 provides group demographics involving 12 men and 13 women. Nine men and 4 women were in the normal group and 3 men and 9 women were in the PN group. The groups were age matched (normal = 59 years, range: 49-73 years and PN = 61 years, range: 47-78 years, p=0.59). Body

surface area and weight of the two groups were not significantly different. The LVEDP of 14 mm Hg for normal and 16 mm Hg for PN (p=0.12) did not differ between groups. The EF of all subjects was normal. Although normal, the EF of the PN group was higher (74%) than the EF of the normal group (67%). The mean resting HR was slightly higher in the PN group (71 bpm) than normal (61 bpm).

Parameter	Normal (n=13)	PN (n=12)	p-value
Age (years)	59 (9)	61 (12)	NS 0.59
Gender	9M, 4F	3M, 9F	
Weight (lbs)	177 (28)	189 (54)	NS 0.49
Height (cm)	173 (8)	160 (14)	0.014
BSA (m^2)	1.95 (0.2)	1.96 (0.3)	NS 0.96
EDP (mm Hg)	14 (3)	16 (4)	NS 0.12
Ejection Fraction (%)	67 (9)	74 (7)	0.03
Mean HR (bpm)	61 (8)	71 (13)	0.04
Beats Analyzed	26 (18)	33 (21)	NS 0.41

Table 5.1: Subject demographics showing data for the 2 groups and the p-value (Column 4). p<0.05 is considered statistically significant. The standard deviation values are in ( ).

5.3.2 Echocardiographic parameters

Table 5.2 gives the group average values of echocardiographic parameters and PDF parameters. There was no statistical difference between Doppler E-wave parameters (conventional and PDF) between the two groups. The E_{peak} was 70 cm/s for normal and was 72 cm/s for PN. The E_{dur}, DT and the velocity time integral (VTI) were not different between the groups. The A_{peak} velocity was higher in PN group (82 cm/s) than normal (55 cm/s). Although E/A was statistically

different between the two groups, the value for both the groups was in the normal range (0.75-1.5) for the age range [4]. In accordance with convention for pseudonormal patterns E'_{peak} velocity was significantly lower in the PN group (normal = 14 cm/s vs. PN = 7 cm/s, p<0.001), however E'_{dur} was not different. In accordance with pseudonormal pattern criteria E/E' was significantly higher than control (normal = 5.3 vs. PN = 10.7, p<0.001).

Parameters	Normal (n=13)	PN (n=12)	p-values
E_{peak} (cm/s)	70 (16)	72 (13)	NS 0.76
E_{dur} (ms)	294 (26)	299 (31)	NS 0.66
DT (ms)	200 (28)	203 (32)	NS 0.81
A_{peak} (cm/s)	55 (11)	82 (16)	<0.001
E/A	1.3 (0.3)	0.9 (0.2)	<0.001
E'_{peak} (cm/s)	14 (5)	7 (1)	<0.001
E/E'	5.3 (1.4)	10.4 (2.0)	<0.001
VTI (cm)	10 (3)	11 (2)	NS 0.67
PDF parameters			
k	263 (53)	254 (53)	NS 0.68
c	23 (6)	25 (7)	NS 0.43
x_o	9.2 (2.1)	10.3 (2.3)	NS 0.21

Table 5.2: E- and E'-wave parameters. The mean values for each group are listed along with p-value. p<0.05 denotes statistical significance. Parentheses denote standard deviations. VTI = velocity-time integral.

5.3.3 VFT values

The mean $VFT_{kinematic}$ for the normal group was 3.15 and for the PN group was 4.75. $VFT_{standard}$ for the normal group was 3.59 and for PN was 4.18. The differences in $VFT_{kinematic}$ were
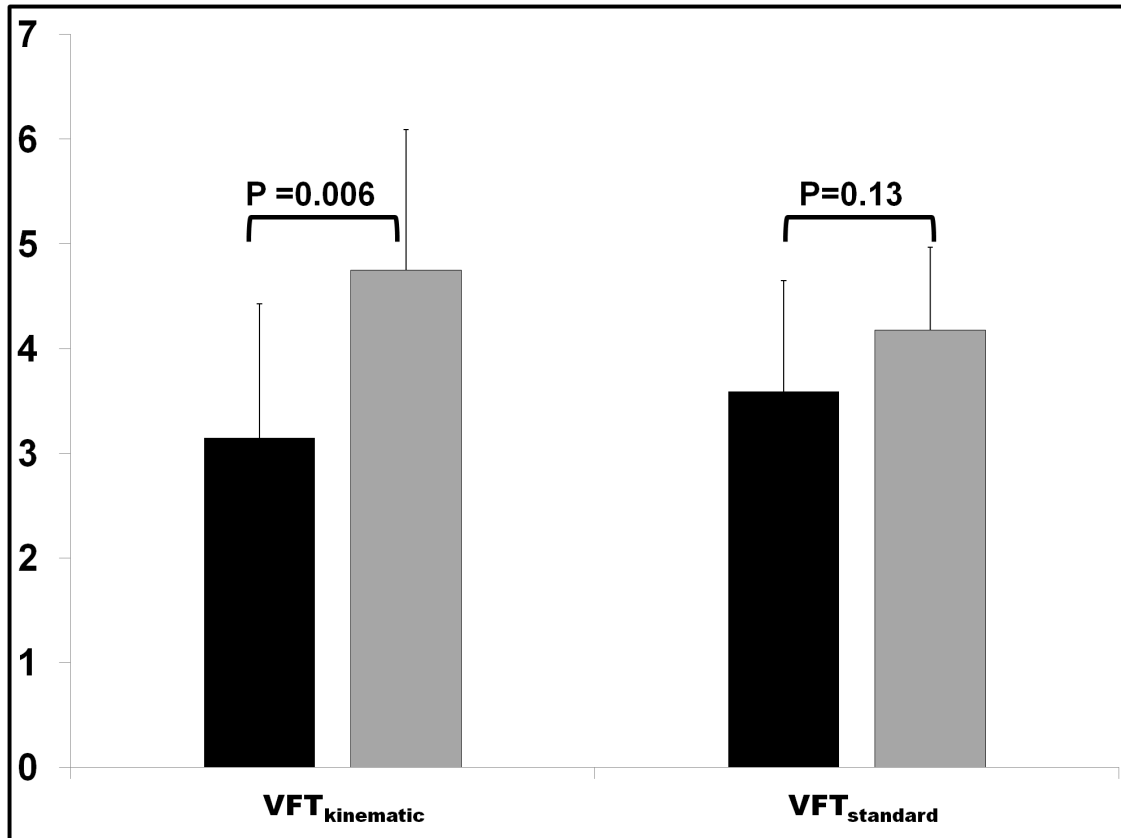
Fig 5.2: Comparing $VFT_{kinematic}$ and $VFT_{standard}$ in the normal and PN groups. The bars on the left compare the value of $VFT_{kinematic}$ in normal (dark grey) and PN (light grey) subjects. The bars on the right show the same comparison for $VFT_{standard}$ values. The error bars represent the standard deviation for the four values. The p-values of the intergroup comparison for each VFT value is given. See text for details.

statistically significant (p = 0.006) while the differences in $VFT_{standard}$ were not (p= 0.13). This is

shown in Fig 5.2. Table 5.3 lists the value of $VFT_{kinematic}$ and $VFT_{standard}$ for all subjects.

In addition similar to previous studies (Chapter 3 and 4) we compared $VFT_{standard}$ and

$VFT_{kinematic}$ to $E/E'^{3/2}$. Similar to previous results we found $VFT_{kinematic}$ had a good correlation

with $E/E'^{3/2}$ ($R^2 = 0.55$) while $VFT_{standard}$ did not ($R^2 = 0.21$). Moreover, the value of $VFT_{kinematic}$

= 4 distinguished between normal and pseudonormal subjects while there was no such threshold

number for $VFT_{standard}$ (Fig 5.3).

5.4 Discussion
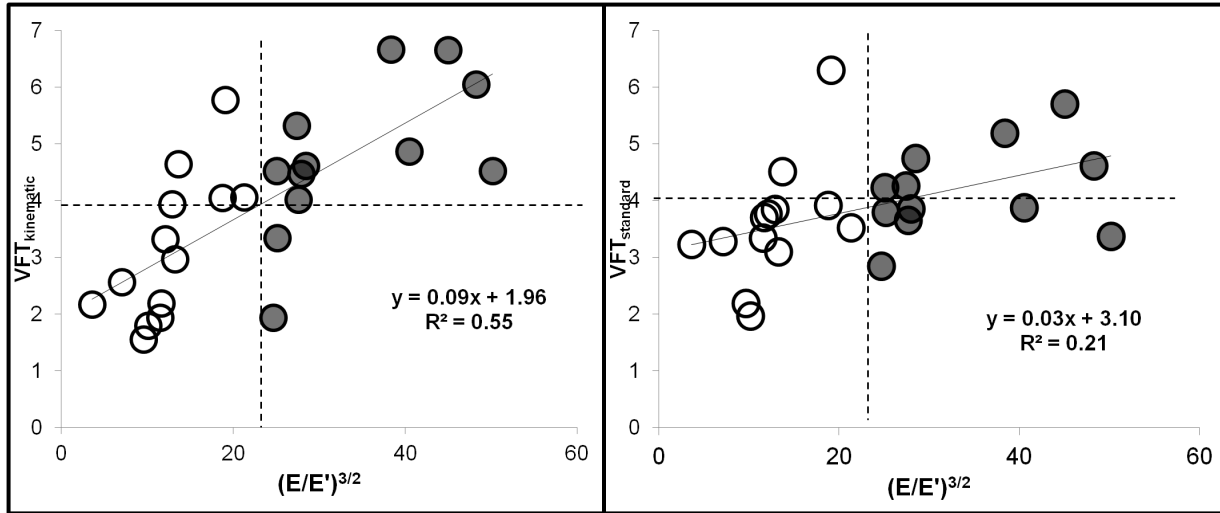
Fig 5.3: Comparing to $VFT_{kinematic}$ and $VFT_{standard}$ to $E/E'^{3/2}$. Open circles represent subjects in the normal group and closed subjects represent subjects in the PN group. (A) Correlation between $VFT_{kinematic}$ and $E/E'^{3/2}$. The 2 ratios are well correlated ($R^2 = 0.55$) and 9 of 13 subjects in the normal group have $VFT_{kinematic}$ <4. 11 of 13 subjects in PN group have $VFT_{kinematic}$ >4. (B) Correlation between $VFT_{standard}$ and $E/E'^{3/2}$. The 2 ratios are not well correlated and no clear cutoff value for $VFT_{standard}$ exists. 10 of 12 normal subjects had $VFT_{standard}$ <4 and 6 of 12 PN subjects had $VFT_{standard}$ >4. See text for details.

Vortex ring formation in the LV manifests nature's solution to the 'atrium to ventricle mass transfer problem', while maintaining efficient filling by helping to preserve the momentum of blood flow and by optimally aligning pathlines toward the outflow tract [27-31]. The fluid mechanics of vortex formation has been extensively studied and adapted to quantify LV filling dynamics [32]. Studying the physiology of filling through *VFT* provides a novel way to assess DF. We previously derived and validated an alternate expression for *VFT* which includes explicit *E/E'* dependence [19]. In this study we build on that foundation by extending the physiologic realm of *VFT* applicability by testing the ability of the alternate *VFT* expression to differentiate between age-matched controls and subjects with pseudonormal filling (characterized by essentially indistinguishable E-wave patterns). Our goal in this study is to demonstrate the advantage of using a physiology- based expression of VFT to quantify diastolic filling, rather than enhancing the understanding of LV vortex dynamics.

Subject No.	VFT$_{kinematic}$	VFT$_{standard}$	Epicardial diameter (cm)	Maximum Leaflet Separation (cm)	E$_{peak}$ (m/s)	E'$_{peak}$ (m/s)	E/E'
1	2.6	3.3	7.0	2.9	0.57	0.15	3.7
2	1.5	2.2	10	3.6	0.50	0.11	4.5
3	1.8	2.0	7.8	3.4	0.52	0.11	4.7
4	1.9	3.3	7.9	2.6	0.53	0.10	5.1
5	2.2	3.7	7.8	2.4	0.65	0.13	5.1
6	3.0	3.1	6.5	2.8	0.66	0.12	5.6
7	4.6	4.5	6.1	2.8	0.90	0.16	5.7
8	4.1	3.9	7.3	3.6	0.86	0.12	7.1
9	5.8	6.3	6.4	2.5	1.02	0.14	7.1
10	3.3	3.8	6.5	2.7	0.70	0.13	5.3
11	3.9	3.8	6.1	2.5	0.71	0.14	5.5
12	2.2	3.2	6.1	3.1	0.67	0.29	2.3
13	4.1	3.5	7.6	3.3	0.84	0.11	7.7
14	3.3	3.8	8.7	2.5	0.69	0.08	8.6
15	4.5	4.2	6.4	2.3	0.62	0.07	8.6
16	1.9	2.8	11	3.0	0.55	0.07	8.5
17	4.5	3.9	5.9	2.4	0.74	0.08	9.2
18	6.7	5.2	6.4	2.5	0.76	0.07	11.4
19	6.7	5.7	6.8	2.4	0.92	0.07	12.7
20	6.0	4.6	6.9	2.5	0.87	0.07	13.3
21	4.5	3.4	6.3	2.5	0.61	0.05	13.6
22	4.9	3.9	6.6	2.7	0.68	0.06	11.8
23	5.3	4.3	6.5	2.7	0.81	0.09	9.1
24	4.6	4.7	9.2	3.0	0.89	0.09	9.3
25	4.0	3.7	6.9	2.5	0.52	0.06	9.1

Table 5.3: VFT$_{kinematic}$ and VFT$_{standard}$ for all 25 subjects with associated component values. Subjects 1-13 are the normal group. Subjects 14-25 are the PN group.

5.4.1 Previous studies

To facilitate clinical application Gharib et al [17] proposed a simplified definition for *VFT* described above (Eq. 5.1). Using this expression they showed that *VFT$_{standard}$* had an optimal

range of values. Other studies [22, 33] have also shown that $VFT_{standard}$ can differentiate between normal E-wave patterns and selected pathologic E-wave patterns.

$VFT_{standard}$ uses only Doppler E-wave features and mitral orifice diameter at a single time-point during filling. However there is a causal relationship between chamber (motion) kinematics and fluid (motion), hence VFT can be shown to depend on the kinematic attributes of the LV [18, 19]. Vortex formation is affected by how the LV accommodates volume, which includes longitudinal (characterized by the tissue Doppler E'-wave) and radial filling volume components. By incorporating near constant-volume physiology, $VFT_{kinematic}$ explicitly takes into account longitudinal motion at the level of the annulus. As a consequence we previously [19] (See Chapter 3) demonstrated that in an idealized (cylindrical) LV aspirating essentially constant E-wave volumes (in reality <10% variation among subjects), VFT is proportional to $(E/E')^{3/2}$. We achieved a significant correlation of $VFT_{kinematic}$ vs. $(E/E')^{3/2}$ while $VFT_{standard}$ failed to achieve a significant correlation vs. $(E/E')^{3/2}$.

Recently Kheradvar et al [33] calculated $VFT_{standard}$ in four groups of subjects grouped according to E-wave patterns: normal, impaired relaxation, pseudonormal relaxation and restrictive filling. They showed that $VFT_{standard}$ was significantly different among the four groups, demonstrating the ability of $VFT_{standard}$ to correlate with altered transmitral filling patterns associated with increasing dysfunction. However, the results were confounded by age, since the age of the normal subject group was less than half of the ages of the other three groups (Normals = 28 years vs. DD = 63 years). Previous work by Gharib et al [Ref 17, Fig. 3] has shown that $VFT_{standard}$ decreases substantially with age. In light of this dependence of $VFT_{standard}$ on age, the reported differences in $VFT_{standard}$ in [33] are confounded by age.

5.4.2 Identifying pseudonormal filling

In moderate DD, characterized by pseudonormal filling, the transmitral E- and A-wave shapes
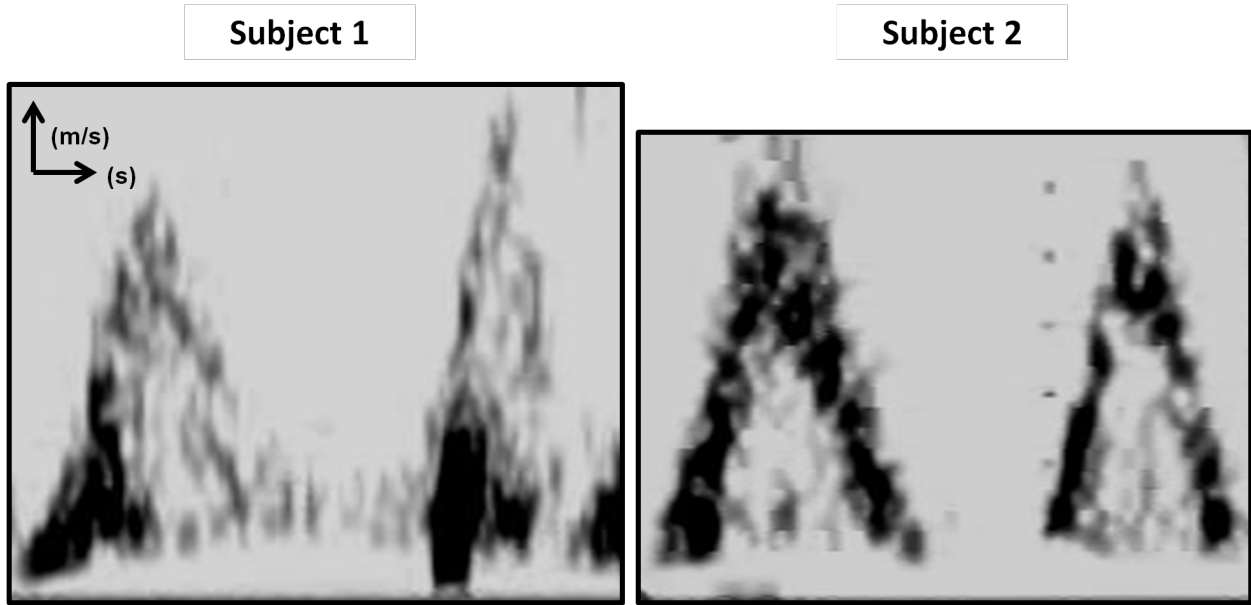
Fig 5.4: Comparing the ability of $VFT_{kinematic}$ and $VFT_{standard}$ to differentiate between 2 similar Doppler E-waves. The E-wave image on the left (marked Subject 1) is from Subject 5 (Table 3; normal group). The image on the right (marked Subject 2) is from Subject 17 (PN group). $VFT_{standard}$ can't differentiate between these 2 waves while $VFT_{kinematic}$ can differentiate between them. See text and Table 5.4 for details.

have the same characteristics as E- and A-waves in normal subjects. An example is shown in Fig.

Parameter	Subject 1	Subject 2
E_{peak} (cm/s)	60	60
E_{dur} (ms)	217	217
HR (bpm)	68	61
E'_{peak} (cm/s)	12	6.6
$VFT_{standard}$ (dimensionless)	2.71	2.69
$VFT_{kinematic}$ (dimensionless)	1.75	3.16

Table 5.4: Features of two Doppler E-waves shown in Figure 3 with associated VFT values. The two E-waves are indistinguishable in terms of mean E_{peak}, E_{dur} and E/A. HR and *VFT_{standard}* values.

5.4 which shows E-waves from 2 subjects. The E-waves are indistinguishable using conventional

metrics such as peak velocity, duration, VTI and E/A (Table 5.4). However, they have different

peak E'. $VFT_{standard}$ cannot distinguish between these two subjects because it depends only on E-wave features. However, $VFT_{kinematic}$ can differentiate between them because it incorporates E'. The pseudonormal pattern of DD has impaired longitudinal motion, elevated LAP while maintaining a normal E-wave shape.

For this study we selected subjects whose echo data satisfy the established criteria for the PN pattern by having E-waves similar to the normal group, normal LV function (EF > 50%) but impaired longitudinal (E') motion. The PN group had E'_{peak} < 10 cm/s and E/E' > 8. Previous studies [9, 21] have used E/E' to estimate filling pressures and assess DF in subjects with normal EF. We used their cut-off value of 8 to dichotomize into PN vs. normal groups. In addition, to ensure that the difference in the E/E' ratio is not due to reduced E_{peak} velocity, we required that lateral E'_{peak} <10 cm/s for the PN group. Previous studies have shown [22, 34] that for the age range in this study, normal E'_{peak} velocities have a mean value of ~ 11 cm/s. Since DF becomes impaired with age [4, 22, 34, 35], we age-matched the groups. The Doppler E-wave attributes in both of the groups studied were similar (Table 5.2). The two groups differed in the Doppler E'_{peak} representing the peak longitudinal volume accommodation rate.

5.4.3 VFT$_{kinematic}$ in identifying pseudonormal filling

Fig 5.2 shows that VFT$_{kinematic}$ can differentiate pseudonormal filling from normal filling while VFT$_{standard}$ could not in the same subjects. This demonstrates the increased physiological sensitivity of VFT$_{kinematic}$ as compared to VFT$_{standard}$ and emphasizes the importance of causality based approximations in deriving VFT.

In our previous work, we derived and demonstrated the relationship between *VFT* and $(E/E')^{3/2}$ (Chapter 4, [19]). Using the constant- volume attribute [20] we demonstrated that for the same E-wave volume, *VFT* is inversely proportional to D^3, where *D* is effective orifice diameter.

Since D is proportional to $\sqrt{(E'/E)}$, VFT is proportional to $(E/E')^{3/2}$. Since $VFT_{kinematic}$ is derived from the constant- volume attribute it provides a better correlation with $(E/E')^{3/2}$ than $VFT_{standard}$. Fig. 5.3 compares $VFT_{kinematic}$ and $VFT_{standard}$ to $(E/E')^{3/2}$. Although the relationship between VFT and $(E/E')^{3/2}$ is based on approximations (assuming that the LV is a cylinder with no epicardial radial expansion and E-wave volumes among subjects remain essentially constant), $VFT_{kinematic}$ had a good correlation with $(E/E')^{3/2}$ ($R^2 = 0.55$). In most of the normal subjects, (open circles; 9 of 13) $VFT_{kinematic} < 4$ and in most PN subjects (10 of 12), $VFT_{kinematic} > 4$ (Fig 5.3a). $VFT_{standard}$ however, had a poor correlation with $(E/E')^{3/2}$ (Fig. 5.3b). There is no clear value of $VFT_{standard}$ which can differentiate between the groups. This is restated in Table 5.3, which lists the mean values of $VFT_{kinematic}$ and $VFT_{standard}$ for all subjects. Hence $VFT_{kinematic}$ not only correlates better with E/E', an established DF index [21] but is also able to better dichotomize between groups. Our study builds upon our previous work and expands the applicability of $VFT_{kinematic}$.

5.4.4 Physiological significance

Traditionally, VFT has been computed in-vitro using a piston-cylinder arrangement where the fluid exited the nozzle and formed vortices in a larger (essentially unbounded) space [36, 37]. In the LV the fluid (blood) is aspirated through the mitral orifice into a smaller (bounded) space (LV chamber) where expanding vortex ring dimension is comparable to expanding chamber dimension [31]. In this scenario the rate of chamber expansion plays an important role in vortex formation by actually generating the space for the vortex ring to expand into while providing the energy to generate the flow (since early transmitral filling is powered by the LV chamber recoil/suction). Optimal vortex formation occurs when vortex ring size and growth are synchronized with chamber size and chamber expansion [32, 37]. A mismatch between these two dynamic (tissue motion and fluid motion) attributes, as seen in enlarged chambers with a low

LVEF, results in sub-optimal vortex formation, indicative of less efficient utilization of recoil energy and associated mass transfer [31]. When the rate of chamber expansion is slower than vortex ring growth, (as in an enlarged chamber) the kinetic energy of blood is lost and fluid momentum is not directed toward the outflow track for optimal subsequent ejection. This has been shown by Carlhäll and Bolger [38] who found that in normal hearts most of the ejected blood volume entered the LV in the same beat while in subjects with moderate heart failure, the volume of blood entering and exiting the LV in the same beat is decreased. Consequently the LV has to provide the energy to eject the stagnant blood thereby making the filling and ejection process less efficient. Tissue Doppler E' velocity has been shown to be reduced in DD. A slower longitudinal chamber expansion rate, corresponding to lower E'$_{peak}$ or a higher *E/E'* ratio is a correlate of higher filling pressures [9, 21]. In terms of energetics, this means that the ventricle does more work to fill to the same volume.

Thus by explicitly including chamber expansion (E'), *VFT$_{kinematic}$* includes the relation of filling physiology to fluid mechanics. The original expression for *VFT = v*t/D=L/D,* where v is flow velocity and t is time of flow duration*,* facilitates inclusion of the near 'constant-volume' attribute of the left heart. Specifically, near constant-volume means that left atrial and ventricular volumes reciprocate as a result of ascent and descent of the mitral annulus and LV wall thickening and thinning throughout the cardiac cycle so the LA-LV summed total (epicardial) volume is essentially constant. This defines the algebraic (volume conserving) relation between LV wall thinning, transmitral flow (E-wave), mitral annular velocity (E'-wave) flow orifice diameter (D) and constant epicardial dimension.

Another issue that affects the calculation of both *VFT$_{kinematic}$* and *VFT$_{standard}$* is the question of relative vs. absolute velocity. In deriving *VFT* and expressing it as *v*t/D=L/D*, the

implicit assumption is that the flow velocity is measured relative to a stationary orifice. In the heart however, the ultrasonic transducer defines the origin of the coordinate system relative to which transmitral flow (E-wave) is measured. While the blood enters the ventricle at the velocity of the E-wave, the orifice (mitral annulus and valve) is moving in the opposite direction (relative to the transducer) at the velocity of the E'-wave. Hence, relative to the orifice itself, the blood is moving at velocity E+E'. This has the effect of increasing the velocity time integral (VTI) relative to the original value by about 10% for normals and by about 5% for pseudonormals (because E' VTI is statistically significantly lower in the pseudonormal group). If we recalculate group differences correcting for the motion of the annulus (i.e. using E+E') for VTI rather than just E, our results remain unaltered, we again find that statistically significant difference between $VFT_{kinematic}$ p = 0.011 vs. $VFT_{standard}$ p = 0.26 is maintained. Recall, prior to the E+E' 'correction' the differences for $VFT_{kinematic}$ were (p = 0.006) while for $VFT_{standard}$ it was (p= 0.13).

5.4.5 Clinical significance

DHF or HFpEF is present in ~50% of patients admitted to hospitals with heart failure. The mortality rate of HFpEF is slightly lower than the subjects with reduced ejection fraction [39, 40]. Echocardiography is the preferred method for non-invasive diagnosis and grading of HF [4]. Previous studies have shown [41] that in patients after a myocardial infarction, pseudonormal filling was an independent predictor of mortality. Subjects with pseudonormal filling had higher mortality than patients with normal filling or impaired relaxation. A specific therapeutic approach for selective treatment of HFpEF still eludes us [42]. Hence the availability of indexes that incorporate fluid mechanics attributes of filling and can differentiate pseudonormal from normal filling is of value.

Although the fact that the pseudonormal and normal groups in this sample can be easily differentiated using conventional metrics (E', EF, A_{peak}) may be initially viewed as a limitation to ultimate clinical utility, the fact that $VFT_{kinematic}$ is derived from basic principles of fluid mechanics, and incorporates near constant volume [20] and suction pump physiology of the LV while providing explicit time dependent expressions for its components enhances its ultimate value in merging fluid mechanics based analysis of DF.

Currently, fluid streamline imaging is in its infancy, but the rapid advancement of noninvasive imaging technology will lead to streamline information application in multiple modalities such as echo, MRI and CT (recall the advances in echo from 1-D (M-mode) to 2-D to Doppler, to color-Doppler to 3-D). The characterization of the relation between VFT and physiology will become increasingly important and will likely lead to understanding of new relationships between flow and chamber function. Currently, this form of VFT is a crude (lumped parameter) metric of the (global) wall motion (diastolic function) to streamline generation relation. When viewed in this context our work is the first step in incorporating the physiology and merging the technology of streamline imaging and characterization and global diastolic function. We anticipate full, high spatial and temporal resolution, 3-D streamline information availability as the technology advances.

5.4.6 Limitations

Limitations arise from the definition (Eq. 5.1 and Eq. 5.2) and the echocardiographic data used to calculate them. The various assumptions and limitations in calculating $VFT_{kinematic}$ and $VFT_{standard}$ have been discussed previously [19]. The peak mitral leaflet separation is calculated from M-mode images in parasternal short axis view that can be affected by a poor acoustic window, transducer position and the angulation relative to LV long axis. To mitigate these effects we made multiple

measurements of the diameter whenever possible and averaged over measured values. We also measure the diameter from one-dimensional M-mode measurement which might result in error if the orifice is not round or if the measurements were not made at the center of the valve plane. Because this is an accepted limitation of M-mode imaging we took care to calculate *VFT* using the method previously used in [17, 19].

The calculation of $VFT_{kinematic}$ should use simultaneous E- and E'-waves. Accordingly we matched E- and E'-waves by selecting beats with R-R intervals within ± 10 ms of each other. All subjects had a diastatic interval, hence the minor R-R differences affect only diastasis duration.

The number of subjects in the groups is constrained by the number of subjects in the Cardiovascular Biophysics Laboratory database who satisfy the inclusion criteria. The large number of beats analyzed (738) mitigates this limitation to an acceptable degree and provides adequate power for our statistics based conclusions. However, clinical use awaits studies having a larger sample size. We have specifically chosen groups with normal ejection fraction and clinically indistinguishable E-waves to demonstrate the advantage of $VFT_{kinematic}$ over $VFT_{standard}$ to detect differences. Gharib et al [17] and Kheradvar et al [33] have shown that *VFT* in subjects with reduced ejection fraction is different from subjects with a normal ejection fraction.

Another potential limitation of the study is gender distribution. While the overall number of men and women studied was nearly equal, they were unequally divided in the two groups. The normal group had 9 men out of 13 while the PN group had 9 women out of 12. The gender based differences in Doppler echocardiographic indexes are well-documented [43, 44]. Claessens et al [45] computed conventional and PDF E-wave parameters (x_o, c and k) and found that in 1606 age-matched subjects (862 females/ 744 males) the PDF parameters- x_o, c and k were significantly lower in males as compared to females. Other studies [46] have reported no significant gender-

based differences in E/A, E-wave DT and E/E' (lateral or septal). However, the effect of gender on VFT has not been studied. In this study, we computed the gender-based group average for $VFT_{kinematic}$ and $VFT_{standard}$ and found that these values were not statistically different between men and women. Hence in our study, gender didn't affect the difference in $VFT_{kinematic}$ between normal and PN group. However, to reliably assess gender related issues larger groups will need to be studied. Nonetheless since HFpEF is more prevalent in women [39], the PN subset in our study approximates that population.

5.5 Conclusion

VFT defined as $VFT_{standard}=$ {E-wave VTI}/{mitral orifice diameter} has been shown to differentiate between diastolic dysfunction groups defined by distinguishable E-wave patterns and decreasing LVEF. To extend the clinical realm of VFT applicability we tested the hypothesis that VFT can also differentiate between age matched groups having PN patterns vs. age matched controls, with normal EF and indistinguishable E-waves. We compared $VFT_{kinematic}$ and $VFT_{standard}$ and found that $VFT_{kinematic}$ could differentiate between groups. Because $VFT_{kinematic}$ incorporates E' it expands the clinical realm of VFT applicability.

Reference:

1. Gheorghidae M, Pang PS. Acute heart failure syndromes. *J. Am. Coll. Cardiol*. 2009; 53: 557-573.

2. Zile MR, Brutsaert DL. New concepts in diastolic dysfunction and diastolic heart failure: Part I. *Circulation*. 2002; 105: 1387- 1393.

3. Klein AL, Garcia MJ. Diastology: Clinical Approach to Diastolic Heart Failure. 1st Ed. Philadelphia. Saunders. 2008.

4. Nagueh SF, Appleton CP, Gillebert TC, Marino PN, Oh JK, Smiseth OA, Waggoner AD, Flachskampf FA, Pellikka PA, Evangelista A. Recommendations for the Evaluation of Left Ventricular Diastolic Function by Echocardiography. *J. Am. Soc. Echocardiogr*. 2009; 22(2):107-133.

5. Little WC, Oh JK. Echocardiographic evaluation of diastolic function can be used to guide clinical care. *Circulation*. 2009; 120: 802- 809.

6. Kovács SJ, Barzilai B, Pérez JE. Evaluation of diastolic function with Doppler echocardiography: the PDF formalism. *Am. J. Physiol*. 1987; 87: H178-H187.

7. Dent CL, Bowman AW, Scott MJ, Allen JS, Lisauskas JB, Janif M, Wickline SA, Kovács SJ. Echocardiographic characterization of fundamental mechanisms of abnormal diastolic filling in diabetic rats with a parameterized diastolic filling formalism. *J Am Soc Echocardiogr*. 2001; 14(12):1166-72.

8. Lisauskas JB, Singh J, Bowman AW, Kovács SJ, Jr. Chamber properties from transmitral flow: prediction of average and passive left ventricular diastolic stiffness. *J. Appl. Physiol*. 2001; 91: 154-162.

9. Lisauskas JB, Singh J, Courtois MR, Kovács SJ, Jr. The relation of the peak Doppler E-wave to peak mitral annulus velocity ratio to diastolic function. *Ultrasound Med. Biol*. 2001; 27: 499-507.

10. Riordian MM, Kovács SJ. Quantitation of mitral annular oscillations and longitudinal "ringing" of the left ventricle: a new window into longitudinal diastolic function. *J. Appl. Physiol*. 2006; 100:112-119.

11. Shmuylovich L, Kovács SJ. A load-independent index of diastolic filling: model-based derivation with in-vivo validation in control and diastolic dysfunction subjects. *J. Appl. Physiol*. 2006; 101: 92-101.

12. Hall AF, Kovács SJ. Automated method for characterization of diastolic transmitral Doppler velocity contours: Early rapid filling. *Ultrasound Med. Biol*. 1994; 20: 107-116.

13. Hall AF, Nudelman SP, Kovács SJ, Jr. Evaluation of Model-Based Processing Algorithms for Averaged Transmitral Spectral Doppler Images. *Ultrasound Med Biol*. 1998 24:1, 55-66.

14. Hall AF, Kovács SJ Jr. Processing parameter effects on the robustness of the solution to the "Inverse Problem" of diastole from Doppler echocardiographic data. *Conf Proc IEEE Eng Med Biol Soc*.1993; I385-387.

15. Hong GR, Pedrizzetti G, Tonti G, Li P, Wei Z, Kim JK, Baweja A, Liu S, Chung N, Houle H, Narula J, Vannan MA. Characterization and Quantification of Vortex Flow in the Human Left Ventricle by Contrast Echocardiography Using Vector Particle Image Velocimetry. *J Am Coll Cardiol Img* 2008; 1(6): 705-717.

16. Ghosh E, Kovács SJ. E-wave associated vortex formation facilitates diastatic mitral leaflet coaptation. *J. Am. Coll. Cardiol*. 2011; 57 (14s1): E663-E663.

17. Gharib M, Rambod E, Kheradvar A, Sahn DJ, Dabiri JO. Optimal vortex formation as an index of cardiac health. *Proc Nat Acad Sciences* 2006; 103(16): 6305 -6308.

18. Ghosh E, Shmuylovich L, Kovács SJ. Determination of early diastolic LV vortex formation time (T*) via the PDF formalism: a kinematic model of filling. *Conf Proc IEEE Eng Med Biol Soc.* 2009; 2883-6.

19. Ghosh E, Shmuylovich L, Kovács SJ. Derivation of the fluid mechanics to left ventricular early, rapid filling relation, with in-vivo validation. *J. Appl. Physiol.* 2010; 109 (6): 1812-1819.

20. Bowman AW, Kovács SJ. Assessment and consequences of the constant-volume attribute of the four-chambered heart. *Am. J. Physiol.* 2003; 285:H2027-H2033.

21. Nagueh SF, Middleton KJ, Kopelen HA, Zoghbi WA, Quinones MA. Doppler Tissue Imaging: A non-invasive technique for evaluation of left ventricular relaxation and estimation of filling pressures. *J. Am. Coll. Cardiol.* 1997; 30: 1527-1533.

22. Klein AL, Burstow DJ, Tajik AJ, Zachariah PK, Bailey KR, Seward JB. Effects of age on left ventricular dimensions and filling dynamics in 117 normal persons. *Mayo Clin. Proc.* 1994; 69: 212- 224.

23. Kasner M, Westermann D, Steendijk P, Gaub R, Wilkenshoff U, Weitmann K, Hoffmann W, Poller W, Schultheiss HP, Pauschinger M, Tschöpe C. Utility of Doppler Echocardiography and Tissue Doppler Imaging in the Estimation of Diastolic Function in Heart Failure with Normal Ejection Fraction: A Comparative Doppler-Conductance Catheterization Study. *Circulation.* 2007; 116 (6): 637- 647.

24. Baumgartner H, Hung J, Bermejo J, Chambers JB, Evangelista A, Griffin BP, Iung B, Otto CM, Pellikka PA, Quiñones M. Echocardiographic assessment of valve stenosis:

EAE/ASE recommendations for clinical practice. *J Am Soc Echocardiogr*. 2009; 22(1): 1- 23.

25. Boskovski MT, Shmuylovich L, Kovács SJ. Transmitral flow velocity- contour variation after premature ventricular contractions: a novel test of the load-independent index of diastolic filling. *Ultrasound Med Biol*. 2008; 34: 1901- 1908.

26. Foppa M, Duncan BB, Rohde LEP. Echocardiography-based left ventricular mass estimation. How should we define hypertrophy? *Cardiovasc. Ultrasound*. 2005; 3:17.

27. Pasipoularides A. Heart's Vortex: Intracardiac Blood Flow Phenomena. 1st Ed. Shelton, CT. People's Medical Publishing House. 2010.

28. Gharib M, Rambod E, Shariff K. A Universal Time-Scale of Vortex Formation Time. *J. Fluid. Mech*. 1998; 360:121-140.

29. Krueger P, Gharib M. The significance of Vortex Ring Formation to the Impulse and Thrust of a Starting Jet. *Phys. Fluids*. 2003; 15(5):1271-1281.

30. Mohseni K, Gharib M. A Model for Universal Time Scale of Vortex Ring Formation. *Phys. Fluids.* 1998; 10(10):2436-2438.

31. Töger J, Kanski M, Carlsson M, Kovács SJ, Söderlind G, Arheden H, Heiberg E. Vortex Ring Formation in the Left Ventricle of the Heart: Analysis by 4D Flow MRI and Lagrangian Coherent Structures. *Annals BME*. 2012; 40(12): 2652-2662.

32. Kheradvar A, Milano M, Gharib M. Correlation Between Vortex Ring Formation and Mitral Annulus Dynamics During Ventricular Rapid Filling. *J. Am. Soc. Artificial Organs*. 2007; 53:8-16.

33. Kheradvar A, Assadi R, Falahatpisheh A, Sengupta PP. Assessment of Transmitral Vortex Formation in Patients in Diastolic Dysfunction. *J. Am. Soc. Echocardiogr.* 2012; 25 (2): 220- 227.

34. Hill JC, Palma RA. Doppler Tissue Imaging for the Assessment of Left Ventricular Diastolic Function: A Systemic Approach for the Sonographer. *J. Am. Soc. Echocardiogr.* 2005; 18: 80- 90.

35. Ommen SR, Nishimura RA. A clinical approach to the assessment of left ventricular diastolic function by Doppler echocardiography: update 2003. *Heart* 2003; 89(Suppl. III): iii18- iii23.

36. Dabiri JO, Gharib M. The role of optimal vortex formation in biological fluid transport. *Proc. R. Soc. B.* 2005; 272: 1557- 1560.

37. Kheradvar A, Gharib M. On Mitral Valve Dynamics and its Connection to Early Diastolic Flow. *Annal Biomed Eng* 2008; 37: 1-13.

38. Carlhäll CJ, Bolger A. Passing Strange: Flow in the Failing Ventricle. *Circ. Heart Fail.* 2010; 3:326-331.

39. Bhatia RS, Tu JV, Lee DS, Austin PC, Fang J, Haouzi A, Gong Y, Liu PP. Outcome of Heart Failure with Preserved Ejection Fraction in a Population-Based Study. *N. Eng. J. Med.* 2006; 355 (3): 260- 269.

40. Owan TE, Hodge DO, Herges RM, Jacobsen SJ, Roger VL, Redfield MM. Trends in prevalence and outcome of heart failure with preserved ejection fraction. *N. Engl. J. Med.* 2006; 355(3): 251- 259.

41. Møller JE, Søndergaard E, Poulsen SH, Egstrup K. Pseudonormal and restrictive filling patterns predict left ventricular dilation and cardiac death after a first myocardial

infarction: a serial color M-mode doppler echocardiographic study. *J. Am. Coll. Cardiol*. 2000; 36: 1841- 1846.

42. Schwartzenberg S, Redfield MM, From AM, Sorajja P, Nishimura RA, Borlaug BA. Effects of Vasodilation in Heart Failure with Preserved or Reduced Ejection Fraction. *J. Am. Coll. Cardiol*. 2012; 59 (5): 442- 451.

43. Bella JN, Palmieri V, Kitzman DW, Liu JE, Oberman A, Hunt SC, Hopkins PN, Rao DC, Arnett DK, Devereux RB. Gender differences in diastolic function in hypertension (the HyperGEN study). *Am. J. Cardiol*. 2002; 89 (9): 1052- 1056.

44. Sadaniantz A, Hadi BJ, Laurent LS. Gender Differences in Mitral Inflow Parameters of Doppler Echocardiography. *Echocardiography*. 1997; 14: 435–439.

45. Claessens T, Raja MW, Pironet A, Chirinos J, Desaive T, Rietzschel E, De Buyzere M, Van Ransbeeck P, Verdonck P, Gillebert T, Segers P. The parametrized diastolic filling formalism: Application in the Asklepios population. *Proc. Assoc. Mech. Eng*. 2011 Summer Bioengineering Conference (SBC-2011:53375); 2011- 06-22, Farmington, PA, USA.

46. Park HS, Naik SD, Aronow WS, Ahn CW, McClung JA, Blekin RN. Age- and sex-related differences in the tissue Doppler imaging parameters of the left ventricular diastolic dysfunction. *Echocardiography*. 2007; 24(6): 567- 571.

Chapter 6: The E-wave generated intraventricular diastolic vortex to L-wave relation: model-based prediction with in-vivo validation.

Abstract

The suction pump feature of the ventricle initiates transmitral flow usually imaged as the Doppler echocardiographic E-wave. In some subjects E-waves are accompanied by L-waves whose occurrence has been correlated with diastolic dysfunction. The causal mechanisms for L-wave generation have not been fully elucidated. In this study we propose that diastolic intraventricular vortex ring formation provides one mechanism for L-wave generation. We imaged intraventricular flow using Doppler echocardiography and phase-contrast magnetic resonance imaging (PC-MRI) in ten healthy volunteers. Depending on sample volume location we observed L-waves in all 10 subjects. Of 345 cardiac cycles recorded in 10 subjects, 189 had L-waves (55 %). Highest L-wave velocities were typically 2 cm below the annulus. Delayed right ventricular flow as a mechanism for L-wave generation was eliminated by color M-mode images of L-waves concomitant with diastatic mitral leaflet coaptation and absence of simultaneous transmitral flow. PC-MRI independently validated echocardiographic findings and enabled visualization of 3-D intraventricular flow patterns. The 'vortex generated L-wave hypothesis' predicts the existence of L-waves in the right ventricle (RV), which was confirmed using echocardiography and PC-MRI. The re-entry of the E-wave generated vortex ring flow through the echocardiographic sample volume can manifest as an L-wave. The waves are a general feature and are a consequence of LV diastolic fluid mechanics. Additionally, L-waves are present in the RV as predicted.

6.1 Introduction

6.1.1 The phenomena of L-waves
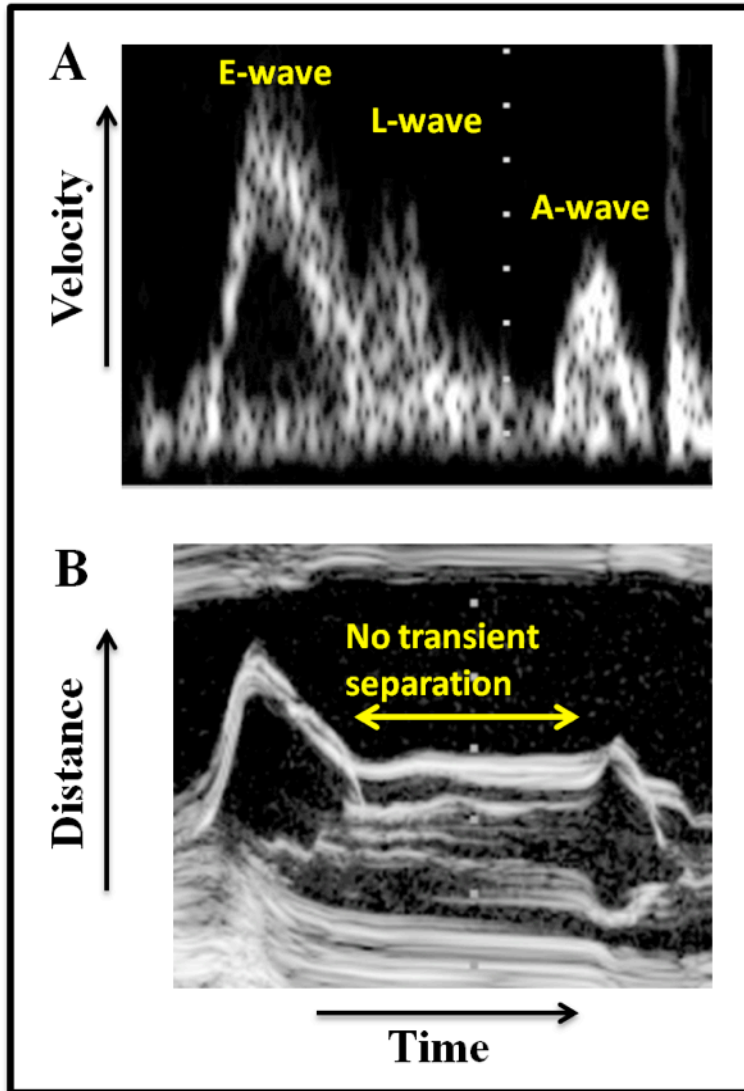
Fig 6.1: (A) Two-dimensional Doppler transmitral velocity profile showing the early filling (E-), L-wave and the atrial filling (A-) wave. (B) Parasternal M-mode image in the same subject showing mitral leaflet tip motion. Mitral leaflets remain coapted, with no transient leaflet separation during diastasis indicating absence of transmitral flow during the L-wave. See text for details.

The mechanical suction pump attribute of all ventricles initiates early rapid filling and inscribes the transmitral E–wave imaged by pulsed Doppler echocardiography. In some cases [1] a wave, called the L-wave (Fig. 6.1A), has been observed in early diastasis, immediately after the E-wave. While L-waves have been thought to be of marginal clinical significance since they are very rarely observed [2], L-waves have been correlated with certain diastolic dysfunction (DD) states [2,3]. Lam et al [4] found that L-waves were associated with the pseudonormal LV filling pattern and were predictors of future HF events. In addition others [5,6] have noted L-wave correlation with

delayed relaxation. These studies did not address the mechanism of L-wave generation. The causal mechanism for L-waves is poorly understood.

6.1.2 Keren hypothesis for L-wave formation

Keren et al [1] sought a mechanistic explanation for L-waves and proposed that L-waves are due to a delayed filling wave generated by the right ventricle traversing the lung, the pulmonary veins to the left atrium. Hence they hypothesized that after the E-wave, a second (L-) wave of transmitral flow enters the LV. To support their hypothesis, they provided parasternal M-Mode images of transient mitral leaflet tip separation during diastasis. However, L-waves can be observed in the absence of transient mitral leaflet separation during diastasis, i.e. while the leaflets remain coapted (Fig 6.1B).

6.1.3 Vortex hypothesis for L-wave formation

To explain the presence of L-waves in the absence of transient mitral leaflet separation during diastasis we propose an alternate mechanism, that near E-wave termination, the leading edge of the expanding vortex ring generated by the E-wave moves into the Doppler echo sample volume and inscribes the L-wave. As E-wave volume accelerates and decelerates through the mitral orifice, the outer layers of the associated expanding vortex curl around and behind the mitral leaflets [7]. The core of the rotating vortex ring detaches from the leaflet tips [8]. The rotating 3-dimensional vortical flow pattern is initially directed towards the lateral and septal walls, then towards the base as the vortex completes its circuit and its core moves in the base to apex direction, parallel to initial mitral inflow. The expanding vortex ring is partly responsible for mid-diastolic mitral leaflet closure (M-mode E to F slope) and coaptation [9] during diastasis. As the leading edge of the vortex rotates it <u>may</u> pass through the Doppler sample volume (depending on Doppler sample volume location). To validate our 'vortex generated L-wave

121

hypothesis' we imaged intraventricular blood flow using echocardiographic and cardiac magnetic resonance imaging (CMRI) in healthy volunteers. Additionally, our hypothesis also predicts the presence of L-waves in the right ventricle (RV). Vortexes form during RV filling [9] and hence by the same mechanism as in the LV, recirculating vortex flow can result in L-waves. Hence we also imaged intraventricular blood flow in the RV using echocardiography and CMRI.

6.2 Methods

6.2.1 Subject selection

Ten healthy volunteers were recruited for the study. All participants had no history of cardiac disease and gave informed consent in accordance with the study protocol approved by the Washington University Medical Center Human Research Protection Office (HRPO). Among the 10 subjects, 7 had an echocardiographic exam and a CMRI performed during the same imaging session, while the remaining 3 subjects had an echocardiographic exam only.

6.2.2 Doppler echocardiographic data acquisition

All subjects had a complete 2D echo-Doppler study in accordance with ASE criteria [10]. These included apical four and five-chamber 2D-echo Doppler views of the mitral inflow aortic outflow and pulmonary vein flow, recorded using a 2.5/3.5 MHz transducer using a clinical echocardiographic imager (Philips iE33). In addition, the apical four-chamber view was used to map intraventricular flow. This was done by moving the echo sample volume first along the LV long-axis (from base to apex direction) (See Fig 6.2A). This characterizes transmitral inflow pattern spatial variation longitudinally. Additionally, while keeping sample volume distance fixed, the sample volume was directed transversely, along the short-axis (lateral to septal wall)

(See Fig 6.2B). Parasternal long- axis and short-axis M-mode imaging was used to measure mitral leaflet motion. Color M-mode Doppler was used to measure velocity along the LV long axis.

6.2.3 CMR data acquisition

To 'over-determine' the flow patterns using and independent imaging modality, CMRI was
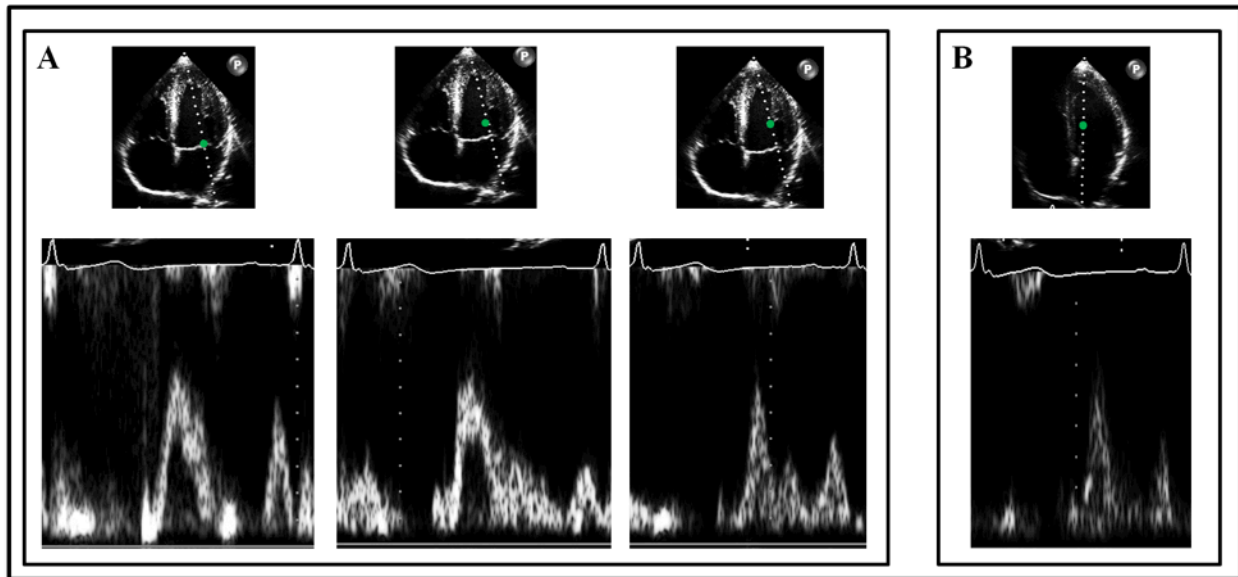
Fig 6.2: Variation of sample volume location on 2D Doppler echocardiography (green dot) to map associated velocity profiles. (A) Apical four chamber views (top) illustrating sample volume locations (at green dots) with associated flow velocity profiles (bottom). Left to right, sequential sample volume placement toward the apex. (B) Sample volume placement variation along the short- axis (lateral to septal wall) in the mid-LV. See text for details

performed in 7 subjects using a Philips Achieva 3T CMR scanner. For high resolution anatomical information, standard functional CMR imaging consisted of balanced turbo field echo (b-TFE) cine images in 2-chamber, 3-chamber, 4-chamber and short axis views. Typical parameters were: slice thickness 2 mm and in-plane resolution 1.25 X 1.25 mm^2. In addition, in the same imaging session, 3 dimensional, time-resolved velocity mapping (PC-MRI) was performed to measure intraventricular flow patterns. Three directional velocities were measured by 3 consecutive scans encoding the velocity in each orthogonal direction. A respiratory-gated

phase contrast (gradient echo) sequence was used. The parameters employed for parallel acquisition techniques (SENSE), were: spatial resolution: 2.5 x 2.6 x 4 mm^3 (acquired) and 2.0 x 2.0 x 2.0 mm^3 (reconstructed), short echo and repetition times (TE= 2.6 ms and TR= 4.6 ms), flip angle = 10° (for short TE), velocity encoding (VENC) = 120 cm/s and SENSE factor of 2. Retrospective ECG triggering was used to ensure complete coverage of the R-R interval, including late diastole. Concomitant gradient compensation was performed as standard, by the CMR scanner software.

6.2.4 Echocardiographic data processing and quantification

All echocardiographic images were downloaded in DICOM format and converted to .bmp image file format using a custom MATLAB program (MathWorks, Natick, MA). The transmitral flow images were classified according to sample volume distance from the mitral annulus. Conventional echocardiographic indexes such as E_{peak}, E-wave duration, AT, DT were calculated. The L-wave parameters such as L_{peak} and L-wave duration were measured. The variations in flow velocity at different positions along the short and long axis were quantified to uncover trends.

Color M-mode images were cropped and the color maps were converted into velocity maps. This was done by calibrating the color bar in each image to the peak velocity values. The color values of each pixel were assigned a specific velocity. Regions of aliasing were identified manually and the velocity values were corrected. Cropped images were used to determine the temporal velocity profile at varying distances from the annular plane of the LV. This was corroborated with the temporal velocity profiles measured by placing the sample volume at different locations along the long-axis as described above.

M-mode imaging, with specific attention to directing the beam at the leaflet tips, was used to assess mitral leaflet separation during diastasis. The mitral leaflet configuration during diastasis was classified as: coapted, having constant separation or having transient diastatic separation, i.e. a 'bump' and a combination type with both coaptation and transient separation in the diastatic interval. Examples of the different mitral leaflet configurations are shown in Fig. 6.3.
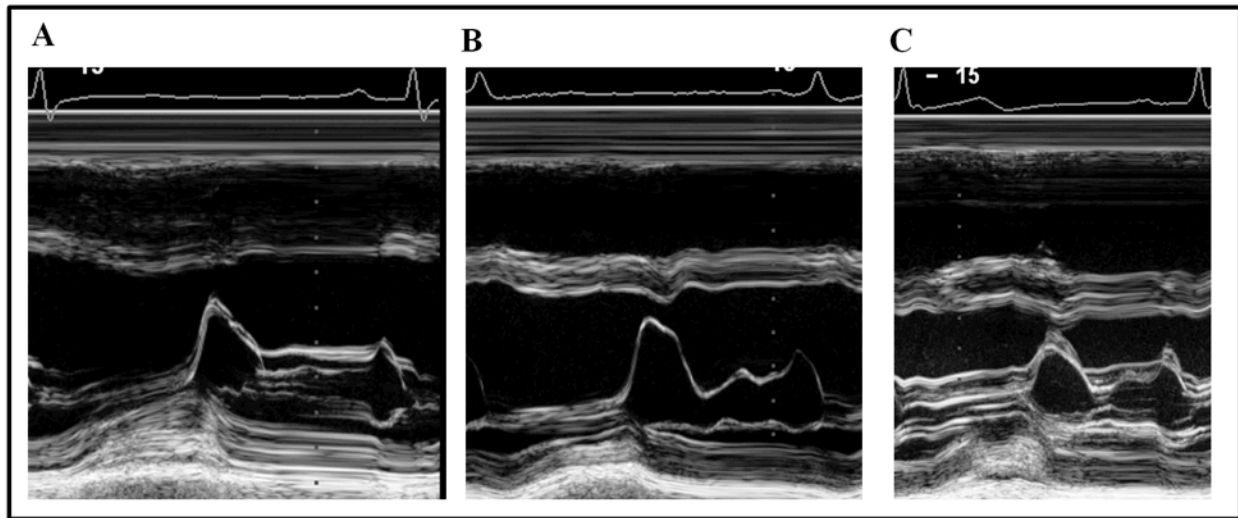
Fig 6.3: Three types of mitral leaflet motion during diastasis via parasternal M-mode imaging. (A) Mitral leaflets remain coapted during diastasis. (B) Mitral leaflets with a transient separation during diastasis. (C) Mitral leaflets are initially coapted and then transiently separated during diastasis. See text for details.

6.2.5 CMRI data processing and quantification

First-order phase background correction, phase unwrapping and rescaling was performed using a custom MATLAB script. For each subject the three directional velocity encoding scans were combined and the values were recalibrated such that the minimum and maximum velocity corresponded to $\pm$ V_{enc}. End-systole (ES) and end-diastole (ED) were determined manually, based on flow through the valve planes. The velocity data were linearly interpolated in time such that 146 data points represented each R-R interval. Streamlines (pixel-tracking) were visualized

by selecting a region in the short-axis view and tracking the pixels during diastole. Starting from the basal (mitral annular) plane, an initial particle plane was marked and the position of the pixels in 3 dimensions was calculated using the interpolated velocity matrixes. An alternate method of visualizing intraventricular flow consisted of measuring the temporal velocity profile at a fixed location. This was done by selecting a pixel in the short axis plane and graphing the velocity in the through-plane direction at the selected pixel location. This method allows comparison of PC- MRI temporal velocity profiles with Doppler temporal velocity profiles in comparable locations. PC-MRI also provides the spatial variation in temporal velocity profiles in the vicinity of the selected pixel.

6.3 Results

Demographics and conventional echo parameters for the 10 subjects (6 males) are shown in Table 6.1.

	Mean	SD
Age (years)	29	11
Gender	6M/4F	
Weight (lbs)	146	21
Height (inches)	69	3
BMI	21.7	1.2
HR (bpm)	58	8
Echo parameter		
E_{peak} (cm/s)	77	9
A_{peak} (cm/s)	41	12
E- wave AT (ms)	101	9
E- wave DT (ms)	197	19
E/A	1.9	0.4
L_{peak} (cm/s)	42	8

Table 6.1: Subject demographics and echocardiographic parameters for all 10 subjects. SD = standard deviation, AT = acceleration time, DT =

6.3.1 Detecting L-waves by pulse wave 2D Doppler

L-waves could be recorded in all 10 subjects. Among a total of 345 beats recorded by 2D Doppler, 189 had L-waves (55%). By varying sample volume location from near the base (mitral annulus) to the mid-LV, L-waves could be observed in all subjects. Fig 6.4 shows the percentage of recorded beats with L-waves as a function of distance from the annulus. The position yielding the highest percentage of recorded L-waves (58%) was about 1 cm from the annulus. Fig 6.4 also shows the number of beats recorded at each sample volume location.

The mean L-wave peak velocity was near 0.4 m/s (varying between 0.38 cm/s and 0.42 cm/s) for sample volumes located up to 1.5 cm from mitral annulus and the maximum was observed about 2 cm from the annulus (0.51 m/s). The E-wave peak velocity remained essentially constant at 0.8 m/s till sample volume locations 2.5 cm away from the annulus. As expected, E-wave peak velocity decreases with increasing distance from the annulus [11]. To illustrate variation among subjects, we note that for Subject 3, the L-wave peak velocity initially decreases as the sample volume is moved away from the annulus. In contrast for Subject 9, the L-wave peak velocity initially increases as the sample volume is moved apically

Fig 6.4: Percent of cardiac cycles with L-waves as a function of sample volume location (black circles) and total number of cardiac cycles (red squares) recorded at each location for all 10 subjects. At each location 40 – 60% of the recorded cardiac cycles had a L-wave. See text for details

until the sample volume is 2.5 cm away from the annulus after which L-wave peak velocity decreases.

6.3.2 Measuring mitral leaflet configuration during diastasis

Mitral leaflet configuration was imaged using M-mode and classified as described above. Fig 6.3 shows different mitral leaflet configurations at diastasis. All 3 different mitral leaflet
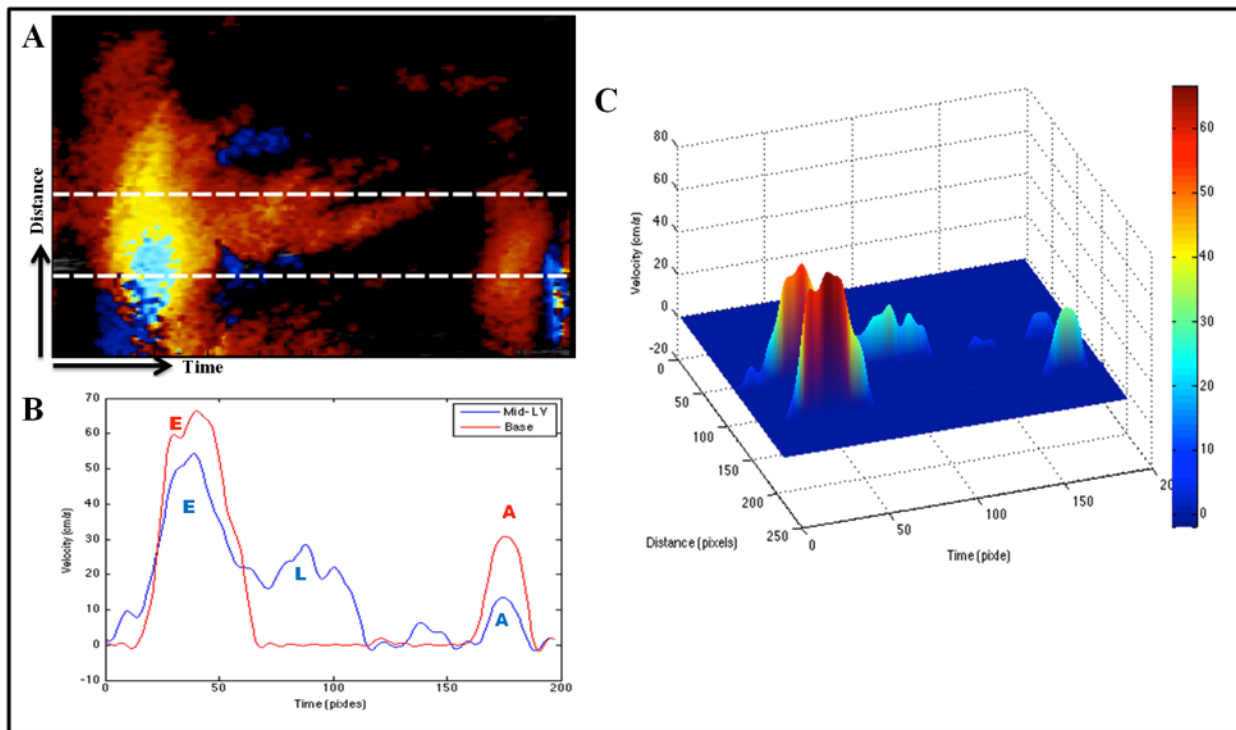
Fig 6.5: Color M-mode Doppler imaging illustrating simultaneous measurement of velocity profiles along the LV long axis. (A) A typical color M-mode Doppler flow image during diastole. The colors represent velocity and the dashed white lines are the positions of the velocity profiles in (B) and (C). (B) Transmitral flow velocity as a function of time near the annulus (red) and mid- LV (blue). (C) 3D contour plot showing the velocity profile as a function of distance from apex (located at 0 pixels). Color bar shows velocity in cm/s. The mid-LV velocity profile shows a L-wave while the profile nearer the annulus shows no L-wave. See text for details.

configurations were observed as shown in the figure.

6.3.3 Color M-mode imaging of flow along LV and RV long axis

Color Doppler M-mode imaging was used to determine presence of diastatic transmitral inflow while also recording the presence of L-waves in the same cardiac cycle. The images were used to quantify velocity at selected locations in the LV. This is shown in Fig 6.5. In all subjects a forked E-wave ('flame') pattern on color Doppler M-mode was observed, with or without
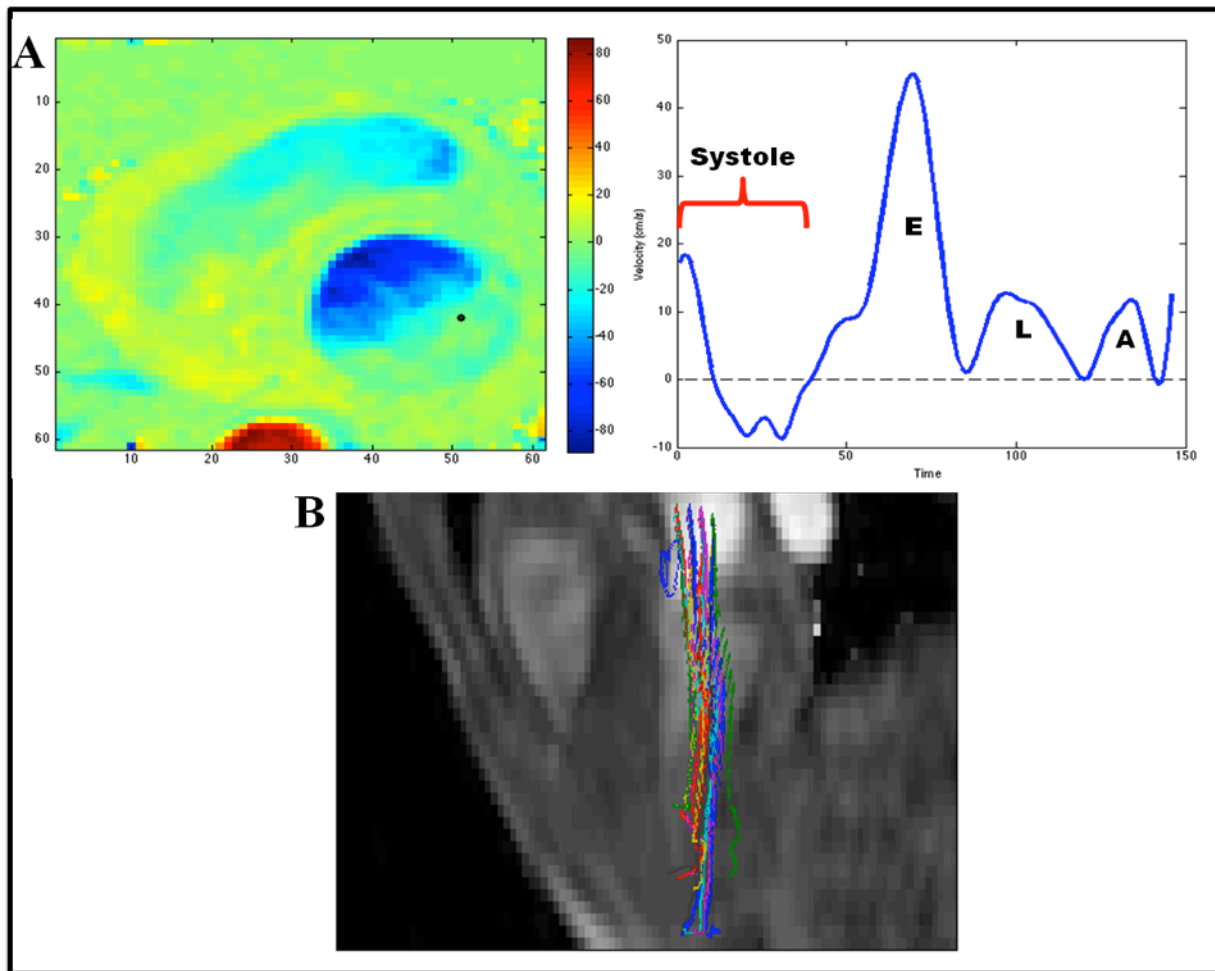
Fig 6.6: LV velocity profile and streamlines from PC-MRI data. (A) Phase contrast cardiac short axis image at the level of the annulus converted to (through-plane) velocity map. Color bar shows velocity in cm/s. Blue-green (negative) velocities indicate flow towards the apex. Through-plane velocity at selected fixed spatial location (black dot in center of annular inflow track) for one cardiac cycle. Note presence of L-wave. (B) Long axis view of the heart with fluid streamlines showing recirculating flow and flow towards the apex. See text for details.

accompanying transmitral flow during diastasis. The forked E-wave flame pattern is known to represent vortical flow component directed apically, along the long axis [9]. In addition color M-

mode imaging of the RV long axis revealed a triple flame pattern corresponding to the E-, L- and A-waves.

6.3.4 Measuring temporal velocity profile using PC-MRI

To independently validate intraventricular diastolic flow patterns we also used PC-MRI in a manner similarly employed by others [8]. We determined through plane velocity for a selected voxel fixed in space for a complete cardiac cycle. Fig 6.6A shows the temporal velocity profile for such a selected voxel for Subject 1. We also inferred streamlines to visualize the path of individual particles by selecting voxels in an initial transverse slice at the level of the annulus and computing their position and velocity forward in time. Fig 6.6B shows one such selected streamline tracking for Subject 1.

6.3.5 Measuring intraventricular flow in the RV

As Pasipoularides and coworkers have previously shown [9, 12-14], vortex formation in diastole is a well-established feature of RV filling. Hence the 'vortex generated L-wave hypothesis' predicts the existence of L-waves in the RV. We therefore imaged right ventricular (RV) trans-tricuspid flow. PC-MRI data included RV flow for 7 subjects and RV echocardiographic data was recorded in 2 subjects. The RV E-wave and A-wave velocities were lower than the corresponding LV velocities as expected. The mean L_{peak} recorded was about 21 cm/s while the mean E_{peak} was 56 cm/s. L-waves were observed in the RV using both echocardiography and PC-MRI. Fig 6.7 shows RV L-waves in one subject. In addition, color Doppler M-mode imaging of RV flow recorded mid-RV vortical (forked E-wave) flow without concomitant flow through the tricuspid valve.

130

6.4 Discussion

6.4.1 Previous studies on L-waves
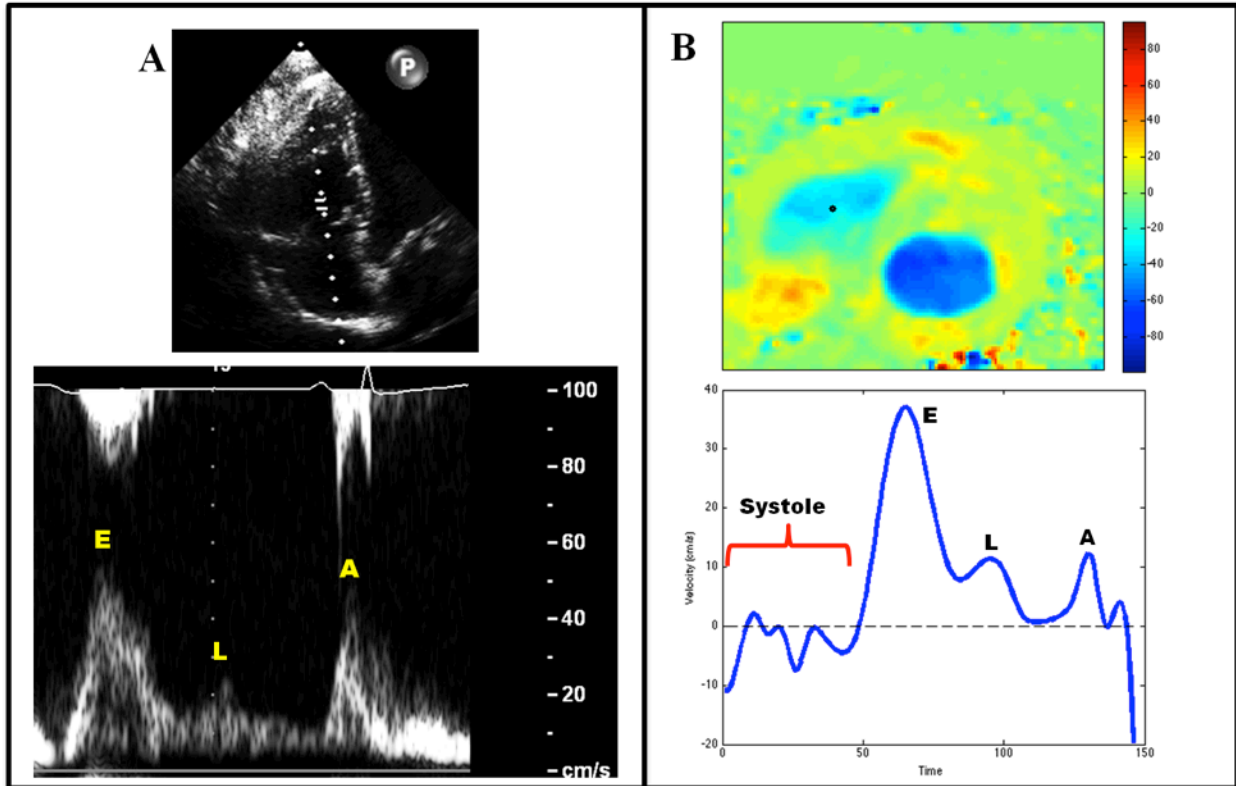
Fig 6.7: RV trans-tricuspid flow measured using 2D Doppler (A) and PC-MRI (B). (A) 2-D image showing sample volume location (upper panel) with Trans-tricuspid flow using 2D Doppler shows L-wave in the RV (lower panel). (B) Phase contrast cardiac short axis image (upper panel) at just below tricuspid annulus converted to (through-plane) velocity map. Color bar shows velocity in cm/s. Blue-green (negative) velocities indicate flow towards the apex. Lower panel: Through-plane velocity at selected fixed spatial location (black dot in center of tricuspid inflow track) for one cardiac cycle. Note presence of L-wave. See text for details.

The pioneering work of Keren et al first described Doppler echocardiographic L-waves [1]. It was recorded as post E-wave, diastatic flow across the mitral valve evidenced by transient leaflet separation on M-mode echocardiography or as a distinct wave on pulsed-wave Doppler. The term "L-wave" was chosen, because it follows the "J-" and "K-" hemodynamic waves of pulmonary vein flow (systolic and diastolic flow waves). However, the full range of possible causal mechanisms for L-wave generation has not yet been elucidated.

131

Studies have noted the presence of L-waves accompanying LV hypertrophy, advanced diastolic dysfunction, pseudonormal filling, delayed relaxation and elevated filling pressures [2-6, 15]. Keren et al [1] proposed that L-waves were due to a delayed filling wave generated by the RV, transiting the pulmonary vein into the LV after the E-wave. It therefore follows that the delayed filling wave mechanism proposed for L-waves in the LV cannot be applied as a causal mechanism for L-waves observed in the RV.

6.4.2 Diastolic intraventricular flow

At the beginning of filling, a column of blood enters the ventricle as a jet with uniform velocity across the cross-sectional area. Upon entering the ventricle, shear forces acting on the periphery of this column of blood creates a boundary layer with increased vorticity. This boundary layer forms a vortex ring at the tips of the mitral leaflets. The vortex ring thus formed is asymmetric and toroidal shaped due to ventricular anatomy. The vortex ring contains entrained blood from the ventricle and grows until it pinches off from the transmitral flow [16]. As the vortex ring develops, the leading edge of the ring curls behind the leaflet tips and contributes in coapting the leaflets during diastasis. The recirculating vortex ring merges with the terminating, decelerating mitral inflow.

We propose the alternate hypothesis that L-waves can also be a manifestation of intraventricular vortex generated flow. Imaging studies [8, 17] clearly illustrate how the leading edge of the recirculating vortex can pass through a Doppler sample volume conventionally located near the leaflet tips, which can be imaged as L-waves.

6.4.3 Predictions of the vortex based hypothesis

L-waves are observed only in subjects in whom diastasis is present, assuring that by the time the leading edge of the recirculating vortex ring reenters the sample volume, the E-wave is nearly

132
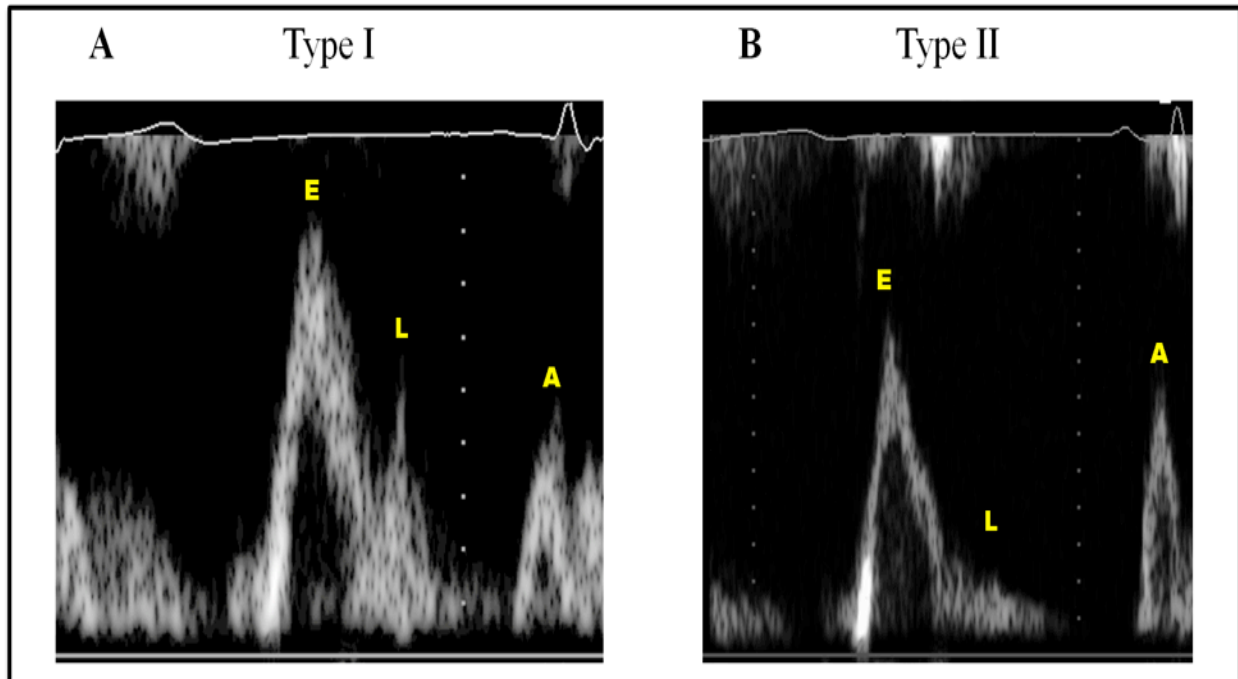
Fig 6.8: Two types of L-waves. (A) Distinct L-wave (Type I) with an accelerating and decelerating portion. (B) Merged L-wave (Type II) having only a decelerating portion, manifesting as an abrupt change in the deceleration segment of the flow profile. See text for details.

complete but atrial contraction has not commenced. Thus, the recirculating vortex inscribes a

wave between the E- and A-wave. Our hypothesis has 3 testable predictions. 1) no new trans

pulmonary vein flow is required (mitral leaflets do not separate) and 2) two types of L-wave

shapes could be generated depending on circumstances and geometric details. Type I L-wave is a

distinct wave with accelerating and decelerating portions (Fig 6.8A), after the end of E-wave and

Type II L-wave, appears as an abrupt change in the deceleration slope of a lengthened E-wave (a

biphasic E-wave) due to the gradual decay of the recirculating vortex in the sample volume (Fig

6.8B). 3) L-waves must exist in the RV.

Thus, because the laws of fluid mechanics require that a recirculating vortex (of variable

strength) be generated by early rapid filling, L-waves are present and can be imaged in all hearts.

Its observation requires the presence of diastasis. Furthermore, L-waves should be observable in

both the left and right ventricles in diastole. Successful imaging of L-waves is keenly dependent on sample volume location in addition to machine settings. To validate our hypothesis we employed multi-modal imaging (Doppler echocardiography and PC-MRI) and imaged left and right intraventricular flow and tracked selected voxel paths of the recirculating vortex in both ventricles.

6.4.4 Echocardiographic imaging: pulsed wave Doppler

Doppler data were acquired by varying sample volume location along the long axis from the mitral valve plane and at different positions along the short axis (septal-lateral direction). As shown in Fig 6.4, L-waves were observed and quantified at locations with varying distances from the annulus. The likeliest place to observe L-waves, in the 10 subjects we studied, was about 1 cm from the annulus (58% of recorded beats had L-waves). Between the annulus and 5.5 cm from the annulus, the percentage of beats with L-waves was 53%, i.e. about half of the 345 beats recorded at these locations had an L-wave. This is much higher than the previously reported incidence of L-waves 2. We excluded the data recorded from 3.5 cm and above from this analysis since the number of beats recorded at these locations were too low (<20 beats at each location) to derive meaningful conclusions.

L-wave peak velocity averaged about 0.4 m/s up to a distance of 1.5 cm from the annulus with a slight variation. The maximum L-wave peak velocity (0.5 m/s) was recorded at about 2 cm from the annulus. By mapping intraventricular flow by 2D Doppler we observed that L-waves could be detected not only near the annulus but also in the mid-LV. Moreover, the maximum L-wave peak velocity can be recorded more apically, about 2 cm away from the annulus. The variation in the number and magnitude of L-waves is consistent with vortex flow

hypothesis since the recirculating jet would merge with the main inflow at a finite distance away from the annulus.

6.4.5 Echocardiographic imaging: parasternal M-mode

In order to determine whether L-waves are a result of delayed, RV generated transmitral flow during diastasis (Keren hypothesis) or due to recirculating intraventricular flow we imaged the mitral leaflet separation using M-mode. Coapted leaflets during diastasis indicate absence of transmitral flow. However, leaflet tip coaptation at diastasis is difficult to record since the thin ultrasound beam has to be precisely directed through the coapted leaflet tips. Thus it is extremely sensitive to the position and the angulation of the recording beam. While coaptation of the leaflets was seen in some cases, in the majority of the images the 2 coapted leaflets were imaged just above their coaptation point generating a constant separation between them indicating that the ultrasound beam was slightly above the tip (Fig 6.3A). In some cases a transient diastatic leaflet separation was observed concordant with the Keren et al [1] hypothesis (Fig 6.3B). Moreover, in some subjects, depending on the beat, both coapted and transiently separated leaflets could be observed (Fig 6.3C). L-waves were recorded in both cases, indicating that both Keren's hypothesis and the recirculating vortex ring hypothesis are feasible and sometimes can occur in the same subject during different beats.

6.4.6 Echocardiographic imaging: color M-mode

Color Doppler M-mode records velocities along the entire scan line directed along the long-axis of the LV. The inflow velocity is encoded by color and the color images are converted into velocity contour maps to visualize inflow temporal velocity profiles at different locations along the LV long axis. A typical color M-mode image recorded from Subject 8 is shown in Fig 6.5A. Fig 6.5B and 6.5C also shows the temporal velocity profile at 2 different long axis positions.

These color Doppler M-mode generated temporal velocity profiles are equivalent to pulsed Doppler recordings obtained by placing the sample volume at the selected locations (indicated by white dotted lines, Fig 6.5A). The more basal velocity profile is similar to the typical transmitral flow profile showing the E- and the A-waves. No diastatic flow is observed at this level (red tracing in fig 6.5B). In the more apical location (blue tracing in fig 6.5B) the temporal velocity profile shows 3 waves with the L-wave commencing near E-wave termination. Since these temporal velocity profiles are from the same cardiac cycle and the L-wave is present only in the mid-LV and not near the annulus, it definitively indicates that this L-wave is due to intraventricular recirculating vortex flow rather than transmitral flow during diastasis. The vortex interpretation of the color Doppler M-mode 'flame' pattern in Fig 6.5 has also been made by Pasipoularides [9], who referred to the 'forked E-wave flame' pattern as vortical flow, without characterizing it as a L-wave.

6.4.7 Inference from echocardiography

Thus from the echocardiographic images, we conclude that L-waves can be observed in healthy subjects with diastasis with the sample volume placed in the vicinity of the path of the recirculating vortex ring along the LV long-axis. While in some cases L-waves are a result of diastatic inflow (as seen by a transient bump in the M-mode mitral leaflet separation during diastasis), intraventricular vortexes also generate L-waves. Subject 3 and Subject 9 manifest both mechanisms. In Subject 3, L_{peak} velocity decreases with distance from the annulus consistent with diastatic inflow hypothesis. In Subject 9, the L_{peak} velocity initially increases with distance and then decreases indicating the intraventricular vortex as the cause of these L-waves.

6.4.8 Measuring flow using cardiac MRI

Cardiac PC-MRI was used as an independent imaging modality. The PC-MRI dataset enabled us to track voxels in space and time and thereby characterize vortexes. We performed 2 types of analyses. We tracked streamlines of selected flow elements (virtual particles) during diastole and measured flow velocity for a complete cardiac cycle at a selected fixed location. Tracking streamlines enabled us to visualize the path of individual voxels. An example is shown in Fig 6.6B and is similar to pathlines previously imaged in other studies [8]. The streamlines depended on the initial location of the starting plane and voxels (volume pixels) in the center of the mitral inflow tract primarily moved toward the apex. As observed previously [8] voxels in the periphery of the core inflow tract (on the septal or the lateral side) tended to be entrained in the recirculating vortex and pass through the core inflow tract again.

To replicate pulsed Doppler, we measured flow velocity at a selected fixed location. We found that at specific regions in the LV, the flow pattern was multiphasic and was similar to the transmitral flow pattern with an L-wave (Fig 6.6A). At other locations, a biphasic E-wave was observed indicating that the L-wave was merged with the E-wave. At other locations no L-wave was observed during diastasis indicating either absence of recirculating vortex at that location or signal strength too low to record. The PC-MRI based analysis corroborated the echocardiographic observations regarding temporal velocity profiles and provided additional, independent information on spatial variation of fluid velocities. The PC-MRI data was particularly helpful in characterizing the dynamic flow pattern in the LV and how the occurrence and morphology of L-wave is location dependent. Because we measured flow velocity at a selected fixed location and tracked voxels to determine selected streamlines and because the

presence and imaging of vortexes have been published previously [8, 17] we did not specifically replicate the large-scale structure and features of the known vortexes from the MR data.

6.4.9 L-waves in the right ventricle

Pioneering work by Pasipoularides and coworkers [9, 12-14] has demonstrated the presence of vortexes in the RV during diastole. Blood entering the RV curls behind the tricuspid leaflet tips and form a 3-D vortex. Although the velocities in the RV are lower than the LV and the crescent shaped cross-section of RV is different from the circular LV, the basic fluid mechanics principles governing flow remain the same. Hence, we predict that L-waves due to the recirculating vortex ring should be present in the RV. Moreover, RV L-waves can only be a result of the recirculating vortex mechanism, since there is no upstream chamber which can generate a delayed filling wave, i.e. Keren mechanism. To test our hypothesis we measured diastolic flow in the RV using both echocardiography and PC-MRI. We found that L-waves were present in the RV (Fig 6.7A). We used color M-mode to image flow along the RV long axis. In cardiac cycles with diastasis we found a 3 flame pattern which corresponded to the E-, L- and A-waves. Since the Keren mechanism is not possible in the RV, color M-mode imaging reinforces the idea that recirculating vortex ring passes along the echo scan line and cause a triphasic pattern to be recorded in the RV. In addition, we also used PC-MRI data to compute temporal velocity profiles at selected pixels located in the RV. Fig 6.7B shows a temporal velocity profile with L-wave. As in the LV, recording RV L-waves is keenly dependent on sample volume location and there is a wide variation in the temporal velocity profiles among neighboring fluid elements.

6.4.10 Physiological significance of L-waves

The laws of fluid mechanics require that in response to (pulsatile) flow through a nozzle (mitral orifice and leaflets) vortices be formed downstream, Hence, L-waves can be viewed as a natural

fluid mechanics consequence of diastolic vortex formation. Previous clinical studies investigated L-waves and their correlation with selected pathophysiologic states [2-6, 15]. However none of these studies proposed a causal mechanistic relationship between L-waves and fluid mechanics. Based on our hypothesis we reason that L-waves must occur naturally during filling. Since recirculating vortex flow passing through the echo sample volume is one possible cause of L-waves, its occurrence, location and magnitude would depend on the strength of the vortex ring formed. Thus hearts with a well-developed intraventricular vortex ring are expected to generate higher amplitude L-waves. In a normal LV, L-waves are typically seen in the periphery of the region of mainstream inflow. However, the location and strength of the L-wave depends on the intraventricular vortex dynamics that are in turn influenced by the complexities of local wall motion and by global chamber kinematics and anatomy. An example of this is seen in hypertrophic chambers where the fluid streamlines are constrained by a smaller chamber. In this case the vortex ring is bounded by the smaller chamber wall and the resulting recirculating flow passes through the entire region of mainstream inflow and hence L-waves are more likely to be recorded. This has been observed in cases of both pathologic and physiologic hypertrophy. In contrast, a dilated LV is an impaired suction pump, it generates weak vortices [18] further from the endocardial surface, resulting in a less well-developed vortex ring having lower rotational velocities. The vortex ring dissipates before the leading edge can recirculate and pass through the sample volume at the leaflet tips. Hence in this case presence of a detectable L-wave is less likely. Thus L-waves are related to the strength of the vortex ring and their presence and location also depends on local and global chamber shape, local anatomy (papillary muscle location) and kinematic features.

6.4.11 Limitations

Our proof of concept validation of a new causal mechanism for L-wave generation imaged a modest number (10) of normal subjects. This is mitigated by the causal, fluid mechanics based mechanism that governs filling and is essentially the same in all hearts. However, larger well-defined populations need to be studied to draw definitive conclusions regarding the clinically useful information that resides in L-wave spatio-temporal features, in addition to L-wave presence. Additionally carefully selected patient groups have to be studied to determine the causal relation between L-wave features and pathophysiology.

The imaging modalities used in this study have individual limitations but when used together provide a comprehensive view of intraventricular flow. The main limitation of pulsed Doppler is that it measures velocity in one direction at a single point (2D Doppler) or along a line (color Doppler). Moreover mitral leaflet separation imaged by M-mode echo is not measured simultaneously with flow. This limitation is partly mitigated by color Doppler M-mode which measures flow near the annulus and in the LV simultaneously. PC-MRI provides 3 dimensional, 3 directional velocity information that aids in visualizing and quantifying vortexes. However, it does not provide beat-to-beat variation. Other advanced MR acquisition techniques on the horizon including under-sampled ultrafast acquisitions [19], may allow interrogation of beat-to-beat flow information.

6.5 Conclusion

Clinical studies have correlated the presence of L-waves with selected pathophysiologic groups. From the mechanistic perspective L-waves have been attributed to delayed RV transmitral flow during diastasis. In this work we propose and validate the 'vortex generated L-wave hypothesis'

as an alternate mechanism. Using multi-modal imaging (echocardiography and CMRI) in 10 healthy volunteers we show that recirculating intraventricular vortex flow can be recorded as an L-wave. By suitable placement of the echocardiographic sample volume we observed L-waves in all 10 subjects. Additionally the 'vortex generated L-wave hypothesis' makes three predictions including the presence of L-waves in the RV. These were confirmed by echocardiography and CMRI. Our results explain the mechanism responsible for Type I and Type II L-wave shapes and indicate that L-waves are a natural consequence of vortex related fluid mechanics present in all hearts. Their observation is keenly dependent on echo sample volume location. These mechanistic results facilitate elucidation of the causal relation between L-wave characteristics and pathophysiology.

References:

1. Keren G, Meisner JS, Sherez J, Yellin EL, Laniado S. Interrelationship of mid-diastolic mitral valve motion, pulmonary venous flow and transmitral flow. Circulation. 1986; 74: 36- 44.

2. Ha JW, Ahn JA, Moon JY, Suh HS, Kang SM, Rim SJ, Jang Y, Chung N, Shim WH, Cho SY. Triphasic mitral inflow velocity with mid-diastolic flow: The presence of mid-diastolic mitral annular velocity indicates advanced diastolic dysfunction. Eur. J. Echocardiogr. 2006; 7: 16- 21.

3. Nakai H, Takeuchi M, Nishikage T, Nagakura T, Otani S. The mitral L wave: a marker of advanced diastolic dysfunction in patients with atrial fibrillation. Circ. J. 2007; 71: 1244- 1249.

4. Lam CS, Han L, Oh JK, Ling LH. The mitral L wave: a marker of pseudonormal filling and predictor of heart failure in patients with left ventricular hypertrophy. J. Am. Soc. Echocardiogr. 2005; 18: 336- 341.

5. Gewillig M, Mertens L, Moerman P, Dumoulin M. Idiopathic restrictive cardiomyopathy in childhood. Eur. Heart. J. 1996; 17: 1413- 1420.

6. Hatle L. Doppler echocardiographic evaluation of diastolic function in hypertensive cardiomyopathies. Eur. Heart J. 1993; 14: 88-94.

7. Kovács SJ, McQueen DM, Peskin CS. Modelling cardiac fluid dynamics and diastolic function. Phil. Trans. R. Soc. Lond. A. 2001; 359: 1299- 1314.

8. Heiberg E, Töger J, Kanski M, Carlsson M, Kovács SJ, Söderlind G, Arheden H. Vortex ring formation in the left ventricle of the heart: Analysis by 4D flow MRI and Langrangian Coherent Structures. Annals BME. 2012; 40: 2652- 2662.

9. Pasipoularides A. Heart's vortex: Intracardiac blood flow phenomena. 2010. Shelton CT. People's Medical Publishing House, Ch 14.

10. Nagueh SF, Appleton CP, Gillebert TC, Marino PN, Oh JK, Smiseth OA, Waggoner AD, Flachskampf FA, Pellikka PA, Evangelista A. Recommendations for the Evaluation of Left Ventricular Diastolic Function by Echocardiography. J. Am. Soc. Echocardiogr. 2009; 22:107-133.

11. Garcia MJ, Thomas JD, Klein AL. New Doppler echocardiographic applications for the study of diastolic function. J. Am. Coll. Cardiol. 1998; 32: 865- 875.

12. Pasipoularides, A.D., Shu, M., Womack, M.S., Shah, A., von Ramm, O., Glower, D.D. RV functional imaging: 3-D echo-derived dynamic geometry and flow field simulations. Am. J. Physiol. Heart Circ. Physiol. 284: H56-65, 2003.

13. Pasipoularides, A., Shu, M., Shah, A., Womack, M.S., Glower, D.D. Diastolic right ventricular filling vortex in normal and volume overload states. Am. J. Physiol. Heart Circ. Physiol. 284: H1064-72, 2003.

14. Pasipoularides, A., Shu, M., Shah, A., Tucconi, A., Glower, D.D. RV instantaneous intraventricular diastolic pressure and velocity distributions in normal and volume overload awake dog disease models. Am. J. Physiol. Heart Circ. Physiol. 285: H1956- 65, 2003.

15. Oh JK, Hatle L, Tajik AJ, Little WC. Diastolic heart failure can be diagnosed by comprehensive two-dimensional and Doppler echocardiography. J. Am. Coll. Cardiol. 2006; 47: 500- 506.

16. Kheradvar A, Pedrizzetti G. Vortex formation in the Cardiovascular System. 2012. Springer- Verlag, London. Ch 3.

17. Sengupta PP, Pedrizzetti G, Kilner PJ, Kheradvar A, Ebbers T, Tonti G, Fraser AG, Narula J. Emerging trends in CV flow visualization. J. Am. Coll. Cardiol: Cardiovasc. Img. 2012; 5: 305- 316.

18. Töger J, Kanski M, Carlsson M, Kovács SJ, Söderlind G, Arheden H, Heiberg E. Diastolic vortex ring formation in the human left ventricle: quantitative analysis using Langrangian coherent structures and 4D cardiovascular magnetic resonance velocity mapping. J. Cardiovasc. Mag. Res. 2012; 14: W30.

19. Kozerke S, Tsao J, Razavi R, Boesiger P. Accelerating cardiac cine 3D imaging using k-t BLAST. Mag. Res. Med. 2004; 52: 19- 26.

Chapter 7: Early left ventricular diastolic function quantitation using directional impedances

Abstract

Impedance has been used in vascular biology to characterize the frequency dependent opposition the circulatory system presents to blood flow in response to a pulsatile pressure gradient. It has also been used to characterize diastolic function (DF) via the early, diastolic left ventricular (LV) pressure-flow relation. In a normal LV, early filling volume is accommodated primarily by wall-thinning and ascent of the mitral annulus relative to the spatially fixed apex, (longitudinal chamber expansion). Simultaneously, the endocardial (transverse or short axis) dimension also increases while epicardial (transverse) external dimension remains essentially constant. To quantify these directional filling attributes, we compute longitudinal (Z_L) and transverse (Z_T) impedances during early rapid-filling (Doppler E-wave). Z_L and Z_T were calculated from 578 cardiac cycles of simultaneous transmitral flow and high fidelity LV pressure data in 17 subjects with normal LV function. Average Z_L was 0.7 ± 0.4 mm Hg.s/cm^4 and average Z_T was 238 ± 316 mm Hg.s/cm^2. Direct comparison, in the same units is achieved by computing Z_T over the ≈ 10 cm^2 cross-sectional area of LV (denoted $\check{Z}_T$) revealing that Z_L is ≈ 34 times smaller than $\check{Z}_T$. This quantifies the physiologic preference for longitudinal LV volume accommodation. Lowest Z_L and Z_T values occurred in the 1st harmonic with monotonically increasing values with higher harmonics. We conclude that Z_L and Z_T characterize longitudinal and transverse chamber properties of DF and therefore, diastolic dysfunction can be viewed as a state of impedance mismatch.

7.1 Introduction

7.1.1 Directional anisotropy of LV filling

Left ventricular (LV) filling occurs in response to the development of pressure gradients. As the LV relaxes, LV pressure drops below atrial pressure, the chamber wall recoils faster than it can fill, thereby creating a gradient that aspirates (dP/dV<0) atrial blood into the chamber. The LV myocardium comprises of a helical band [1], which allowed for twisting- untwisting motion [2]. The orientation of the fibers changes transmurally from oblique in subepicardium to circumferential in the center to longitudinal in the subendocardium [3]. This structure allows the creation of greater strain relative to myocyte shortening. It also predicts that the normal LV fills primarily in the longitudinal direction. Hence due to chamber geometry, the LV expands anisotropically as it accommodates the aspirated volume. The LV has two dominant volume accommodating spatial degrees of freedom- longitudinal (base to apex i.e. long-axis) and transverse (radial or short-axis).

The left heart, comprised of the left atrium and the LV, can be kinematically approximated as a (near) constant-volume pump [4]. Accordingly, the atrial and ventricular volumes simultaneously reciprocate so that when LV volume is ejected the atrium fills and vice-versa. The outer (epicardial) surface remains relatively stationary. The LV fills in diastole by thinning of the LV wall and simultaneous ascent of the plane of the mitral annulus. Hence chamber filling dynamics can be decomposed into longitudinal and radial expansion components or volume accommodation properties of the chamber.

7.1.2 Flow impedances to characterize LV filling

LV pressure and flow are oscillatory and these oscillations are out of phase with each other. Most diastolic function (DF) quantification techniques measure either pressures or flow. However, these 2 quantities are related since in the LV pressure causes flow. Hence an index which quantifies both pressure and flow and takes into account their oscillatory nature can provide a more comprehensive characterization of DF. Flow impedance uses both pressure and flow data. Moreover, since impedances are calculated as a function of harmonics, they can capture the oscillatory nature of these 2 signals. The energetics associated with filling can be quantified by evaluating the characteristic impedance of the chamber.

Flow impedances have been previously employed to characterize properties of the aorta and the arterial system. Studies [5-7] have shown that the aortic impedance increased with vascular dysfunction (stiffening) and age. Arterial impedance has also been used to evaluate the power required by the LV to generate the needed pressure gradient [8]. Based on the ability of flow impedances to quantify vascular system properties, Wu et al [9] have applied the concept of impedance analysis to LV filling. They found that LV characteristic impedance increases with higher harmonics, concluding that efficient filling occurred at lower harmonics.

7.1.3 Directional impedances to quantify anisotropy

Total (characteristic) impedance can be decomposed into longitudinal and transverse impedance components. Longitudinal impedance is defined as the resistance to flow in the primary flow direction. It is evaluated using the pressure change in the direction of the flow. Transverse impedance is defined as the resistance to flow in the direction perpendicular (transverse) to flow. It is evaluated using the flow rate change in the direction perpendicular to flow. These directional impedances permit characterization of diastolic function. Hence, in this work, we extend Wu et

148

al's [9] global LV impedance analysis to include directional impedances during early, rapid filling. We compared longitudinal impedance to characteristic impedance and to transverse impedance. The lowest value of impedance reveals the preferred spatial mode of filling. Our analysis can also reveal how longitudinal or transverse impedances may be altered relative to control in response to diastolic dysfunction.

In this work we modified the established expressions for directional and characteristic impedance to compute impedances during early rapid filling using simultaneous cardiac catheterization and Doppler echocardiography data. We hypothesize that transverse and longitudinal impedance will reveal the preferred spatial mode of filling, i.e. filling volume accommodation.

7.2 Methods

7.2.1 Theory: Derivation of directional flow impedances

Flow impedance is defined in analogy to electrical impedance as the ratio of the pressure over flow rate harmonic values. The expressions for input and characteristic impedance are well established [10, 11]. They are assumed to be at the same spatial location, and apply over the cross-sectional area of flow. According to Milnor [10] the input impedance (Z_I) is:

$$Z_I = \frac{P(\omega)}{Q(\omega)}$$

Eq. 7.1

$P(\omega)$ is the Fourier transform of LV pressure and $Q(\omega)$ is the Fourier transform of the flow rate. Z_I is calculated by taking the ratio of the amplitudes at the same harmonic. The longitudinal impedance (Z_L) is defined as the ratio of the spatial pressure gradient and flow rate. Z_L is also

calculated by using the Fourier coefficients of pressure gradient and flow rate. Mathematically the expression is:

$$Z_L = -\frac{1}{Q(\omega)} \times \frac{dP}{dz}(\omega)$$

Eq. 7.2

$dP(\omega)/dz$ is the Fourier transform of the LV pressure gradient. Transverse impedance (Z_T) is defined as the ratio of the pressure to the flow gradient. Z_T is also calculated using the Fourier coefficients of pressure and flow gradient. The equation for Z_T is:

$$Z_T = -\frac{P(\omega)}{dQ(\omega)/dz}$$

Eq. 7.3

$dQ(\omega)/dz$ represents the Fourier transform of the LV flow gradient. Because Z_T has different units from Z_L, direct numerical comparison is facilitated by computing Z_T over the cross-sectional area (≈ 10 cm^2) of the LV where it is measured. This is denoted as Z_T` and is obtained by dividing $Z_T$ by the $\approx 10$ cm$^2$ cross-sectional area of the chamber. $Z_T$` has the same units as Z_L.

7.2.2 Experimental: Subject selection

We selected datasets of 17 subjects (total of 578 cardiac cycles) from our simultaneous echocardiography and cardiac catheterization database. The criteria for selection were: normal ejection fraction (EF > 50%), normal sinus rhythm, absence of wall-motion abnormalities or bundle branch block on the ECG, normal valvular function and clearly identifiable E- and A-waves and E'-waves. All patients underwent elective cardiac catheterization at the request of their referring cardiologist. The data included simultaneous transmitral flow (Doppler E-wave) and high fidelity, micromanometric (MILLAR) multi-transducer LV pressure recording from 2 intraventricular locations. Prior to data acquisition, all subjects provided signed, informed consent for participation in accordance with the Institutional Review Board (Human Research Protection Office) at Washington University School of Medicine.

7.2.3 Data acquisition

Our method of simultaneous echocardiography and high fidelity LVP data acquisition during cardiac catheterization has been previously detailed (Chapter 2) and [12-14]. Briefly, transthoracic echocardiography was performed in accordance with American Society of Echocardiography (ASE) criteria [15] by a certified sonographer prior to arterial access in the catheterization laboratory. We used a 6F micromanometer-tipped pigtail (triple pressure transducer) pressure-volume, conductance catheter (Model 560-1, 560-5, Millar Instruments, Houston, TX) which was directed into the mid-LV in a retrograde fashion across the aortic valve under fluoroscopic control to measure intracardiac pressures and volumes. The pressures were sampled at 250 Hz and fed to the catheterization laboratory amplifier (Quiton Q-Cath Physiological Recording System) and simultaneously into the input ports of the physiological amplifier of the Doppler imaging system for synchronization (Philips iE33). The LV and AO (aortic) pressures and one ECG channel were also simultaneously recorded on disk in digital format using our multichannel Physiologic Data acquisition system. With the catheter in the LV, Doppler E-and E'- waves were recorded using the apical 4-chamber view. High fidelity pressure and Doppler transmitral flow data were synchronized and analyzed off-line using custom software. Pressure-flow synchronization was achieved through the alignment of a fiducial pressure square-wave sent to both echocardiographic and pressure signals during data acquisition. The flow chart for data acquisition and processing is shown in Fig 7.1A. Fig 7.1B shows the schematic of the LV with the approximate position of the pressure transducers and the Doppler sample volume position.
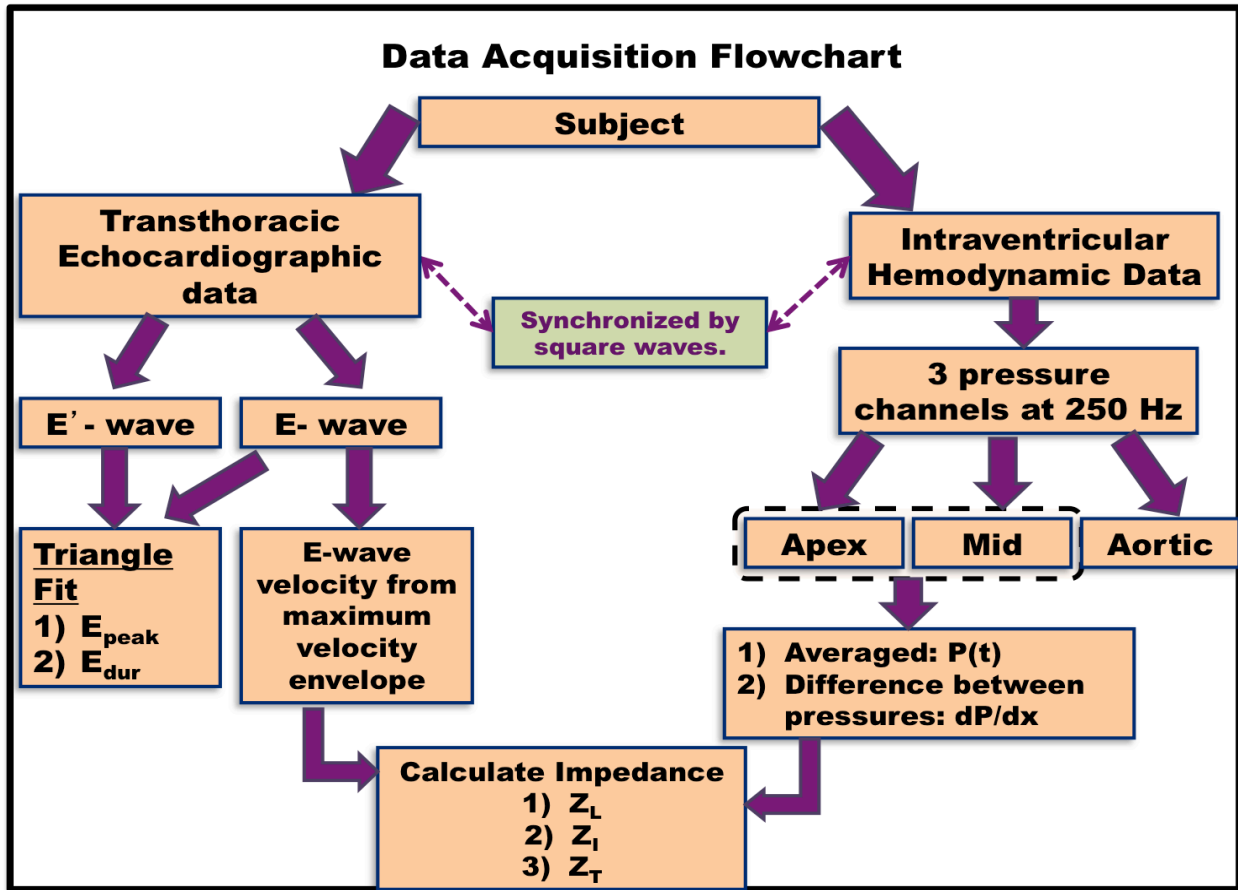
Fig 7.1: (A) Data acquisition flowchart including data processing and impedance calculation steps.
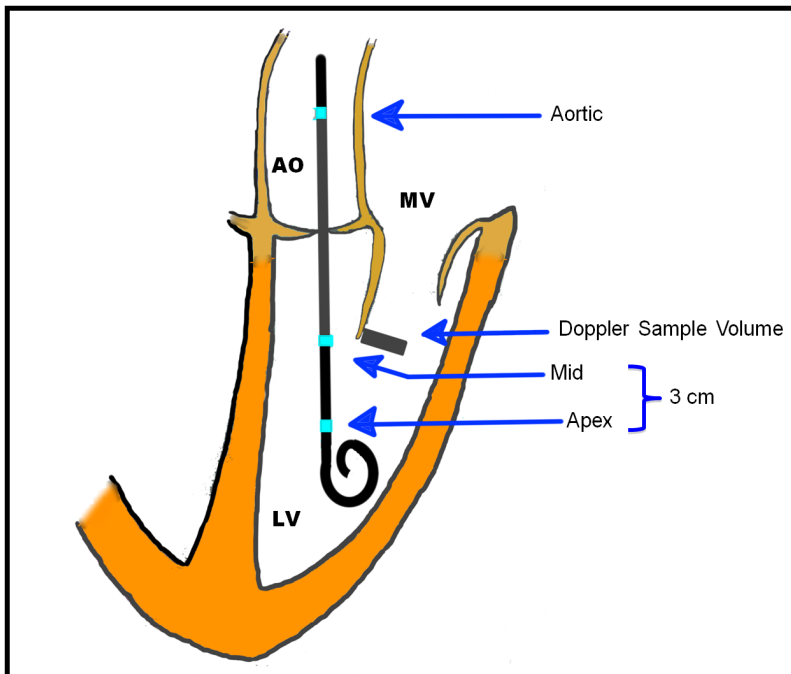
Fig 7.1: (B) Schematic of LV with the catheter showing approximate transducer position and location of the echo sample volume. LV = Left ventricle, MV = Mitral Valve, AO = Aortic Outflow Tract. The 3 transducer positions are marked as aortic, mid and apex. See text for details.

7.2.4 Hemodynamic data analysis

Pressure was processed via a custom Matlab script (Matlab 6.0; MathWorks, Natick, MA). Data sets were smoothed digitally using a five-point average to suppress noise in the derivative (See Chapter 2) [12, 16], attenuating 50% of signal at 40 Hz and 90% above 60 Hz, followed by calculation of continuous dP/dt vs. time t from the smoothed data. For each beat, LV end-diastolic pressure (LVEDP) and peak negative dP/dt denoted $(dP/dt)_{min}$ were extracted from the pressure phase-plane (dP/dt vs. P axes; PPP) or equivalent time-domain contours for both pressure signals.

7.2.5 Echocardiographic data analysis

The features of Doppler E-waves and tissue Doppler E'-waves were determined using standard methods [17]. E-wave peak (E_{peak}) denotes maximum wave height and E_{dur} denotes E-wave duration. The same notation is used for the Doppler E'-wave features, E'_{peak} and E'_{dur}. Digitized maximum velocity envelope (MVE) of E-wave images (MVE), sampled at 4 ms intervals were stored and provided instantaneous E-wave velocity as a function of time. Volumetric flow rate was calculated as the product of instantaneous E-wave velocity and effective mitral orifice cross-sectional area, which, as previously [18, 19] was approximated as constant (4 cm^2).

7.2.6 Synchronizing pressure flow data

To match Doppler E-waves with their simultaneous pressure contour, a fiducial marker was used. A square wave was created in the distal pressure channel which was recorded both in the hemodynamic data and in the echocardiographic image. During processing, the time point of the start of the square wave in the hemodynamic data and the time point as seen on the video containing echocardiographic images were matched. The time axis of the pressure dataset was changed to the linked time of the video. To synchronize individual images, a custom MATLAB

script was written which matched the ECG R peak index (in the pressure dataset) to the time point of ECG R peak index (in the echocardiographic image). Thus for each Doppler E-wave we obtained the simultaneous pressure values.

7.2.7 Calculation of directional impedance

The spatial pressure gradient is the difference in readings between the two pressure sensors on the micromanometric pigtail catheter in the LV, divided by the 3 cm distance between them. The volumetric flow rate (cm^3/sec) is calculated as noted above. Using pressure and flow rate, Z_I is computed according to Eq 7.1. Fourier transform of pressure gradient and the flow rate provide Z_L. However, the data acquisition format is not suited for computing the longitudinal flow gradient ($dQ(\omega)/dz$) (since flow is measured at only one location). Hence to calculate Z_T, we used the standard expression that relates the characteristic impedance Z_C to the spatial impedances [10]:

$$Z_C = \sqrt{Z_L \times Z_T}$$

Eq. 7.4

This relationship stems from the Moens-Koerteweg equation for pulse wave velocity. The derivation is straight forward [20]. By definition, characteristic impedance is $Z_C = \rho c/A$, where c, is flow velocity, ρ is blood density and A is vessel (i.e. LV) area. From the Moens-Koerteweg equation, $c = \sqrt{[A/\rho C_A]}$ where C_A is area compliance, yielding $Z_C = \rho/A \cdot \sqrt{[A/\rho C_A]} = \sqrt{[(\rho/A) \cdot (1/C_A)]}$ But, by definition, $1/C_A$ is proportional to transverse impedance Z_T and ρ/A is proportional to longitudinal impedance Z_L hence $Z_C = \sqrt{[Z_L \cdot Z_T]}$.

A custom MATLAB program (Matlab 6.0; MathWorks, Natick, MA) aligned fiducially phase locked E-waves with the simultaneous pressure data as described above. Impedances were calculated according to Eq 7.1, 7.2 and 7.4. For every beat, the 0th harmonic (resistance) and the first 4 harmonics (1st, 2nd, 3rd and 4th) of Z_L, Z_T and Z_I were calculated and saved in a separate file

for each subject. The phase angle of Z_I (θ), denoting the phase difference between pressure and flow and the power at each harmonic given by the product of the pressure harmonic and the flow rate harmonic.

7.2.8 Statistical analysis

We compared impedance, propagation coefficient and power to conventional DF metrics such as E-wave DT (deceleration time), and E/E'. Differences among the amplitudes at different harmonics were tested for significance using 1-way analysis of variance (ANOVA). A p-value of less than 0.05 was considered statistically significant. We used Pearson's correlation coefficient (R^2) to determine the correlation between variables.

Parameters	Mean ± SD
Age (yrs)	61 ± 11
Gender	9 M/ 8 F
Weight (lbs)	175 ± 27
Height (cm)	168 ± 9
Maximum LV pressure(mm Hg)	136 ± 24
End diastolic pressure (mm Hg)	14 ± 3
EF (%)	66 ± 10
Heart Rate (bpm)	63 ± 10
No. of beats analyzed	36 ± 13

Table 7.1: Group (n=17) demographics.

7.3 Results

The average age of 17 subjects (9 male) was 61 years (range: 46-79 years). All subjects had normal ejection fraction (> 50%). The subject demographics are shown in Table 7.1.

7.3.1 Trends in impedance values

The 0th harmonic, $Z_L(0)$, $Z_T(0)$ and $Z_I(0)$ is the purely resistive (i.e. DC) component of the pressure-flow relation. The mean values of the 0th and the first 4 harmonics are given in Table 7.3 with p-values for inter-harmonic comparison of each type of impedance using 1-tailed ANOVA. The lowest impedance globally, and in each direction was observed in the 1st harmonic while the subsequent harmonics had monotonically increasing values. Fig 7.2 shows the magnitude of the 3 impedances in the first 3 harmonics. For all 3 impedances there was a statistically significant increase in amplitudes with increasing harmonics (ANOVA, $p<0.05$). The standard deviation of Z_T was larger than the mean due to large inter-subject variation. In addition the phase difference between pressure and flow rate (θ) from the argument of Z_I for the 1st and 2nd harmonics is: $\theta(1) = 1.4 \pm 0.7$ rad and $\theta(2) = 1.3 \pm 0.4$ rad.
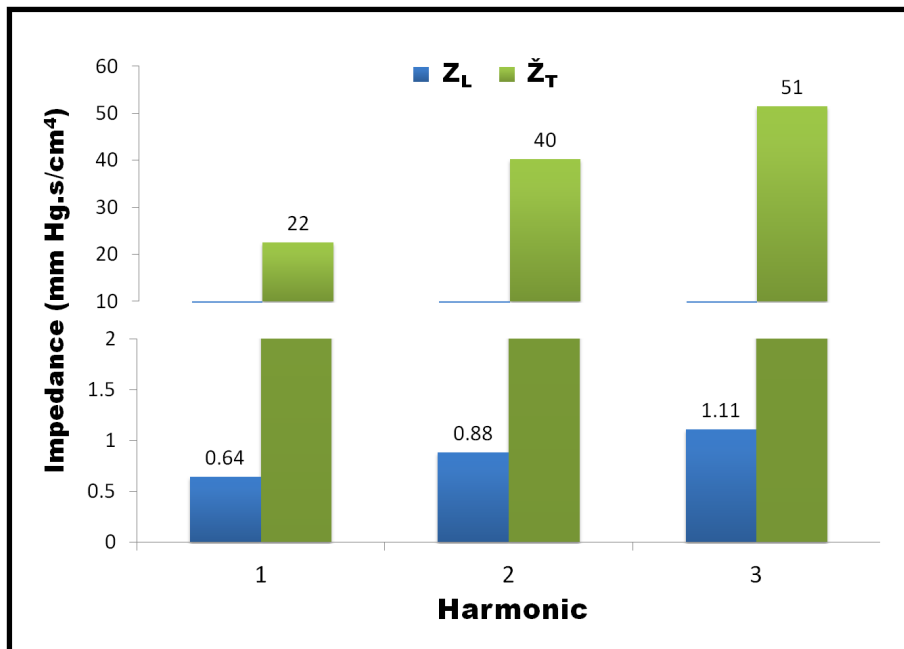
Fig 7.2: Comparison between longitudinal and {cross sectional area connected) transverse impedance amplitudes for the 1st 3 harmonics. Numbers above bars represent mean values. See text for details.

We calculated the total power (P_{total}) at each harmonic. The maximum power amplitude resided at the 0th harmonic and the power decreased sharply with increasing harmonics. The mean values were: $P_{total}(0) = 0.88$ W, $P_{total}(1) = 0.03$ W and $P_{total}(2) = 0.01$ W (Fig. 7.3).
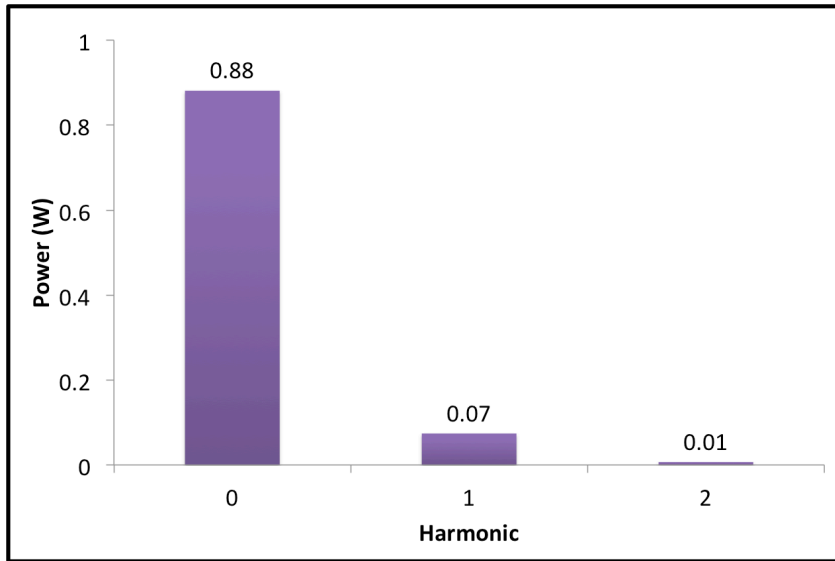
Fig 7.3: Power, averaged for all 17 subjects in the 0th, 1st and 2nd harmonics. See for text details.

7.3.2 Correlation with Doppler echocardiographic indexes

Parameters	Mean ± SD
E_{peak} (cm/s)	65 ± 13
E_{dur} (ms)	297 ± 64
DT (ms)	224 ± 67
A_{peak} (cm/s)	70 ± 18
E'_{peak} (cm/s)	10 ± 3
E/A	1 ± 0.3
E/E'	7.2 ± 2.6

Table 7.2: Echocardiographic parameters

Doppler E-wave mean values were: E_{peak} =65 cm/s and E_{dur} =297 ms (Table 7.2). We compared the 3 first harmonics of the impedances to E_{peak} and E_{dur}. While none of the 3 impedances had a significant correlation with E_{peak}, they had a negative correlation with E_{dur}. $Z_L(1)$ with E_{dur} had R^2 = 0.22, $Z_I(1)$ with E_{dur} had $R^2 = 0.22$ and $Z_T(1)$ with E_{dur} had R^2 = 0.06.

157

We calculated the 0th, 1st and 2nd harmonic power amplitudes and compared it to E_{peak}. We found that P_{total} had a significant positive correlation with E_{peak} (P_{total} (0), $R^2 = 0.62$; P_{total} (1),
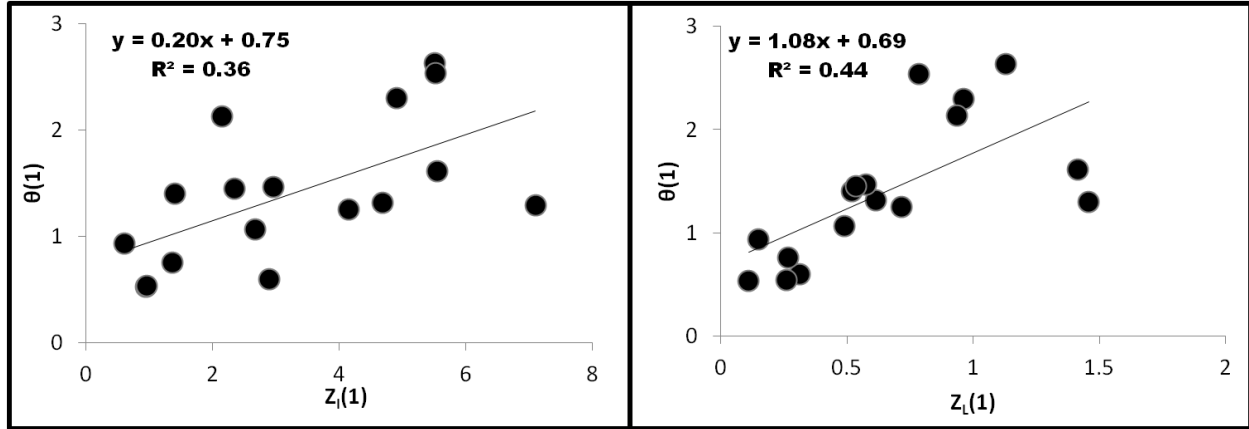
Fig 7.4: The phase difference between pressure and flow rate in the 1st harmonic for input impedance (left) and longitudinal impedance (right). See text for details.

$R^2 = 0.56$; P_{total} (2), $R^2 = 0.21$). The phase difference (θ) was compared to the impedance magnitude. Both $Z_L(1)$ ($R^2 = 0.44$) and $Z_I(1)$ ($R^2 = 0.36$) had a positive correlation with $\theta(1)$ (Fig. 7.4).

7.4 Discussion

7.4.1 Directionality of LV filling

Normal LV filling occurs in response to the rapid development of an atrioventricular pressure gradient created by chamber relaxation and recoil (mechanical suction) [21, 22]. The expanding endocardial chamber accommodates the incoming volume by expanding longitudinally (along the LV long axis) and radially (along the short axis) in accordance with (near) constant volume 4-chamber heart physiology [4]. Due to the helically woven nature of the LV chamber wall [2], the longitudinal expansion accommodates most of the inflowing volume [23]. As the chamber expands longitudinally, the wall simultaneously thins, generating expansion of the chamber's internal

transverse dimension thereby allowing for 'transverse' accommodation of a portion of the inflowing volume. The relation between longitudinal and (endocardial) radial wall motion is a key feature of DF. Previous DF quantitation methods mostly employed echocardiography based flow rate or wall-motion derived indexes (strain, strain rate) or invasive hemodynamic data. One limitation imposed by the use of only hemodynamic or flow rate (echo) or wall-motion (strain rate) data is that the interaction between pressure and flow remains hidden. Impedance analysis resolves this limitation and also provides phase information by quantifying the spatio-temporal interaction between pressure and flow.

7.4.2 Previous studies

In the LV, the flow rate is not only dependent on the instantaneous pressure but also on pressure and flow at previous time points (due to inertia and LV chamber properties). Flow impedances have been used in vascular biology to characterize vessel properties such as viscoelasticity and stiffness. Milnor [24] characterized ventricular afterload using aortic impedance. Murgo et al [25] calculated aortic input impedance in humans and found that the pressure waveforms were correlated with input impedance. Aortic and pulmonary arterial impedance has been calculated in humans and experimental animals [26, 27] and it has been shown to be influenced by age, physiologic stimuli, disease and pharmacologic interventions [28-30]. More recently, Yano et al [31] showed that aortic wave reflection influenced LV relaxation and coronary flow.

Because pulsatile flow in an elastic vessel involves pulse wave propagation along the vessel and change in vessel cross sectional area, characteristic impedance is naturally resolved into directional components as in Eq. 7.4. Impedance depends on the local properties of the vessel and the blood. While input impedance (Z_I) characterizes flow at the input to the vessel, Z_L represents the local vessel properties (inertance and resistance) [32]. Curi et al [32] have shown that

Z_L is not influenced by the impedance of the downstream vascular bed. Transverse impedance (Z_T) - the ratio of pressure to axial flow gradient, accounts for radial (transverse) displacement of blood due to cross sectional area change in an elastic vessel in response to pulsatile pressure [10], thereby reflecting elastic properties (compliance) of the vessel wall [33].

Impedance as a LV DF metric was first proposed in 1999 [34, 35]. Subsequently, the input impedance concept was extended to LV filling by Wu et al [9]. Characteristic and input impedance of the LV during early filling (E-wave) using simultaneous echocardiography and cardiac catheterization data (Eq. 7.1) was calculated. They found that E-waves manifesting the delayed relaxation pattern (prolonged DT > 220msec) showed increased phase differences between pressure and flow relative to normal, revealing a sub-optimal pressure-flow relationship. Subsequently, Wu and Kovács [36] investigated the relationship between increasing harmonics and E-wave deceleration time. In addition, De Mey et al [37] have proposed a method for the non-invasive estimation of Z_L in LV using echocardiography and used it to analyze data from a pulse/flow duplicator.

7.4.3 Trends in impedance values

We computed the 0th harmonic (resistance) and the first four harmonics for all 3 impedances for every analyzed beat in every subject (total beats analyzed = 578). We found that Z_L was lower than Z_I, which was lower than Z_T ($Z_L < Z_I << Z_T$, Fig 2) in every subject. Although, the 3 impedances have different dimensions ([P/Q] vs. [(P/cm)/Q] vs. [P/(Q/cm)]) comparing these quantities has value since they quantify the inertance and compliance aspects of the same physical phenomenon i.e. early diastolic filling (chamber recoil) and, therefore they are not independent as seen in Eq. 7.4. In the specific setting of early rapid filling, direct comparison of Z_L and Z_T is facilitated by taking into account the effective cross-sectional (approx. 10 cm^2) area

of the chamber. When considered in that light, the units of Z_L and $\check{Z}_T$ are the same and $\check{Z}_T$ dominates Z_L by a factor of 34. Moreover, directional features of LV filling have been studied previously using other imaging modalities [23, 38]. These studies have also shown that longitudinal volume accommodation is the dominant mode of LV filling.

The trend in harmonic variation of Z_L and Z_T amplitudes showed that in both the directions the impedance amplitude was lowest in the first harmonic and then increased with higher harmonics (Table 7.3). This was similar to the trends seen in Z_I, which was also lowest at the 1st harmonic and then increased steadily with higher harmonics in all the subjects. The input resistance (0th harmonic) should be viewed as the resistance of the process if it were nonpulsatile. In both the directions, the resistance was higher in value than the 1st harmonic. Earlier work by Wu et al [9] noted a similar trend in Z_I. In addition, De Mey et al [37] calculated Z_L and found that Z_L was lowest in the 1st harmonic and increased subsequently. Our results agree with these previous

	0th	1st	2nd	3rd	4th	p-value
Z_I (mm Hg. s/cm^3)	16±7	3±2	5±3	6±4	7±5	p<0.001
Z_L (mm Hg. s/cm^4)	1.3±0.9	0.7±0.4	0.9±0.6	1.1±0.8	1.4±0.9	0.022
Z_T (mm Hg. s/cm^2)	4623±7313	238±316	426±567	545±582	584±683	p<0.001
$\check{Z}_T$ (mm Hg. s/cm^4)	462±731	22±31	40±56	51±58	55±68	p<0.001

Table 7.3: Impedance values. The average value of input (Z_I), longitudinal (Z_L) and transverse impedance (Z_T and Z_T`) for the 0th – 4th harmonics for all 17 subjects and standard deviations. The last column shows p-value for inter harmonic comparison of each type of impedance via single tailed ANOVA. See text for details.

studies. The trend in Z_L shows that for a given pressure gradient (dP/dz) in the LV, the flow rate (Q) decreases with increase in harmonics. In the transverse direction, our results indicate that the pressure required to generate a given axial flow gradient (dQ/dz), is higher in higher harmonics.

161

Power was calculated as the product of pressure and flow rate amplitude for each harmonic. It was highest at the 0th harmonic (resistive component) and decreased with higher harmonics (Fig 7.3) indicating that the maximum filling power is generated when the pressure and flow rate have no phase difference. By definition, the 0th component has no phase difference between P and Q. The phase difference between P and Q manifests with the first harmonic (1.4 rad) and partly explains the observed reduction of oscillatory power at higher harmonics. In addition, the amplitude of P and Q both were highest in the 0th harmonic and decreased with higher harmonics. This trend is in concordance with findings of Wu et al [9].

7.4.4 Connection between impedances and E-wave parameters

We compared impedances to conventional echocardiographic parameters- E_{peak} and E_{dur}. The correlation with E_{peak} was insignificant for all the three impedances. When compared to E_{dur}, the first harmonic of Z_L and Z_I both were well correlated ($R^2 = 0.44$, $R^2 = 0.36$) with a negative slope. This indicates that as the duration of the E-wave increased the amplitude of impedance decreased in the first harmonic.

Power had a strong positive correlation with E_{peak} in the steady state ($R^2 = 0.62$), 1st ($R^2 = 0.56$) and 2nd ($R^2 = 0.21$) harmonic. The phase difference between pressure and flow rate (θ) was calculated as the argument of Z_I. For the 0th term (steady state) $\theta(0) = 0$. The phase difference, $\theta(1)$ had a positive correlation with both $Z_I(1)$ and $Z_L(1)$ indicating that as the phase difference increases, the magnitude of impedance also increases (Fig. 7.4). Because mechanical suction (dP/dV<0) initiates LV filling, P leads Q. Hence the phase difference between P and Q is positive. This is in contrast to the sign of the phase in vascular physiology where the vessel wall is passive and flow causes local pressure variations hence the flow leads the pressure. Thus in arterial impedance the phase difference is typically negative [39, 40] for the first few harmonics.

7.4.5 Significance of flow impedances in DF

This study uses directional flow impedances to quantify volume accommodation in spatial terms. We found that longitudinal filling is preferred over transverse. In the 0th harmonic, Z_L is more than 300 times smaller than $\check{Z}_T$ and in next higher harmonics the trend is similar (Fig. 7.2, Table 7.3). Imaging studies indicate that longitudinal volume changes dominate transverse volume changes in the LV [23, 38]. Our method provides a pressure-flow relation derived index rather than a wall motion or volume imaging based measurement to quantify the anisotropy. In addition, similar to the harmonic trends reported in Z_I [9], we found that impedance in both directions is lowest in the first harmonic and it increases subsequently. This shows that for higher harmonics to achieve the same flow rate a larger pressure gradient is needed, and for the same flow gradient larger pressure amplitude is needed. Novel insight in quantifying filling in terms of impedance is provided by the phase information. It was positively correlated with both Z_L and Z_I showing that a larger θ corresponded to larger impedance. Additionally the variation in power harmonics (Fig 7.3) is expected from the trends in pressure and flow rate amplitudes. As expected power was strongly positively correlated with E_{peak}.

This work introduces and advances the method for quantifying diastolic function via directional LV filling in terms of Z_L and Z_T. Additionally, power, Z_L and Z_T correlate with conventional Doppler echocardiographic indexes such as E_{peak}, E_{dur} indicating that Z_L and Z_T can quantify changes in DF. Although this study did not specifically compare how impedance is altered in subjects with diastolic dysfunction (DD), Courtois et al [41] have shown that spatial intraventricular pressure gradients – the determinant of Z_L – are impaired after infarction. We therefore expect impedances to reflect dysfunction, but future studies in selected clinical pathologic groups are needed to quantify the extent to which directional impedances are altered

in the setting of dysfunction. Another pathophysiologic state effecting directional flow impedances is mitral valve disease. Mitral valve disease (stenosis for example) would alter effective mitral orifice area and pressure as a function of time. It would therefore significantly modify the incoming velocity profile spatially and temporally. This would alter associated impedance values. The measurement of the effect of mitral valve disease on directional impedances should be part of studies specifically aimed at characterizing pathologic states.

7.4.6 Limitations

In order to compute Z_L and Z_T from clinical data some approximations were required. Ideally pressure and flow measurement should be at the same location, however, in the LV, pressure is measured via a catheter aligned along the long-axis along the outflow tract with 2 pressure transducers whose position with respect to the echo sample volume at the mitral leaflet tips is close but not exactly the same (Fig 7.1B). Hence, the approximate co-location of pressure and flow sampling introduces a systematic error. The large number of beats analyzed and the fact that pressure and flow are measured simultaneously mitigates this to an acceptable degree. Moreover, we calculated the pressure gradient as the difference of pressures measured at 2 locations in the LV divided by the distance between them (3 cm). While the pressure gradient could be, and has been alternately calculated from color M-mode Doppler [42], the accuracy and fidelity of the color M-mode method depends on the image processing methods used to convert the velocity field into pressure gradient field. Our methods were not suitable for direct calculation of the spatial flow gradient, thus, Z_T was calculated from Eq. 4 relating Z_L and Z_T to Z_C. Z_C and Z_I are related via the reflection coefficient [10]. The major assumptions related to the Moens- Korteweg (from which Eq. 7.4 is derived) are that the vessel surrounding the fluid be thin- walled, linearly elastic, isotropic and homogenous. Clearly none of these conditions are fulfilled by the LV. Nevertheless

we can to a first approximation apply this equation for our purposes of estimating transverse impedance. The method for reflection coefficient computation from LV pressure has been previously provided by Wu et al [9].

As is customary, [19, 36] to compute volumetric flow rate we assumed a constant effective mitral valve area of ≈ 4 cm^2 since the normal mitral valve area is $\approx$ 4-5 sq. cm [18]. Treating the effective valve area as constant for all subjects instead of measuring effective orifice area (EOA) or geometric orifice area (GOA) by echo in each subject can have a slight effect on the amplitudes. However the Fourier derived frequency information will not change since EOA or GOA variation is a passive response to the flow (E-wave), assuring that valve area itself (i.e. valve leaflet separation that determines EOA/GOA) is not an independent frequency source.

We calculate and compare Z_L to Z_T. Although these 2 indexes have different units comparison remains meaningful [33] because these indexes quantify the 2 components of impedance. Hence contrasting Z_L to Z_T compares inertance and compliance effects. The legitimate concern regarding direct comparison of impedances having different units can be addressed two independent ways, arriving at the same conclusions. Z_T and Z_L will have the same units if Z_T is computed for the ≈ 10cm^2 cross section of the LV chamber cavity. This decreases Z_T values by a factor of 10 – but maintains the significant difference between Z_T and Z_L Alternatively, one could opt to express Z_L as previously [32], as the pressure difference over flow ($\Delta P/Q$) and Z_T as the ratio of pressure over longitudinal flow difference ($P/\Delta Q$). This choice assures that both Z_L and Z_T have the same units as Z_C. Mathematically this definition would increase Z_L by a factor of 3 (since pressure gradient was obtained by dividing the pressure difference by 3, the distance in cm between transducers) and a decrease in Z_T by a factor of 3. From Table 7.3 it is evident that Z_L is more than 3 times smaller than Z_I and Z_T is more than 3

times larger than Z_L. (Note this approximation is essentially the same as dividing Z_T by 10 cm^2 as noted above) Hence, had we selected either of these alternate expressions spatial impedance units would be the same, while keeping the conclusions regarding the dominance of Z_T over Z_L intact.

7.5 Conclusions

We compute longitudinal and transverse flow impedance (Z_L and Z_T) in humans from in-vivo data to quantify DF via the propensity for longitudinal vs. transverse volume accommodation. Since the resistive (0th harmonic) component of Z_L is nearly 300 times smaller than $\check{Z}_T$ and more than 34 times smaller in the 1st harmonic, our results show that longitudinal volume accommodation is nature's preferred solution to the atrium-to-ventricle mass transfer problem in early diastole. We also calculated Z_L and Z_T amplitudes up to the 4th harmonic and found that the 1st harmonic had the lowest impedance with magnitudes significantly increasing with increasing harmonics. Power had a strong positive correlation with E_{peak}. The phase difference, indicating that pressure leads flow, revealed that higher θ corresponds to higher impedance values (worse DF). Hence directional flow impedances provide a novel method of quantifying DF. This approach advances our understanding of the physiology of normal diastole and suggests that, relative to normal, diastolic dysfunction is a state of impedance mismatch.

Reference:

1. Torrent- Guasp F. Sobre morfologia y funcionalismo cardiocos. *Re. Esp. Cardiol*. 1967; 20:14.

2. Buckberg G, A Mahajan, S Saleh, JI Hoffman, and C Coghlan. Structure and function relationships of the helical ventricular myocardial band. J Thorac Cardiovasc Surg 136: 578-89, 89 e1-11, 2008.

3. Ho SY. Anatomy and myoarchitecture of the left ventricular wall in normal and in disease. *Eur. J. Echocardiogr*. 2009; 10: iii3-iii7.

4. Bowman AW, Kovács SJ. Assessment and consequences of the constant- volume attribute of the four- chambered heart. *Am. J Physiol. Heart Circ. Physiol*. 2003; 285(5): H2027-33.

5. O'Rourke MF. Vascular Impedance in Studies of Arterial and Cardiac Function. *Physiol. Rev*. 1982; 62;1;570-623.

6. Yin FCP, Weisfeldt ML, Milnor WR. Role of aortic input impedance in the decreased cardiovascular response to exercise with aging in dogs. *J. Clin. Invest*. 1980; 68: 28- 38.

7. Sweitzer NK, Palta M, Shenoy M, LeCaire T, Stein JH, Mitchell GF, Keles S. Increases in central aortic impedance precede alterations in arterial stiffness measures in Type 1 diabetes. *Diabetes Care*. 2007; 30(11): 2886- 2891.

8. Pahlevan NM, Gharib M. Low pulse pressure with high pulsatile external left ventricular power: Influence of aortic waves. *J Biomechanics*. 2011; 44: 2083- 2089.

9. Wu Y, Bowman AW, Kovács SJ. Frequency- based analysis of diastolic function: The early rapid filling phase generates negative intraventricular wave reflections. *Cardiovasc. Engg*. 2005; 5(1): 1- 12.

10. Milnor WR. *Hemodynamics*. Baltimore, MD: Williams & Wilkins.

11. Nichols W, M O`Rourke. *McDonald's Blood Flow in Arteries*. London: Hodder & Arnold, 2005.

12. Chung CS, Ajo DM, Kovács SJ. Isovolumic pressure-to-early rapid filling decay rate relation: model-based derivation and validation via simultaneous catheterization echocardiography. *J. Appl. Physiol.* 100: 528-34, 2006.

13. Hall AF, Kovács SJ. Automated method for characterization of diastolic transmitral Doppler velocity contours: early rapid filling. *Ultrasound Med. Biol.* 20: 107-16, 1994.

14. Hall AF, Nudelman SP, Kovács SJ. Evaluation of model-based processing algorithms for averaged transmitral spectral Doppler images. *Ultrasound Med. Biol.* 24: 55-66, 1998.

15. Nagueh SF, Appleton CP, Gillebert TC, Marino PN, Oh JK, Smiseth OA, Waggoner AD, Flachskampf FA, Pellikka PA, Evangelista A. Recommendations for the evaluation of left ventricular diastolic function by echocardiography. *Eur. J Echocardiogr*. 10: 165-93, 2009.

16. Shmuylovich L, Kovács SJ. Stiffness and relaxation components of the exponential and logistic time constants may be used to derive a load-independent index of isovolumic pressure decay. *Am. J Physiol. Heart Circ. Physiol.* 295: H2551-9, 2008.

17. Appleton CP, Firstenberg MS, Garcia MJ, Thomas JD. The echo- Doppler evaluation of left ventricular diastolic function. *Cardiol. Clin*. 18: 513- 546, 2000.

18. Baumgartner H, Hung J, Bermejo J, Chambers JB, Evangelista A, Griffin BP, Iung B, Otto CM, Pellikka PA, Quiñones M. Echocardiographic assessment of valve stenosis: EAE/ ASE Recommendations for clinical practice. *J. Am. Soc. Echocardiogr*. 22 (1): 1-23; 2009.

19. Ghosh E, Shmuylovich L, Kovács SJ. Vortex formation time- to- left ventricular early rapid filling relation: model-based prediction with echocardiographic validation. *J Appl. Physiol*. 109: 1812- 9, 2010.

20. Westerhof N, Stergiopulos N, Noble MIM. Snapshots of Hemodynamics. 2nd Edition. Springer 2010.

21. Katz LN. The role played by the ventricular relaxation process in filling the ventricle. *Am. J. Physiol*. 95: 542–553, 1930.

22. Robinson TF, Factor SM, Sonnenblick EH. The heart as a suction pump. *Sci. Am*. 254(6): 84- 91; 1986.

23. Carlsson M, Ugander M, Heiberg E, Arheden H. The quantitative relationship between longitudinal and radial function in left, right, and total heart pumping in humans. *Am. J. Physiol. Heart Circ. Physiol*. 293: H636-44, 2007.

24. Milnor WR. Arterial impedance as ventricular afterload. *Circ. Res*. 36: 565- 70, 1975.

25. Murgo JP, Westerhof N, Giolma JP, Altobelli SA. Aortic input impedance in normal man: relationship to pressure wave forms. *Circulation* 62: 105-16, 1980.

26. Avolio AP, O'Rourke MF, Mang K, Bason PT, Gow BS. A comparative study of pulsatile arterial hemodynamics in rabbits and guinea pigs. *Am. J Physiol*. 230: 868-75, 1976.

27. Merillon JP, Fontenier GJ, Lerallut JF, Jaffrin MY, Motte GA, Genain CP, Gourgon RR. Aortic input impedance in normal man and arterial hypertension: its modification during changes in aortic pressure. *Cardiovasc. Res*. 16: 646-56, 1982.

28. Eaton GM, Cody RJ, Binkley PF. Increased aortic impedance precedes peripheral vasoconstriction at the early stage of ventricular failure in the paced canine model. *Circulation* 88: 2714-21, 1993.

29. Pepine CJ, Nichols WW. Aortic input impedance in cardiovascular disease. *Prog. Cardiovasc. Dis.* 24: 307-18, 1982.

30. Yin FCP, Weisfeldt ML, Milnor WR. Role of aortic input impedance in the decreased cardiovascular response to exercise with aging in dogs. *J. Clin. Invest.* 68: 28-38, 1981.

31. Yano M, Kohno M, Kobayashi S, Obayashi M, Seki K, Ohkusa T, Miura T, Fujii T, Matsuzaki M. Influence of timing and magnitude of arterial wave reflection on left ventricular relaxation. *Am. J. Physiol. Heart Circ. Physiol.* 280: H1846-52, 2001.

32. Curi MA, Skelly CL, Quint C, Meyerson SL, Farmer AJ, Shakur UM, Loth F, Schwartz LB. Longitudinal impedance is independent of outflow resistance. *J. Surg. Res.* 108: 191-7, 2002.

33. Westerhof N, Stergiopulos N, Noble MIM. Snapshots of Hemodynamics. Appendix 3 and 4. 2nd Edition. Springer 2010.

34. Milde J, Sessoms M, Lisauskas J, Bowman AW, Courtois M, Kovács SJ. Ventricular Diastolic Impedance: A New Index of Global Diastolic Function. *J. Am. Coll. Cardiol.* 53, 2000.

35. Milde J, Sessoms M, Lisauskas J, Courtois M, Kovács SJ. Validation of a New, Model-Based Image Processing Derived Index of Global Diastolic Function. *Proc. 1st Joint BMES/ EMBS Conference*, 1999.

36. Wu Y, Kovács SJ. Frequency-based analysis of the early, rapid- filling pressure-flow relation elucidates diastolic efficiency mechanisms. *Am. J Physiol. Heart Circ. Physiol*. 291: H2942- H9, 2006.

37. De Mey S, Dumont K, Geeraerts J, Vandervoort P, Verdonck P. Non-invasive assessment of left ventricular longitudinal impedance using color M-mode Doppler echocardiography. *Computers in Cardiology* 27: 17-20, 2000.

38. Toger J, Carlsson M, Soderlind G, Arheden H, Heiberg E. Volume Tracking: A new method for quantitative assessment and visualization of intracardiac blood flow from three-dimensional, time-resolved, three-component magnetic resonance velocity mapping. *BMC Med Imaging* 11: 10, 2011.

39. O'Rourke M F, Taylor M. Vascular Impedance of the femoral bed. *Circ. Res*. 18: 126-39, 1966.

40. O'Rourke MF. Pressure and flow waves in systemic arteries and the anatomical design of the arterial system. *J. Appl. Physiol*. 23: 139-49, 1967.

41. Courtois MR, Kovács SJ, Jr., Ludbrook PA. Physiologic early diastolic pressure gradient is lost during acute myocardial ischemia. *Circulation*, 81, 1688-1696, 1990.

42. Greenberg NL, PM Vandervoort, MS Firstenberg, MJ Garcia, JD Thomas. Estimation of diastolic intraventricular pressure gradients by Doppler M-mode echocardiography. *Am J Physiol Heart Circ Physiol* 280: H2507-15, 2001.

Chapter 8: Spatiotemporal attributes of left ventricular pressure decay rate during isovolumic relaxation

Published as: Ghosh E, Kovács SJ. Spatio-temporal inhomogeneity of left ventricular pressure during isovolumic relaxation. *Am J Physiol Heart Circ Physiol*. 2012; 302(5):H1094-101.

Abstract

Global left ventricular (LV) chamber relaxation rate has been characterized: 1) via the time-constant of isovolumic relaxation τ or 2) via the logistic time-constant τ_L. An alternate method, characterizes isovolumic relaxation (IVR) in accordance with Newton's Law. The model's parameters - stiffness E_k, and damping/relaxation μ result from best fit of model-predicted pressure to in-vivo data. All three models (exponential, logistic and kinematic) characterize global relaxation in terms of pressure decay rates. However, IVR is inhomogeneous and anisotropic. Apical and basal LV wall segments untwist at different times and rates, transmural strain and strain-rates differ due to the helically variable pitch of myocytes and sheets. Accordingly, we hypothesized that the exponential model (τ) or kinematic model (μ and E_k) parameters will elucidate the spatiotemporal variation of IVR pressure decay rate. LV pressures in 20 subjects were recorded using a high fidelity, multi-pressure transducer (3 cm apart) catheter. Simultaneous, dual-channel pressure data was plotted in the pressure phase-plane (dP/dt vs. P) and τ, μ and E_k were computed in 1631 beats (average: 82 beats per subject). Tau differed significantly between the two channels ($p<0.05$) in 16 of 20 subjects, whereas μ and E_k differed significantly ($p<0.05$) in all 20 subjects. These results show that quantifying relaxation rate from data recorded at a single location has limitations. Moreover, kinematic model based analysis allows characterization of whether and when during IVR restoring (recoil) forces dominate resistive (crossbridge uncoupling) forces, and their spatiotemporal dependence, thereby elucidating the relative roles of stiffness vs. relaxation as IVR rate determinants.

173

8.1 Introduction

8.1.1 Physiology of isovolumic relaxation

Diastole begins at aortic valve closure when the ventricle relaxes with both the aortic and mitral valves closed. This phase of the cardiac cycle is called isovolumic relaxation (IVR). IVR is defined as time from aortic valve closure to mitral valve opening and it typically lasts about 60-90 ms. During IVR the ventricular pressure drops as the chamber relaxes and this generates the pressure gradient for filling. The extent of myocardial chamber relaxation at the end of the filling and the rate of relaxation, both play an important role in diastolic filling. Impairment of the extent of relaxation results in a larger number of coupled cross-bridges during diastole that lead to filling at higher pressures. The rate of relaxation plays a crucial role in early filling since it determines the atrioventricular (AV) pressure gradient and rate of change of AV pressure gradient. Diastolic dysfunction is accompanied by delayed left ventricular relaxation [1]. Hence quantifying the rate of relaxation is an important step in the assessment of diastolic function.

8.1.2 Models to quantify the rate of isovolumic relaxation

IVR time interval (IVRT) measured as the duration of isovolumic relaxation is a typically used index. However models of isovolumic pressure decay have been developed to quantify relaxation.

Monoexponential model

The isovolumic pressure contour from just beyond peak -dP/dt to just before MVO has been fit using a mono-exponential by Weiss et al [2]. The assumed exponential pressure decay rate relation is fit to recorded pressure using 3 parameters: τ the time-constant of IVR, P_o - the LV pressure

(in mm Hg) at peak -dP/dt and P_∞ - the asymptote to which pressure declines. The pressure decay relation is:

$$P(t) = P_\infty + P_o e^{(-t/\tau)} \qquad \text{Eq. 8.1}$$

τ is the e-folding time, the time it takes for the pressure to drop by a factor of 1/e. It is used clinically to assess relaxation rate as a diastolic function index [3]. Prolongation of τ relative to normal is associated with the 'delayed relaxation' pattern observed in Doppler echocardiographic transmitral Doppler E-waves.

Logistic model

In order to overcome the drawbacks of the monoexponential model, another model was developed by Matsubara et al [4]. This model proposes a logistic curve fit to the isovolumic pressure decay relation beyond peak –dP/dt is:

$$P(t) = \frac{P_A}{(1 + \exp(-t/\tau_L))} + P_B \qquad \text{Eq. 8.2}$$

P_A is amplitude constant, P_B - a pressure asymptote and τ_L - the logistic time constant.

Kinematic model

A third isovolumic pressure decay model was developed by our lab [5]. It uses Newton's Second Law in accordance with the (slight) known motion of tissue (chamber shape change) during IVR. It is a kinematic model that predicts IVR pressure from before peak –dP/dt to near mitral valve opening. Pressure decay is due to cross bridge uncoupling unmasking stored elastic (titin [6], ECM [7], visceral pericardium [8], etc.) recoil/restoring forces that oppose the decaying contractile forces. The model is parametrized by stiffness (restoring) E_k and damping/relaxation μ. The differential equation for LV pressure during this phase of IVR is:

$$\frac{d^2 P}{dt^2} + \frac{1}{\mu}\frac{dP}{dt} + E_k (P - P_\infty) = 0 \qquad \text{Eq. 8.3}$$

where P_∞ represents the pressure asymptote. These parameters can be uniquely determined from each IVR pressure contour by solving the 'inverse problem' i.e. by using appropriate mathematical methods to fit the model predicted solution to the experimentally recorded pressure and dP/dt data.

8.1.3 Spatial heterogeneity of the left ventricle

All these methods have been used to quantify global LV relaxation rates. However, relaxation is spatially inhomogeneous as evidenced by different rates and amounts of untwisting during IVR [9]. The LV wall is constructed of helically woven layers and sheets of myocardial fibers (including ECM) assembled in interwoven sheets [10] such that fiber orientation changes both transmurally and along the long axis of the ventricle. This geometric arrangement generates the spatially and temporally inhomogeneous relaxation pattern accounting for observed intraventricular pressure gradients (IVPG) during <u>filling</u>. IVPG has been studied previously by various groups using both noninvasive methods such as echocardiography [11] and MRI [12], and invasive methods such as catheterization [13]. Most of these studies have focused on calculating atrio-ventricular or intraventricular pressure gradients <u>during filling</u>, rather than during IVR, when all valves are closed. Typically, any pressure differences within the LV at the instant of mitral valve opening were not considered, thereby disregarding pre-mitral valve opening chamber relaxation rate phenomena.

However in light of the known spatiotemporal dispersion of wall motion (twist, global shape change) during IVR as documented by ventriculography, tagged cardiac MRI [14], speckle tracking [15], strain and strain-rate imaging, the expectation that different pressure decay rates develop at different spatial locations in the LV is justified. To validate this hypothesis, we recorded LV pressure using a multi pressure transducer (3 cm spacing) catheter in the LV to

determine if pressure decay rates differed at the two locations. Furthermore, we hypothesized that timing and magnitude of relaxation mechanisms would differ at the two transducer locations. For validation, we calculated τ (exponential model) and μ and E_k (kinematic model) from simultaneous LV pressure data from each transducer and performed a comparison. We interpreted our results in kinematic terms in order to elucidate physiologic mechanisms operative during IVR.

8.2 Methods

8.2.1 Inclusion criteria and data collection

We analyzed data from 20 subjects selected from our Cardiovascular Biophysics Laboratory database of high-fidelity micromanometric triple pressure transducer recordings. Prior to data acquisition, subjects provided signed, informed consent for participation in accordance with the Institutional Review Board (Human Research Protection Office) at Washington University School of Medicine. The criteria for inclusion included: normal sinus rhythm, absence of valvular abnormalities and the absence of wall motion abnormalities or bundle branch block on the ECG. Subject demographics are summarized in Table 8.1. All patients underwent elective cardiac catheterization at the request of a referring cardiologist. The data acquisition methods have been described previously (See Chapter 2) [16]. Briefly, high-fidelity simultaneous LV pressure-volume and aortic root pressure measurements were obtained using a 6-F triple transducer-tipped pigtail pressure-volume conductance catheter (SSD-1034; Millar Instruments, Houston, TX) amplified and calibrated via standard transducer control units (TC-510; Millar Instruments). The distal (apical) and middle (mid-LV) pressure transducers were located 3cm apart. Pressure signals were input to clinical monitoring systems (Quinton Diagnostics, Bothell,

WA or GE Healthcare, Milwaukee, WI) and a custom personal computer via a research interface (Sigma-5DF; CD Leycom, Zoetermeer, The Netherlands) at a sampling rate of 250 Hz. Conductance signals were also stored on the research interface but were not used in this study. The ejection fraction was computed from the suitably calibrated ventriculogram.

Subject No.	Age (yrs)	Weight (lbs)	EDP (mm Hg)	Ejection fraction	Heart rate (bpm)	No. of beats analyzed
1	46	180	21	74%	61	99
2	66	200	14	60%	60	85
3	45	240	16	67%	75	36
4	53	135	14	74%	72	66
5	51	172	14	77%	52	74
6	52	194	11	72%	73	80
7	57	154	16	62%	76	63
8	58	115	13	85%	90	104
9	70	180	16	79%	92	85
10	75	175	12	73%	59	90
11	74	196	15	75%	59	89
12	54	161	13	63%	65	94
13	49	155	16	64%	56	83
14	55	165	17	54%	60	63
15	**79**	**159**	**15**	**48%**	**60**	**90**
16	61	175	15	75%	57	99
17	43	335	16	81%	59	85
18	57	290	20	86%	54	85
19	66	135	22	80%	55	77
20	69	178	15	62%	76	84

Table 8.1: Subject demographics: age (yrs), weight (lbs), LV end-diastolic pressure (mm Hg), ejection fraction (%), mean heart rate (bpm) and number of beats analyzed per subject. See text for details.

8.2.2 Hemodynamic data processing and analysis

Pressure was converted for analysis via a custom Matlab script (Matlab 6.0; MathWorks, Natick, MA). Data sets were smoothed digitally by using a five-point average to suppress noise in the derivative [16], attenuating 50% of signal at 40 Hz and 90% above 60 Hz, followed by calculation of continuous dP/dt vs. time t from the smoothed data. For each beat, LV end-diastolic pressure (LVEDP) and peak negative dP/dt denoted $(dP/dt)_{min}$ were extracted from the pressure phase-plane (dP/dt vs. P; PPP) or equivalent time-domain contours for both pressure signals.

8.2.3 Exponential model fits

A custom Matlab script performed the exponential (Eq. 8.1) fit to the pressure contours. Apical and mid-LV pressures were plotted in the PPP [17] as shown in Fig. 8.1(c and d). According to convention [5] the segment starting from 4 ms after $(dP/dt)_{min}$ to 4 ms before mitral valve opening was used to determine τ. The IVR segment of the PPP is well approximated by a straight line as shown in Fig. 8.2a, with slope $-1/\tau$. This method was used to calculate τ for both mid-LV and apical pressure contours. Asymptotic pressure - P_∞ was calculated from the intercept of this line along the pressure axis.

8.2.4 Kinematic model fits

Kinematic model parameters (μ and E_k) were determined as previously [5, 16] using the Levenberg-Marquardt algorithm. The start point for fitting was defined by a drop in $d^2P(t)/dt^2$ of one-half after the inflection point in dP/dt, which defined $\dot{P}_o$. Data were fit until 5 ms before mitral valve opening pressure (defined by LVEDP). The algorithm provided parameters for μ, $E_{k,}$, P_o, and P_∞ was calculated by minimizing the root mean squared error (RMSE) in fitting P(t).
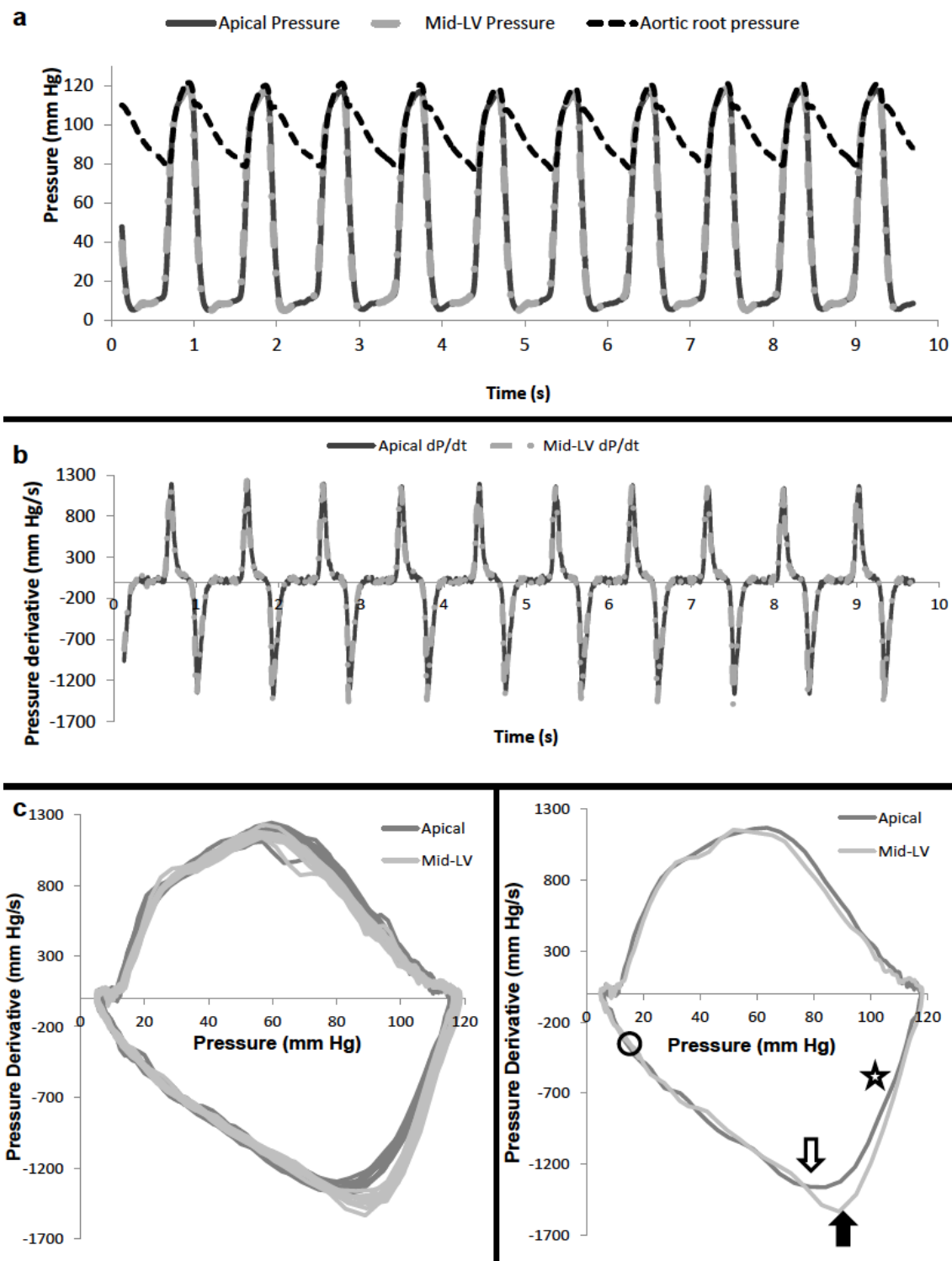
Fig 8.1: Typical pressure data from one subject. Solid line: 1st transducer (LV apex). Grey dashed Line: 2nd transducer (mid LV). Black dashed line: 3rd transducer (Aortic root pressure). Top: a) Pressure as a function of time, all 3 transducers, 10 consecutive beats. Middle: b) Pressure derivative (dP/dt) as a function of time for data in (a). Bottom: c) Pressure phase-plane - dP/dt vs P, for data in (a) only the apical and mid-LV pressures are shown. d) For clarity single cardiac cycle shown inscribes a clockwise loop. Star denotes IVR onset, solid up arrow is mid-LV (dP/dt)$_{min}$, down arrow is apical (dP/dt)$_{min}$, circle is IVR termination. See text for details.

180
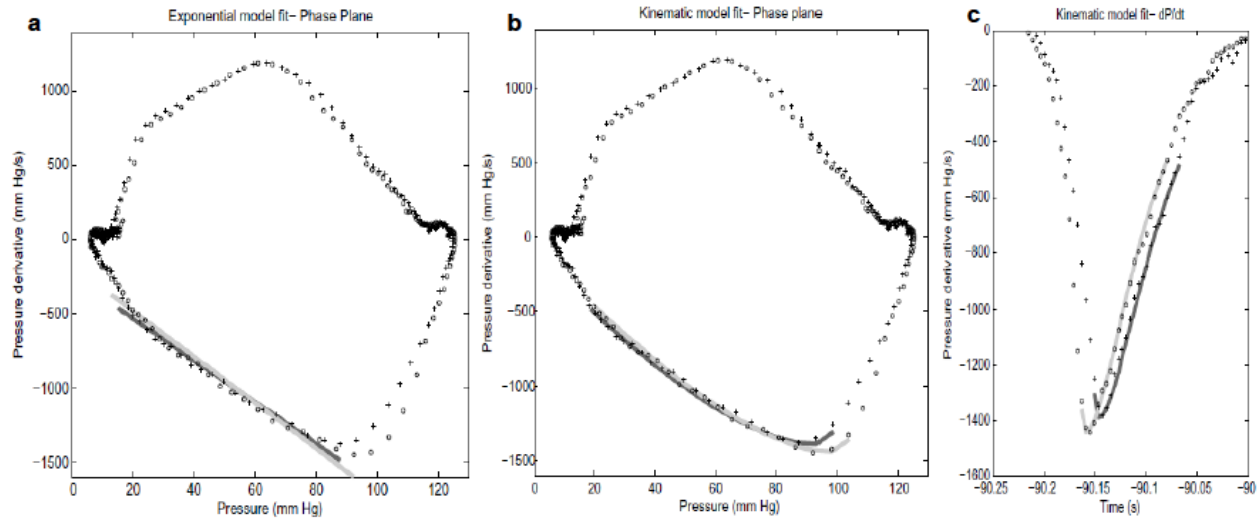
Fig 8.2: Pressure phase-plane comparison of tau model and kinematic model fits for one cardiac cycle. Same subject as Fig.1. LV apex pressure (+), Mid LV pressure (o). a: Tau model fit : τ_{apex} = 71 ms and τ_{mid} =65 ms. Apical pressure fit (dark grey), mid-LV pressure fit (light grey). Note tau model fit utilizes data only after peak negative dP/dt. b: Kinematic fit to same data. μ_{apex} = 1.6ms, $E_{k,apex}$ = 872.42 s^{-2} and μ_{Mid} = 1.57ms, $E_{k,Mid}$=916 s^{-2}. Apical pressure fit (dark grey), mid-LV pressure fit (light grey). c: Kinematic model predicted fit to dP/dt vs. time data. Note kinematic fit includes data before and after peak negative dP/dt. See text for details.

This was implemented using Matlab and the model parameters were calculated for each cardiac cycle. (Fig. 8.2b and c)

8.2.5 Statistical analysis

The unsurpassed sensitivity of micromanometric (piezoelectric) pressure recording also includes noise. Hence, to eliminate noisy beats, we calculated the correlation between the actual data and the model derived (exponential and kinematic) fits using Pearson's correlation coefficient for each beat. Beats, in which the correlation coefficient (R^2) was less than 0.97 for either pressure channel, were excluded from analysis. After this filtering, 1631 beats were selected. The exponential and kinematic model parameters were calculated as previously for both pressure channels. The 2-tailed Student's t-test was used to compare apical and mid-LV relaxation parameters in each subject. A value of p < 0.05 was considered significant.

181

Additionally, in order to evaluate how well each parameter- τ, P_∞, μ and E_k could differentiate between the two locations a percentage difference was calculated for each parameter. This percentage difference was calculated by dividing the difference in the values by the average of the parameter values at the two locations.

8.3 Results

8.3.1 Subject demographics

We selected 20 datasets (mean age 59 years) that comprised a typical cross section of our database (mean age 58.6 years) and analyzed 1631 beats from these 20 patients (~82±16 beats per person, 13 men). Patient demographics are shown in Table 8.1. To assure physiologic robustness we took care to include a representative range diastolic function – from low normal to elevated LVEDP - commonly encountered in such a group. Nineteen of the 20 subjects had a normal ejection fraction (EF > 50%). The mean EF of the group was 71 ± 10%. The mean LVEDP varied from 11 mm Hg to 22 mm Hg (16±3 mm Hg). In the study, 9 subjects had LVEDP < 15 mm Hg, 9 subjects had LVEDP between 15 mm Hg and 20 mm Hg and 2 subjects had LVEDP > 20 mm Hg. The heart rate for the group was 66±12 bpm. Table 8.1 lists weight, LVEDP, ejection fraction, mean heart rate and the number of beats analyzed for each subject. Thirteen of 20 subjects had a distinct diastatic interval on transmitral echo.

Fig. 8.1 shows typical data for both pressure phase plane (PPP) and P vs. t plots. Fig. 8.1a shows 10 beats from a selected subject. Apical (solid black) and mid-LV (dashed grey) pressures are shown. Dashed black is aortic root pressure from the third, most-proximal transducer. Fig. 8.1b shows the pressure derivative (dP/dt) for the same beats as a function of time. Fig. 8.1c shows the PPP plot for the 10 beats (all 3 transducers). Fig 8.1d shows one cardiac cycle in the

PPP (all 3 transducers) for clarity. Fig. 8.2a and 8.2b compare the exponential fit and the kinematic model fit to the same beat. Fig. 8.2c shows the same data as Fig. 8.2b on a dP/dt vs. t plot.

8.3.2 Monoexponential model results

Due to the availability of a large number of beats for analysis, subject comparisons utilized mean values for the parameters for each subject. Table 8.2 shows the average and standard deviation of the four parameters- τ, P_∞, μ and E_k from all subjects. Table 8.2 lists τ (mean $\pm$ SD) for the two recording sites - τ_{mid} and τ_{apex}. The fourth column lists the p-value per subject. Using $p<0.05$ to indicate statistical significance, 16 of the 20 subjects had significantly different values of τ between the two transducers. In 17 of the 20 subjects, τ_{apex} was greater than τ_{mid}. The subjects in which τ_{apex} was less than τ_{mid}, the difference was not statistically significant. Asymptotic pressures were also calculated (Table 8.2). The asymptotic pressure fitting parameter - P_∞ was statistically different at the 2 locations in 19 subjects and the apical P_∞ was greater in magnitude than mid-LV P_∞ in all subjects.

8.3.3 Kinematic model results

The data was also fit using the kinematic model to determine μ and E_k. Table 8.3 shows μ and E_k values (mean $\pm$ SD) for the apical and mid-LV pressure transducers. The fourth and seventh columns indicate the p-values for μ and E_k respectively. Using $p<0.05$ for statistical significance, we found that all 20 subjects had μ and E_k values which were statistically significantly different between the two spatial locations. The subjects in which the τ_{mid} and τ_{apex} were not statistically significantly different are denoted by bold.

The percentage difference between mid-LV and apical transducer τ values ranged from

Subject No.	τ_{apex} (ms)	τ_{Mid} (ms)	p-value	$P_{\infty, apex}$ (mm Hg)	$P_{\infty, Mid}$ (mm Hg)	p-value
1	63±4	61±3	<0.0001	-4.3±3.2	-3.7±2.3	0.008
2	56±2	54±2	<0.0001	-6.1±2.8	-4.4±2.5	<0.0001
3	73±6	68±5	<0.0001	-9.9±6.5	-6.2±6.5	<0.0001
4	54±5	52±4	<0.0001	-9.5±4.3	-7±3.2	<0.0001
5	67±4	62±8	<0.0001	-15.8±4.4	-8.2±5.8	<0.0001
6	65±5	62±3	<0.0001	-14.8±5.1	-8.9±3.6	<0.0001
7	65±5	62±4	<0.0001	-11.1±7	-10.3±6	0.03
8	45±8	44±8	0.02	-7±3.8	-6.5±4.9	0.31*
9	55±3	53±3	<0.0001	-6.4±3.6	-3.9±3	<0.0001
10	62±3	61±2	0.008	-9.5±3	-6.3±2.2	<0.0001
11	73±8	66±6	<0.0001	-18.5±8.4	-10.9±6	<0.0001
12	66±4	64±3	<0.0001	-13.2±2.9	-10.8±2.1	<0.0001
13	**76±5**	**75±5**	**0.05***	**-17.7±3.7**	**-13.7±3.1**	**<0.0001**
14	**89±11**	**89±8**	**0.95***	**-22.8±9.3**	**-20.5±6.4**	**0.001**
15	71±7	70±6	0.0002	-13.1±7.4	-11.5±6.6	<0.0001
16	60±4	58±5	0.004	-5.2±4.1	-4.7±4.2	0.02
17	69±6	66±5	<0.0001	-3.6±3.4	-1.3±3.1	<0.0001
18	82±4	79±3	<0.0001	-12.6±5.5	-11.1±4.6	<0.0001
19	**66±9**	**66±7**	**0.42***	**-19.6±8.9**	**-14.3±6.8**	**<0.0001**
20	**64±4**	**64±4**	**0.25***	**-14.9±6.2**	**-13.6±5.2**	**<0.0001**

Table 8.2: Mean τ, P_{∞} (apex, mid), p-value. $p < 0.05$ denotes significant. * denotes $p > 0.05$ values . These subjects are also highlighted in bold font. See text for details.

0.1% to 10.6% (mean: 3.5%). The percentage difference between mid-LV and apical transducer

μ values ranged from 5.3% to 95.5% (mean: 33%). The percentage difference between mid-LV

and apical transducer E_k ranged from 2.2% to 78.9% (mean: 46%).

Subject No.	μ_{apex} (ms)	μ_{Mid} (ms)	p-value	$E_{k,apex}$ (1/s^2)	$E_{k,mid}$ (1/s^2)	p-value
1	11±3	6±2	<0.0001	1619±591	2646±841	<0.0001
2	10±3	6±2	<0.0001	1804±513	3235±954	<0.0001
3	13±4	8±2	<0.0001	1317±445	2095±605	<0.0001
4	14±2	12±2	<0.0001	1319±230	1446±261	<0.0001
5	9±2	7±2	<0.0001	1639±411	3019±1733	<0.0001
6	16±5	11±2	<0.0001	1126±306	1577±377	<0.0001
7	15±2	14±5	0.004	1078±280	1310±990	<0.0001
8	11±2	7±3	<0.0001	2017±350	3818±1530	<0.0001
9	13±3	9±2	<0.0001	1402±222	1955±399	<0.0001
10	10±4	6±2	<0.0001	1705±684	2884±937	<0.0001
11	12±3	8±3	<0.0001	1233±343	1962±621	<0.0001
12	11±3	8±2	<0.0001	1368±315	1888±541	<0.0001
13	15±3	9±5	<0.0001	991±213	2169±1459	<0.0001
14	17±3	15±4	<0.0001	751±152	834±280	0.0005
15	13±4	10±4	<0.0001	1210±453	1610±997	<0.0001
16	14±8	10±3	<0.0001	1434±581	1797±647	<0.0001
17	12±4	4±2	<0.0001	1338±596	4471±2532	<0.0001
18	16±4	12±4	<0.0001	824±241	1056±393	<0.0001
19	14±3	13±3	<0.0001	1148±300	1232±343	<0.0001
20	17±5	15±3	<0.0001	984±181	1042±217	<0.0001

Table 8.3: Kinematic model parameters. Mean μ, E_k values from apical and mid-LV pressure data including p-values. For comparison τ having p>0.05 (from Table S1) are in bold. See text for details.

8.3.4 Effect of diastatic interval

Of the 20 subjects 13 had clearly discernible diastatic interval (separated Doppler E- and A-waves). Five had Doppler E-waves with A-wave onset at E-wave termination, hence no diastatic interval. The remaining two had A-waves that merged with the end of the Doppler E-wave. To determine if the presence or absence of diastasis influenced the results we compared the average

mid-LV and apical τ, P_∞, μ and E_k values in subjects with and without diastasis. Using $p<0.05$ criteria, μ, E_k, τ and P_∞ for both locations were not statistically different.

8.4 Discussion

It is established that the atrioventricular pressure gradient that generates the Doppler E-wave also includes the observed intraventricular pressure gradients within the LV during the E-wave itself. However, the spatiotemporal characteristics of LVP during isovolumic relaxation, before mitral valve opening are unknown. In light of the known spatiotemporal heterogeneity of wall motion during IVR, we hypothesized that relaxation rate heterogeneity can be quantified by spatial differences in pressure decay rate during IVR. For validation simultaneously recorded isovolumic pressure data from two locations in the LV (apex and mid-LV, 3 cm apart) was fit using both the exponential (Weiss) and kinematic (Chung) pressure decay models. Both models generated statistically different relaxation rate parameters (between locations), thereby characterizing spatially different isovolumic relaxation rates. We also sought to understand the physiology responsible for differential relaxation rates.

8.4.1 Previous studies

Pressure gradients during filling have been previously reported using invasive and noninvasive methods [11, 18, 19]. Courtois et al [18, 20] measured the Doppler E-wave features and intraventricular regional pressure variation during the E-wave in a canine, closed chest model. Nikolic et al [21] measured intraventricular pressure gradients in early diastole for both filling and non-filling beats in dogs. They related the pressure gradients to elastic recoil and ventricular shape changes. In addition, intraventricular pressure gradients of 3 mm Hg during early filling (Doppler E-wave) have also been observed via color M-mode echocardiography [13, 21].

All these studies focus on pressure gradients <u>after</u> mitral valve opening. Intraventricular pressure gradients during the IVR phase have not been considered. Sasson et al [19] recorded intraventricular, apically directed flow during IVR using continuous wave Doppler echocardiography –but relaxation rates were not considered in the study. Pioneering work regarding IVR has been performed by Davis et al [22] where the variation of τ from base to apex in an open chest canine model involving transapical and transatrial puncture, was studied using a single transducer catheter. Pressure was measured by moving the catheter to 6 different locations in the canine LV. Three different methods of analysis were used to calculate τ. They found conflicting results in the trend of spatial variation of τ depending on the method of analysis. In concordance with our observations they reported that τ increased from the base to apex using Eq. 8.1. However using an error minimizing algorithm to estimate τ and P_∞ they arrived at the opposite conclusion. Their work showed that τ varied in the LV with changes in transducer location, limited by uncertainty regarding the pattern of variation and potential mechanistic explanations.

8.4.2 Difference in τ_{apex} vs. τ_{mid} from the exponential model

We used the mono-exponential (Weiss) model to evaluate relaxation rate for simultaneously measured apical and mid-LV pressures. We found 16 of 20 subjects had statistically different values for τ_{apex} vs. τ_{mid} Table 8.2. τ_{apex} was greater than τ_{mid} in 17 of the 20 subjects. In 4 of the subjects statistically significant difference between τ_{apex} vs. τ_{mid} was not observed. Some contributing factors for this include: choice of method for calculating τ [22], fidelity of data acquisition, data processing techniques etc. In addition, when two simultaneous pressures are measured, the hydrostatic position of the pressure sensors in the LV, the orientation of the LV itself and that of the catheter with respect to the LV may also play a role. The exact position of

the pressure transducers in a given LV is somewhat variable (for example to avoid catheter induced ectopy) while the orientation of the catheter in general is along the long axis of the chamber, as verified by echocardiography during data acquisition, but in location with respect to the apex, some variability is unavoidable.

The calculated P_∞ values were negative. The apical P_∞ was significantly lower than the mid LV P_∞. This implies that apical recoil generates a lower P_∞. It is consistent with achieving the lowest pressure in a completely relaxed ventricle (in case of no filling) [21].

8.4.3 Differences in kinematic model parameters

To elucidate and characterize mechanistic attributes of relaxation rate beyond Weiss' exponential model's capabilities we used Chung's kinematic model [5] which commences before dP/dt $_{min}$ until mitral valve opening. It provides a better fit for wider range of PPP contours [Ref 16, Fig. 2] than the τ model. We calculated the kinematic model parameters for the simultaneous, dual pressure data (Table 8.3). In contrast to τ, kinematic model parameters were statistically significantly different in every subject. We found $\mu_{apex} > \mu_{mid}$ in all subjects and $E_{k,mid} > E_{k,apex}$ in all subjects.

The numerical difference in μ and E_k values at the 2 locations is larger than the numerical difference in τ values. Numerically, the difference in τ was $\approx 3\%$ of the actual value whereas the difference in μ was 33% of the actual value and the difference in E_k was 46% of the actual value. Hence the kinematic model is more sensitive to spatial heterogeneity in rate of pressure decay than the exponential (τ) model.

8.4.4 Spatial pattern of intraventricular pressure decay

The difference in pressure and pressure derivative (dP/dt) between the apex and mid-LV is clearly displayed in the PPP plots (Fig. 8.1c and d). Fig. 8.1d shows that after the aortic valve closes (denoted by star) mid-LV pressure decreases faster (evidenced by the higher magnitude of

dP/dt (mid-LV)) than apex. This continues until $(dP/dt)_{min}$ is reached (solid arrow for mid-LV and open arrow for apex) and after these minima, dP/dt starts to increase for both. During this portion of IVR, the differences in dP/dt magnitude at the two locations are smaller than the differences before $(dP/dt)_{min}$. These differences in slopes cannot be appreciated in Fig. 8.1a or b due to the large range of values of pressure (10 mm Hg to 120 mm Hg) and *dP/dt* (-1500 mm Hg/s to 1300 mm Hg/s) relative to the difference in the values at the two locations.

The exponential model fits the PPP segment after $(dP/dt)_{min}$ till near mitral valve opening (open circle in Fig. 8.1d). During this part of IVR, we found that τ_{apex} is greater than τ_{mid}. This implies that apical relaxation rate is slower than mid-LV relaxation rate, seen in Fig. 8.2a where the fit to the mid-LV (light grey) is steeper than the apical (dark grey) fit. Although the τ model does not provide mechanistic insight regarding the rate of pressure decay during IVR, the data indicate that the relaxation rate depends on spatial location.

The kinematic model assumes that pressure decay is determined by the interplay of stored elastic restoring force overcoming the opposing, but decaying contractile forces as a result of crossbridge uncoupling. After aortic valve closure, stored elastic restoring forces dominate the decaying contractile forces thereby accelerating the rate of pressure decay magnitude until the peak rate of pressure decay, $(dP/dt)_{min}$ is reached. At the instant of $(dP/dt)_{min}$ the restoring force and the damping force are precisely balanced, and the second derivative of pressure, d^2P/dt^2, is zero. After this point damping (resistive) force dominates restoring force and slows the rate of relaxation.

Our model-based fit to the data reveal that stiffness - E_k is higher in the mid-LV than the apex. Thus the kinematic restoring force is higher in the mid-LV, encountered during the initial part of IVR (i.e. before mid-LV $(dP/dt)_{min}$) and the rate of pressure decay (dP/dt) is faster in mid-

LV than the apex (Fig. 8.1d). This is also corroborated by the dP/dt vs. time plot (Fig. 8.2c) where the decrease in dP/dt (mid-LV) is faster than dP/dt (apex). The mid-LV pressure contour reaches its minimum value first (Fig. 8.2c). After $(dP/dt)_{min}$ the balance of forces changes sign and damping forces dominate pressure decay (as seen by the decreasing magnitude of dP/dt). The μ_{apex} is higher than μ_{mid-LV}. Since the damping force is inversely proportional to μ, the mid-LV pressure decay is more damped. Hence the apical dP/dt is less damped and decays (in magnitude) slower as shown in Fig. 8.1d and 8.2c. This agrees with the results of the exponential model which also showed that apical relaxation proceeds at a slower rate.

The quantification of relaxation rate by the two models also proves that the pressure gradients are caused not only by a temporal difference in the onset of relaxation at different locations but also by inherent differences in chamber kinematic properties (stiffness, relaxation) at the different locations themselves. If intraventricular pressure gradients were solely caused by differences in the onset of relaxation at the mid-LV and apex then there wouldn't be any difference in chamber parameters (τ, μ and E_k) and relaxation <u>rates</u> between the two locations, and the two *dP/dt* contours (Fig. 8.2c) could be superimposed by shifting the contour in time – which is not the case.

8.4.5 Physiological significance

Intraventricular pressure differences <u>during filling</u> have been previously calculated from color Doppler M-mode data and velocity of propagation V_p [23]. Because V_p is zero during IVR a pressure gradient cannot be calculated. Hence although a pressure difference has been noted during early filling, not much is known about the relaxation rates operative during IVR. Using two different models of pressure decay we have shown that the parameters determining the rate of pressure decay are significantly different at two different locations. This extends the work of

Davis et al where they noted the variation in τ as a function of intraventricular location. Our results agree with their results in terms of similar trends of τ variation in the LV and a similar coefficient of correlation between the exponential fit and the actual data (R^2 = 0.98 in both the studies). Our study has the advantage of being performed in humans under closed chest, physiologic conditions, implying clinical translational potential. Furthermore, analyzing the data via the kinematic model of IVR has allowed us to elucidate and further characterize the physiology underlying the mechanism of intraventricular pressure decay rate variation. Recent studies [24] have shown that the PEVK region of titin generates resistive (i.e. viscous) forces by transiently interacting with actin during LV relaxation. Other studies [8, 25, 26] characterized the role of extracellular matrix in contributing to passive LV mechanical properties. Although these studies have not looked at IVR specifically, they demonstrate that stiffness and damping (viscosity/relaxation) have cellular and sub-cellular analogs. Therefore it is reasonable to interpret our results as evidence for the spatial dependence of stiffness and relaxation elements of the chamber.

Beyond facilitating interpretation of the physiology in kinematic terms, an advantage of the kinematic approach resides in its ability to fit the PPP contour from before $(dP/dt)_{min}$ as shown in Fig 8.2b. The initial conditions of the fit, dP/dt_o (rate of relaxation) before the minima affects the rate of relaxation after. The relative rates (apical vs. mid-LV) are influenced by $(dP/dt)_{min}$ values, which is taken into account only by the kinematic model. Hence kinematic modeling of IVR process facilitates mechanistic understanding of pressure decay attributes during IVR.

8.4.6 Clinical significance and future work

In this study we investigated the differences in rates of isovolumic pressure decay at different locations in the LV and sought to understand it in causal, physiologic, mechanistic terms. Our results show that the mechanics of relaxation differ depending on spatial location. This is important because it affects how we interpret the results of experiments using isovolumic relaxation rates (τ). Studies [27, 28] often use τ to quantify the relaxation rate of the LV and to differentiate between groups or the effect of an intervention. However prior studies failed to consider the spatial variation in τ which has a bearing on the significance of conclusions drawn based on variation in τ.

The method used in this study can quantify alterations in LV relaxation rates in selected pathological conditions. In the scenario of conduction abnormalities such as a bundle branch block, AV block etc. the regular electrical activation pattern is disrupted. This leads to a modified pattern of myocardial contraction and relaxation. By studying the normal spatiotemporal variation in ventricular mechanics, we can quantify changes in ventricular function due to the conduction abnormalities. Additionally, the deviation from a normal activation pattern can be used as a guide for cardiac resynchronization therapy. Given our current knowledge of how relaxation rate depends on spatial location, the future study of intraventricular pressure gradients during IVR and their relation to suction (*dP/dV*<0) during the E-wave should be particularly enlightening. Additionally, the magnitude of intraventricular pressure gradients could be used as potential predictor of early diastolic filling.

8.4.7 Limitations

The main limitations pertain to data acquisition methods. As noted previously [16], calibration, catheter placement and orientation with respect to the LV axis may influence pressure

recordings. However calibration issues will affect both pressure channels equally and offsets the pressure by a constant value. This should not affect the model's pressure decay rate parameter (μ) since it is fit to *dP/dt*. Calibration and drift are mitigated by pre- and post-calibration of transducers to zero hydrostatic pressure in a 37^0C saline bath. Precise orientation within the LV from subject to subject is not possible beyond orientation along the long-axis of the chamber after crossing the aortic valve and positioning to exclude catheter induced ectopy. The consistency of apical and mid-LV locations is assured by echocardiographic imaging of the catheter in the LV using the parasternal long axis view. Hence, within practical anatomic constraints, our data represent measurement of the apical and mid-LV region.

Other issues may involve signal processing which we have addressed previously [16]. Another limitation concerns subjects in whom the diastatic interval was zero. Since diastasis defines the in-vivo equilibrium volume of the LV [29], when a diastatic interval is not clearly present the LV may not have completely relaxed before atrial filling onset. This might influence our conclusions and the parameters computed from the data for the previous IVR interval. To check this, we compared the model parameters: τ, P_∞, μ and E_k among the subjects with and without clear diastasis and found no statistical difference between the two groups (see Results).

In this physiologic study we selected datasets of 20 subjects with essentially normal EFs (19 subjects EF > 50%) and a wide range of LVEDP (range: 11mm Hg- 22 mm Hg) characteristic of what one encounters in clinical practice. Our goal was to quantify physiology in terms of the spatial differences in relaxation rates within the LV. The performance of a clinical study which compares normal vs. pathologic cases with respect to changes in rate of pressure decay (and model parameters) as a function of location within the LV in different pathologic subsets is reserved for future work.

8.5 Conclusion

The time-constant of isovolumic relaxation τ and the kinematic model of isovolumic pressure decay were employed to elucidate and characterize spatiotemporal physiologic IVR mechanisms. Our results demonstrate that isovolumic relaxation rates at 2 locations in the LV, 3 cm apart are distinguishable. Although τ is conventionally used to measure the global relaxation component of diastolic function [30] its ability to provide the full picture is limited. In contrast, kinematic model based analysis of IVR allows characterization of whether and when during IVR restoring (recoil) forces dominate resistive (crossbridge uncoupling) forces, and their spatio-temporal dependence. Because relaxation proceeds at different rates in different regions of the LV, reliance on data recorded at a single location in the LV has limitations. The physiological significance of these findings are: 1) all hearts decrease their pressures during IVR by the same physiologic mechanism of stored elastic strain generated recoil modulated by crossbridge uncoupling, 2) these processes can be quantified via Eq. 8.3 (Chung equation) by direct determination of stiffness (E_k) and relaxation (viscosity μ) from in-vivo data, 3) the relative values of E_k and μ at different spatial locations determine the dominance of each of these forces including their potential dependence on pathology. Application in specific clinical subsets including assessment of model parameter variation in response to selected pharmacologic agents intended to treat diastolic dysfunction is warranted.

Reference:

1. Ommen SR, Nishimura RA. A clinical approach to the assessment of left ventricular diastolic function by Doppler echocardiography: update 2003. *Heart*. 2003;89 (Suppl) iii8- iii 23.

2. Weiss JL, Frederiksen JW, Weisfeldt ML. Hemodynamics determinants of the time course of fall in canine left ventricular pressure. *J. Clin. Invest*. 1976; 58: 751- 760.

3. Stoddard MF, Pearson AC, Kern MJ, Ratcliff J, Mrosek DG, Labovitz AJ. Left ventricular diastolic function: comparison of pulsed Doppler echocardiographic and hemodynamic indexes in subjects with and without coronary artery disease. *J Am Coll Cardiol*. 1989; 13(2): 327- 336.

4. Matsubara H, Takaki M, Yasuhara S, Araki J, Suga H. Logistic time constant isovolumic relaxation pressure- time curve in the canine left ventricle. *Circulation*. 1995; 92: 2318- 2326.

5. Chung CS, Kovács SJ. The physical determinants of left ventricular isovolumic pressure decline: Model-based prediction with in-vivo validation. *Am J Physiol Heart Circ Physiol*. 2008;294:H1589-H1596.

6. LeWinter MM, Granzier H. Cardiac Titin. Circulation. 2010, 121 (19): 2137 -2145.

7. Robinson TF, Factor SM, Sonnenblick EH. The heart as a suction pump. *Sci. Am*. 1986, 254(6): 84- 91.

8. Jöbsis PD, Ashikaga H, Wen H, Rothstein EC, Horvath KA, McVeigh ER, Balaban RS. The visceral pericardium: macromolecular structure and contribution to passive mechanical properties of the left ventricle. *Am. J. Physiol Heart Circ Physiol*. 2007; 293 (6): H3379- H3387.

9. Kerckhoffs RCP, Omens JH, McCulloch AD, Mulligan LJ. Ventricular Dilation and Electrical Dyssynchrony Synergistically Increase Regional Mechanical Nonuniformity But Not Mechanical Dyssynchrony. *Circ Heart Fail*. 2010; 3: 528- 536.

10. Buckberg G, Mahajan A, Saleh S, Hoffman JIE, Coghlan C. Structure and function relationship of the helical ventricular myocardial band. *J Thoracic Cardiovasc Surg*. 2008; 136(3): 578- 589.

11. Bermejo J, Antoranz JC, Yotti R, Moreno M, García-Fernández MA. Spatio-temporal mapping of intracardiac pressure gradients. A solution to Euler's equation from digital postprocessing of color Doppler M-mode echocardiograms. *Ultrasound Med & Biol*. 2001, 27(5); 621- 630.

12. Dong S, Hees PS, Siu CO, Weiss JL, Shapiro EP. MRI assessment of LV relaxation by untwisting rate: a new isovolumic phase measure of τ. *Am. J. Physiol. Heart. Circ. Physiol*. 281: H2002- H2009, 2001.

13. Steine K, Stugaard M, Smiseth OA. Mechanisms of diastolic intraventrcular regional pressure differences and flow in the inflow and outflow tracts. *J Am Coll Cardiol*. 2002, 40(5): 983- 990.

14. Götte MJW, Germans T, Rüssel IK, Zwanenburg JJM, Marcus JT, van Rossum AC, van Veldhuisen DJ. Myocardial strain and torsion quantified by cardiovascular magnetic resonance tissue tagging: Studies in normal and impaired left ventricular function. *J Am Coll Cardiol*. 2006, 48(10): 2002-2011.

15. Al-Naami GH. Torsion of young hearts: a speckle tracking study of normal infants, children and adolescents. *Eur. J Echocardiogr*. 2010, 11: 853-862.

16. Shmuylovich L, Kovács SJ. Stiffness and relaxation components of the exponential and logistic time constants may be used to derive a load-independent index of isovolumic pressure decay. *Am J Physiol Heart Circ Physiol*. 2008; 295(6): H2551-2559.

17. Eucker SA, Lisauskas JB, Singh J, Kovács SJ, Jr. Phase-plane Analysis of Left Ventricular Hemodynamics, *J Appl Physiol*. 90: 2238-2244, 2001.

18. Courtois MR, Kovács SJ, Jr., Ludbrook PA. Transmitral pressure-flow velocity relation. Importance of regional pressure gradients in the left ventricle during diastole. *Circulation*. 1988, 78: 661-671.

19. Sasson Z, Hatle L, Appleton CP, Jewett M, Alderman EL, Popp RL. Intraventricular flow during isovolumic relaxation: Description and characterization by Doppler Echocardiography. *J Am Coll Cardiol*. 1987, 10(3): 539- 546.

20. Courtois MR, Kovács SJ, Jr., Ludbrook PA. Loss of early diastolic intraventricular pressure gradient during acute myocardial ischemia. *J Am Coll Cardiol*. 1989, 13, 1218.

21. Nikolic SD, Feneley MP, Pajaro OE, Rankin JS, Yellin EL. Origin of regional pressure gradients in the left ventricle during early diastole. *Am. J. Physiol. Heart Circ. Physiol*. 1995. 268 (37): H550- H557.

22. Davis KL, Mehlhorn U, Schertel ER, Geissler HJ, Trevas D, Laine GA, Allen SJ. Variation in Tau, the time constant for isovolumic relaxation, along the left ventricular base-to-apex axis. *Basic Res Cardiol*. 1999. 94: 41- 48.

23. Ebbers T, Wigström L, Bolger AF, Wranne B, Karlsson M. Noninvasive Measurement of Time-Varying Three-Dimensional Relative Pressure Fields Within the Human Heart. *J. Biomech. Eng*. 2002, 124: 288-293.

24. Chung CS, Methawasin M, Nelson OL, Radke MH, Hidalgo CG, Gotthardt M, Granzier HL. Titin based viscosity in ventricular physiology: An integrative investigation of PEVK- actin interactions. *J. Mol. Cell. Cardiol*. 2011; 51 (3): 428- 434.

25. Brower GL, Gardner JD, Forman MF, Murray DB, Voloshenyuk T, Levick SP, Janicki JS. The relationship between myocardial extracellular matrix remodeling and ventricular function. *Eur. J. Cardiothorac. Surg*. 2006; 30(4): 604- 610.

26. Nishimura S, Nagai S, Katoh M, Yamashita H, Saeki Y, Okada J, Hisada T, Nagai R, Sugiura S**.** Microtubules Modulate the Stiffness of Cardiomyocytes Against Shear Stress. *Circ. Res*. 2006; 98(1):81- 87.

27. Ishida Y, Meisner JS, Tsujioka K, Gallo JI, Yoran C, Frater RW, Yellin EL. Left ventricular filling dynamics: influence of left ventricular relaxation and left atrial pressure. *Circulation*, 1986, 74(1): 187-196.

28. Nitenberg A, Lecarpentier Y, Antony I, Chemla D. Dipyridamole slows the rate of isovolumic pressure fall in patients with normal coronary arteries. *Eur. Heart J*. 1995, 16 (11): 1721- 1725.

29. Shmuylovich L, Chung CS, Kovács SJ. Last word on point: Counterpoint: Left ventricular volume during diastasis is the physiological in vivo equilibrium volume and is related to diastolic suction. *J Appl Physiol*. 2010; 109(2):612-4.

30. Zile MR, Brutsaert DL. New Concepts in Diastolic Dysfunction and Diastolic Heart Failure: Part I- Diagnosis, Prognosis, and Measurements of Diastolic Function. *Circulation*. 2002, 105: 1387-1393.

Chapter 9: The quest for load-independent left ventricular chamber properties: Exploring the normalized pressure phase plane

Abstract

The pressure phase plane (*PPP*), defined by dP(t)/dt vs. P(t) coordinates has revealed novel physiologic relationships not readily obtainable from conventional, time domain analysis of left ventricular pressure (LVP). We extend the methodology by introducing the normalized pressure phase plane (*nPPP*), defined by $0 \leq P \leq 1$, and $-1 \leq dP/dt \leq +1$. Normalization eliminates load dependent effects facilitating comparison of conserved features of *nPPP* loops. Hence, insight into load-invariant systolic and diastolic chamber properties and their coupling to load can be obtained. To demonstrate utility, high fidelity P(t) data from 14 subjects (4234 beats) were analyzed. P_{NR}, the *nPPP* (dimensionless) pressure, where $-dP/dt_{peak}$ occurs, was 0.61 and had limited variance (7%). The relative load-independence of P_{NR} was corroborated by comparison of *PPP* and *nPPP* features of normal sinus rhythm (NSR) and (ejecting and non-ejecting) premature ventricular contraction (PVC) beats. PVCs had lower $P(t)_{max}$ and lower peak negative and positive dP(t)/dt values vs. NSR beats. In the *nPPP*, $+dP/dt_{peak}$ occurred at higher (dimensionless) P in PVC beats than in regular beats (0.44 in NSR vs. 0.48 in PVC). However, P_{NR} for PVC vs. NSR remained unaltered ($P_{NR} = 0.64$; $p > 0.05$). Possible mechanistic explanation includes a (near) load-independent (constant) ratio of maximum cross-bridge uncoupling rate to instantaneous wall stress. Hence *nPPP* analysis reveals LV properties obscured by load and by conventional temporal P(t) and dP(t)/dt analysis. *nPPP* identifies chamber properties deserving molecular and cellular physiologic explanation.

9.1 Introduction

9.1.1 Load dependence of hemodynamic indexes

The gold standard for characterization of chamber properties utilizes high fidelity, micromanometric left ventricular (LV) pressures (P) as a function of time. The usual parameters include: maximum and minimum LV pressures (P_{max} and P_{min}), peak positive and peak negative rate of change of pressure ($+dP/dt_{peak}$ and $-dP/dt_{peak}$), diastatic pressure, and end-diastolic pressure (EDP). Previous studies have noted the load dependence of diastolic function indexes [1,2,3]. Specifically relaxation properties changed during pacing- induced ischemia [4,5] and the
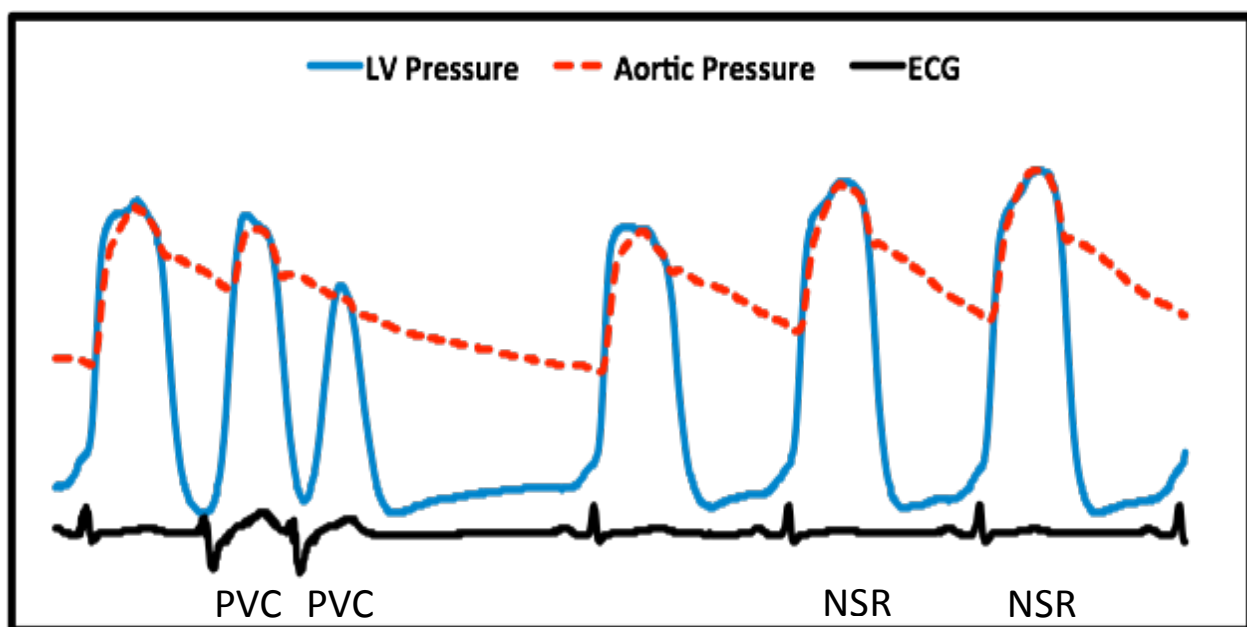
Fig 9.1: LV pressure (blue) and aortic pressure (red) for 6 consecutive beats in a subject. PVC = premature ventricular contractions, NSR = normal sinus rhythm. ECG is shown by the black line.

application of vasodilator and vasoconstrictor drugs [6,7] due to changes in the loading conditions of the heart.

In order to evaluate cardiac function, it is essential to be able to separate the effects of acute changes in load from the chronic changes in function due pathology. Another example of acute load changes are spontaneously occurring premature ventricular contractions (PVC). PVCs

occur when the ventricle contracts prematurely during the cardiac cycle resulting in little to no filling. This alters the hemodynamics of the cardiac cycle and results in a lower systolic pressure (Fig 9.1). PVCs are followed by a 'compensatory pause' in which the diastolic filling portion of following beat is longer than the normal sinus rhythm (NSR) beat [8]. Hemodynamic indexes measured during PVC beats are significantly different from the corresponding values measured during NSR. Hence it is essential to develop load independent methods to analyze the cardiac cycle. Previous research [9] has focused on developing load-independent indexes which quantify a portion of the cardiac cycle. However a method to separate the load effects from the physiological changes has not been developed before.

9.1.2 Phase plane method for cardiac cycle analysis

Phase planes are used in non-linear dynamics to visualize the behavior of a physical system. Our lab has previously used phase plane analysis to evaluate the cardiac cycle dynamics. Eucker et al [10] adopted the phase plane analysis method to analyze LVP in the pressure phase plane (*PPP)* and physiological hyperspace [11]. The oscillatory nature of P during the cardiac cycle generates closed *PPP* loops (analogues of limit cycles) allowing visualization of dP/dt vs. P relation especially during the isovolumic phases when dP/dt reaches its respective systolic and diastolic maxima. *PPP* analysis has been used to characterize LV relaxation using various mathematical assumptions [12-15]. Here we extend PPP analysis and introduce the normalized pressure phase plane (nPPP) defined by $-1 \leq dP/dt \leq 1, 0 \leq P \leq 1$. Thus normalization eliminates load dependent components of P and dP/dt and retains intrinsic contraction and relaxation features of the loops and helps to elucidate and characterize their differences and similarities.

Specifically, we focus on the values of normalized (dimensionless) pressure during isovolumic contraction (IVC) at $+dP/dt_{peak}$ (P_{NC}) and during IVR at $-dP/dt_{peak}$ (P_{NR}).

Additionally, we analyze loops of NSR and PVC beats within and among subjects. We hypothesize that nPPP analysis will elucidate novel chamber properties.
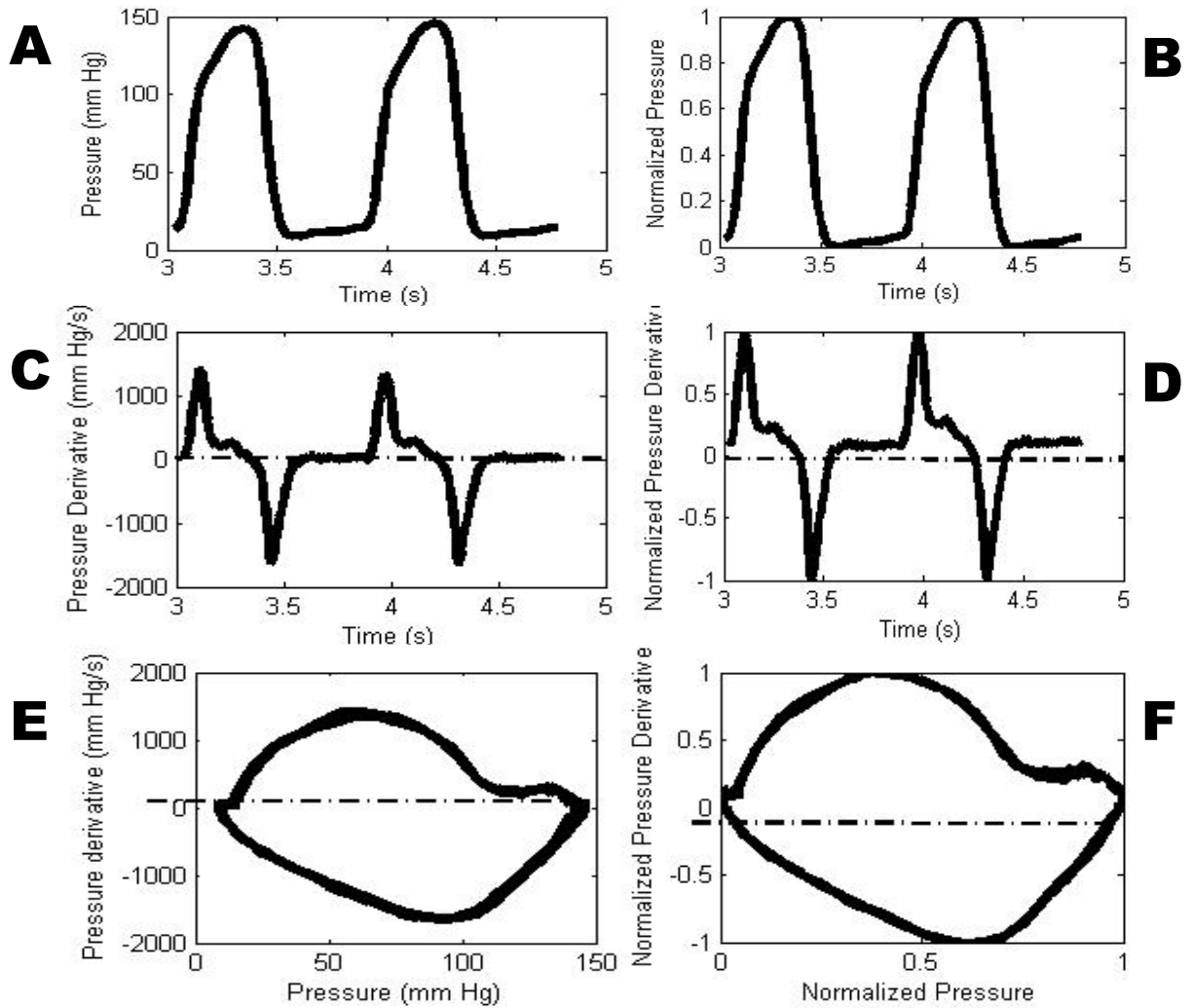
Fig 9.2: Method for converting P and dP/dt into normalized contours and creating PPP and nPPP shown in 2 beats.

9.2 Method

9.2.1 Theory: Derivation of normalized P and dP/dt contours

For each cardiac cycle, LVP was normalized according to:

$$P_N(t) = \frac{(P(t) - P_{min})}{(P_{max} - P_{min})}$$

Eq. 9.1

which assures that $P_{min} = 0$ and $P_{max} = 1$. Figures 9.2a and 9.2b illustrate three beats before and after normalization.

The LV dP/dt was normalized according to:

$$\left(\frac{dP}{dt}\right)_N = \frac{\left(\frac{dP}{dt}(t) - \frac{1}{2}\left[\frac{dP}{dt}_{max} + \frac{dP}{dt}_{min}\right]\right)}{\frac{1}{2}\left(\frac{dP}{dt}_{max} - \frac{dP}{dt}_{min}\right)}$$

Eq. 9.2

yielding $-dP/dt_{peak} = -1$ and $+dP/dt_{peak} = +1$ for each beat. Results are illustrated in Figures 9.2c and 9.2d with normalized loops in Fig 9.2e and 9.2f.

9.2.2 Inclusion Criteria and Data Acquisition

We analyzed 17 datasets from our Cardiovascular Biophysics Laboratory database of simultaneous echocardiographic and high-fidelity hemodynamic recordings. Group clinical characteristics are listed in Table 9.1 (14 subjects) and Table 9.2 (3 subjects). Prior to data acquisition, each subject provided signed, informed consent for participation in accordance with the Institutional Review Board (Human Research Protection Office) of Washington University School of Medicine. The criteria for data selection included: normal LV ejection fraction, normal sinus rhythm, absence of valvular abnormalities and the absence of wall-motion abnormalities or bundle branch block on the ECG. None of the subjects (in Table 9.1) had a history of coronary artery disease or myocardial infarction. 1 subject (Table 9.2) had a history of coronary artery disease/ myocardial infarction. All patients underwent elective cardiac catheterization at the request of a referring cardiologist to establish the presence or absence of suspected coronary artery disease.

Our method of high fidelity, multi-channel micromanometric LVP and simultaneous echocardiography recording has been previously detailed (Chapter 2) [9, 13, 16]. Briefly, simultaneous LV pressure and aortic root pressure measurements were obtained using a 6-F triple transducer pigtail-tipped pressure-volume conductance catheter (SSD-1034; Millar Instruments, Houston, TX). The signal was amplified and calibrated via standard transducer control units (TC-510; Millar Instruments). Catheter placement was achieved by using fluoroscopy to cross the aortic valve, noting that both (distal and mid) pressure channels displayed LV pressure waveforms while the proximal (3rd) sensor displayed aortic root pressures. Pressure signals were input to clinical monitoring systems (Quinton Diagnostics, Bothell, WA or GE Healthcare, Milwaukee, WI) and a custom personal computer via a research interface (Sigma-5DF; CD Leycom, Zoetermeer, The Netherlands) at a sampling rate of 250 Hz. Conductance signals were stored but were not used in this study. Ejection fraction was computed from the calibrated ventriculogram (33 ml of contrast at 11ml/sec, via 6F pigtail catheter (Cordis Corporation, NJ)) immediately after hemodynamic recording.

9.2.3 Hemodynamic data analysis

Pressure was converted for analysis via a custom Matlab script (Matlab 6.0; MathWorks, Natick, MA). Data sets were smoothed digitally by using a five-point average to suppress noise in the derivative [9, 16], attenuating 50% of signal at 40 Hz and 90% above 60 Hz, followed by calculation of continuous dP/dt vs. time t from the smoothed data. For each beat, EDP and $-dP/dt_{peak}$ were extracted from *PPP* or equivalent time-domain contours for both pressure signals.

From the *nPPP*, the P_{NC} and P_{NR} were obtained as shown in Fig 9.2 using a custom MATLAB script. For all subjects, the mean value of P_{max}, P_{min} +dP/dt$_{peak}$ and –dP/dt$_{peak}$, pressure at +dP/dt$_{peak}$ (P_C), pressure at –dP/dt$_{peak}$ (P_R), P_{NC} and P_{NR} were calculated and saved.
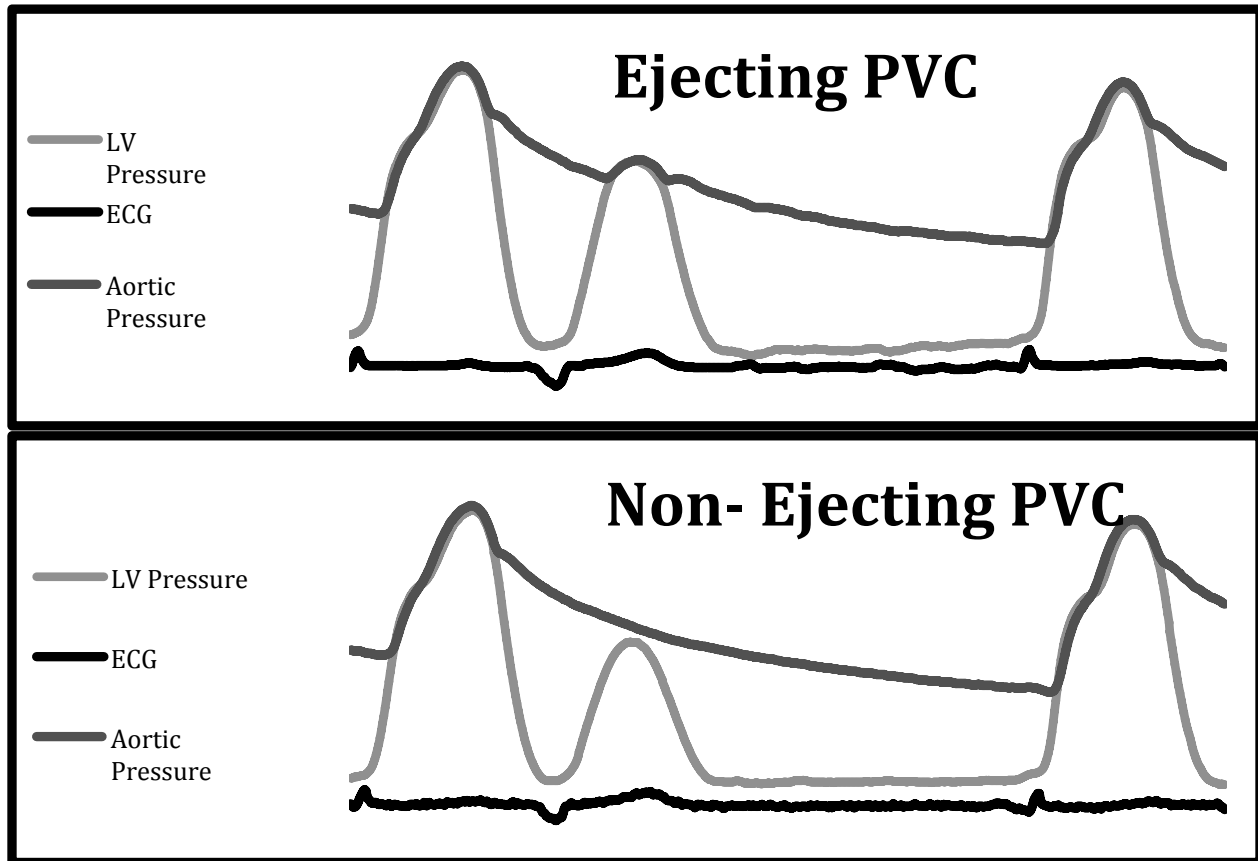
Fig 9.3: Raw hemodynamic data illustrating criteria by which ejecting and non-ejecting PVCs were identified. (Top) Ejecting PVC transiently exceeds aortic root pressure. (Bottom) Non-ejecting PVC does not exceed aortic root pressure. See text for details.

We selected 3 subjects' datasets for PVC analysis. PVCs were first identified from ECG recordings and then classified as ejecting PVCs (E-PVC) or non-ejecting PVCs (NE-PVC) by comparing to the simultaneous aortic root pressure recordings. If the LV pressure and the aortic root pressure recordings intersected or the aortic pressure showed a rise and fall concordant with the LV pressure then it was classified as E-PVC otherwise it was classified as NE-PVC as shown in Fig 9.3. For the subjects the mean value of P_{max}, P_{min}, +dP/dt$_{peak}$, –dP/dt$_{peak}$, P_C and P_R were

calculated for NSR beats as well as E-PVC beats and NE-PVC beats. Mean values for P_{NC} and P_{NR} in NSR, E-PVC and NE-PVC beats were calculated.

9.2.4 Statistical analysis

The mean, standard deviation (SD), maximum and minimum values were calculated for the points of interest in the regular PPP and nPPP. In addition, to determine variation we calculated the coefficient of variation, defined as the ratio of standard deviation to the mean value of the parameter, (as shown in Table 9.3) expressed as a percentage for the 14 subjects included in the inter-subject analysis. To compare NSR and PVC features we used the Student's two-tailed t-test to determine statistical significance, with $p < 0.05$ denoting significance.

9.3 Results

9.3.1 Inter-subject comparison of NSR beats

Table 9.1 shows the subject characteristics for the 14 subjects. Table 9.3 shows the mean, SD, minimum, maximum and the coefficient of variation values of the points of interest in the regular PPP and nPPP based on 4234 cardiac cycles. By definition, normalization reduced the variation in P_{max}, P_{min}, $+dP/dt_{peak}$ and $-dP/dt_{peak}$ to 0. The variation of P_C (9.6%) changed slightly compared to P_{NC} (10.5%) while the variation P_{NR} (6.6%) decreased compared to P_R (11.3%). The variation of both nEDP (27.1%) and nESP (8.9%) increased in comparison to EDP (17.9%) and ESP (6.9%). Among all these P_{NR} had the lowest variation. To illustrate inter-subject variation in PPP loop shape and features Fig. 9.4a shows individual, superimposed beats from 3 subjects. Fig 9.4b shows same beats in the *nPPP*, illustrating the effect of normalization in eliminating the differences in Panel 9.4a.

Parameter	Mean ± SD
Age (years)	62 ± 9
Gender	7M/ 7F
Height (cm)	167±9
Weight (lb)	182±43
BMI (kg/m^2)	29.7±7.8
EDP (mm Hg)	18 ± 3
ESP (mm Hg)	105 ± 7
Ejection Fraction	72 ± 8
No. of beats	302 ± 43
Hypertension	7 (50 %)

Table 9.1: Subject demographics (n= 14). Values are mean ± standard deviation or number (% of total subjects).

	Subject B1	Subject B2	Subject B3
Age (years)	43	63	56
Gender	M	M	M
Ejection Fraction (%)	81	24	54
Height (cm)	196	183	170
Weight (lb)	335	206	165
BMI (kg/m^2)	40	28	26
EDP (mm Hg)	17	15	10
Hypertension	+	+	-
CAD/ previous MI	-	+	-
Total NSR beats	150	232	210
Total PVC beats	9 (NE)	78 (E)	17 (E)

Table 9.2: Subject demographics for intra-subject (n=3) PVC analysis. +/ – denote presence or absence of condition. NE = non-ejecting PVC, E = ejecting PVC.

9.3.2 Intra-subject comparison of NSR and PVC beats

To investigate *nPPP* features and determine the effect of normalization on P_{NR} we compared NSR beats to E-PVCs and NE-PVCs in the same subject. We selected 3 datasets that had significant number of PVCs to permit statistical analysis Table 9.2 shows the clinical

Parameter	Mean	SD	Min	Max	Variation
P_{max} (mm Hg)	137	17	119	165	12.1%
P_{min} (mm Hg)	9.3	3	3.6	13.4	29.7%
dP/dt_{max} (mm Hg/s)	1257	136	1062	1531	10.8%
dP/dt_{min} (mm Hg/s)	-1496	182	-1834	-1266	12.2%
P_C (mm Hg)	61	6	49	72	9.6%
P_R (mm Hg)	87	10	75	104	11.3%
P_{NC} (dimensionless)	0.41	0.04	0.34	0.48	10.5%
P_{NR} (dimensionless)	0.61	0.04	0.56	0.69	6.6%
EDP (mm Hg)	18	3	13	23	17.9%
ESP (mm Hg)	105	7	93	116	6.9%
nEDP (dimensionless)	0.07	0.02	0.03	0.1	27.1%
nESP (dimensionless)	0.76	0.07	0.64	0.9	8.9%

Table 9.3: Group values (n=14) of hemodynamic parameters. SD = Standard deviation; Coefficient of variation is defined in Methods.

Parameter	Subject B1		Subject B2		Subject B3	
	NSR	PVC	NSR	PVC	NSR	PVC
P_{max} (mm Hg)	116	101[#]	140	127[#]	132	92[#]
P_{min} (mm Hg)	11	11	12	12	9	8
dP/dt_{max} (mm Hg/s)	996	758[#]	1190	1026[#]	1007	652[#]
dP/dt_{min} (mm Hg/s)	-1121	-861[*]	-1169	-1019[#]	-1136	-584[#]
P_C (mm Hg)	61	52	73	73	53	47
P_R (mm Hg)	73	61[#]	99	88[#]	87	60[#]
P_{NC}	0.47	0.45	0.48	0.53[#]	0.36	0.46[*]
P_{NR}	0.63	0.59	0.67	0.66	0.63	0.63
EDP (mm Hg)	16	-NA-	16	-NA-	16	-NA-
ESP (mm Hg)	106	-NA-	123	-NA-	89	-NA-

Table 9.4: Mean hemodynamic parameters in NSR vs. PVC analysis subjects. The number of beats is given in Table 2. * represents $p < 0.01$ and # represents $p < 0.0001$.

characteristics. Fig. 9.5 shows PPP and *nPPP* for a NSR and E-PVC beat in the same subject. For clarity, Fig. 9.5C and 9.5D magnifies the P_{NC} and P_{NR} portions of panel 9.5B. As these figures illustrate, normalization aids in visualizing features masked by the differences in P_{max}, P_{min}, $+dP/dt_{peak}$ and $-dP/dt_{peak}$. In Subject B1 (see Table 9.2) we compared NE-PVCs to NSR beats. In concordance with previous results [17], we found that P_{max}, $+dP/dt_{peak}$ and $-dP/dt_{peak}$ were significantly lower in magnitude in the PVC beats (p<0.01). While P_R was statistically different between the 2 types of beats; P_{NR} was not statistically different (p=0.09). In subjects B2 and B3 (Table 9.2), we compared NSR beats to E-PVC beats but not to NE-PVCs because of limited numbers. Similar to subject B1, we found that in B2 and B3, P_{max}, $+dP/dt_{peak}$ and $-dP/dt_{peak}$ were
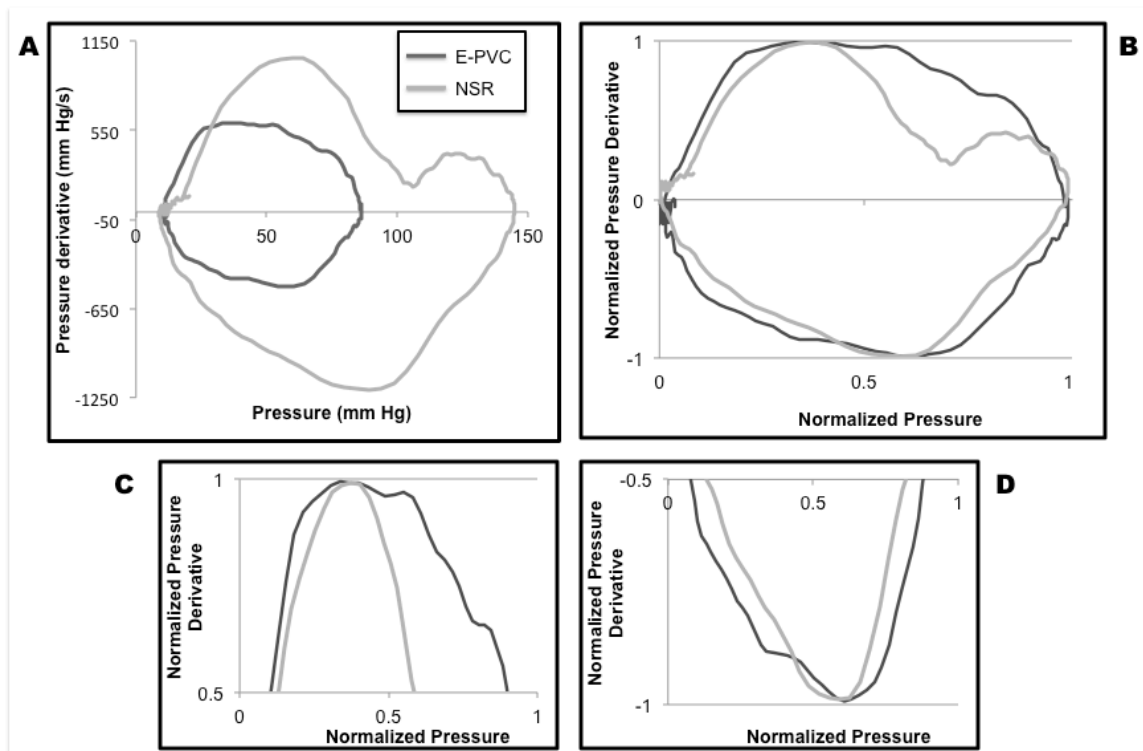
Fig 9.5: A: PPP from 2 beats- NSR and E-PVC recorded from Subject B3. B: Normalization of the same 2 beats. C: Magnified view of nPPP top portion, including $+dP/dt_{peak}$, D: Magnified view of nPPP bottom portion including $-dP/dt_{peak}$. Data points were smoothed using 3 point moving average. See text for details.

much lower in magnitude in the PVC beats ($p<10^{-7}$). Also P_R was statistically different between the 2 types of beats; the value of P_{NR} was not statistically different ($p=0.09$ and $p=1$). This suggests that P_{NR} remains essentially unaltered between NSR and PVC beats. The mean value of P_{NR} (0.64) was comparable to the value of P_{NR} (0.61) obtained from the first part of the study. While P_C did not differ between NSR and PVC due to large intra-subject variation (12.3%), P_{NR} did not differ in spite of the low beat to beat variation (6.3%) indicating a much smaller distribution of P_{NR} values in NSR and PVC beats. Table 9.4 gives mean parameter values and measures of statistical significance.

9.4 Discussion

Normalization of diastolic physiologic data has been employed in a different context previously. Klotz et al [18] proposed a method to estimate the end-diastolic pressure-volume relationships by normalizing LV volumes. They found that normalization generated end-diastolic pressure volume curves having the same shape across different species and pathologies.

The phase plane method has been used in biological and physiological systems [19, 20]. LV pressure phase plane analysis, a component of 4-dimensional physiologic hyperspace [11], has been previously employed [10, 12, 21] to identify new cardiac cycle features. In the quest to identify load-independent chamber properties we explored LV hemodynamics in the *nPPP*. Normalization maps the variable maximum and minimum pressure and dP/dt limits of consecutive beats to the same values and thereby removes loading effects while contraction and relaxation related loop shape features are retained. We evaluated IVC and IVR loop features in different subjects to characterize differences and similarities. We also compared NSR beats to PVCs in 3 subjects.

Both studies showed that P_{NR} remains essentially invariant while other *nPPP* points of interest varied significantly. Hence *nPPP* analysis indicates that P_{NR} is closely conserved.

9.4.1 Phase plane analysis of dynamic systems

Phase plane methods are well established in analysis of nonlinear systems analysis [19]. The method has been used in biological and physiological systems to study behavior involving simple and complex oscillations [19, 20]. *PPP* analysis of IVR has led to novel, causality based, rather than curve fitting based models of pressure decay allowing for modeling pressure decay from before $-dP/dt_{peak}$ to MVO analogous to damped oscillatory behavior [13]. *PPP* analysis provides a way to visualize spatio-temporal differences in LV hemodynamics [16] in diastole. Several studies have used *PPP* to study IVR [15, 18]. Senzaki et al [15] fit the curvilinear relation (using the parameter τ_L) between P and dP/dt during IVR in the *PPP* in failing hearts using a logistic model and showed that it provides a better fit than the linear fit (τ) provided by the customary, exponential model of IV pressure decay.

9.4.2 Load dependence of LV relaxation

Chamber relaxation is known to be determined in part by cross-bridge uncoupling and other load dependent mechanisms [22-29]. Cross-bridge uncoupling requires dissociation of Ca^{2+} from troponin and its sequestration in the sarcoplasmic reticulum [30, 31]. Increased afterload, quantified by end-systolic pressure or volume has a slowing effect on the rate of pressure decay during IVR [23]. Other studies have reported that in normal hearts IVR is load independent while failing hearts show increased load sensitivity [2, 32, 33]. In failing hearts, $-dP/dt_{peak}$ is lower than in normal hearts [32] and its cause remains uncertain.

9.4.3 Inter-subject comparison of nPPP

To determine if *nPPP* can characterize chamber properties that are minimally load-dependent or are load independent, we analyzed data from 14 subjects (302 beats/subject, 4234 beats total; Table 9.1). Normalization eliminated the inter subject variance of P_{max}, P_{min}, $+dP/dt_{peak}$ and $-dP/dt_{peak}$. Normalization did not alter the variation of pressure at which $+dP/dt_{peak}$ occurs (P_C variance = 10% vs. P_{NC} variance = 11%), but it did decrease the variation of pressure at which $-dP/dt_{peak}$ occurs (Table 9.3) (P_R variance =11%, vs. P_{NR} variance = 6.6%). Thus, in contrast to IVC, normalization generated a much <u>smaller</u> variation in P_{NR} during IVR. This is illustrated in Fig. 9.4 comparing *PPP* (left) and *nPPP* (right) in 3 selected subjects.

Since EDP and ESP depend on preload and afterload respectively we normalized these indexes, which generated increased variation in the *nPPP*. The observed increase in variation can be understood by considering at least 2 effects which influence variation. First, the amplitude of pressure oscillation for each beat i.e. its pressure range and second, the intrinsic contraction/relaxation mechanics. Normalizing removes absolute value effects of pressure without altering intrinsic mechanism effects that determine loop features. Hence the observed increased in after normalization suggests that the intrinsic mechanism effects (that determine EDP and ESP) between subjects have higher variation which had been masked by the pressure range variation in PPP.

9.4.4 Hemodynamics of premature ventricular contractions

PVCs provide natural (in contrast to pharmacologic) beat-to-beat load variation. Many studies have utilized PVCs to characterize load effects in contraction and relaxation. Carroll et al [17] studied IVR during PVCs and found that PVCs enhance shortening and augment restoring forces producing a smaller end-systolic chamber. PVCs also delay inactivation and prolong relaxation,

generating increased values of τ while impairing LV filling [34]. PVCs have also been employed to more extensively validate a load independent index of diastolic function [35].

9.4.5 Effect of normalization on PVC hemodynamics

We exploited PVC generated load variation to assess load-dependent features in the *PPP* and the *nPPP*. Information on the PVC datasets is given in Table 9.2 and Table 9.4. Fig 9.5A shows a NSR and E-PVC beat in the PPP and Fig. 9.5B shows the same beats in *nPPP*. As seen in the figure, E-PVC has lower values of P_{max}, $+dP/dt_{peak}$ and $-dP/dt_{peak}$. P_C was not significantly different between NSR and PVC beats although large beat-to-beat variation in each subject was present. P_R was significantly lower in PVCs in all the 3 subjects ($p < 0.001$).

The value of P_{NR} was not significantly different among the 3 subjects between NSR and PVC beats. This revealed that there is essentially no change in the dimensionless pressure at which the peak rate of pressure decay occurred in both NSR and PVC beats. This value is comparable to the value of P_{NR} obtained from the first part of the study (Table 9.3, $P_{NR} = 0.61$). P_{NC} on the other hand was higher in E-PVC compared to NSR. Hence unlike contraction, which shows changes in the rate of pressure rise as a function of pressure in PVCs, the rate of pressure decay as a function of pressure is essentially unchanged during IVR in PVCs suggesting a (relatively) conserved intrinsic relaxation mechanism.

9.4.6 Physiological significance of normalization and possible mechanism

LV contraction and relaxation involves actin-myosin cross-bridge coupling and uncoupling regulated by Ca^{2+} bound to troponin [36-38] and further modulated by the loading conditions involving pressure and its variation. Studies have attempted to understand the contribution of load as factors in contraction and relaxation [2, 22, 26, 32, 33] by physiologic, pharmacologic or surgical interventions to modify load and evaluate response.

Some of the factors determining these intrinsic mechanisms include calcium cycling, sarcomere kinetics, mitochondrial (ATP) function, extracellular matrix, etc. The similar variation of P_C and P_{NC} (Table 9.3) suggests that its variation is determined by factors other than load. On the other hand, the reduced variation of P_{NR} as compared to P_R suggests that its variation is load-dependent but the intrinsic mechanism that constrains P_{NR} to be in the 0.61-0.64 range is conserved. This underscores that *nPPP* is not merely a scaled down version of the regular *PPP*. Rather normalization removes P and dP/dt magnitude effects while maintaining shape based features.

Maintenance of shape-based features was borne out by the intra-subject PVC analysis. The value of P_{NR} was similar in NSR and PVC beats within and across subjects (Table 9.4). Its value was also similar to the value reported in the inter-subject analysis (Table 9.3). This permits the inference that intrinsic relaxation mechanisms are more (tightly regulated) conserved than intrinsic contraction mechanisms. Moreover, contractility and the associated value of P_{NC} in NSR and E-PVC beats is governed by the beat-to-beat variation of preload and afterload while in NE-PVCs it is primarily determined by the Frank- Starling Law and the timing of the PVC relative to the prior beat. Hence an *nPPP* based prediction is that because of the beat-to-beat variation of load, we expect P_{NC} to have larger variation than P_{NR}. Our observations corroborate this prediction. Sarcomere kinetics is a major determinant of relaxation mechanisms [39, 40]. Two features of sarcomere kinetics likely to have a bearing on the limited variation of P_{NR} include [41]- 1) kinetics of Ca^{2+} binding and dissociation from troponin and 2) cross-bridge attachment/detachment and subsequent sarcomere shortening/ lengthening. The relative constancy of P_{NR} suggests that the ratio of maximum rate of crossbridge dissociation to instantaneous pressure (force, wall stress) at which that maximum dissociation rate takes place is

tightly constrained. This preliminary, proof of concept study demonstrates the utility of *PPP* normalization in elucidating novel LV diastolic properties.

9.4.7 Limitations

The main limitations pertain to data acquisition. As noted previously [16], calibration, catheter placement and orientation with respect to the LV axis may have a slight effect on pressure recordings. However calibration offsets the pressure by a constant value which should not affect the normalization process. Calibration and drift are mitigated by pre- and post-calibration of transducers to zero hydrostatic pressure in a $37^{\circ}C$ saline bath. Other issues involving signal processing have been addressed previously [9, 13, 16]. Noisy beats were not analyzed. Moreover, the large (average) number of beats studied in every subject (302) mitigates the effect of noise to an acceptable degree.

Since this is a proof of concept study, the number of datasets analyzed is necessarily limited although the 4234 cardiac cycles analyzed mitigates that limitation to an acceptable degree. Although eight of the datasets analyzed in this study have been previously analyzed for different purposes (16), repeat analysis using a different method (normalization) to test a different hypothesis (load independence of phase plane loop features) is appropriate. Relative physiologic uniformity is achieved as a result of enrollment criteria (normal ejection fraction, no coronary artery disease or myocardial infarctions, no diabetes). P and dP/dt values were not very different (< 50% variation in P_{max}, $+dP/dt_{peak}$, P_C and P_R values). This limitation is mitigated by the second part of the study where we compared NSR to PVC beats in the same subject. The *PPP* in PVC is much smaller and has a different shape from a NSR *PPP* (Fig. 3, Ref 9). In spite of this, P_{NR} remained an essentially conserved feature among the 3 subjects. However, we only studied PVCs in 3 subjects, which is insufficient to draw definitive conclusions regarding trends.

Hence additional studies are needed to elucidate the magnitude of these changes and differentiate between the changes in E-PVCs vs. NE-PVCs. Further work in the *PPP* and physiologic hyperspace is needed involving a greater sample size and specific pathophysiologic states.

9.5 Conclusions

We introduce the *nPPP* for LV hemodynamic analysis. Normalization removes beat-to-beat and inter-subject variation in P and dP/dt limits and thereby, minimizes load effects. We tested applicability in $\sim$ 4400 beats in 14 subjects. In the *nPPP*, the variation of P_{NR}, the (dimensionless) pressure at which $-dP/dt_{peak}$ was inscribed, was very substantially reduced. Comparison of NSR beats to both ejecting and non-ejecting beats PVCs revealed that P_{NR} remained tightly controlled. The observed near constancy of P_{NR} reveals a new aspect of the physiology of diastole and indicates the existence of intrinsic (intracellular) IVR mechanisms for which a possible mechanism is discussed. Thus *nPPP* analysis elucidates novel LV chamber properties, and identifies potential research targets in need of molecular and cellular physiologic explanation.

Reference:

1. Gillebert TC, Sys SU, Brutsaert DL. Influence of loading patterns on peak systolic length- tension relation and on relaxation in cardiac muscle. *J Am. Coll. Cardiol*. 1989; 13: 483- 490.

2. Little WC. Enhanced load dependence of relaxation in heart failure. Clinical implications. *Circulation*. 1992; 85: 2326- 2328.

3. Zile MR, Gaasch WH. Load-dependent left ventricular relaxation in conscious dogs. *Am. J Physiol. Heart Circ. Physiol*. 1991; 261: H691- H699.

4. McLaurin LP, Rolett EL, Grossman W. Impaired left ventricular relaxation during pacing –induced ischemia. *Am. J. Cardiol*. 1973; 32 (6): 751- 757.

5. McCann LL, Parker JO, Butler J. Left ventricular pressure-volume relationship during myocardial ischemia in man. *Circulation*. 1973; 48: 775- 778.

6. Alderman EL, Glantz SA. Acute hemodynamic interventions shift the diastolic pressure-volume curve in man. *Circulation*. 1976; 54: 662- 671.

7. Ludbrook PA, Byrne JD, McKnight RC. Influence of right ventricular hemodynamics on left ventricular diastolic pressure volume relations in man. *Circulation*. 1979; 59: 21- 31.

8. Cooper MW. Postextrasystolic potentiation. Do we really know what it means and how to use it? *Circulation*. 1993; 88: 2692- 2971.

9. Shmuylovich L, Kovács SJ. Stiffness and relaxation components of the exponential and logistic time constants may be used to derive a load-independent index of isovolumic pressure decay. *Am J Physiol Heart Circ Physiol*. 295(6): H2551-9, 2008.

10. Eucker SA, Lisauskas JB, Singh J, Kovács SJ. Phase Plane Analysis of Left Ventricular Hemodynamics, *J. Appl. Physiol*. 90: 2238-2244, 2001.

11. Eucker SA, Lisauskas J, Courtois MR, Kovács SJ. Analysis of left ventricular hemodynamics in physiological hyperspace. *J Appl. Physiol.* 92:323-30, 2002.

12. Chung CS, Kovács SJ. Pressure Phase-Plane Based Determination of the Onset of Left Ventricular Relaxation. *Cardiovasc Eng.* 7:162-171, 2007.

13. Chung CS, Kovács SJ. The physical determinants of left ventricular isovolumic pressure decline: Model-based prediction with in-vivo validation. *Am J Physiol Heart Circ Physiol.* 2008; 294: H1589-H1596.

14. Leite-Moreira AF, Correia-Pinto J, Gillebert TC. Load dependence of left ventricular contraction and relaxation. Effects of caffeine. *Basic Res. Cardiol.* 1999; 94: 284- 293.

15. Senzaki H, Kass DA. Analysis of isovolumic relaxation in failing hearts by monoexponential time constants overestimates lusitropic change and load dependence. *Circ. Heart Fail.* 2010; 3: 268-276.

16. Ghosh E, Kovács SJ. Spatio-temporal attributes of left ventricular pressure decay rate during isovolumic relaxation. *Am J Physiol Heart Circ Physiol.* 2012; 302(5): H1094-1101.

17. Carroll JD, Widmer R, Hess OM, Hirzel HO, Krayenbuehl HP. Left ventricular isovolumic pressure decay and diastolic mechanics after postextrasystolic potentiation and during exercise. *Am. J. Cardiol.* 1983; 51: 583- 590.

18. Klotz S, Hay I, Dickstein ML, Yi GH, Wang J, Maurer MS, Kass DA, Burkhoff D. Single-beat estimation of end-diastolic pressure-volume relationship: a novel method with potential noninvasive application. *Am J Physiol Heart Circ Physiol.* 2006; 291(1): H403-412.

19. Keener J, Sneyd J. Mathematical Physiology: Interdisciplinary Applied Mathematics; v.8. Springer- Verlag, New York, 1998.

20. Paniflov AV, Hogeweg P. Spiral break-up in a modified FitzHugh- Nagumo model. *Phys. Lett. A*. 1995; 176:295- 299.

21. Chung CS, Strunc A, Oliver R, Kovács SJ. Diastolic ventricular-vascular stiffness and relaxation relation: elucidation of coupling via pressure phase plane-derived indexes. *Am J Physiol Heart Circ Physiol*. 2006;291(5):H2415-23.

22. Brutsaert DL, Housmans PR, Goethals MA**.** Dual control of relaxation. Its role in the ventricular function in the mammalian heart. *Circ. Res*. 1980; 47: 637- 652.

23. Chemla D, Coirault C, Hébert J, Lecarpentier Y. Mechanics of relaxation of the human heart. *News Physiol. Sci*. 2000; 15: 78- 83.

24. Eichhorn EJ, Willard JE, Alvarez L, Kim AS, Glamann DB, Risser RC, Grayburn PA. Are contraction and relaxation coupled in patients with and without congestive heart failure? *Circulation*. 1992; 85: 2132- 2139.

25. Gaasch WH, Blaustein AS, Andrias W, Donahue RP, Avitall B. Myocardial relaxation II. Hemodynamic determinants of rate of left ventricular isovolumic pressure decline. *Am J Physiol Heart Circ Physiol*. 1980; 239: H1- H6.

26. Hori M, Inoue M, Kitakaze M, Tsujioka K, Ishida Y, Fukunami M, Nakajima S, Kitabatake A, Abe H. Loading sequence is a major determinant of afterload- dependent relaxation in intact canine heart. *Am J Physiol Heart Circ Physiol*. 1985; 249: H747- H754.

27. Janssen PML. Myocardial contraction- relaxation coupling. *Am J Physiol Heart Circ Physiol*. 2010; 299: H1741- H1749.

28. Karliner JS, Lewinter MM, Mahler F, Engler R, O'Rourke RA. Pharmacologic and hemodynamic influences on the rate of isovolumic left ventricular relaxation in the normal conscious dog. *J Clin Inves*. 1977; 60: 511- 521.

29. Katz LN. The role played by the ventricular relaxation process in filling the ventricle. *Am J Physiol*. 1930; 95: 542- 543.

30. Rice JJ, de Tombe PP. Approaches to modeling crossbridges and calcium- dependent activation in cardiac muscle. *Prog. Biophys. Mol. Biol*. 2004; 85: 179- 195.

31. Bers DM. Calcium fluxes involved in control of cardiac myocytes contraction. *Circulation*. 2000; 87: 275- 281.

32. Prabhu SD. Load sensitivity of left ventricular relaxation in normal and failing hearts: evidence of a nonlinear biphasic response. *Cardiovasc. Res*. 1999; 43: 354- 363.

33. Starling MR, Montgomery DG, Mancini GBJ, Walsh RA. Load independence of the rate of isovolumic relaxation in man. *Circulation*. 1987; 76 (6): 1274- 1281.

34. Stoddard MF, Pearson AC, Kern MJ, Labovitz AJ. The effect of premature ventricular contraction on left ventricular relaxation, chamber stiffness and filling in humans. *Am Heart J*. 1989; 118 (4): 725- 733.

35. Boskovski M, Shmuylovich L, Kovács SJ. Transmitral Flow Velocity-Contour Variation After Premature Ventricular Contractions: A Novel Test of the Load-Independent Index of Diastolic Filling. *Ultrasound Med Biol*. 2008; 34(12): 1901-1908.

36. Baker AJ, Figueredo VM, Keung EC, Camacho SA. Ca^{2+} regulates the kinetics of tension development in intact cardiac muscle. *Am J Physiol Heart Circ Physiol*. 1998; 275: H744- H750.

37. Bombardini T. Myocardial contractility in the echo lab: molecular, cellular and pathophysiological basis. *Cardiovasc. Ultrasound*. 2005; 3- 27.

38. de Tombe PP, Mateja RD, Tachampa K, Mou YA, Farman GP, Irving TC. Myofilament length dependent activation. *J Mol. Cell. Cardiol*. 2010; 48: 851- 858.

39. Piroddi N, Belus A, Scellini B, Tesi C, Giunti G, Cerbai E, Mugelli A, Poggesi C. Tension generation and relaxation in single myofibrils from human atrial and ventricular myocardium. *Eur. J. Physiol*. 2007; 454: 63- 73.

40. Stehle R, Solzin J, Iorga B, Poggesi C. Insights into the kinetics of Ca2+- regulated contraction and relaxation from myofibril studies. *Eur. J. Physiol*. 2009; 458: 337- 357.

41. Little SC, Biesiadecki BJ, Kilic A, Higgins RSD, Janssen PML, Davis JP**.** The rates of Ca^{2+} dissociation and cross-bridge detachment from ventricular myofibrils as reported by a fluorescent cardiac Troponin C*. *J. Biol. Chem*. 2012; 287 (33): 27930- 27940.

Appendix: Abstracts of additional contributions

A1: Relating early diastolic vortex formation to kinematic properties of the ventricle

Erina Ghosh, Leonid Shmuylovich, Sándor J. Kovács

BACKGROUND: Suction initiated early, rapid filling (Doppler E-wave) volume forms an asymmetric toroidal vortex. Its growth is governed by energy transfer constraints which can serve as an index of optimized filling. To quantify vortex growth and assess filling efficiency a dimensionless index - vortex formation time (VFT) has been proposed. VFT is defined as $\int(vdt/D)$ where v is E-wave velocity and D is effective mitral flow orifice diameter. Vortex formation is causally related to chamber properties since suction initiated atrioventricular pressure gradients that generate flow are caused by stored energy manifesting as left ventricular chamber recoil unmasked by relaxation. VFT is a correlate of heart failure and E/E' (ratio of E-wave peak to mitral annular tissue velocity peak E').

HYPOTHESIS: We hypothesized that VFT is related to chamber properties such as stiffness and stored energy.

METHODS: We tested the hypothesis by determining both the VFT to peak instantaneous AV pressure gradient, and the VFT to peak stored elastic recoil energy regressions. We used the parameterized diastolic filling (PDF) formalism as the kinematic model for transmitral flow. By using the clinical E-wave contour as input, we solved the inverse problem for harmonic oscillatory motion to obtain chamber stiffness (k), viscoelasticity (c) and load (x_o). We derived an alternate expression for VFT (VFT$_{kinematic}$) by computing $\int vdt$ with v given by PDF formalism divided by the effective mitral orifice diameter. We also fit the Doppler E-wave as a triangle, whose area divided by the peak M-mode mitral orifice diameter provided VFT$_{geometric}$. We have previously shown that VFT$_{kinematic}$ is analogous to VFT$_{geometric}$. For validation, multiple beats from each of 12 datasets were selected (total beats analyzed 262) from our database of

simultaneous echocardiography – cardiac catheterization (Millar) recordings. VFT was calculated by both the kinematic and geometric methods for each subject. Peak instantaneous pressure gradient (kx_o) and peak recoil energy ($1/2kx_o^2$) were also computed for each beat. VFT values and the kinematic indexes were averaged for each subject and least mean square linear regression was determined.

RESULTS: Results are shown in the Fig A1.1. For peak instantaneous pressure gradient kx_o:
$VFT_{kinematic} = 0.13*(kx_o) +0.83$, $\mathbf{R^2 = 0.34}$ and $VFT_{geometric} = 0.1*(kx_o) +1.62$, $\mathbf{R^2 = 0.45}$. For peak stored energy $1/2kx_o^2$: $VFT_{kinematic} = 1.57*(1/2kx_o^2) +1.86$, $\mathbf{R^2 = 0.42}$ and $VFT_{geometric} = 1.35*(1/2kx_o^2) +2.23$, $\mathbf{R^2 = 0.70}$.

CONCLUSIONS: Our findings support our hypothesis and are the first to relate VFT (a fluid mechanics based index) to kinematic chamber properties. VFT is strongly correlated with peak stored recoil energy ($1/2kx_o^2$). VFT is less strongly correlated with peak atrioventricular gradient (kx_o). Hence we conclude that VFT is determined in part by chamber kinematic properties.
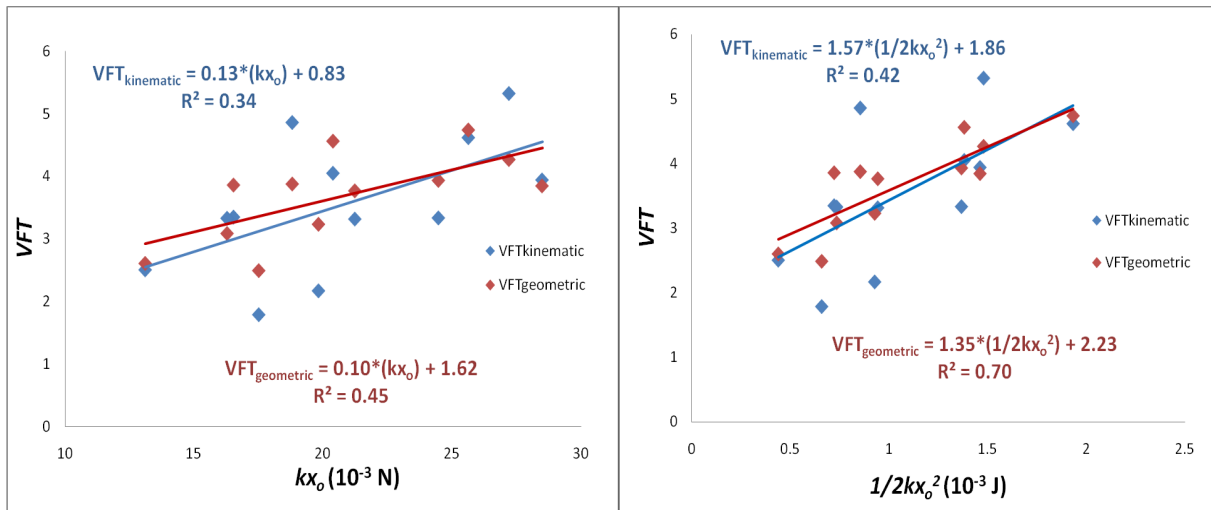

Fig A1.1: (Left) Comparing VFT$_{kinematic}$ (blue) and VFT$_{geometric}$ (red) to PDF determined peak recoil force. (Right) Comparing VFT$_{kinematic}$ (blue) and VFT$_{geometric}$ (red) to PDF determined peak recoil energy.

A2: E-wave associated vortex formation facilitates diastatic mitral leaflet coaptation.

Erina Ghosh, Sándor J. Kovács

BACKGROUND: Coaptation of mitral leaflets during diastasis depends on ventricular compliance, and on multiple other mechanisms including vortex ring formation. During the E-wave, the (toroidal) vortex ring grows behind the leaflets and at diastasis coapts them. Hence vortex ring growth, measured by vortex formation time (VFT), provides a mechanism-based measure of leaflet closing velocity (CV). VFT is a known diastolic function (DF) correlate. We hypothesized that VFT is related to CV (M-mode, E to F slope).

METHODS: 12 datasets (average age 56, 6 men) with normal LVEF, normal coronary anatomy and normal valve function were selected from our simultaneous echocardiography-high fidelity (MILLAR) catheterization database. VFT was calculated using established methods. CV was determined from M-mode via a custom MATLAB program. For each dataset an average of 27 cardiac cycles were analyzed (total 322 cycles) to generate averaged VFT values and CVs for each subject.

RESULTS: In accordance with the hypothesis, the linear correlation between VFT vs. CV was significant ($R^2 = 0.55$, slope = -0.02). VFT vs. CV are linearly correlated. The negative slope indicates that as VFT increases (worsening DF) closing velocity decreases.

CONCLUSION: Efficient vortex formation facilitates normal leaflet coaptation at mid-diastole (diastasis) and is a DF correlate.
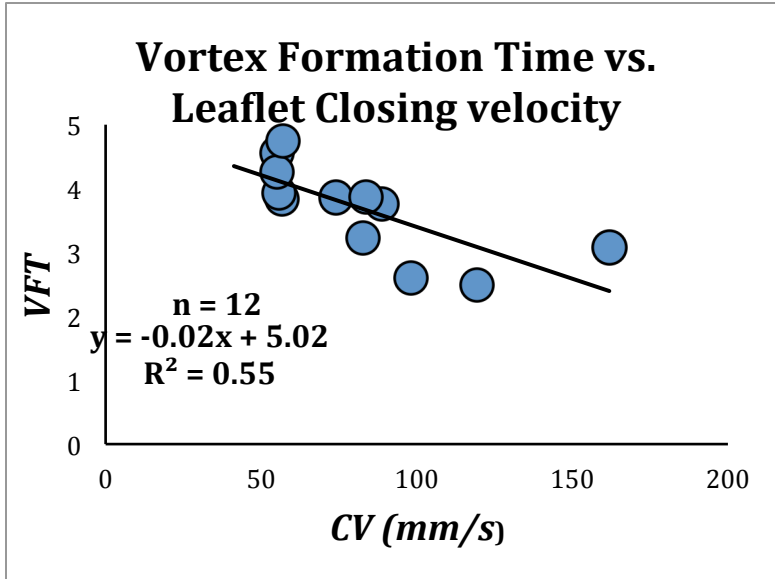
Vortex Formation Time vs. Leaflet Closing velocity

VFT

n = 12
y = -0.02x + 5.02
$R^2 = 0.55$

CV (mm/s)

Fig A2.1: Correlating VFT with anterior mitral leaflet closing velocity.

A3: Diastolic Function in Olympic Athletes vs. Controls: Stiffness and Relaxation Based Echocardiographic Comparison

Astrid Apor, Béla Merkely, Thomas Morrell, Simeng Zhu, Erina Ghosh,

Hajnalka Vágó, Péter Andrássy, Sándor J. Kovács

Relative to controls, the athlete heart's physiologic hypertrophy is characterized by increased left ventricular (LV) chamber dimension, mass and wall-thickness. Diastolic function (DF) comparison between athletes and controls has employed conventional echocardiographic transmitral flow (Doppler E-wave) derived indexes (peak flow velocity, deceleration time, etc), which are load-dependent and obscure the mechanistic (stiffness, relaxation, load) determinants of the E-wave. In this study, conventional, kinematic model-derived and load-independent indexes of DF were used to compare athletes to controls with a focus on stiffness and relaxation chamber properties. Echocardiographic and MRI data from 22 master athletes (canoeing) and 21 sedentary controls was analyzed (1290 Doppler E-waves; 702 in athletes, 588 in controls, 30 per subject, average). LV mass and chamber size was determined from MRI data. Quantitative DF assessment utilized an established kinematic model of filling that uses the digitized Doppler E-wave contour as input and characterizes DF in terms of chamber stiffness (k), relaxation/viscoelasticity (c), load (x_o). We observed significant chamber stiffness (k), load (x_o) and E-wave duration differences between groups. Concordant with prior studies, significant group differences in LV mass and dimension were also noted. These results indicate that physiological LV remodeling of the athlete heart at rest generates numerically quantifiable alterations in specific chamber properties. Assessment of DF using these methods during exercise will further elucidate the dynamic interplay between relaxation and stiffness as DF determinants.

A4: Diastolic Function Alteration Mechanisms in Physiologic vs. Pathologic Hypertrophy are Elucidated by Model-Based Doppler E-Wave Analysis

Simeng Zhu, Thomas Morrell, Astrid Apor, Erina Ghosh, Sándor J. Kovács

One cardiac specific result of athletic training is increased left ventricular (LV) wall-thickness termed physiologic hypertrophy (PhH). In contrast, pathologic hypertrophy (PaH) can be due to chronic hypertension, aortic stenosis or to genetic mutation of sarcomeric proteins causing hypertrophic cardiomyopathy (HCM). Because morphologic similarities (LV dimension, wall thickness, mass, etc) and functional index similarities (LVEF, cardiac output, peak filling rate, etc) limit diagnostic specificity, a method that differentiates between PhH vs. PaH has practical value. Conventional echocardiographic, diastolic function (DF) indexes have limited ability to differentiate and cannot provide chamber property (stiffness, relaxation, load) information. We hypothesized that compared to conventional metrics, kinematic model-based DF assessment can differentiate between PhH vs. PaH and, by providing chamber properties, has even greater value. For validation, we assessed DF in three age-matched groups: pathologic (HCM) hypertrophy (PaH, n=14), physiologic hypertrophy (olympic athletes, PhH n=21) and controls (n=21). MRI confirmed presence of both types of hypertrophy and determined LV mass and chamber size. Model-based indexes were: chamber stiffness (k), relaxation/ viscoelasticity (c), and load (x_o). Conventional indexes were: E_{peak}, E/A, AT, DT. We analyzed 1500 E-waves distributed as: 328 (PaH), 672 (athletes), 500 (controls). E_{peak} and E/A did not differentiate between groups, while AT and DT did. Load (x_o) did not differ between groups. PaH had significantly higher relaxation/viscoelasticity (c) and chamber stiffness (k) vs. PhH. Hence, model-based DF analysis differentiates PhH vs. PaH while quantifying chamber stiffness and relaxation. It simultaneously

elucidates the offsetting role of impaired relaxation vs. increased stiffness on E-wave shape that

explains why E_{peak} and E/A are incapable of differentiating between groups.

A5: Low-Sodium DASH Diet Improves Diastolic Function, Contractility, and Ventricular-Arterial Coupling in Hypertensive Heart Failure with Preserved Ejection Fraction

Scott L. Hummel, E. Mitchell Seymour, Robert D. Brook, Samar S. Shet, Joanna M. Wells,

Erina Ghosh, Simeng Zhu, Alan B. Weder, Sándor J. Kovács, Theodore J. Kolias

Background: Heart failure with preserved ejection fraction (HFPEF) involves failure of cardiovascular reserve in multiple domains. In HFPEF animal models, dietary sodium restriction improves ventricular and vascular stiffness and function. We hypothesized that the sodium-restricted Dietary Approaches to Stop Hypertension diet (DASH/SRD) would improve left ventricular diastolic function, arterial elastance, and ventricular-arterial (V-A) coupling in hypertensive HFPEF.

Methods and Results: Thirteen patients with treated hypertension and compensated HFPEF consumed the DASH/SRD for 21 days. We measured baseline and post- DASH/SRD brachial and central blood pressure (via radial arterial tonometry), and cardiovascular function with Doppler-based echocardiographic measures (all previously invasively validated). Diastolic function was quantified via the Parametrized Diastolic Filling formalism, which yields relaxation/viscoelastic (**c**) and passive/stiffness (**k**) constants through analysis of Doppler mitral inflow velocity (E-wave) contours. Effective arterial elastance (Ea) was calculated as central end-systolic pressure divided by stroke volume. Contractility was defined as the maximum rate of change of pressure normalized stress (dσ*/dTmax), and V-A coupling as the ratio dσ*/dTmax:Ea.

The DASH/SRD reduced clinic and 24-hour brachial systolic pressure (155±35 to

138±30 and 130±16 to 123±18 mmHg, both p=.02) and central end-systolic pressure trended lower (116±18 to 111±16 mmHg,p=.12). In conjunction, diastolic function improved (**c**, 24.3±5.3 to 22.7±8.1 s-1;p=.03; **k**, 252±115 to 170±37 s-1;p=.03), d**σ***/dtmax increased (1.6±0.5 to 1.8±0.5 s-1;p=.01), Ea decreased (2.0±0.4 to 1.7±0.4 mmHg/ml;p=.007), and V-A coupling improved (d**σ***/dtmax:Ea, 0.8±0.3 to 1.1±0.4 mmHg/ml/s;p=.02).

Conclusions: In HFPEF patients, the sodium-restricted DASH diet was associated with favorable changes in ventricular diastolic function and systolic performance, arterial elastance, and V-A coupling.

A6: Normalized Pressure Phase Plane (NPPP) analysis reveals invariant properties of isovolumic relaxation

Erina Ghosh, Sándor J. Kovács

Background: To fit the left ventricular (LV) isovolumic relaxation contour after minimum dP/dt, an exponential decay with time constant τ is assumed. A simple graphical method to calculate τ is provided by the pressure phase plane (PPP), spanned by the rate of change in pressure (dP/dt) vs. pressure (Fig.1 -C). LV relaxation has been previously characterized in the PPP. To reveal the underlying mechanisms of relaxation we define the normalized PPP (NPPP) as follows: $0 \leq P \leq 1$ and $-1 \leq dP/dt \leq +1$ (Fig 1.D). This eliminates the effect of load on P and dP/dt. We calculated the normalized pressure when peak -dP/dt ($P_{N,-1}$) is reached and its associated normalized τ value (τ_n). We hypothesize that the normalized τ value is a physiologic invariant among subjects and it can be used to accurately predict the actual τ value.

Methods: Pressure data for 10 subjects was plotted in the NPPP (1352 beats). For each subject $P_{N,-1}$ and τ_n for each beat was calculated and averaged. For validation τ_n per beat provided average τ_n for all 10 subjects. We derived the mathematical relationship between τ_n and actual τ and used the relationship to estimate the actual τ (τ_{Avg_Calc}) of each subject.

Results: The mean and variance for τ_n was 0.713 ± 0.0035 and τ_{Avg_Calc} showed excellent correlation with actual τ for each subject ($R^2 = 0.87$).

Conclusion: Computing τ_n in the NPPP, reveals that τ_n is essentially invariant among subjects. The mean τ_n (0.713) can be used to estimate actual τ with very little error (mean absolute error = 0.004 s) and the calculated values (τ_{Avg_Calc}) correlate very well with the measured (MILLAR) τ values. Hence NPPP analysis of hemodynamic data removes load related P and dP/dt effects and reveals the underlying, load-independent dynamic attributes of isovolumic relaxation

Curriculum Vitae

Erina Ghosh
Washington University School of Medicine
Campus Box 8086
660 S. Euclid Avenue
St. Louis, MO 63110
314-454-7614
Erina.ghosh@gmail.com

MAILING ADDRESS
274 Nob Hill Drive
Elmsford, NY 10523

DEGREES
Ph.D. Biomedical Engineering, August 2014
M.Tech. Biotechnology and Biochemical Engineering, May 2008
B.Tech. Biotechnology and Biochemical Engineering, May 2008

TEACHING
Department of Biomedical Engineering, Washington University in St Louis, MO   2011
Teaching Assistant for Quantitative Physiology

EDUCATION
Washington University School of Engineering and Applied Sciences, St Louis, MO 2008-2014
Currently pursuing Biomedical Engineering PhD.
Current GPA of 3.92

Indian Institute of Technology, Kharagpur   2003-2008
M.Tech in Biotechnology and Biochemical Engineering
Final GPA of 8.21/10

Indian Institute of Technology, Kharagpur   2003-2008
B. Tech (Honors) in Biotechnology and Biochemical Engineering
Final GPA of 8.21/10

HONORS/ AWARDS
American Heart Association, Predoctoral fellowship   2011- 2012

POSITIONS/ EMPLOYMENT
Cardiovascular Biophysics Laboratory, Washington University in St Louis, MO   2009- 2014
Graduate Research Assistant

Department of Biotechnology, Indian Institute of Technology, Kharagpur   2007
Undergraduate Teaching Assistant, Microbiology

PUBLICATIONS
MANUSCRIPTS
1. Zhu S, Morrell T, Apor A, **Ghosh E**, Kovács SJ. Diastolic function alteration mechanism in physiologic vs. pathologic hypertrophy are elucidated by model- based Doppler E-wave analysis. *In review, Journal of Exercise Science and Fitness*.
2. **Ghosh E**, Caruthers SD, Kovács SJ. The intraventricular diastolic vortex to L-wave relation: model-based prediction with in-vivo validation. *J. Appl Physiol*. 117(3): 316-324, 2014.
3. **Ghosh E**, Kovács SJ. The Vortex Formation Time to Diastolic Function Relation: Assessment of Pseudonormalized vs. Normal Filling. *Physiol. Rep*. 1(6): e00170, 2013.
4. **Ghosh E,** Mossahebi S, Zhu S, Chen H, Shmuylovich L, Kovács SJ. Quantification of global diastolic function by kinematic modeling–based analysis of transmitral flow via the Parametrized Diastolic Filling formalism. *In press, Journal of Visual Experiments.*
5. **Ghosh E**, Kovács SJ. The quest for load- independent left ventricular chamber properties: Exploring the normalized pressure phase plane. *Physiol. Rep.* 1(3): e00043, 2013.
6. Hummel SL, Seymour EM, Brook RD, Sheth SS, **Ghosh E**, Zhu S, Weder AB, Kovács SJ, Kolias TJ. Low-sodium DASH diet improves diastolic function, contractility and ventricular- arterial coupling in hypertensive heart failure with preserved ejection fraction. *Circ. Heart Failure.* 2013.
7. Apor A, Merkely B, Morrell T, Zhu S, **Ghosh E**, Vágó H, Andrássy P, Kovács SJ. Diastolic Function in Olympic Athletes vs. Controls: Stiffness and Relaxation Based Echocardiographic Comparison. *Journal of Exercise Science and Fitness.* 11(1): 29-34, 2013.
8. **Ghosh E,** Kovács SJ. Early left ventricular diastolic function quantification using directional impedances. *Ann. Biomed. Eng.* 2013; 41(6): 1269- 1278.
9. **Ghosh E**, Kovács SJ. Spatio-temporal inhomogeneity of left ventricular pressure during isovolumic relaxation. *Am J Physiol Heart Circ Physiol*. 2012; 302(5):H1094-101.
10. **Ghosh E**, Shmuylovich L, Kovács SJ. The vortex formation time to left ventricular early, rapid filling relation: model based prediction with echocardiographic validation. *J Appl Physiol*. 109(6): 1812-1819, 2010.

CONFERENCE PUBLICATIONS

Conference Proceedings Papers

1. **Ghosh E**, Kovács SJ. Quantitative assessment of left ventricular diastolic function via Longitudinal and Transverse flow impedances. *Conf Proc IEEE- Eng Med Biol Soc,* 2012: 5595-5598.
2. **Ghosh E**, Shmuylovich L, Kovács SJ. Determination of early diastolic LV vortex formation time (T*) via the PDF formalism: a kinematic model of filling. *Conf Proc IEEE Eng Med Biol Soc*. 2009:2883-6.

Abstracts

1. **Ghosh E**, Kovács SJ. Model-based re-definition of vortex formation time differentiates between pseudonormal vs. normal left ventricular echocardiographic filling patterns. November 2013. American Heart Association Scientific Sessions. Dallas, TX.

2. **Ghosh E**, Kovács SJ. Normalized Pressure Phase Plane (NPPP) analysis reveals invariant properties of isovolumic relaxation. November 2012. American Heart Association Scientific Sessions, Los Angeles CA.

3. **Ghosh E**, Kovács SJ. Longitudinal and Transverse Impedance can Quantify Left Ventricular Diastolic Function. March 2012. 61st Annual Scientific Sessions of the American College of Cardiology, Chicago, IL.

4. **Ghosh E**, Kovács SJ. E-wave associated vortex formation facilitates diastatic mitral leaflet coaptation. April 2011. 60th Annual Scientific Sessions of the American College of Cardiology. New Orleans, LA.

5. **Ghosh E**, Shmuylovich L, Kovács SJ. Relating early diastolic vortex formation to kinematic properties of the ventricle. September 2010. 19th Cardiovascular Systems Dynamics Society. Fukoka, Japan.

RESEARCH SUPPORT

Completed Support
American Heart Association, Heartland Affiliate
Predoctoral Fellowship: 01/01/11- 12/31/12
Project Number: 11PRE4950009
Role: PI
Title: Kinematic derivation and validation of left ventricular vortex formation time (LVVFT) as an index of diastolic function.